Measurement of Higgs Boson Decays to Bottom and Charm Quarks in the WH Production Channel with the ATLAS Experiment

by

Irina Ene

A dissertation submitted in partial satisfaction of the

requirements for the degree of

Doctor of Philosophy

in

Physics

in the

Graduate Division

of the

University of California, Berkeley

Committee in charge:

Professor Heather Gray, Chair
Professor Matt Pyle
Professor Karl Van Bibber

Spring 2024

Measurement of Higgs Boson Decays to Bottom and Charm Quarks in the WH Production Channel with the ATLAS Experiment

Abstract

Measurement of Higgs Boson Decays to Bottom and Charm Quarks in the WH Production Channel with the ATLAS Experiment

by

Irina Ene

Doctor of Philosophy in Physics

University of California, Berkeley

Professor Heather Gray, Chair

This thesis presents a measurement of Higgs boson decays to bottom and charm quarks, where the Higgs boson is produced in association with a W boson, using proton-proton (pp) collision data with a total luminosity of 140 fb^{-1} at a center-of-mass energy of $\sqrt{s} = 13$ TeV, collected with the ATLAS detector during Run 2 of the Large Hadron Collider (LHC). The analysis makes use of machine learning techniques to identify bottom and charm quarks and discriminate between signal and background, and implements a coherent treatment in the modelling of the systematic uncertainties affecting the measurement of the $WH(H \to b\bar{b})$ and $WH(H \to c\bar{c})$ processes, which leads to an enhancement in the sensitivity of the measurement compared to previous similar analyses. The $WH(H \to b\bar{b}/c\bar{c})$ processes are found to be compatible with the predictions of the Standard Model. For the $WH(H \to b\bar{b})$ process, an excess of events over the background expectation is observed with a significance of 4.8σ (5.3σ expected). The ratio between the signal yield and the Standard Model prediction is measured to be 0.88 ± 0.14 (stat.) $\pm$ 0.14 (syst.). For the $WH(H \to c\bar{c})$ process, no excess is observed over the background prediction and an observed (expected) upper limit of 19.1 (18.4) times the Standard Model predicted cross section times the branching ratio is set at the 95% confidence level. Direct constraints on the Higgs-bottom and Higgs-charm coupling modifiers are also set, with the ratio $|\kappa_c/\kappa_b|$ being constrained to be less than 4.9 ($|\kappa_c/\kappa_b| < 4.5$ expected) at the 95% confidence level.

For the identification of Higgs decays to bottom and charm quarks, jet reconstruction and flavor tagging represent crucial data processing tasks. They depend, in turn, on information about the reconstructed tracks which correspond to the trajectories of charged particles produced in pp collisions at the LHC and recorded with the ATLAS detector. The ATLAS track reconstruction algorithm, based on a combinatorial Kalman filter, requires an initial estimate (seed) of the track parameters in order to subsequently perform track finding. This thesis presents the implementation and performance of the seed finding algorithm used

by ATLAS during Run 3 of the LHC. The efficiency of seed finding is found to be high (85%−95% for a fiducial selection of charged particles produced in $t\bar{t}$ events), as is required in order to maintain a high efficiency during the subsequent track finding stage. The duplicate and fake track seed creation rates are also found to be comparatively high, with the latter depending directly on the number of interactions per bunch crossing, μ. While the seed finding algorithm has been extensively optimized for Run 3, the high-luminosity upgrade of the LHC (HL-LHC), slated to begin operation around 2029, is expected to have μ up to 200, which is well in excess of the average value of $\langle\mu\rangle = 45$ seen in Run 3. Hence, the seed finding algorithm must be revisited to cope with the much harder combinatorics and updated to exploit the characteristics of the planned Inner Detector upgrade: the ATLAS Inner Tracker (ITk).

The measurement of $H \to c\bar{c}$ decays will significantly benefit from the at least 3000 fb^{-1} dataset that will be collected during the operation of the HL-LHC. However, the harsh conditions at the HL-LHC pose a significant problem for track reconstruction, given that the time needed for reconstructing complex events scales combinatorially with pile-up. In order to stay within the limited computing budget, the track reconstruction algorithm for the ITk must be updated to minimize the total processing time per event. This thesis presents a study of the CPU timing and tracking performance of the fast ITk track reconstruction chain, a variant of the offline track reconstruction chain with significantly reduced CPU requirements, within the context of performing track reconstruction at trigger level where the latency requirements are stringent. The fast ITk reconstruction is found to provide nearly the same tracking performance as the offline ITk reconstruction, but with only a quarter of the CPU needs. This makes the fast ITk track reconstruction algorithm a viable candidate for track reconstruction at trigger level.

"It is the struggle itself that is most important. We must strive to be more than we are. It does not matter that we will never reach our ultimate goal. The effort yields its own rewards."

Lt. Cmdr. Data, Star Trek: The Next Generation

Contents

List of Figures

List of Tables

Acknowledgments

The work presented in this thesis could not have been possible without the support from many colleagues (including but not limited to UC Berkeley, Lawrence Berkeley National Lab, and ATLAS collaborators), friends, and family, for which I will always be very grateful; thank you to every single person who took some time out of their busy day to help me, professionally and/or otherwise! Although there were times when external circumstances made it seem like getting a PhD would not be feasible for me, I am happy that I managed to persevere in spite of the obstacles and to achieve this significant milestone.

I'd like to thank my advisor, Heather Gray, for taking me on as her mentee and seeing me through my journey in experimental particle physics. Among other things, she has introduced me to charged particle track reconstruction and the study of Higgs to charm decays, two topics for which I will always have a deep fondness. She also harbored a very welcoming and inclusive enviroment in her research group, one that prioritized a balanced approach between life inside and outside of research, which came as a much appreciated and needed change during one of the lowest points of my graduate years. I also thank my other thesis committee members, Matt Pyle and Karl Van Bibber, for reviewing this manuscript.

I feel extremely grateful that I got to be a part of the ATLAS group at LBNL. Every person in the group is extremely knowledgeable about various aspects of ATLAS operation and/or physics analysis and it was very reassuring to know that if I had any questions, there was always an expert an email or Mattermost message away! I am very thankful for everybody that I had some overlap with, past or present – regardless of whether we had any direct interaction or not, I have definitely learned a lot from you!

I want to thank my first postdoc mentor, Xiaocong Ai, for the help and support she provided during my first particle physics related project – the positive experience I had helped me decide that it was worth transitioning the focus of my PhD to a new field. Thank you to Miha Muskinja for helping me get started with contributing to the $VH(H \to b\bar{b}/c\bar{c})$ legacy analysis. A huge thank you also goes to Maria Mironova for all the continued help she has provided, in particular during the past few months of working on this thesis, as I was trying to understand the many subtleties of the legacy analysis – her help has proved indispensable as I was writing Chapter 5. On this note, I am also very thankful for the pleasant interactions I had with all the other members of the $VH(H \to b\bar{b}/c\bar{c})$ legacy analysis group. Additionally, I am very grateful to Louis-Guillaume Gagnon for all the hard work he put in to make sure that the seeding pub note saw the light of day in a timely manner, so that it could be included in Chapter 6. I am also thankful for all the help I have received at some point or another from the other postdocs in the group: Tomohiro Yamazaki, Beomki Yeo, and Carlo Varni.

I have also enjoyed all the interactions I had with the other ATLAS graduate students: Johannes, Robin, Ryan, Cesar, Greg. I am very grateful for these interactions, which range from collaborating on the same projects to answering general questions about ATLAS and/or particle physics to just providing some kind words when I needed to hear them or sharing some great memes – thank you all, I am glad that I got to experience what it means to receive support from your fellow graduate students!

Thank you to everybody who keeps the Berkeley physics department up and running, and especially to Joelle Miles for always looking out for me and helping me navigate all the bureaucracy associated with a mid-PhD transition.

I am very thankful for the support I have received from my friends during this long journey. I am especially grateful to Joanne Tan for always providing me with a safe space to vent about the struggles of being a graduate student, as well as cheering me up with stories that involve ignoring all sense of reason when it comes to chili oil. I am also thankful that I got a chance to appreciate the beauty of many animal friends during my daily walks: the Berkeley campus squirrels (especially Rupert), kitties and chickens in the neighborhood, and bunnies, goats, and sheep at Tilden Little Farm and in Goleta.

Lastly, but most importantly, I want to thank my family in Romania and New York for always supporting me in my endeavors and making me feel valued and loved, even though we have been physically separated by thousands of miles for many years – I love you and miss you all! I am also extremely thankful for my partner, John Mark, who has always been my biggest supporter during this 9 year journey (the first 5 years of which we both experienced the ups and downs of being physics graduate students at Berkeley). We have both grown a lot (remember those times when we struggled with those nearly intractable integrals on the statistical mechanics problem sets?) and I can't wait to see what the future brings for us (but I know it will definitely involve more Pusheen plushies)!

Chapter 1

Introduction

This thesis presents a measurement of Higgs boson decays to bottom and charm quarks, where the Higgs boson is produced in association with a W boson, using pp collision data with a total luminosity of 140 fb^{-1} at a center-of-mass energy of $\sqrt{s} = 13$ TeV, collected with the ATLAS detector during Run 2 of the Large Hadron Collider (LHC).

The research presented in this thesis was completed within the ATLAS Collaboration, in close collaboration with many colleagues. The goal of this thesis is to present the main results obtained during my PhD and highlight my personal contributions, which are also summarized below. Figures and results obtained by others are indicated by providing the reference(s) for the appropriate sources. The thesis is structured as follows:

Chapter 2 provides a brief theoretical introduction to the Standard Model of particle physics, with an emphasis on the Higgs mechanism and the properties of the Higgs boson. An overview of the phenomenology of events produced at the LHC and the generation and simulation of events is also provided.

Chapter 3 introduces the Large Hadron Collider and the ATLAS experiment.

Chapter 4 provides an overview of the ATLAS algorithms used to reconstruct raw detector signal into physics objects that correspond to different observed particles.

Chapter 5 represents the main part of this thesis. This work was primarily performed as part of a larger analysis, the ATLAS $VH(H \to b\bar{b}/c\bar{c})$ Legacy Run 2 analysis. As a member of this analysis group, I was responsible for deriving the necessary modelling uncertainties for the $W+$jets background in the $VH(H \to c\bar{c})$ regime. I additionally helped with validating the harmonized implementation of the $VH(H \to b\bar{b}/c\bar{c})$ likelihood fit within the statistical analysis framework and performed several studies relevant to the implementation of the $W+$jets modelling uncertainties within the fit model. Within the context of this thesis, I performed the measurements of the $WH(H \to b\bar{b})$ and $WH(H \to c\bar{c})$ processes using data from the 1-lepton channel only and the interpretation of the results in terms of the Higgs coupling modifiers, both of which are presented in Section 5.8.

Chapter 6 presents a study of the performance of the seed finding algorithm used by ATLAS during Run 3 of the LHC. As one of the main analyzers, I worked on developing a codebase to study the performance of the seed finding algorithm, generated plots of the relevant performance metrics, and contributed to writing the paper. This study is published as Ref. [1].

Chapter 7 presents a study of the CPU timing and tracking performance of the fast ITk track reconstruction chain, within the context of performing track reconstruction at trigger level at the High-Luminosity LHC. I was in charge of developing the codebase necessary to run the study workflow and generated the performance plots shown in this chapter. Additionally, I ran the HEP-SPEC06 benchmarking needed to quantify the CPU timing performance of the fast ITk reconstruction chain. The results presented in this chapter are included in Ref. [2], were they are used to highlight the fast ITk track reconstruction as a software-based demonstrator for tracking at the Event Filter level for the High-Luminosity LHC.

Chapter 8 contains the overall conclusions.

Before joining the ATLAS Collaboration, I spent several years performing research in the field of astrophysics. My focus was on studying the kinematics of massive elliptical galaxies located up to a distance of 108 Mpc in the northern sky. The results of my work have been published in Refs. [3–5]. This work is not included as part of this thesis.

Chapter 2

Theoretical Introduction

The Standard Model (SM) of particle physics represents the theoretical framework used to describe the fundamental particles in the Universe and their interactions [6–32]. It provides the most successful description of the experimental data that has been collected so far (although there are still questions that the SM does not explain, such as the origin of dark matter). This chapter provides an outline of the SM framework, with an emphasis on the formalism of the Higgs mechanism. It also includes a description of Higgs boson properties that can be measured at the LHC and a brief introduction to how theoretical predictions are generated for hadron collider experiments.

2.1 The Standard Model

The SM is a quantum field theory (QFT) in which the particles are excitations of fundamental quantum fields. The theory is based on the Lagrangian formalism, with the Lagrangian density $\mathcal{L}(\psi(x), \partial_\mu \psi(x))$ being used to describe the dynamics of a field $\psi(x)$. In this formulation, symmetries (transformations that keep the Lagrangian density unchanged) play an important role as, per Noether's theorem, each symmetry corresponds to a conserved quantity [34]. Symmetries can be global or local. For a global symmetry, the transformation is the same at all space-time points, while for a local symmetry, the transformation is allowed to vary as a function of space-time.

The fundamental particles of the SM can be grouped according to their quantum numbers into a scheme like the one shown in Figure 2.1. Based on their intrinsic angular momentum (spin), the particles can be classified as either fermions or bosons, with fermions being particles with half-integer spin that follow Fermi-Dirac statistics [35, 36] and bosons being particles with integer spin that follow Bose-Einstein statistics [37, 38].

The fermions are divided into three generations. The first generation fermions make up all the stable matter in the observable Universe. The second and third generation fermions can be thought of as heavier versions of the first generation fermions, as they have identical quantum numbers but larger masses. The second and third generation fermions are unstable

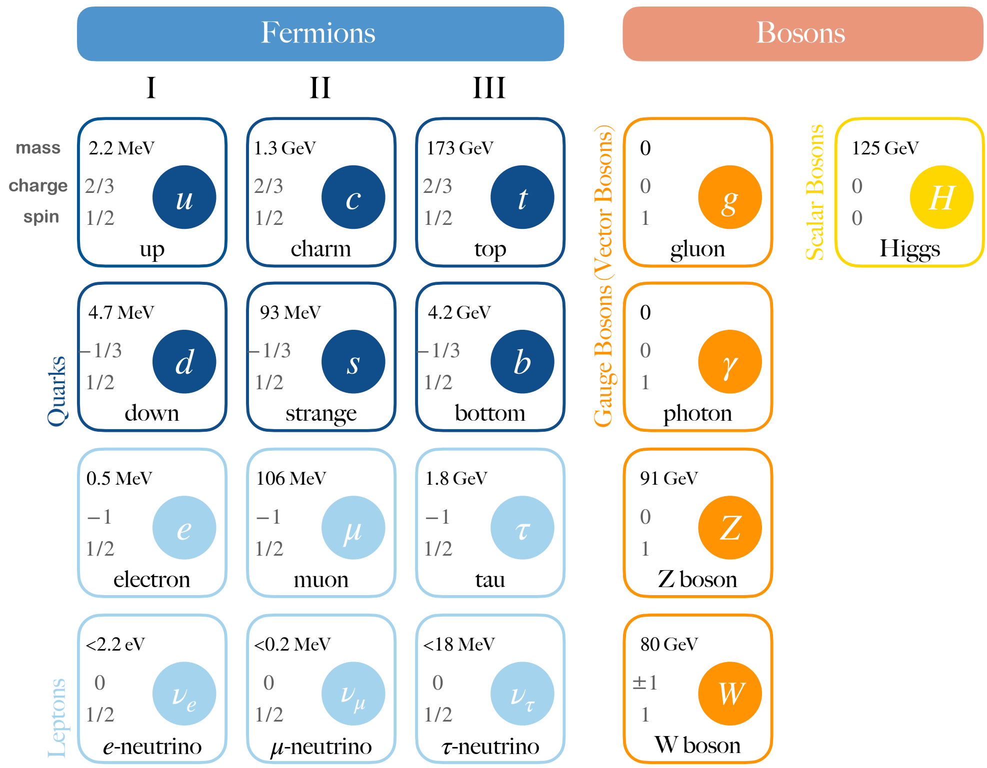

Figure 2.1: The fundamental particles of the Standard Model, grouped according to some shared properties. The mass values are compiled from Ref. [33].

and decay into fermions of lower generations. The fermions can also be grouped into quarks and leptons. Quarks are particles that carry the color charge of the strong interaction and have fractional electric charge and are further divided into up-type and down-type. The up-type quarks exist in three flavors, up (u), charm (c), and top (t), and all have an electrical charge of $+\frac{2}{3}|e|$. The down-type quarks also exist in three flavors, down (d), strange (s), and bottom (b), and all have an electrical charge of $-\frac{1}{3}|e|$. Leptons are fermions which do not carry the color charge and can have integer ($-|e|$) or neutral electric charge. The interaction between leptons is mediated by the weak force, which couples each charged lepton to a neutral one. The charged leptons are represented by the electron (e), the muon (μ), and the tau lepton (τ). The neutral counterparts to the charged leptons are the neutrinos, ν_e, ν_μ, and ν_τ.

All observed interactions between particles can be described by the four fundamental forces of nature: the strong, electromagnetic, weak, and gravitational force. Out of the four, the gravitational interaction has the weakest relative strength at the microscopic level (by about $30-40$ orders of magnitude compared to the other forces), hence it is not included in the SM formulation[1]. The remaining three forces are mediated by spin-1 gauge bosons. The photon (γ), a massless and electrically neutral particle, is the mediator for the electromagnetic force. The gluon (g), a massless particle that carries the color charge, represents the mediator for the strong interaction. The mediators for the weak force are the massive weak bosons, the charged $W^{\pm}$ bosons (usually denoted as W for simplicity) and the neutral Z boson. The final gauge boson in the SM is the Higgs boson (H), which is a massive, spin-0 scalar particle that is responsible for the mechanism through which all SM particles acquire mass.

In the SM, the dynamics of relativistic free fermions are governed by the Dirac equation [7]

$$(i\gamma^{\mu}\partial_{\mu} - m)\psi = 0, \tag{2.1}$$

where γ^{μ} are the Dirac γ-matrices, m is the fermion mass, and ψ is the fermion field spinor. The Dirac equation has two positive energy solutions and two negative energy solutions. The negative energy solutions are interpreted as negative energy particles which propagate backwards in time and correspond to physical (positive energy) anti-particles that propagate forward in time and which have the same mass but opposite charge to the particles. The corresponding Dirac Lagrangian density is given by

$$\mathcal{L}_{\text{Dirac}} = \bar{\psi}(i\gamma^{\mu}\partial_{\mu} - m)\psi. \tag{2.2}$$

Interactions between the fermions are introduced by requiring that the Lagrangian density satisfy certain global or local symmetries. Invariance under a global symmetry will result in a conserved current (for example, the electric charge), while invariance under a local symmetry (gauge invariance) will result in the spin-1 gauge bosons that mediate the different interactions.

Quantum Electrodynamics

Quantum Electrodynamics (QED) describes the electromagnetic interactions between the fermions [8–13]. In QED, the Dirac Lagrangian density is required to be invariant under a $U(1)$ local phase transformation, which can be written as

$$\psi \rightarrow \psi' = e^{iq\chi(x)}\psi. \tag{2.3}$$

In order to guarantee gauge invariance, the partial derivative ∂_{μ} has to be replaced by the covariant derivative

$$D_{\mu} = \partial_{\mu} + iqA_{\mu}, \tag{2.4}$$

where A_{μ} is a vector field that transforms as

$$A_{\mu} \rightarrow A'_{\mu} = A_{\mu} - \partial_{\mu}\chi \tag{2.5}$$

[1] The theory of general relativity successfully describes the gravitational interaction at large scales. However, a theory that describes the gravitational interaction at microscopic scales using the principles of quantum mechanics is yet to be found.

and represents the gauge boson for the electromagnetic interaction, i.e. the photon, which interacts with strength q. As mass terms of the form $m_\gamma^2 A^\mu A_\mu$ are not gauge invariant under the transformation of Equation 2.5, the photon is required to be massless. This results in the following QED Lagrangian

$$\begin{aligned}\mathcal{L}_{\text{QED}} &= \bar{\psi}(i\gamma^\mu D_\mu - m)\psi - \frac{1}{4}F_{\mu\nu}F^{\mu\nu} \\ &= \bar{\psi}(i\gamma^\mu \partial_\mu - m)\psi - q\bar{\psi}\gamma^\mu A_\mu \psi - \frac{1}{4}F_{\mu\nu}F^{\mu\nu},\end{aligned} \tag{2.6}$$

where $\frac{1}{4}F_{\mu\nu}F^{\mu\nu}$ represents the kinetic energy term, constructed from the electromagnetic field tensor $F_{\mu\nu} = \partial_\mu A_\nu - \partial_\nu A_\mu$. The term $q\bar{\psi}\gamma^\mu A_\mu \psi$ describes the interaction between the gauge boson and the fermions, with the electric charge $q = -|e|$ representing the conserved quantity associated with the $U(1)$ gauge symmetry. Hence, the photon only interacts with electrically charged particles.

Quantum Chromodynamics

Quantum Chromodynamics (QCD) describes the strong interaction between particles [14–21]. In QCD, the Lagrangian is required to be invariant under $SU(3)_C$ local gauge transformations. The conserved quantity associated with this symmetry is the color charge, which can be red, blue, or green and is carried only by the quarks. The QCD Lagrangian has a similar form to the QED Lagrangian:

$$\mathcal{L}_{\text{QCD}} = \sum_q \bar{\psi}_q(i\gamma^\mu D_\mu - m_q)\psi_q - \frac{1}{4}G^a_{\mu\nu}F^{\mu\nu}_a, \tag{2.7}$$

where q corresponds to summation over the quark flavors and m_q is the quark mass. The QCD covariant derivative is given by

$$D_\mu = \partial_\mu + ig_s \frac{\lambda_a}{2} G^a_\mu, \tag{2.8}$$

where g_s represents the coupling constant for the strong interaction, from which the strong coupling strength can be defined as $\alpha_s = g_s^2/4\pi$. λ_a correspond to the eight Gell-Mann matrices, a set of 3×3 matrices that generate[2] the $SU(3)$ group, and G^a_μ represent the eight gluons, the spin-1 gauge bosons that mediate the strong interaction. As in the case of QED, the gluons are required to be massless in order the preserve the $SU(3)$ invariance of the Lagrangian. The strong interaction tensor is defined as

$$G^a_{\mu\nu} = \partial_\mu G^a_\nu - \partial_\nu G^a_\mu - g_s f^{abc} G^b_\mu G^c_\nu, \tag{2.9}$$

[2] Any $SU(3)$ transformation can be expressed as a linear combination of $T_a = \lambda_a/2$ and the identity matrix.

with f^{abc} representing the structure constants[3] of $SU(3)$. The gluons also carry the $SU(3)$ color charge and can interact with each other.

Quarks and gluons are subject to color confinement, which states that only objects with no net color charge can propagate as free particles [16, 18]. As a result, individual gluons cannot propagate over macroscopic distances (unlike photons) and quarks are observed as hadrons, bound states of neutral color charge. The process through which hadron states are formed is known as hadronization. Hadrons can be further divided into mesons (consisting of an even number of quarks, usually a quark–anti-quark pair) and baryons (consisting of an odd number of quarks, usually three). Hadron states consisting of more than three quarks, known as exotic hadrons, are also hypothesized to exist; some exotic hadrons, such as tetraquarks [39–43] and pentaquarks [44, 45], have been discovered in recent years.

Another feature of QCD relates to the variation in the strong coupling over the energy range relevant to particle physics: the strength of the coupling decreases with increasing energy, a behavior known as asymptotic freedom [22, 23]. At small energy scales (~ 1 GeV) the value of α_s is $\mathcal{O}(1)$, hence perturbation theory cannot be used as the expansion does not converge rapidly. At large energy scales ($\gtrsim 100$ GeV), the value of α_s becomes sufficiently small ($\alpha_s \sim 0.1$) that perturbative methods can be used to derive QCD predictions. Even so, higher-order corrections are not negligible and need to be included in QCD calculations. However, some higher-order corrections (such as quark self-energy corrections) can lead to infinite terms. This issue is addressed by redefining fields or parameters to absorb the divergent terms through a procedure known as renormalization, which requires the introduction of two scale parameters: the renormalization scale μ_R and the factorization scale μ_F [46, 47].

Electroweak Unification

In the SM, the weak interaction (responsible for β decay and nuclear interactions) and the electromagnetic interaction are unified into a single electroweak (EW) interaction through the Glashow-Weinberg-Salam (GWS) model [26–28]. In the GWS model, the Lagrangian is required to be gauge invariant under an $SU(2)_L \times U(1)_Y$ local transformation.

An $SU(2)$ local transformation can be defined as

$$\psi \to \psi' = e^{ig_W \frac{\sigma_a}{2} \chi^a(x)} \psi, \tag{2.10}$$

where σ_a are the three Pauli matrices, which relate to the generators of the $SU(2)$ group, and $\chi^a(x)$ are three functions that specify the local phase at each space-time point. The gauge covariant derivative is then given by

$$D_\mu = \partial_\mu + ig_W \frac{\sigma_a}{2} W_\mu^a, \tag{2.11}$$

[3] The structure constants are scalars that arise from the commutation relation of $SU(3)$ generators $[T_a, T_b] = i \sum_{c=1}^{8} f^{abc} T_c$.

where $W_\mu^{(1)}$, $W_\mu^{(2)}$, and $W_\mu^{(3)}$ are the three gauge fields that couple with interaction strength g_W.

The L subscript in the $SU(2)_L$ group of the GWS model is used to indicate that the charged-current interaction only couples to left-handed (LH) particles and right-handed (RH) anti-particles[4]. To this end, the weak isospin charge is introduced, and LH particles are placed into isospin doublets. LH particles have total weak isospin $I_W = \frac{1}{2}$ and third component of weak isospin $I_W^{(3)} = \pm\frac{1}{2}$. For RH particles, $I_W = I_W^{(3)} = 0$ and they are placed into isospin singlets, hence the W_μ^a bosons can only couple to LH particles. The physical $W^\pm$ bosons can be identified as the linear combinations

$$W_\mu^+ = \frac{1}{\sqrt{2}}\big(W_\mu^{(1)} - W_\mu^{(2)}\big), \tag{2.12}$$

$$W_\mu^- = \frac{1}{\sqrt{2}}\big(W_\mu^{(1)} + W_\mu^{(2)}\big). \tag{2.13}$$

As the Z boson has been experimentally shown to couple to both LH and RH particle states, it cannot be identified with the $W^{(3)}$ gauge boson of the $SU(2)_L$ local gauge symmetry, which only couples to LH particles (RH anti-particles). To accommodate this, the GWS model replaces the $U(1)$ symmetry of electromagnetism with a $U(1)_Y$ local gauge symmetry. This introduces a new gauge field B_μ, with coupling strength g', and a corresponding new charge, the weak hypercharge Y, which relates to the electromagnetic charge Q as

$$Y = 2(Q - I_W^{(3)}). \tag{2.14}$$

The covariant derivative for the $SU(2)_L \times U(1)_Y$ symmetry group is given by

$$D_\mu = \partial_\mu - ig_W\frac{\sigma_a}{2}W_\mu^a - ig'\frac{Y}{2}B_\mu. \tag{2.15}$$

The photon A_μ and Z boson (Z_μ) are then written as linear combinations of the $W_\mu^{(3)}$ and B_μ fields:

$$A_\mu = +B_\mu \cos\theta_W + W_\mu^{(3)}\sin\theta_W, \tag{2.16}$$

$$Z_\mu = -B_\mu \sin\theta_W + W_\mu^{(3)}\cos\theta_W, \tag{2.17}$$

where θ_W is the weak mixing angle. The GWS model of electroweak unification further implies that the weak and electromagnetic couplings are related to each other through the weak mixing angle:

$$e = g_W \sin\theta_W = g'\cos\theta_W. \tag{2.18}$$

As shown for QED and QCD, the gauge bosons of the weak interaction also need to be massless in order to preserve the invariance of the Lagrangian under the combined $SU(3)_C \times$

[4]Fermion fields can be divided into LH and RH components using projection operators, with $\psi_L = P_L\psi = \frac{1-\gamma^5}{2}\psi$ and $\psi_R = P_R\psi = \frac{1+\gamma^5}{2}\psi$.

$SU(2)_L \times U(1)_Y$ symmetry group. The split of the fermion fields into LH and RH components also breaks the gauge invariance, unless the fermions are massless. Yet, the W and Z bosons and the fermions have been experimentally observed to have non-zero masses. This mismatch between theory and experiment is solved by the Brout-Englert-Higgs mechanism, which provides a way to spontaneously break the symmetry in the electroweak sector and allows the fundamental particles to acquire mass [30, 31, 48].

2.2 The Higgs Mechanism

In the Higgs mechanism, particles gain mass through interactions with the Higgs field. The simplest Higgs model requires the introduction of two complex scalar fields (one neutral and one charged) that are placed in a weak isospin doublet

$$\phi = \begin{pmatrix} \phi^+ \\ \phi^0 \end{pmatrix} = \frac{1}{\sqrt{2}} \begin{pmatrix} \phi_1 + i\phi_2 \\ \phi_3 + i\phi_4 \end{pmatrix}, \tag{2.19}$$

where the four degrees of freedom will account for the electroweak bosons (W^+, W^-, Z) and the Higgs boson.

The Lagrangian for the Higgs doublet can then be written as

$$\mathcal{L} = (D_\mu \phi)^\dagger (D^\mu \phi) - V(\phi). \tag{2.20}$$

The first term describes the kinetic energy of the field, while the second term is the Higgs potential

$$V(\phi) = \mu^2 \phi^\dagger \phi + \lambda (\phi^\dagger \phi)^2, \tag{2.21}$$

where μ and λ are scalar free parameters. The potential has contributions from the mass (first term) and from the self-interaction (second term) of the field. The vacuum state corresponds to the minimum of the Higgs potential.

In order to have a finite potential minimum, the constant λ must be chosen to be positive. No restriction is needed for the value of μ^2 and two cases can be identified, both of which are schematically shown in Figure 2.2. For $\mu^2 > 0$, the potential will have a minimum at $\phi = 0$ and the Lagrangian corresponds to a scalar particle with mass μ. For $\mu^2 < 0$, the potential will have an infinite number of degenerate minima which satisfy the condition

$$\phi^\dagger \phi = \frac{1}{2}(\phi_1^2 + \phi_2^2 + \phi_3^2 + \phi_4^2) = \frac{v^2}{2} = -\frac{\mu^2}{2\lambda}, \tag{2.22}$$

where the parameter $v = \sqrt{\frac{-\mu^2}{\lambda}}$ is the vacuum expectation value (vev) of the Higgs field. The degenerate minima are all equivalent to each other and connected through an $SU(2)$ transformation. The choice of any one particular minimum will thus break the symmetry of the Lagrangian through a process known as spontaneous symmetry breaking. To ensure that the neutral photon remains massless after symmetry breaking, the choice has to be made

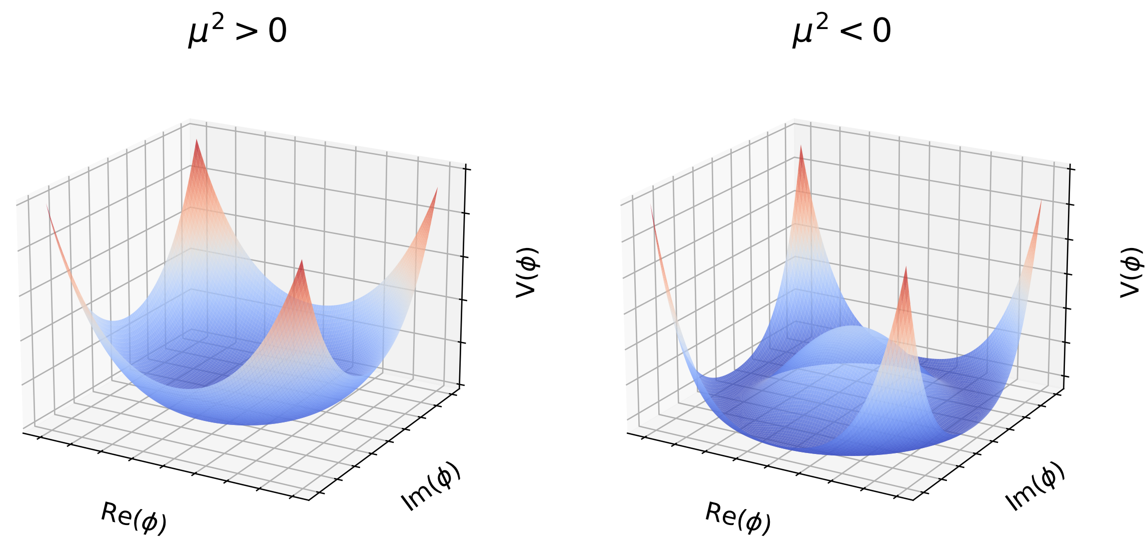

Figure 2.2: Illustration of the potential $V(\phi) = \mu^2\phi^\dagger\phi + \lambda(\phi^\dagger\phi)^2$ for a complex scalar field ϕ. The case $\mu^2 > 0$ (left) corresponds to a potential with a unique minimum at $\phi = 0$. The case $\mu^2 < 0$ (right) corresponds to the Higgs potential, which has a set of infinite degenerate minima.

such that the minimum of the potential corresponds to a non-zero vev only for the neutral field ϕ^0; that is,

$$\langle 0|\phi|0\rangle = \frac{1}{\sqrt{2}}\begin{pmatrix} 0 \\ v \end{pmatrix}. \tag{2.23}$$

Excitations of the Higgs field can be expanded around the potential minimum in the following way:

$$\phi(x) = \frac{1}{\sqrt{2}}\begin{pmatrix} \phi_1(x) + i\phi_2(x) \\ v + \eta(x) + i\phi_4(x) \end{pmatrix}. \tag{2.24}$$

$\eta(x)$ corresponds to a physical scalar field, with an associated massive scalar boson. ϕ_1, ϕ_2, and ϕ_4 are massless scalar fields, whose excitations are known as Goldstone bosons [29, 49] and provide the degrees of freedom for the $W^\pm$ and Z bosons. By making an appropriate gauge transformation (known as choosing unitary gauge), the Goldstone fields can be eliminated from the expression of the Higgs Lagrangian and the expression for the Higgs doublet reduces to

$$\phi(x) = \frac{1}{\sqrt{2}}\begin{pmatrix} 0 \\ v + h(x) \end{pmatrix}. \tag{2.25}$$

In unitary gauge, the expression for the Lagrangian becomes (after plugging in the expression for the GWS gauge covariant derivative):

$$\begin{aligned}\mathcal{L}_{\text{Higgs}} = & \frac{1}{2}(\partial_\mu h)(\partial_\mu h) + \frac{1}{4}g_W^2 W_\mu^+ W^{\mu-}(v+h)^2 \\ & + \frac{1}{8}(g_w^2 + g'^2)Z_\mu Z^\mu (v+h)^2 \\ & + \frac{\mu^2}{2}(v+h)^2 - \frac{\lambda}{4}(v+h)^4,\end{aligned} \tag{2.26}$$

where the physical $W^\pm$ bosons, the Z boson, and the photon have been identified as linear combinations of the fundamental fields:

$$W_\mu^\pm = \frac{1}{\sqrt{2}}\big(W_\mu^{(1)} \mp W_\mu^{(2)}\big), \tag{2.27}$$

$$Z_\mu = \frac{1}{\sqrt{g_w^2 + g'^2}}\big(g_W W_\mu^{(3)} - g' B_\mu\big), \tag{2.28}$$

$$A_\mu = \frac{1}{\sqrt{g_w^2 + g'^2}}\big(g' W_\mu^{(3)} + g_W B_\mu\big). \tag{2.29}$$

From the quadratic terms in Equation 2.27, the masses for the W and Z bosons can be extracted as:

$$m_w = \frac{1}{2}g_w v \qquad m_Z = \frac{1}{2}v\sqrt{g_w^2 + g'^2} = \frac{m_W}{\cos\theta_W}. \tag{2.30}$$

The photon is massless, as the Higgs Lagrangian does not contain any mass terms of the form $m_A A_\mu A^\mu$. Excitations of the field $h(x)$ correspond to the physically observed Higgs boson with a mass of

$$m_H = \sqrt{2\lambda v^2}. \tag{2.31}$$

The Higgs mechanism for spontaneous symmetry breaking can also be used to generate the masses of the fermions. Interactions of the fermionic fields with the Higgs can be described through Lagrangian terms that are invariant under $SU(2)_L \times U(1)_Y$ transformations:

$$\mathcal{L}_{\text{Yukawa}} = \sum_f -\frac{y_f v}{\sqrt{2}}\bar{\psi}_f \psi_f - \frac{y_f h}{\sqrt{2}}\bar{\psi}_f\psi_f, \tag{2.32}$$

where the constants y_f are known as the Yukawa couplings of the fermions to the Higgs field. The values of the Yukawa couplings are not predicted by the Higgs mechanism, but they can be chosen to be consistent with the observed fermion masses:

$$y_f = \sqrt{2}\frac{m_f}{v}, \tag{2.33}$$

which leads to the following expression for the Lagrangian:

$$\mathcal{L}_{\text{Yukawa}} = \sum_f -m_f\bar{\psi}_f\psi_f - \frac{m_f}{v}\bar{\psi}_f\psi_f h. \tag{2.34}$$

The first term of the Lagragian is the mass term, by construction, and represents the coupling of the fermions to the Higgs field through its non-zero vev. The second term gives rise to the coupling between the fermions and the Higgs boson h.

A subtlety arises in the quark sector, where an additional matrix accounts for the transformation from the mass eigenstate basis to the weak eigenstate basis. This matrix is known as the Cabbibo-Kobayashi-Maskawa (CKM) matrix [50]:

$$V_{\mathrm{CKM}} = \begin{pmatrix} V_{ud} & V_{us} & V_{ub} \\ V_{cd} & V_{cs} & V_{cb} \\ V_{td} & V_{ts} & V_{tb} \end{pmatrix}, \tag{2.35}$$

and it allows for transitions betwen up-type and down-type quark flavors through charged-current $W^{\pm}$ interactions. The matrix entries are determined experimentally and the CKM matrix is measured to be almost diagonal, with relatively small off-diagonal terms. The implication is that the charged-current interaction favors transitions between quarks of the same generation. In particular, for c-hadrons the preferred decay mode is through the $c \to s$ decay. For b-hadrons, the $b \to t$ decay is kinematically suppresed as a result of the large mass of the top quark. Hence, b-hadrons decay primarily through the CKM off-diagonal $b \to c$ transition, which results in b-hadrons having much longer lifetimes than c-hadrons.

The spontaneous symmetry breaking of the Higgs mechanism can also be used to give rise to masses of the neutrinos. In this case, the gauge invariant Dirac mass term for the neutrino is written as:

$$\mathcal{L}_D = -m_D(\overline{\nu_R}\nu_L + \overline{\nu_L}\nu_R), \tag{2.36}$$

which requires the existence of right-handed neutrinos (and left-handed antineutrinos[5]). The presence of right-handed neutrino states further allows the introduction of a gauge invariant Majorana mass term, as is done in the seesaw mechanism, where the Lagrangian for the combined Dirac and Majorana masses is given by

$$\mathcal{L}_{DM} = -\frac{1}{2}\left[m_D\overline{\nu_L}\nu_R + m_D\overline{\nu_R^c}\nu_L + M\overline{\nu_R^c}\nu_R\right] + \text{h.c.}. \tag{2.37}$$

If the Majorana mass M is much larger than the Dirac mass m_D, then the neutrino mass is $|m_\nu| \approx m_D^2/M$. In the seesaw mechanism, the Majorana mass is chosen to be sufficiently large such that $m_\nu \sim 0.01$ eV, providing a hypothesis to explain the observed smallness of the neutrino masses.

The Parameters of the Standard Model

To summarize, the SM provides a framework to describe the elementary particles through properties such as electric charge, color charge, isospin, and hypercharge. The dynamics

[5] The left-handed antineutrinos appear as the charge-parity conjugate fields of the right-handed neutrino, ν_R^c.

of particle interactions are predicted by requiring that the SM Lagrangian be invariant under the local gauge transformation of $SU(3)_C \times SU(2)_L \times U(1)_Y$. Additionally, the Higgs mechanism provides a way through which particles can acquire mass without breaking the underlying symmetries of the theory. However, as outlined in the previous sections, the components of the SM Lagrangian are expressed in terms of 26 free parameters whose values are not known a priori and must be obtained from experimental measurements. The set of parameters consists of:

- twelve Yukawa couplings of the fermions to the Higgs field
- three coupling constants for the strong and electroweak interactions (g_W, g', and g_s)
- two parameters to describe the Higgs potential (μ and λ, or equivalently m_H and v)
- four parameters to describe the CKM matrix (3 mixing angles and 1 phase)
- five additional parameters relating to charge-parity violation in the strong interaction and neutrino oscillations (topics which are not discussed within the scope of this thesis)

Measuring the SM parameters and their effects on physics observables is one of the main goals of modern particle physics experiments, as any observed deviations from the theoretical predictions could provide evidence for physics beyond the SM (BSM).

2.3 Hadron Collider Phenomenology

At the LHC, high-energy proton-proton (pp) collisions are used to experimentally verify the predictions of the SM. Many of the processes of interest involve the production of a massive particle, for e.g. the Higgs boson. In order for such a process to take place, the energy available in the collision must be larger than the sum of the masses of the particles being produced. This energy is quantified through a Lorentz invariant quantity, $s = (p_1 + p_2)^2$, where p_1 and p_2 represent the four-momenta of the colliding particles. When evaluating the expression in the center-of-mass frame where there is no net momentum, this simplifies to:

$$s = (E_1 + E_2)^2 - (\vec{p} + (-\vec{p}))^2 = (E_1 + E_2)^2, \tag{2.38}$$

where $\sqrt{s} = E_1 + E_2$ represents the *center-of-mass energy*, i.e. the total energy available in the center-of-mass frame of the colliding protons.

The production processes are quantified in terms of their *cross section*[6] to a final state X, $\sigma_{pp\to X}$, which provides the probability for the scattering process $pp \to X$ to take place. The determination of the cross section must take into account the fact that protons are composite particles consisting of bound states of quarks and gluons (which, for historical

[6] In general, the cross section provides the probability for any given scattering process $ab \to X$ to occur, e.g. it is also used to describe electron-positron annihilation or electron-proton elastic or inelastic scattering.

reasons, are commonly referred to as partons[7]). Therefore, the interaction of interest (i.e the hard scatter) occurs between two individual partons, with each of them carrying some fraction of the total momentum of the proton. The probability for the partons to transition from initial states a and b to some final state X is given by the partonic cross section $\sigma_{ab\to X}$ and can be computed from the relevant interaction term in the Lagrangian using perturbative methods.

However, the proton is not an internally static system, as the quarks continuously interact with each other by exchanging gluons. The dynamics of these interactions result in distributions of quark momenta called parton distribution functions (PDFs). The PDF, $f(x, \mu_F)$, represents the probability that a parton carrying a fraction x of the total proton momentum P will participate in the hard scatter interaction. The inclusive cross section for the $pp \to X$ process can then be computed as a convolution between the perturbative partonic cross section and the PDFs via the factorization theorem [47], which allows for the separation of the perturbative and non-perturbative parts:

$$\sigma_{pp\to X} = \sum_{a,b} \int_0^1 dx_1 \int_0^1 dx_2 f_a(x_1, \mu_F) f_b(x_2, \mu_F) \int d\sigma_{ab\to X}(x_1 P_1, x_2 P_2, \mu_R, \mu_F) \qquad (2.39)$$

As the PDFs depend on the dynamics of the proton, they cannot be calculated from theory and must be determined from experiment. The PDFs are measured at an arbitrary energy scale using a well-understood process, such as deep inelastic scattering. Their dependence on the energy scale of the collision is then parametrized using the factorization scale μ_F. PDF sets, which can vary in model parametrization, treatment of various theoretical parameters, or experimental data used to determine them, are provided by several collaborations, including CTEQ [52], MRST2007 [53], NNPDF [54], and PDF4LHC [55].

Other processes of interest consist of the decays of particles produced in pp collisions, as many of them are unstable and will decay to kinematically allowed combinations of other particles. The probability that a particle A decays to a final state X is quantified through the *branching ratio* (BR), which is computed as

$$\mathrm{BR}(A \to X) = \frac{\Gamma_A^X}{\Gamma_A^{\mathrm{total}}} = \frac{\Gamma(A \to X)}{\sum_i \Gamma(A \to X_i)}, \qquad (2.40)$$

where Γ_A^X represents the partial decay width[8] for the decay of particle A into final state X and $\Gamma_H^{\mathrm{total}}$ is the total decay width, which accounts for the all the possible decay modes of particle A.

Additional phenomenological aspects of QCD must also be taken into account in order to fully describe pp collisions. The hard scatter interaction produces particles with large energy,

[7]The term "parton" was used to describe the point-like constituents of hadrons in what is known as the QCD parton model, proposed by Richard Feynman to explain high-energy hadronic collisions [51].

[8]The decay width Γ is also known as the decay rate and represents the probability per unit time that a particle will decay.

and any outgoing quarks or gluons produced at this step will be too energetic to form bound states. Instead, they will produce additional partons through radiation or gluon splitting. This process repeats until the energy of the produced particles reaches non-perturbative levels and is known as the *parton shower*. The evolution of the parton shower is performed using computer programs known as parton shower generators. The parton shower models use perturbative QCD and are tuned to match the experimental data. Once the energy becomes $\mathcal{O}(1)$ GeV, the partons start forming bound, colorless hadronic states due to color confinement. For energetic quarks and gluons, this results in the presence of highly collimated sprays of hadrons. Since perturbative QCD is no longer applicable at these energy scales, *hadronization* is described using phenomenological QCD models. Partons can also radiate off gluons (or photons) in either the ingoing (*initial state radiation*, ISR) or outgoing (*final state radiation*, FSR) directions relative to the hard scatter interaction, which also have to be considered.

The remaining partons of the protons (i.e. those not involved in the hard scattering) can also interact in what is known as the *underlying event* (UE). Finally, as the LHC beams consist of bunches of billions of protons, other proton-proton interactions occur simultaneously with the hard scattering and are referred to as *pile-up* events.

2.4 Monte Carlo Simulation

To perform a measurement of a process of interest, the data that is collected by the experiment must be compared against the predictions of theory. However, generating theoretical predictions for *pp* collisions is a complex process, as it involves calculating multi-dimensional integrals, such as the cross section of Eqn. 2.39, which are intractable to solve with analytical methods. Thus, the calculations are performed using numerical methods based on Monte Carlo (MC) techniques [56]. For this purpose, *pp* collision events are generated using computer programs knows as Monte Carlo event generators, which take into account all the components of a hadronic collision that were described in the previous section. Figure 2.3 provides an illustration of a *pp* collision event as simulated by an MC event generator.

A number of MC event generators are available to generate *pp* collisions, with each using different algorithms to implement the physics contributions to the event. Some event generators can be used to calculate multiple of the contributing physics effects, while others have to be interfaced together to generate a full event. An example of the former category is the Pythia [58] event generator, which is generally used for computing the parton shower, the hadronization, and the underlying event (UEPS). It can also compute the partonic cross section (matrix element calculation), but only at leading-order[9] (LO) accuracy. Sherpa [59–61] is another general-purpose generator, with an UEPS implementation similar to that of Pythia, but for which the partonic cross section can be computed at different orders,

[9]This means including only the lowest-order terms in the perturbation expansion for QCD. Including the next higher-order terms is known as next-to-leading order (NLO), the next set of terms after that is next-to-next-to-leading order (NNLO), and so on.

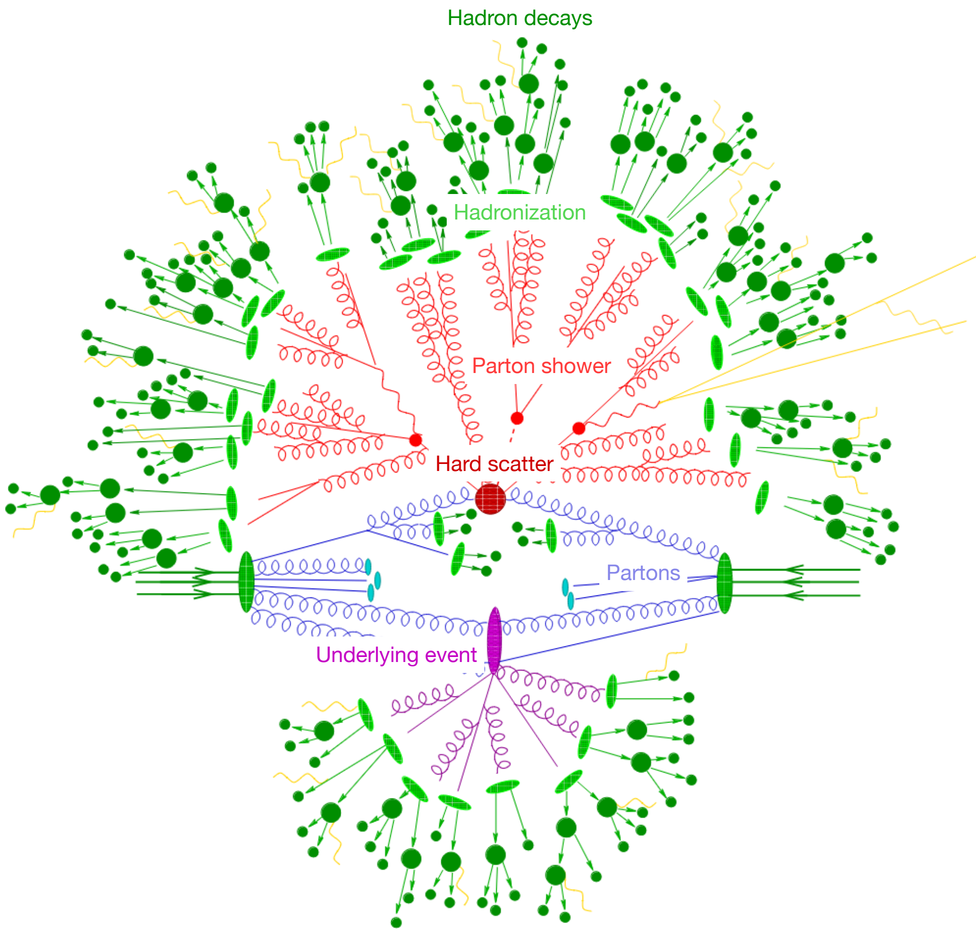

Figure 2.3: Schematic illustration of a proton-proton collision as simulated from a Monte Carlo event generator, highlighting the different parts of the collision. Adapted from Ref. [57].

ranging from LO to NNLO, depending on the process. SHERPA can also produce complete events. The latter category consists of generators such as POWHEG [62–64], HERWIG [65], or MADGRAPH [66]. POWHEG calculates the matrix element at NLO or higher, and is usually interfaced to PYTHIA which provides the prediction for the UEPS. The HERWIG generator is generally used to obtain an alternative UEPS prediction from that of PYTHIA, as HERWIG uses different models for the parton shower and hadronization compared to PYTHIA. MADGRAPH can perform the matrix element calculation at LO or NLO, and, like POWHEG, is usually interfaced to a different generator for the UEPS prediction, typically PYTHIA. An important consideration occurs when an MC generator that computes the matrix element at NLO is interfaced with a different generator for the parton shower computation. In order the guarantee the accuracy of the NLO calculation for the hard scatter and keep the same level of accuracy in the parton shower, different matching and merging schemes are used [67].

Examples include the CKKW-L and MEPS@NLO algorithms used by SHERPA [60, 68–70] and the FXFX merging prescription used by MADGRAPH [71].

Events that are produced by the MC event generators have to be passed through a simulation of the detector, in order to match the reconstruction procedures that are performed on data observed with the true detector. For the ATLAS experiment, the simulation chain [72] uses the GEANT4 simulation toolkit [73] and is implemented within the ATHENA software framework [74]. The simulation chain has four steps, which are shown schematically in Figure 2.4 and summarized in the following.

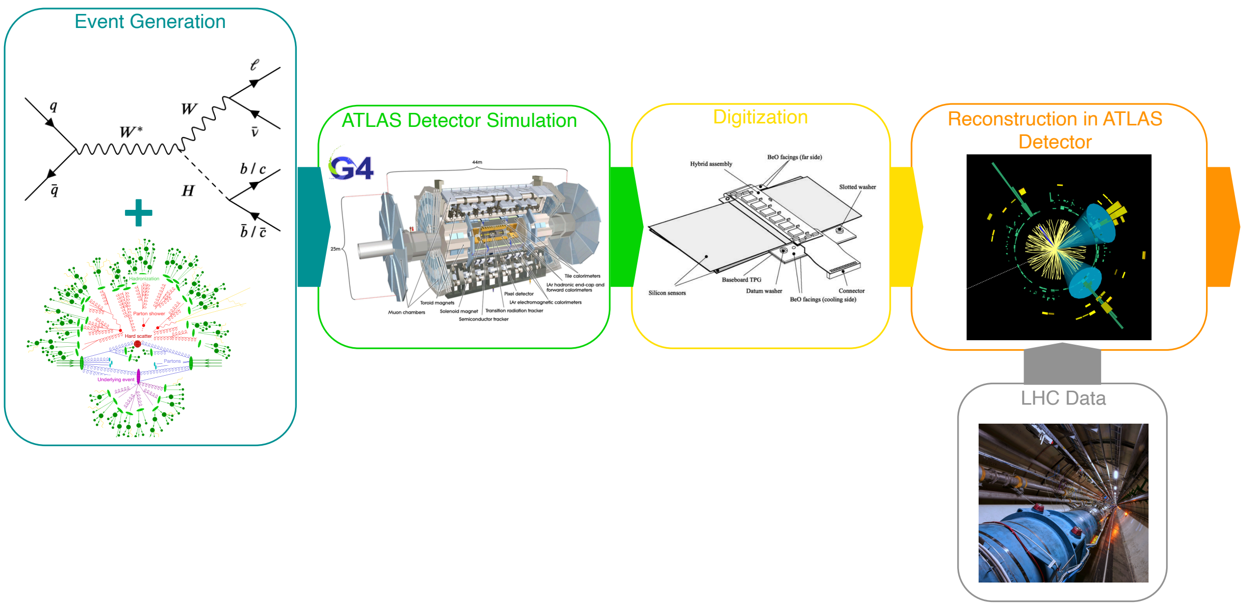

Figure 2.4: Diagram of the four steps in the ATLAS simulation chain. Individual images are adapted from Refs. [57, 75–78]. The chain starts at event generation (dark green), followed by the detector simulation(light green), digitization (yellow), and ends at event reconstruction (orange).

In the first step, one of the MC event generators is used to *generate* a full set of particles that are produced in the pp collision events, and the truth information (which consists of a history of relevant interactions) is stored for each stable particle. The particles are then processed through the detector *simulation*, which uses the GEANT4 toolkit and includes the most accurate description of the geometry, material, and response of the ATLAS detector. The simulated particles propagate through the detector and interact with the sensitive detector elements – the interactions are recorded as *hits*, which contain information about the total energy deposited during the interaction, position, and time. The third step of the simulation chain consists of *digitization*, where the hits are converted into digital signals for each sub-detector. These are used as inputs for the various physics object reconstruction algorithms, which are described in more detail in Chapter 4. The *reconstruction* of simulated events is performed using the same[10] procedures as for data events, which allows for the direct comparison between simulation predictions and data. The output of the reconstruction stage is available to physics analyses for further processing.

2.5 Higgs Boson Properties

For proton-proton collisions at the LHC, the dominant Higgs production modes consist of gluon-gluon fusion (ggF), vector boson fusion (VBF), associated production with a vector boson (VH), and associated production with top quarks ($t\bar{t}H$). Example of leading-order Feynman diagrams for these processes are shown in Figure 2.5, while the predicted cross sections at center-of-mass energy $\sqrt{s} = 13$ TeV as a function of Higgs boson mass are provided in Figure 2.6.

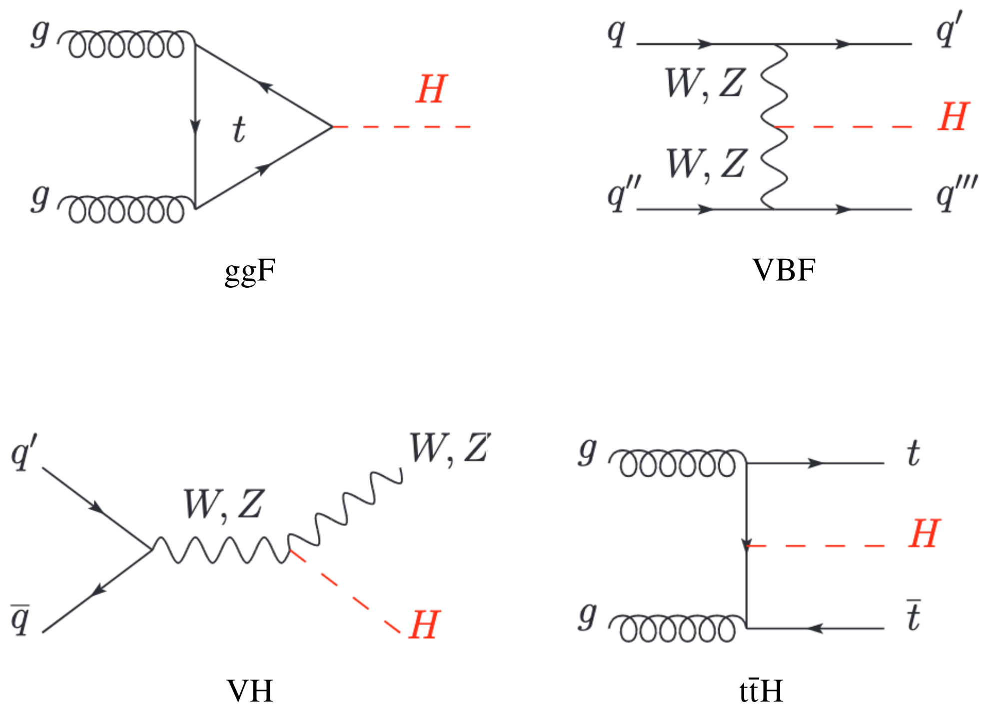

Figure 2.5: Feynman diagrams for the dominant Higgs production modes at the LHC. Adapted from Ref. [33].

As seen in Figure 2.6, at $\sqrt{s} = 13$ TeV the gluon fusion process represents the most common Higgs production mode and has the largest cross section resulting from the significant contribution of gluons to the PDFs [80]. As gluons are massless, they do not couple directly

[10]The only difference is that truth information is only available for simulated events.

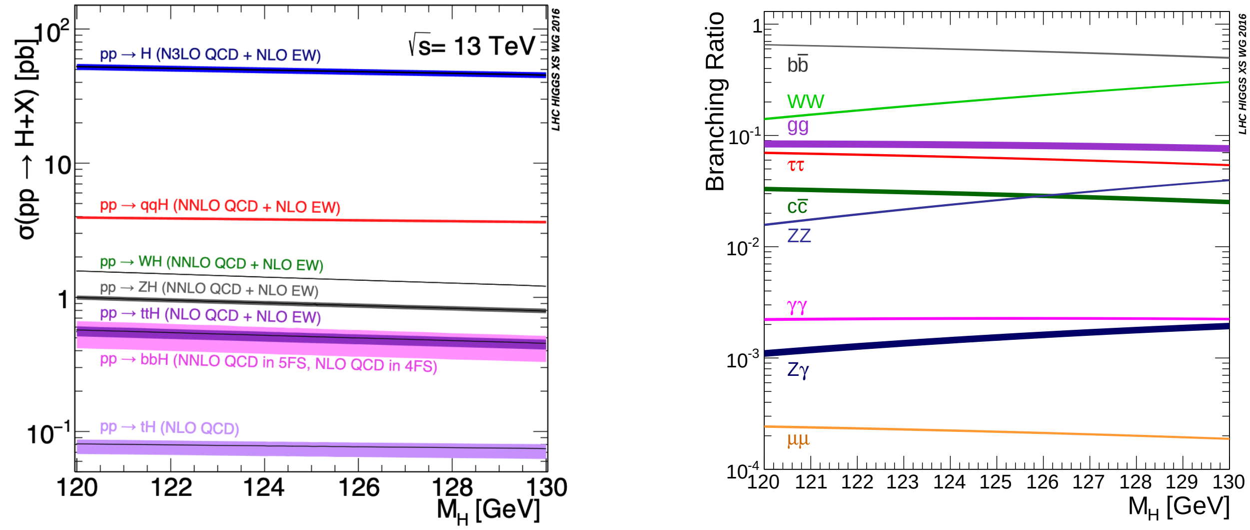

Figure 2.6: Predicted values for the Higgs production cross sections (left) and decay branching ratios (right) as a function of Higgs boson mass [79].

to the Higgs field, so the Higgs boson has to be produced via a quark loop instead. Given that the Yukawa couplings are directly proportional to mass, the dominant contribution to the loop originates from the top quark, while loops with lighter quarks are suppressed. Despite the large production cross section, the ggF production mode can be difficult to study for some Higgs decay modes, such as $H \to b\bar{b}(c\bar{c})$, due to the significant background from non-resonant QCD processes[11].

The VBF mode has the second largest Higgs production cross section at $\sqrt{s} = 13$ TeV. In this process, two quarks will scatter by radiating massive vector bosons (W or Z), which can then fuse into an outgoing Higgs boson. This production mode has a distinctive final state signature, consisting of two forward jets (originating from the scattered quarks) observed in addition to the Higgs boson decay products.

The third largest production mode at $\sqrt{s} = 13$ TeV is represented by VH production, where a heavy vector boson radiates off a Higgs boson (leading to this mode also being called Higgsstrahlung). Despite the modest cross section, this mode can have a very clean final state signature by triggering on the leptonic decays of the vector boson. The final important Higgs production mode at $\sqrt{s} = 13$ TeV is the $t\bar{t}H$ mode, which provides information about the direct coupling of the Higgs boson to the top quark.

As the Higgs boson is an unstable particle with a lifetime $\mathcal{O}(10^{-22})$ s, shortly after production it decays into other SM particles. Given that the Yukawa couplings are proportional to the masses of the particles, the preferred direct decay modes are into the heaviest particles

[11]The ggF production mode can be used to study Higgs decays with distinctive final state signatures, such as $H \to ZZ$ or $H \to \gamma\gamma$, where it is easier to distinguish against the QCD background.

that are kinematically accessible, while decays into lighter particles occur less frequently. Indirect decay modes into massless particles (photons or gluons) also exists and occur through virtual loops of heavy quarks or W bosons.

The predicted branching ratios for the main decay modes of the Higgs boson are shown in Figure 2.6 as a function of Higgs boson mass. For a mass of 125 GeV, the dominant decay mode is the decay to a pair of bottom quarks $H \to b\bar{b}$, with a braching ratio of 58%. A similar decay mode is the decay into a pair of charm quarks $H \to c\bar{c}$, which has a branching ratio of 3%. The $H \to b\bar{b}$ and $H \to c\bar{c}$ decay modes are important to study as they directly probe the coupling of the Higgs boson to third and second generation quarks. However, these modes are difficult to measure experimentally due to the large QCD backgrounds that have a similar final state signature. Additionally, the $H \to c\bar{c}$ mode is more challenging to measure than the $H \to b\bar{b}$ mode due to difficulties in distinguishing the signatures of charm quarks from those of bottom or lighter quarks and the ~ 20 times smaller branching ratio. A simultaneous measurement of Higgs boson decays into bottom and charm quarks in the WH production channel represents the focus of this thesis and is discussed in more detail in Chapter 5.

Although they have lower branching ratios, the Higgs decay modes into gauge bosons or leptons have signatures which are easier to identify experimentally. In particular, the $H \to \gamma\gamma$, $H \to ZZ \to 4\ell$, and $H \to WW^* \to 2\ell 2\nu$ modes were used by the ATLAS and CMS collaborations to discover, in 2012, a particle consistent with the properties of the SM Higgs boson [81, 82]. Since then, more properties of the Higgs boson have been measured with increasing precision. For example, the Higgs boson mass has now been measured with an uncertainty of 0.09%, at a value of $m_H = 125.11 \pm 0.11$ GeV [83] measured by the ATLAS experiment. Additional Higgs production and decay modes have also been measured. Figure 2.7 summarizes recent results for the Higgs production cross sections and couplings to fermions and vector bosons, which are found to be in good agreement with the SM predictions [84].

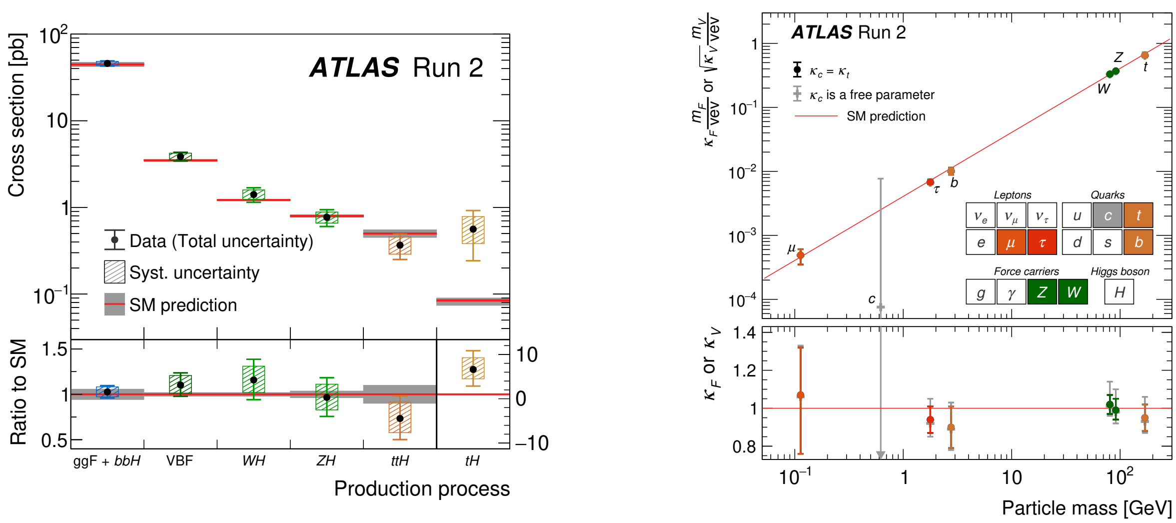

Figure 2.7: Measured Higgs production cross sections (left) and coupling strength modifiers for fermions and massive vector bosons (right) compared to SM predictions [84].

Chapter 3

The ATLAS Experiment

This chapter briefly introduces the Large Hadron Collider (LHC) and presents the main experimental features of the ATLAS detector during the data taking period between 2015 and 2018 (Run 2).

3.1 The Large Hadron Collider

The Large Hadron Collider [85–87], located at CERN in Geneva, Switzerland, is currently the world's largest proton-proton[1] collider facility, which was built for the purpose of studying particle physics at high energies. The high energy of the collisions allows for a wide range of SM and BSM phenomenology to be probed.

Figure 3.1 illustrates the various components of the CERN accelerator complex. Several pre-accelerators are used to bring the protons to the correct center-of-mass energy. The protons, which are obtained by ionizing hydrogen gas, are first accelerated to an energy of 50 MeV by a linear accelerator (Linac2[2]). They are then injected into the Proton Synchrotron Booster (PSB), which accelerates the protons to an energy of 1.4 GeV and splits them up into bunches. From here, the proton bunches are sequentially injected into the Proton Synchrotron (PS), where brings up the energy to 25 GeV, and then into the Super Proton Synchrotron (SPS), which increases the energy to 450 GeV. At this stage, the protons enter the LHC ring, where they circulate in opposite directions until they reach a total energy of 13 TeV. The LHC operates at a 40 MHz frequency, hence the proton bunches are spaced 25 ns apart.

The collisions between the two proton beams occur at four interaction points (IPs), where the large LHC experiments are located: ATLAS [75, 89], CMS [90, 91], LHCb [92], and ALICE [93]. The experiments span a diverse physics program, with ATLAS and CMS both

[1]The LHC also accelerates and collides heavy ions, however this thesis will focus on proton-proton collisions only.

[2]Linac2 operated until the end of 2018. In 2020, it was replaced by Linac4, which can accelerate the protons to 160 MeV.

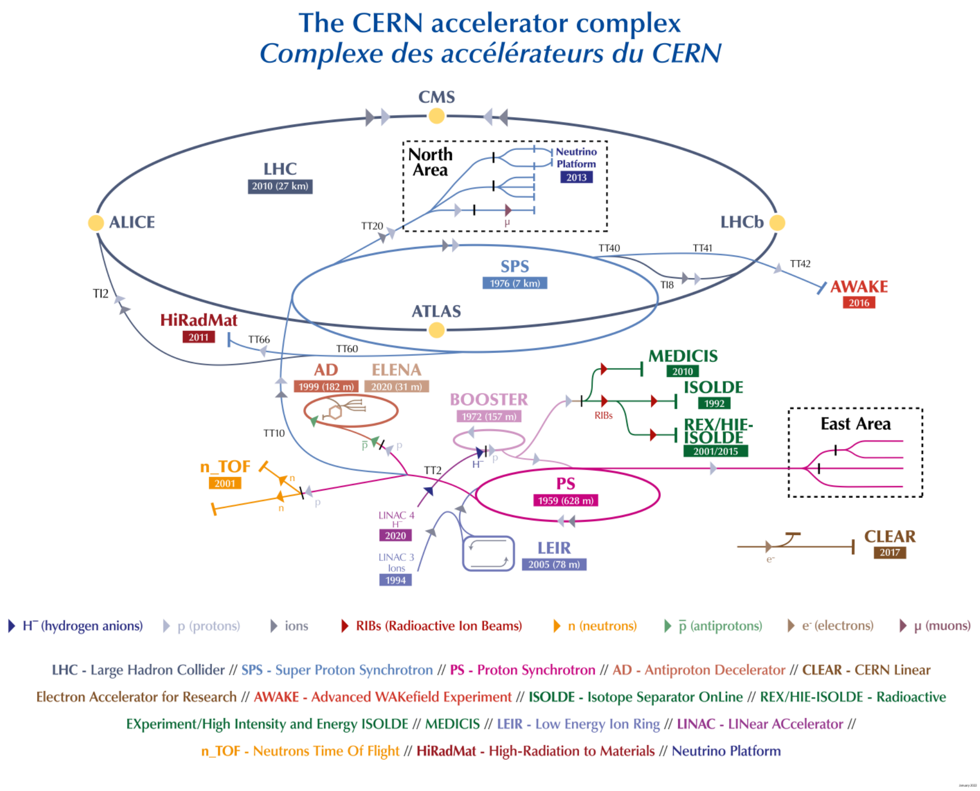

Figure 3.1: Diagram of the CERN accelerator complex [88].

performing precision measurements of the properties of SM particles and searches for BSM physics[3], while LHCb focuses on studying the properties of hadrons containing heavy quarks, and ALICE on heavy-ion collisions and high-density QCD states, such as the quark-gluon plasma. The LHC also hosts five smaller experiments, whose goals are to study "forward" particles that brush past each other when the beams collide at the IP (TOTEM [94] and LHCf [95]), look for magnetic monopoles (MoEDAL-MAPP [96, 97]), and look for light new particles and study neutrinos (FASER [98] and SND@LHC [99]).

An important quantity for describing the LHC is the instantaneous luminosity, L_{inst}, which determines the event rates that can be achieved:

$$\frac{dN}{dt} = L_{\text{inst}} \times \sigma, \tag{3.1}$$

where σ is the cross section of the physics process. During its first run (2009 − 2013), the LHC achieved a peak instantaneous luminosity of $L_{\text{inst}} = 8 \times 10^{33}$ cm^{-2}s^{-1} [85], which increased

[3] Having two independently designed detectors that can perform the same measurement is important for verifying the validity of new discoveries.

to $L_{\text{inst}} = 2 \times 10^{34}$ cm^{-2}s^{-1} [100] during Run 2. The total number of events produced is obtained by integrating Eqn. 3.1, and is directly proportional to the integrated luminosity:

$$L_{\text{int}} = \int L_{\text{inst}}\, dt. \tag{3.2}$$

The dataset collected by the ATLAS experiment during Run 2 corresponds to an integrated luminosity of $L_{\text{int}} = 140.1 \pm 1.2$ fb^{-1} [101]. This is expected to be surpassed in the ongoing Run 3 [102] of the LHC, where up to 300 fb^{-1} of data at $\sqrt{s} = 13.6$ TeV will be collected between 2022 and 2025.

During the collision of the proton bunches, in addition to the hard scattering between two protons, a number of additional soft pp interactions, known as pile-up, also occur. Large amounts of pile-up make the reconstruction of the hard scatter event more challenging. During Run 2, the average number of pile-up interactions per bunch crossing was ~ 30 [100].

3.2 The ATLAS Detector

The ATLAS detector is a general-purpose detector located on the LHC ring. The detector has a cylindrical geometry, with the LHC beam pipe defining the main axis, and as a result of the forward-backward symmetry, it covers nearly the entire solid angle around the collision point. The ATLAS detector has a length of 44 m, a height of 25 m, and a weight of approximately 7000 tons – a diagram is shown in Figure 3.2.

A right-handed coordinate system is used to describe the ATLAS detector, with the origin placed at the nominal proton-proton interaction point in the center of the detector. The z-axis is chosen to point along the beam pipe direction, while the x-axis points from the interaction point to the center of the LHC ring and the y-axis points upwards. A natural choice for defining positions in the detector consists of using cylindrical coordinates $(r,\, \theta,\, \phi)$: r and ϕ are used in the $x - y$ plane (also known as the transverse plane), with ϕ being the azimuthal angle around the z-axis, while the polar angle θ is the angle from the z-axis. The momentum of particles is projected on the transverse plane to obtain the transverse momentum $p_T \equiv \sqrt{p_x^2 + p_y^2} = p\sin(\theta)$. The pseudorapidity is defined in terms of the polar angle θ as $\eta \equiv -\ln\tan(\theta/2)$. In the limit that the particle mass is much smaller than its momentum, the pseudorapidity approaches the true rapidity y and thus pseudorapidity differences are Lorentz invariant under boosts in the z-direction. Angular distance is measured in units of $\Delta R \equiv \sqrt{(\Delta\eta)^2 + (\Delta\phi)^2}$.

The ATLAS detector consists of different sub-detectors that are designed such that each type of particle will generate a unique combined signature as it traverses the detector – this is illustrated schematically in Figure 3.3. The sub-detectors consist of an inner tracking detector surrounded by a thin superconducting solenoid, electromagnetic and hadronic calorimeters, and a muon spectrometer surrounded by a toroidal magnet.

Charged particles are measured in the Inner Detector [104–106] – their trajectories are bent due to the magnetic field and the resulting curvature can be used to determine the

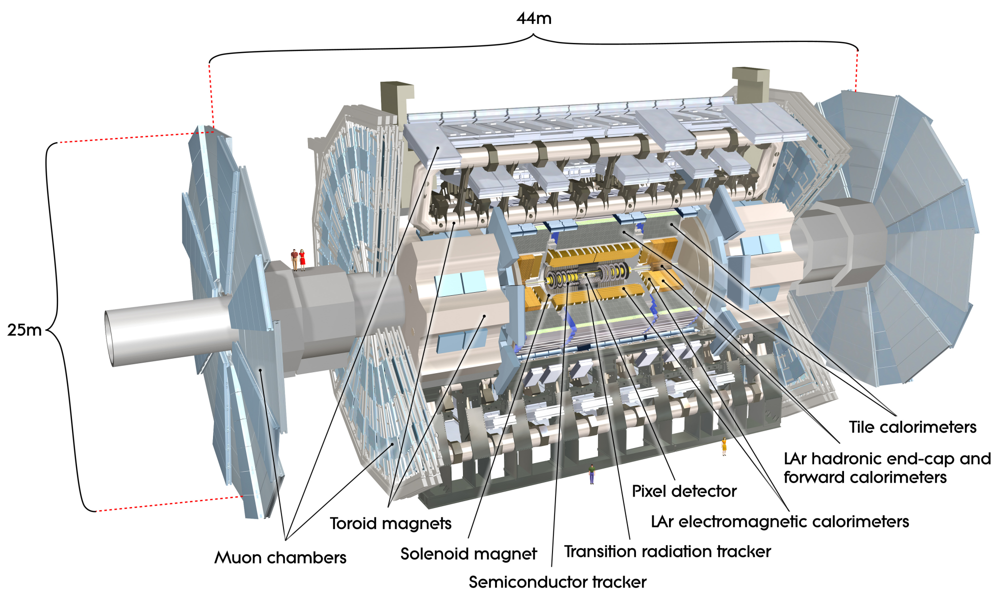

Figure 3.2: Schematic diagram of the ATLAS detector [75].

particle momenta. Electrons and photons are measured and stopped in the Electromagnetic Calorimeter [107, 108]. Since photons are electrically neutral, they will not leave any tracks in the inner detector, unless they convert to a pair of e^+e^-, in which case the electrons will generate tracks. Hadrons, such as the proton and neutron, are measured and stopped in the Hadronic Calorimeters [107–110]. Charged and neutral hadrons are distinguished from one another by the fact that the latter do not leave any signature in the Inner Detector. Since the main energy loss mechanism for muons is ionization, the muons interact minimally with the calorimeters and are instead measured in the Muon Spectrometer [111, 112]. Neutrinos do not interact directly with any of the sub-detectors and their presence is instead inferred from the energy imbalance in the transverse plane (the so-called missing transverse energy).

Table 3.1 summarizes the ATLAS detector general design goals in terms of measuring the energy and momentum resolution of particles. In the Inner Detector, the momentum of charged particles is determined from the amount of bending in their trajectories, with particles with large momentum undergoing less bending than particles with small momentum. Hence, the relative uncertainty on the momentum measurement increases with momentum. In the calorimeters, highly energetic particles tend to generate larger showers, hence the resolution of the energy measurement decrease with energy. For high momentum muons, the performance of the Muon Spectrometer is independent of the Inner Detector system.

In terms of angular coverage, both the Inner Detector and the calorimeters can be used in the region $|\eta| < 2.5$. For jet detection, while the coverage of the Hadronic Calorimeters extends all the way up to $|\eta| < 4.9$, the identification of jet flavor requires tracking informa-

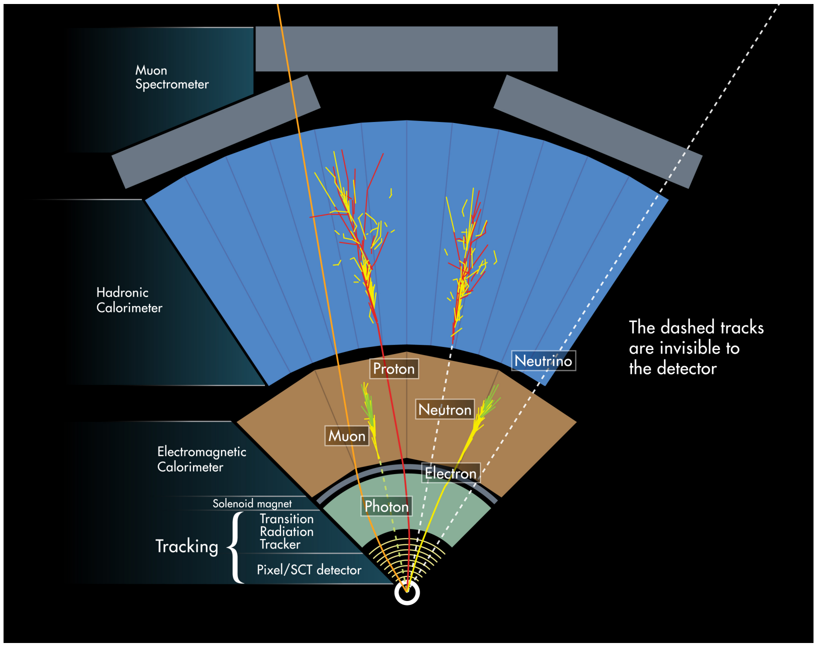

Figure 3.3: Schematic representation of the signatures left by different particles in the ATLAS detector [103].

tion and can only be performed up to $|\eta| < 2.5$. The muon measurements can be used up to $|\eta| < 2.7$.

Detector component	Required resolution	η coverage Measurement	Trigger
Tracking	$\sigma_{p_T}/p_T = 0.05\%\ p_T \bigoplus 1\%$	$\|\eta\| < 2.5$	
EM Calorimetry	$\sigma_E/E = 10\%/\sqrt{E} \bigoplus 0.7\%$	$\|\eta\| < 3.2$	$\|\eta\| < 2.5$
Hadronic Calorimetry (jets)			
Barrel and End-cap	$\sigma_E/E = 50\%/\sqrt{E} \bigoplus 3\%$	$\|\eta\| < 3.2$	$\|\eta\| < 3.2$
Forward	$\sigma_E/E = 100\%/\sqrt{E} \bigoplus 10\%$	$3.1 < \|\eta\| < 4.9$	$3.1 < \|\eta\| < 4.9$
Muon Spectrometer	$\sigma_{p_T}/p_T = 10\%$ at $p_T = 1$ TeV	$\|\eta\| < 2.7$	$\|\eta\| < 2.4$

Table 3.1: General performance of the ATLAS detector [75].

The following sections describe in detail the three sub-detector systems: the Inner Detector in Section 3.2.1, the calorimeters in Section 3.2.2, and the Muon Spectrometer in Section 3.2.3.

3.2.1 Inner Detector

The Inner Detector (ID) represents the innermost ATLAS system and consists of four sub-detectors that are located closest to the interaction point: the Insertable B-Layer (IBL) [113, 114], the Pixel Detector [115, 116], the Semiconductor Tracker (SCT) [117], and the Transition Radiation Tracker (TRT) [118]. The full layout of the ID is shown in Figure 3.4, while Figure 3.5 and Table 3.2 show the radial position and $|z|$ extent of all sub-detector layers. All sub-detectors provide coverage in the $|\eta| < 2.5$ range. Since the ID needs to provide precise measurements of particle positions and momenta, each sub-detector is designed to achieve μm level measurement precision in order to meet the track reconstruction requirements (track reconstruction is described in Section 4.1). Due to the TRT, the ID can also provide electron identification for pseudorapidities up to $|\eta| = 2.0$.

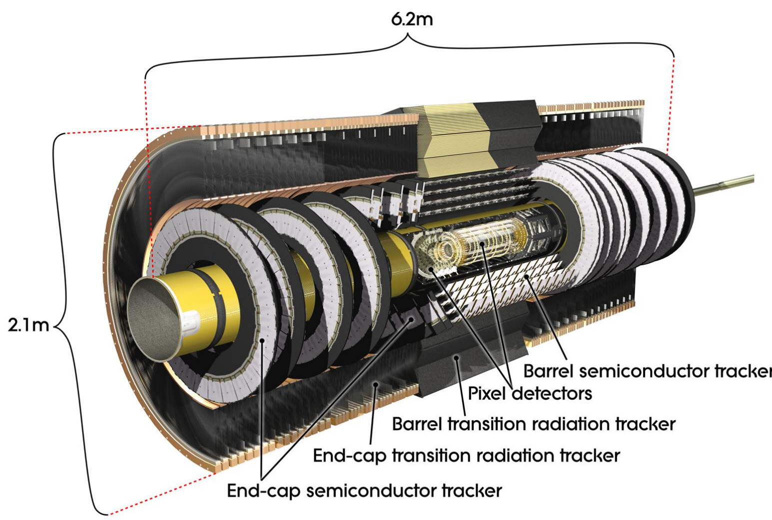

Figure 3.4: Schematic layout of the ATLAS Inner Detector [106].

Pixel Detector and Insertable B-Layer

As shown in Figure 3.5, the Pixel Detector and the IBL represent the two innermost systems of the ID. These high-granularity detectors cover the vertex region and provide precise measurements of particle trajectories. The sensitive elements consist of silicon pixel sensors, which measure the ionization energy deposited by charged particles as they are moving through the detector.

The Pixel Detector sensors [119] are arranged on three cylindrical layers, parallel to the beam axis, in the barrel region and on three disks, perpendicular to the beam axis, in each of the two end-cap regions. This design provides at least three measurements per charged

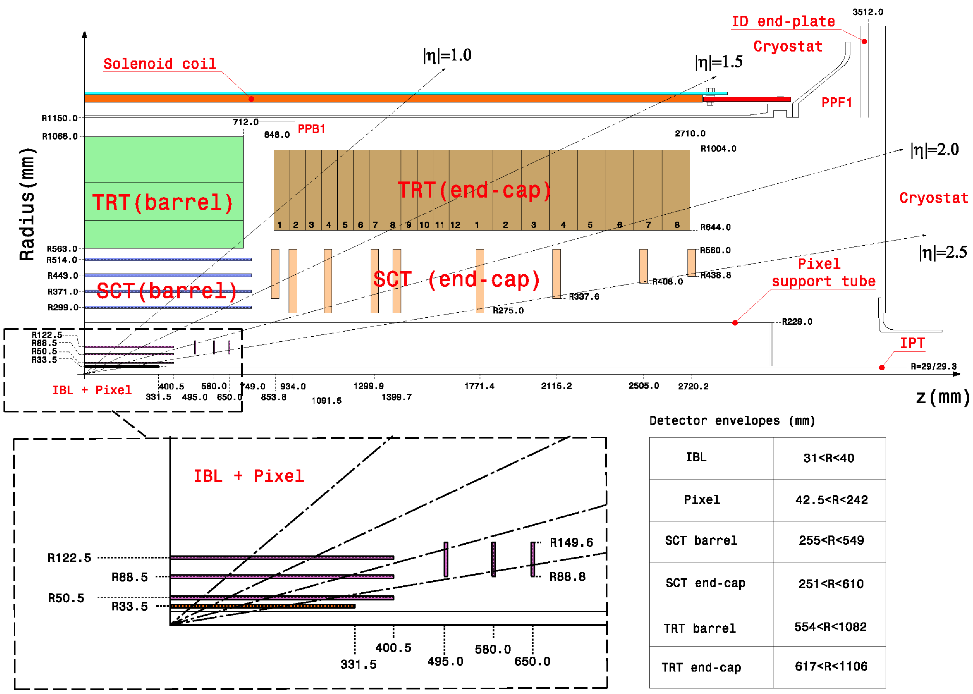

Figure 3.5: Quarter layout of the ATLAS Inner Detector, including the Insertable B-Layer [113].

particle track over the $|\eta| < 2.5$ range. The layers are segmented in $r - \phi$ and z into pixels that have a nominal size of 50×400 μm^2. The intrinsic resolution for pixels in the barrel is 10 μm in $r - \phi$ and 115 μm in z, and for pixels in the end-caps it is 10 μm in $r - \phi$ and 115 μm in r. The detector has 1744 pixel sensors, with 47232 pixels per sensor, and approximately 80.4 million readout channels.

The IBL is located before the first layer of the Pixel Detector, at a radius of 33 mm from the center of the beam pipe. It was installed before LHC Run 2 and now represents the innermost layer of the Pixel Detector, providing an additional high-precision measurement per track. The IBL consists of pixel sensors that have a smaller nominal size of 50×250 μm^2 and has approximately 12 million readout channels. As the IBL is located closer to the interaction point and has a smaller pixel size, the addition of the high-precision measurements from the IBL improves the impact parameter resolutions for low momentum particles by a factor of up to 2 compared to using only the nominal Pixel Detector layers. The presence of the IBL also enhances the primary and secondary vertex reconstruction, which in turn improves the performance of flavor tagging algorithms (described in Section 4.6). In particular, when including the additional measurement from the IBL, the rate at which c-jets (light-flavor jets) are mis-identified as b-jets is reduced by a factor of up to 1.6 (4) for jets with $p_T \lesssim 100$ GeV [120].

Sub-detector	Region	Layers	Radial extent [mm]	$\|z\|$ extent [mm]
IBL	Barrel	1 cylindrical layer	33.5	$0-330.15$
Pixel	Barrel	3 cylindrical layers	$50.5-122.5$	$0-400.5$
	End-cap	2×3 disks	$88.8-149.6$	$495-650$
SCT	Barrel	4 cylindrical layers	$299-514$	$0-749$
	End-cap	2×9 disks	$275-560$	$839-2735$
TRT	Barrel	73 straw planes	$563-1066$	$0-712$
	End-cap	160 straw planes	$644-104$	$848-2710$

Table 3.2: Spatial extent of the sensitive regions of the ATLAS Inner Detector subsystems [75, 113].

Semiconductor Tracker

The Pixel Detector is followed by the SCT , a microstrip detector that also relies on silicon semiconductor technology. The SCT has four cylindrical layers in the barrel region and nine disks in each of the end-cap regions and typically provides four measurements per charged particle track.

The modules are composed of two strips that are offset by a stereo angle of 40 mrad, with each pair of strips providing a two-dimensional measurement in the plane of the module. In the barrel region, one of the two strips is oriented along the z direction, while in the end-cap region, it is oriented radially. Each strip consists of two daisy-chained sensors; the sensors have a length of 6.4 cm with a pitch of 80 μm in the barrel and an average length of 6.1 cm with a mean pitch of 80 μm in the end-caps. The intrinsic $r-\phi$ resolution of SCT strips is 17 μm in both the barrel and the end-caps. The z resolution is 580 μm in the barrel and the r resolution is 580 μm in the end-caps. The SCT has 15912 sensors, with 768 active strips per sensor, and approximately 6.3 million readout channels.

Transition Radiation Tracker

The silicon detectors are complemented by the TRT, for which the basic detector elements are drift tubes (straws), filled with a xenon-based gas mixture in some channels and an argon-based gas mix in others[4], that contain a 30 μm diameter gold-plated tungsten anode wire. The straws are placed parallel to the beam axis in the barrel region, while in the end-cap regions they are arranged radially in wheels. They have a diameter of 4 mm and

[4]The TRT used a xenon-based gas mixture during Run 1. Due to significant gas leaks, the gas system was modified for Run 2 to use a cheaper argon-based gas mixture in some channels [121].

can provide only $r - \phi$ information at an intrinsic resolution of 130 μm per straw. The TRT has approximately 351,000 readout channels.

Despite having a lower precision compared to the silicon detectors, the TRT performance is compensated by the large number of measurements it provides, around 36 hits per charged particle. This enables radially extended track reconstruction up to $|\eta| = 2.0$ and significantly improves the measurement of particle momentum. It can also provide useful information for identifying photon conversions. The TRT can also be used to perform particle identification[5]: by measuring the amount of energy above a high energy-deposit threshold corresponding to transition radiation, the TRT can provide discrimination between electrons and charged hadrons (pions), as the latter are less likely to produce transition radiation, while the former give the largest effect.

3.2.2 Calorimeters

The ATLAS calorimeters are sampling calorimeters that contain alternating layers of passive and active materials. Incoming particles interact with the calorimeter passive material, which initiates a showering process. The energy of the particles is then measured in the active layers of the calorimeter. The innermost calorimeter, the Electromagnetic Calorimeter, typically contains the electromagnetic showers produced by electrons and photons. The Hadronic Calorimeters (Tile Calorimeter [109, 110], Hadronic End-cap Calorimeters [107, 108], and Forward Calorimeters [107, 108]) contain showers that are initiated by hadrons – because hadrons travel through more material before being absorbed, the Hadronic Calorimeters take up a larger fraction of the ATLAS volume compared to the Electromagnetic Calorimeter. Figure 3.6 shows the general layout of the ATLAS calorimeter system, while details about the coverage of each sub-system are summarized in Table 3.3. Overall, the calorimeter system covers the pseudorapidity range $|\eta| < 4.9$.

LAr Electromagnetic Calorimeter

The liquid argon Electromagnetic Calorimeter (ECAL) uses lead as the passive material (absorber) and liqud argon as the active material, with the layers arranged in an accordion-like geometry to provide complete coverage in the ϕ direction. The ECAL is composed of a barrel region, covering the range $|\eta| < 1.475$, and two end-cap regions, covering the range $1.375 < |\eta| < 3.2$. The ECAL barrel is divided into three layers in depth. In the region $|\eta| < 1.4$, each layer is segmented into fine granularity $\Delta\eta \times \Delta\phi$ regions of size 0.003×0.1, 0.025×0.025, and 0.05×0.025, respectively. For $|\eta| > 1.4$, the granularity of the layers becomes coarser. Each end-cap consists of two coaxial wheels: an outer wheel covering $1.375 < |\eta| < 2.5$ and an inner wheel covering $2.5 < |\eta| < 3.2$. The outer wheel calorimeter is divided into three longitudinal layers of fine $\Delta\eta \times \Delta\phi$ granularity, with region size varying

[5] The particle identification is affected by the use of different gas mixtures in different parts of the detector, as argon has a lower transition radiation absorption probability compared to xenon [121].

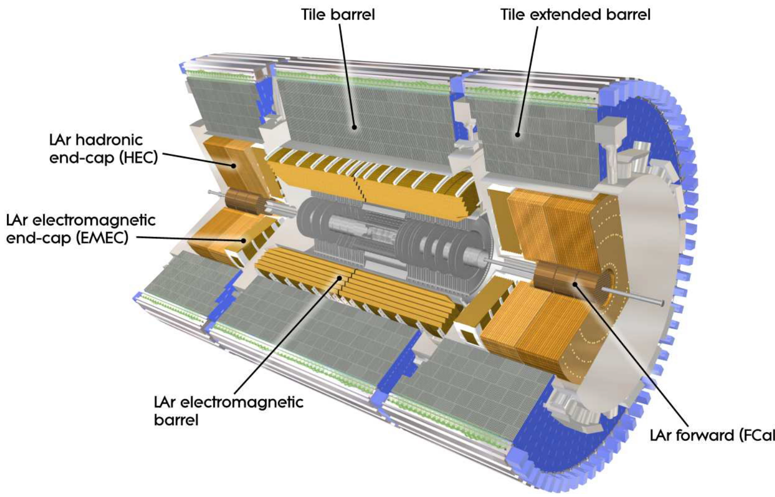

Figure 3.6: Schematic layout of the ATLAS calorimeter system [75].

	Barrel		End-cap	
Sub-system	Layers	$\lvert\eta\rvert$ coverage	Layers	$\lvert\eta\rvert$ coverage
Presampler	1	$\lvert\eta\rvert < 1.52$	1	$1.5 < \lvert\eta\rvert < 1.8$
EM calorimeter	3	$\lvert\eta\rvert < 1.35$	2	$1.375 < \lvert\eta\rvert < 1.5$
	2	$1.35 < \lvert\eta\rvert < 1.475$	3	$1.5 < \lvert\eta\rvert < 2.5$
	–	–	2	$2.5 < \lvert\eta\rvert < 3.2$
LAr hadronic end-cap	–	–	4	$1.5 < \lvert\eta\rvert < 3.2$
LAr forward calorimeter	–	–	3	$3.1 < \lvert\eta\rvert < 4.9$
Tile calorimeter (extended)	3 (3)	$\lvert\eta\rvert < 1.0$ $(0.8 < \lvert\eta\rvert < 1.7)$	–	–

Table 3.3: Number of layers and pseudorapidity extent of the ATLAS calorimeter system [75].

as a function of $|\eta|$, with the exception of the $|\eta| < 1.5$ region which is divided into only two layers. The inner wheel calorimeter is segmented into two sections in depth with a coarser granularity of $\Delta\eta \times \Delta\phi = 0.1 \times 0.1$. In order to correct for energy losses due to material interactions in the ID, a presampler detector (consisting of one active layer of liquid argon) is placed upstream of the ECAL in the region $|\eta| < 1.8$.

Tile Calorimeter

The Tile Calorimeter, located directly outside of the ECAL, is a sampling calorimeter that uses scintillating tiles as the active material and steel as the absorber. It has an inner radius of 2.28 m and extends to an outer radius of 4.25 m, which corresponds to 9.7 interaction lengths at $\eta = 0$. The Tile Calorimeter consists of a barrel region that covers the $|\eta| < 1.0$ range and two extended barrel regions that cover the $0.8 < |\eta| < 1.7$ regions. The barrels are divided into 64 modules along the ϕ direction and into three layers in depth. The scintillation light is collected by wavelength-shifting fibers into two photomultiplier tubes (PMTs) located at the outer edge of each module. Along the η direction, the grouping of the readout fibers into the PMTs gives a pseudo-projective geometry centered at the interaction point.

LAr Hadronic End-cap Calorimeter

The liquid argon Hadronic End-cap Calorimeter (HEC) is located behind each ECAL end-cap. It extends from a radius of 0.475 m up to a radius of 2.03 m and covers the $1.5 < |\eta| < 3.2$ range. This sampling calorimeter is composed of copper plates (passive material) and liquid argon (active material) is used to fill the gaps between the plates. The HEC contains two wheels per end-cap, with each wheel constructed from 32 wedge-shaped modules. In depth, the wheels are divided into two segments, resulting in a total of four layers per end-cap. In the two wheels closest to the detector origin, the copper plates have a thickness of 25 mm, while in the other two wheels the thickness of the plates is doubled.

LAr Forward Calorimeter

The liquid argon Forward Calorimeter (FCAL) extends from a radius $r = 72$ mm to $r = 455$ mm, has a depth of approximately 10 interaction lengths, and provides coverage over the range $3.1 < |\eta| < 4.9$. As this region is close to the beam line, the FCAL is designed to be resistant against radiation damage from the high flux of particles present. Each end-cap of the FCAL contains three layers of absorber material. The first layer uses copper, while the other two layers are made of tungsten. Each layer consists of a regularly spaced matrix of longitudinal tubes which contain concentric cathode rods. The gap between the rod and the tube is filled with liquid argon, which serves as the active material.

3.2.3 Muon Spectrometer

Figure 3.7 shows the layout of the Muon Spectrometer (MS), the largest of the ATLAS subsystems. The MS measures the deflection of muon tracks due to the magnetic field generated by three superconducting air-core toroidal magnets. The larger barrel toroid provides the magnetic field in the $|\eta| < 1.4$ range, while the two smaller end-cap toroids bend the muon tracks in the $1.6 < |\eta| < 2.7$ region. In the transition region $1.4 < |\eta| < 1.6$

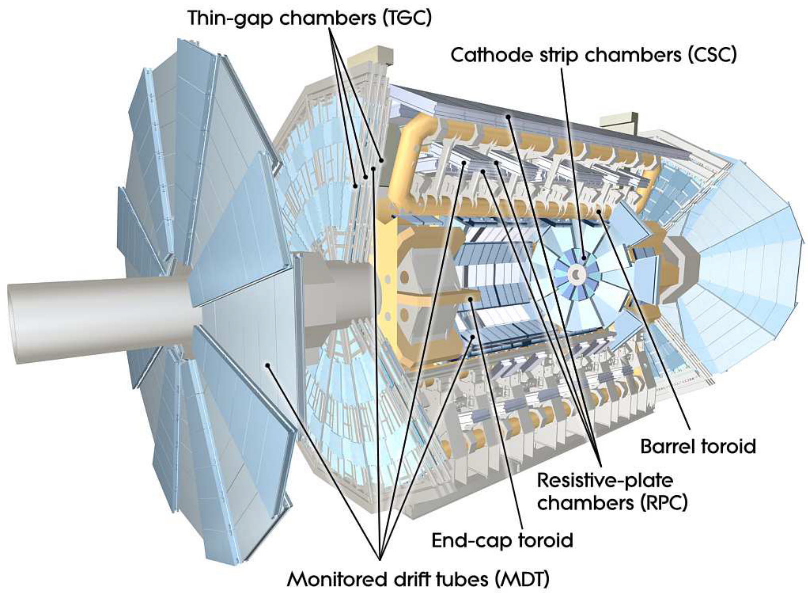

Figure 3.7: Schematic layout of the ATLAS Muon Spectrometer [75].

magnetic bending is provided by both the barrel and the end-cap magnets. The field integral of the magnets ranges between 2.0 and 6.0 T m across most of the detector.

The MS consists of four sub-detectors, two that are used for high-precision tracking and two that are used for the trigger. The measurements are performed in chambers that are arranged in three cylindrical layers parallel to the beam axis in the barrel region, while in the transition and end-cap regions, the chambers are installed in three layers that are perpendicular to the beam direction. For the tracking sub-detectors, Monitored Drift Tubes (MDT) provide precise measurements of the track coordinates over most of the η range. In the forward region between $2 < |\eta| < 2.7$ where the background is highest, the measurements are provided by higher granularity Cathode Strip Chambers (CSC).

Chamber Type	Role	Resolution (RMS)		
		z/r	ϕ	timing
MDT	tracking	35 μm (z)	–	–
CSC	tracking	40 μm (r)	5 mm	7 ns
RPC	trigger	10 mm (z)	10 mm	1.5 ns
TGC	trigger	2-6 mm (r)	3-7 mm	4 ns

Table 3.4: Spatial and timing resolution of the ATLAS muon system [75].

The trigger sub-detectors cover the range $|\eta| < 2.4$. They are composed of Resistive

Plate Chambers (RPC) in the barrel region and Thin Gap Chambers (TGC) in the end-cap regions. These chambers provide bunch crossing identification, well-defined p_T thresholds, and measurements of the track coordinates in the direction perpendicular to that determined by the tracking chambers. As shown in Table 3.4, the trigger chambers have a better timing resolution compared to the tracking chambers to allow for fast triggering on muons.

To account for the increased radiation background in Run 3, the innermost layer of the MS end-cap was replaced with the New Small Wheel (NSW), which uses Micromegas (MM) detectors as the precision tracking chambers combined with small-strip TGC (sTGC) for triggering [122].

3.3 Trigger and Data Acquisition

The proton bunches inside the LHC collide at a rate of 40 MHz. In order to store the information recorded by the ATLAS detector, about 1 MB of data must be saved for each event, which implies that a minimum data rate of 40 TB/s would be needed to record all the events produced in the collisions. However, hardware capabilities currently limit this rate to $\mathcal{O}(1)$ GB/s and most ATLAS systems require longer that the 25 ns between bunch crossings for full read-out of the signals. In order to address these limitations, ATLAS uses a two-level trigger system [123] to decide which events are most relevant to the physics program and should be saved, thereby reducing the amount of data that needs to be stored and subsequently processed. A schematic representation of the ATLAS Trigger and Data Acquisition (TDAQ) system used in Run 2 is shown in Figure 3.8.

The first level of the trigger, Level 1 (L1), is implemented with custom hardware and is designed to use information from the calorimeter and muon systems in Regions of Interest only (regions of the detector where activity is detected). The calorimenter selections are based on information from reduced-granularity calorimeter towers ($\Delta\eta \times \Delta\phi = 0.1 \times 0.1$ in the barrel region), while muon candidates are identified using the trigger chambers of the MS. The L1 trigger can select events containing high p_T muons, electrons, photons, jets, hadronically decaying τ-leptons, and missing transverse energy. During the time needed for the L1 trigger to accept or reject an event, the information is stored on front-end (FE) buffers on the detector, after which it is transferred to read-out-drivers (ROD) outside the detector. After the L1 selection, the total event rate is reduced to $\lesssim 100$ kHz.

The second level of the trigger, the High Level Trigger (HLT), processes the events that pass the L1 selection. The HLT is software-based, running on a dedicated computing farm, and performs full event reconstruction using information from all ATLAS systems, including tracking information from the ID and the muon tracking chambers and energy deposits in the calorimeters, read out at full detector granularity. While the HLT is making the decision, the event information is stored in the readout system buffer. After the HLT selections, the total rate is further reduced to approximately 1.5 KHz or lower.

The events that pass the HLT selection are permanently stored and transferred to the CERN Data Center for full offline reconstruction. The CERN Data Center is part of the

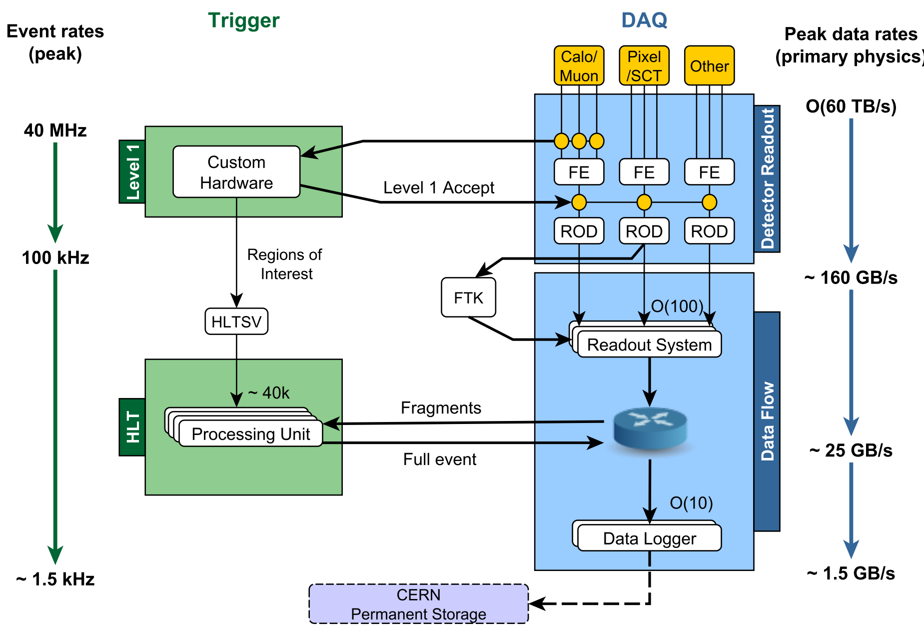

Figure 3.8: Diagram of the ATLAS Trigger and Data Acquisition system during Run 2 [124].

LHC Computing Grid [125], a four-tiered system which provides the resources for storing, accessing, and analyzing all the data produced at the LHC, with the CERN Data Center representing Tier 0. Tier 1 comprises computing centers that are large enough to store LHC data. They receive raw and reconstructed output from Tier 0, reprocess and store the corresponding output, and distribute the data to Tier 2 centers. Tier 2 consists of universities and institutes with enough computing power to produce and reconstruct simulated events – part of the simulated data produced by Tier 2 sites is stored at the Tier 1 centers. Tier 3 is made up of small computing clusters or individual computers that can access the Grid.

3.4 Upgrades for the High-Luminosity LHC

The High-Luminosity Large Hadron Collider (HL-LHC) [126] is the next planned upgrade to the LHC, which aims to achieve an instantaneous luminosity 5 to 7.5 times larger than the LHC design value and to reach a design center-of-mass energy of 14 TeV. Over the 12 years of HL-LHC operation, the total amount of data collected is expected to be $\sim 3000 - 4000$ fb^{-1}, which is one order of magnitude larger than that of the baseline LHC program. Data taking at the HL-LHC is expected to start in 2029 with Run 4 which would achieve a maximum peak luminosity of 5×10^{34} cm^{-2}s^{-1}, corresponding to an average of 140 simultaneous *pp* collisions per bunch crossing. This would be followed by Run 5, nominally starting in 2032, which would achieve a maximum peak luminosity of 7×10^{34} cm^{-2}s^{-1} corresponding to an average pile-up of 200.

In preparation for the expected increase in instantaneous luminosity and pile-up, the ATLAS experiment has developed a Phase-II detector upgrade program. A key part of this program consists of replacing the current Inner Detector with the Inner Tracker (ITk) [127, 128], a new all-silicon detector that is designed for optimal track reconstruction in the high pile-up conditions expected at the HL-LHC. A schematic $R-z$ view of the active sensors of the ITk detector is shown in Figure 3.9.

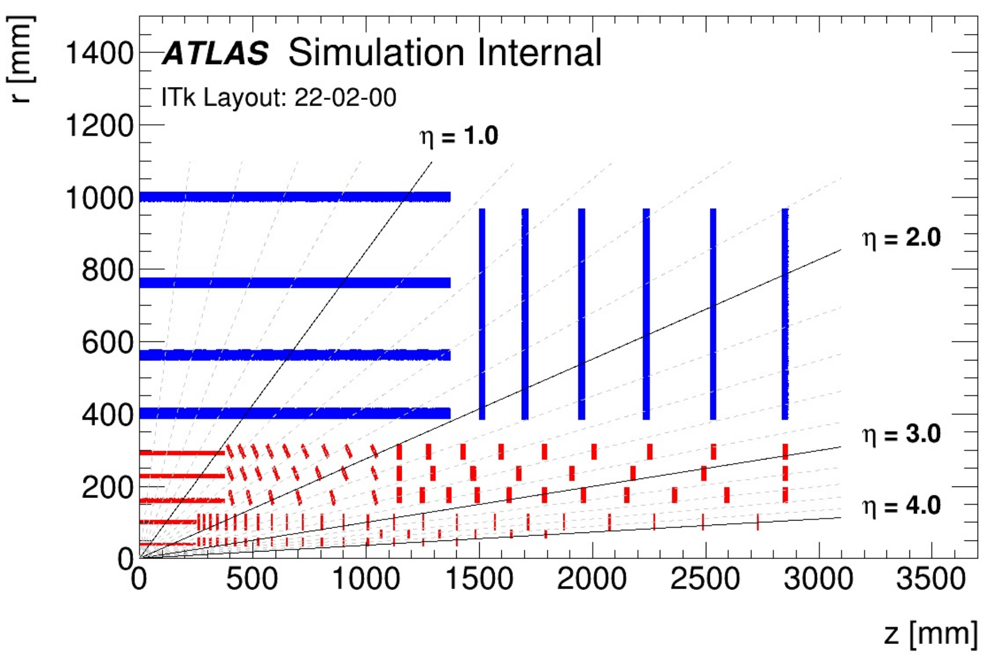

Figure 3.9: Schematic view of the ATLAS ITk Layout tag 22-02-00, showing the positions of the active sensors for the Pixel (red) and the Strip Detector (blue) [2].

The ITk detector will consist of two sub-detectors: a Pixel Detector and a Strip Detector. The Strip Detector will have four double-sided layers in the barrel region, with a small stereo angle between the sides of each layer. In the end-cap region, it will consist of six disks with strips mounted on both sides of petal support structures. The pseudorapidity coverage of the Strip Detector will extend up to $|\eta| = 2.7$.

The Pixel Detector will have five layers divided into three parts. The inner part will consist of a two-layer barrel section and an end-cap section with rings, both located within an Inner Support Tube (IST) to make the inner part replaceable. The two outer parts will consist of a three-layer barrel and a three-layer end-cap with rings. The central part of the barrel will consists of flat layers, while the outermost part will consist of inclined rings that are tilted intermediately between central barrel and end-cap such that particles at large pseudorapidity will cross the sensors with an incidence angle close to normal. The Pixel Detector will extend the pseudorapidity coverage up to $|\eta| = 4.0$ (compared to the current ATLAS ID coverage of up to $|\eta| = 2.5$) and will provide at least nine measured hits in the forward region. Additionally, for the rings in the inclined and end-cap sections of the Pixel Detector, the distance between pairs of modules can vary. This provides an important advantage, as placing adjacent rings close to each other results in multiple hits per track in a given layer.

Another part of the Phase-II program is represented by the upgrade of the ATLAS Trigger and Data Acquisition System. The goal of the TDAQ upgrade is to increase the event readout rate by an order of magnitude (1 MHz versus 100 kHz for Run 2) [129]. The upgraded TDAQ system will consist of a hardware-based Level 0 (L0) Trigger, a Data Acquisition System (DAQ), and the Event Filter (EF) System. The L0 system will perform the initial identification of physics objects and make trigger decisions, reducing the event rate from 40 MHz down to 1 MHz. Then, the complete event information will be transmitted through the DAQ into the EF. The EF will reconstruct and select events matching specific criteria, further reducing the rate at which data is transferred to permanent storage to 10 KHz.

A study of the performance of a fast prototype of the ITk track reconstruction chain and its feasibility as a software-based solution for tracking at the EF level is presented in Chapter 7.

Chapter 4

Physics Object Reconstruction

The raw signals collected by the ATLAS detector are reconstructed into physics objects, that are used to represent final state particles, through the use of dedicated reconstruction algorithms. The *reconstruction* process begins with low-level information consisting of tracks, vertices, and calorimeter clusters. These low-level objects are used to reconstruct high-level physics objects that correspond to different particles, based on the expected signatures left in the detector[1]. As there is some level of similarity between the signatures of different objects, *identification* algorithms are used to select collections of physics objects of a particular type. Additionally, to further suppress contamination from background sources, *isolation* requirements are applied to objects which are expected to have little additional detector activity in their proximity (typically leptons). Finally, a *calibration* step is performed to correct for any differences between data and simulation due to detector-related effects. Within the ATLAS experiment, these algorithms are implemented centrally in the Athena framework [74]. Different ATLAS software releases[2] are available to be used for different purposes, such as Monte Carlo production or processing and analysis of data recorded during a specific LHC run.

This chapter introduces the reconstruction algorithms used to process data collected by the ATLAS detector during Run 2 of the LHC. The focus is on providing an overview of the representative stages for each algorithm and introducing the main working points that are relevant to the analysis presented in Chapter 5.

[1] As the reconstruction for physics objects is generally done independently of one another, an overlap removal procedure is employed to avoid using detector signals corresponding to a single particle in the reconstruction of different physics objects.

[2] The ATLAS software releases are numbered with an identifier of the form `A.B.X`. For example, releases `21.x.x` are used for Run 2 data taking, processing, and MC generation. Within it, release `21.2` is used specifically by physics analyses, while release `21.9` is used for developments related to Run 4. `X` is a release number that is monotonically increased as bug fixes and improvements are added to the code.

4.1 Tracks, Vertices, and Clusters

4.1.1 Track Reconstruction

The reconstruction of the trajectories of particles produced in proton-proton collisions is a first crucial step for particle identification. Since the ATLAS Inner Detector is immersed in an axial magnetic field, charged particles produced in the hard scattering will follow helical trajectories. In the ATLAS convention, the trajectories (also referred to as tracks) can be uniquely described by a set of five parameters [130]

$$\tau = (d_0, z_0, \phi_0, \theta, q/p), \tag{4.1}$$

which define the trajectory at the perigee, the point of closest approach with respect to the beamspot position (the average position of the pp collisions).

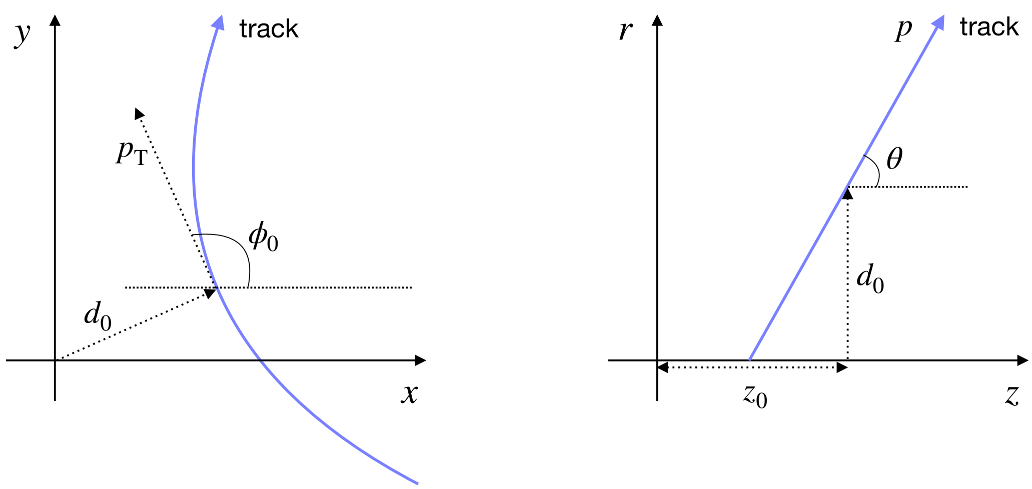

Figure 4.1: Illustration of a helical track and the five parameters used to describe it, as seen from the $x - y$ (left) and $r - z$ (right) planes.

Figure 4.1 provides a schematic view of the five track parameters. The transverse impact parameter d_0 represents the distance of closest approach in the transverse plane, while the longitudinal impact parameter z_0 provides the z-coordinate of the track at the point of closest approach. ϕ_0 and θ represent the azimuthal and polar angles, respectively. The ratio q/p is the inverse of the momentum p multiplied by the electric charge q and is related to the track curvature κ through

$$\kappa = \frac{0.3 \cdot B \text{ [T]}}{p \text{ [GeV]}}, \tag{4.2}$$

where B is the magnetic field.

As particles propagate through the detector, they interact with the detector material and deposit energy through ionization in the detector sensors. The energy deposits registered by the detector are then used to reconstruct the trajectories of the particles [131]. This section provides an overview of the main steps of the track reconstruction strategy for the ATLAS ID [132].

Primary Track Reconstruction

The first stage consists of assembling the raw measurements from the Pixel and SCT detectors into clusters. The clusterization algorithm groups together pixels or strips in a given sensor that pass a threshold on the charge yielded from the deposited energy and that share a common edge or corner. The clusters are then converted into three-dimensional measurements called space-points, which provide coordinates for the intersection points (also known as hits) between the charged particle trajectory and the active sensors of the ID. Since the Pixel detector already provides three-dimensional information, a Pixel space-point consists of a single cluster. For the SCT, clusters from both sides of a module are combined to obtain a space-point, making use of the 40 mrad stereo angle between strips on opposite sides. The space-points are used as inputs for the primary track reconstruction algorithm, which follows an inside-out approach that begins from the Pixel layers and builds tracks moving outwards through the ID. A simplified illustration of the inside-out approach is shown in Figure 4.2. The goal of the primary track reconstruction is to efficiently reconstruct tracks for charged particles originating from the hard scatter interaction or from the decay of short-lived particles.

Triplets of space-points are used to form track seeds, which serve to initialize the track building procedure. As the seed purity (fraction of seeds that produce good quality tracks) is highly dependent on the origin of the constituent space-points, seeds are constructed starting with SCT only (SSS), then Pixel only (PPP), and mixed detector seeds (PPS and PSS), listed in order of decreasing purity [134]. In order to avoid reconstructing seeds that would produce low quality tracks, several requirements are imposed on the momenta and impact parameters of the seeds. The seed purity is also improved by requiring the presence of an additional space-point that is compatible with the trajectory estimated from the seed. The sharing of space-points between multiple seeds is carefully controlled.

In the next stage, a combinatorial Kalman filter [135] extends the tracks by finding additional hits in the remaining detector layers that are compatible with the preliminary trajectory estimated from the seeds. If more than one compatible additional hit is found on the same layer, the filter will create multiple track candidates per seed. An additional check is performed for seeds that fail the track finding stage. If the seeds are found to be compatible with a region of interest in the calorimeter, then track finding is repeated to allow for a change in the track direction due to electrons emitting Bremsstrahlung radiation. This procedure is known as Bremsstrahlung recovery and is used to improve the efficiency of electron reconstruction. As the combinatorial Kalman filter takes into consideration all realistic combinations of hits, the final set of track candidates will contain tracks that have multiple hits in common (duplicate tracks) or incorrect combinations of unrelated hits (fake tracks).

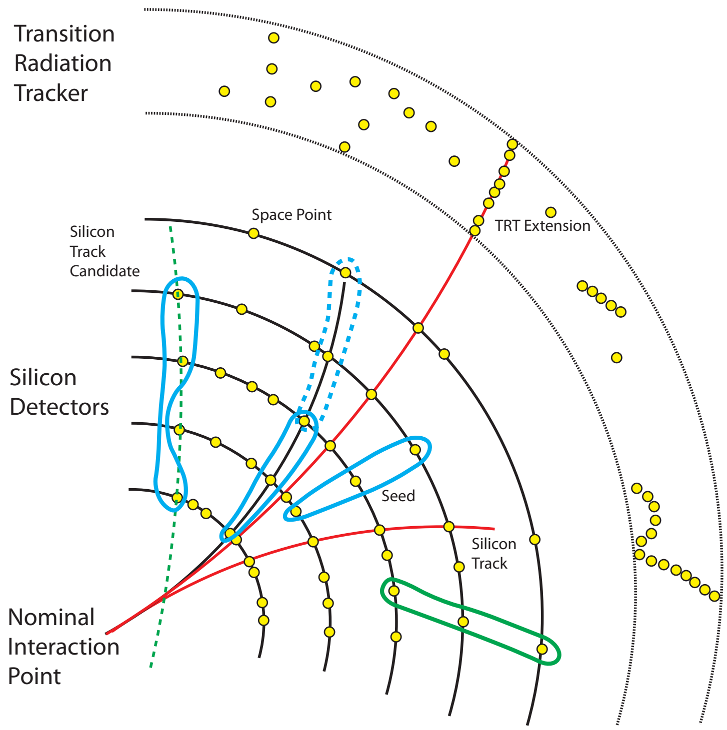

Figure 4.2: Simplified illustration of the inside-out approach for track reconstruction [133]. Detector hits (yellow dots) are grouped into triplets to form seeds (outlined in blue). Some seeds can correspond to the same trajectory (dashed blue outline), while other seeds are rejected because they do not originate from the interaction point (green outline). Seeds are extended into tracks (red lines) by finding additional compatible hits in the outer layers of the detector, including the TRT. The dashed green line illustrates a track candidate that is incompatible with the nominal interaction point.

A dedicated ambiguity resolution algorithm is implemented to choose between multiple track candidates and reject fake tracks. The algorithm uses a scoring function to rank the track candidates, with tracks that are more likely to represent a correct particle trajectory being scored higher than other tracks. The track score is computed using quantities that reflect the quality of the track. Hits assigned to a track increase the score, while holes[3] decrease it. The hits are weighted to reflect the different intrinsic resolutions of the subdetectors, with the highest weight being assigned to Pixel hits. A track fit is performed and the fit χ^2 is used to penalize candidates with low quality. The track momentum is also used to select energetic tracks and to reduce the number of low p_{T} fake tracks. The ambiguity algorithm then rejects lower quality tracks that share a significant number of hits with higher

[3]Holes are counted when the intersection points between the estimated trajectory and the active sensors do not contain any matching clusters.

quality ones and the shared hits are assigned to the kept tracks. Some amount of hit sharing is allowed to account for dense environments such as the cores of highly energetic jets, where the separation between tracks is expected to be smaller than the sensor size. In such cases, the shared cluster is divided between the track candidates, and a neural network-based algorithm is used to update the estimated positions and uncertainties for each particle and to compute a probability for one, two, or more particles having contributed to the cluster [136].

The track candidates that pass the ambiguity resolution are then re-fit using a global χ^2 method [137], which determines the final, high-precision estimates of the track parameters. The fit runs until it achieves the necessary precision or reaches the maximum number of allowed iterations. Track candidates that fail the fit are discarded at this step. The surviving tracks are extended into the TRT sub-detector by finding drift-circles that are compatible with the extrapolated trajectory, which are added to the track and a re-fit with the global χ^2 fitter is performed. The additional TRT hits improve the momentum resolution and help with particle identification.

All reconstructed tracks are required to pass basic quality selections on the hit content, such as having a minimum of 7 Pixel and SCT hits, a maximum of two shared hits, and a maximum of two Pixel and SCT holes, as well as selections on the track impact parameters that enforce compatibility with the primary vertex. Tracks are also required to be within the acceptance of the ID ($|\eta| < 2.5$) and to have a transverse momentum greater than 500 MeV.

Secondary Track Reconstruction

A secondary track reconstruction algorithm (back-tracking), which follows an outside-in approach, is used to reconstruct particles that are produced at greater distances from the interaction point, such as electrons generated from photon conversions or the decay products of long-lived hadrons. This algorithm uses only detector hits that have not been already assigned to tracks by the primary track reconstruction algorithm. For the back-tracking pass, track reconstruction is performed only in regions of interest within the EM calorimeter and starts from segments of TRT hits that are found within the regions of interest. Based on the compatibility with the TRT segments, track seeds formed from only two space-points are constructed in the Pixel and SCT sub-detectors. The seeds are extended into track candidates using the same combinatorial Kalman filter as in the primary track reconstruction. The track candidates are processed by the ambiguity resolution algorithm and the surviving tracks are extended back into the TRT and re-fit with the global χ^2 fitter.

4.1.2 Primary Vertex Reconstruction

After track reconstruction, another crucial ingredient needed for physics analyses consists of determining the locations where particle interactions occur, a process known as vertex finding. During Run 2, an average of ~ 30 simultaneous interactions take place per proton-proton bunch crossing, which means that, for most events, multiple interaction vertices can be identified. One of the most important vertices is the primary vertex, as it provides the location where the proton-proton hard scatter interaction takes place.

The primary vertex is reconstructed using a dedicated algorithm that has two stages: vertex finding and vertex fitting [138, 139]. The vertex finding stage associates the reconstructed tracks to possible vertex candidates, while the vertex fitting stage reconstructs the vertex position and its uncertainty. Tracks that serve as inputs to the vertex reconstruction algorithm are required to pass quality cuts based on p_{T} and the transverse and longitudinal impact parameters in order to ensure compatibility with the primary interaction. These tracks are used to compute a starting (seed) position for the first vertex. Using the vertex seed and the selected tracks, the algorithm performs an iterative χ^2 minimization to find the optimal vertex position as follows. Each track is assigned a weight which reflects the track's compatibility with the current vertex position estimate. The weights are computed to minimize the contribution of outlier tracks (those with large χ^2 values) to the vertex position calculation, and the vertex position is recomputed using the weighted tracks. This procedure is repeated for a fixed number of steps, with the track weights being recomputed each time with respect to the new vertex position. After the last iteration, tracks found to be incompatible with the final vertex candidate are used as inputs for the next vertex finding pass. This procedure is repeated until all tracks are associated to a vertex or until no additional vertex can be found with the remaining tracks.

Vertices with at least two associated tracks are considered as primary vertex candidates. Among them, the primary vertex is chosen to be the one that has the highest sum of squared transverse momenta ($\sum p_{\mathrm{T}}^2$) of the associated tracks, which reflects the fact that the hard scattering interaction is expected to produce particles with higher energies than those generated by pile-up interactions.

4.1.3 Calorimeter Clusters

Calorimeter information is used for the reconstruction of many physics objects, such as electrons or jets. Dedicated clustering algorithms are used to group related energy deposits in the calorimeter into clusters [140]. In particular, a topological clustering algorithm is used to generate topo-clusters, which consist of neighboring calorimeter cells that are grouped together in order to extract a significant signal from the background [141]. The algorithm uses the signal significance ζ, defined as the ratio between the cell energy and the expected cell noise, to determine how to group the cells. First, cells that have a signal significance $\zeta \geq 4$ are considered as seed cells, with each seed cell forming a proto-cluster. Then, neighboring cells that have signal significance $\zeta \geq 2$ are added to the corresponding proto-cluster. If two proto-clusters share the same cells with $\zeta \geq 2$, they are merged into a single proto-cluster. A final pass adds neighboring cells with signal significance $\zeta \geq 0$. This procedure is repeated until all topologically connected cells are found.

Proto-clusters formed this way typically result in a core of cells with high signal significance, surrounded by an envelope of cells with low signal significance. The resulting proto-clusters are checked for local signal maxima greater than 500 MeV. The presence of multiple local maxima indicates that two or more particle have deposited energy in the calorimeter in proximity to each other. In such cases, a dedicated cluster splitting algorithm uses a weighting technique to determine how to split the energy between the multiple signal peaks. After splitting, the final collection of proto-clusters become the topo-clusters that are used as input to other reconstruction algorithms.

4.2 Electrons

Electrons ($e^{\pm}$) in the central $|\eta| < 2.5$ region of the ATLAS detector are reconstructed using ID tracks and energy deposits in the electromagnetic calorimeter. As the forward region $2.5 < |\eta| < 4.9$ falls outside the ID coverage, electrons can be reconstructed using only information from the calorimeter, but additional information about the shape of the electromagnetic shower can be used to aid with the electron identification. This section provides an overview of the reconstruction procedure for central electrons only [142].

Reconstruction

The electron reconstruction algorithm proceeds by creating the ID tracks and calorimeter clusters needed for later steps. It first reconstructs clusters of energy deposits measured in topologically connected calorimeter cells (EM topo-clusters) using a dedicated topo-cluster reconstruction algorithm [140, 141], while ID tracks are first reconstructed using the procedure outlined in Section 4.1. Any reconstructed tracks that are found to have energy losses compatible with the electron hypothesis (up to 30% energy loss for each material interaction) are matched to the EM topo-clusters by restricting the angular separation in $\Delta\eta$ and $\Delta\phi$ between the extrapolated position of the track into the calorimeter and the center of the topo-cluster. If multiple tracks are matched to the same cluster, then a ranking based on the number of hits is performed, with tracks with Pixel hits being ranked before tracks with SCT hits but no Pixel hits. Within each category, tracks with a smaller ΔR separation from the cluster are preferred. In the end, the highest-ranked track is chosen as the best-match to the topo-cluster.

In the next step of the reconstruction procedure, a dynamic clustering algorithm is used to produce variable-sized electron superclusters, using the matched topo-clusters as input. As a first clustering step, the EM topo-clusters are tested to become seed cluster candidates, by requiring that the cluster have $E_{\mathrm{T}} > 1$ GeV and be matched to a track with at least four silicon hits. During the second clustering step, the algorithm attempts to find satellite cluster candidates, which are clusters originating from Bremsstrahlung radiation or topo-cluster splitting. A cluster is categorized as a satellite cluster if it passes certain selection criteria, such as being found within a $\Delta\eta \times \Delta\phi = 0.075 \times 0.125$ window around the seed cluster center or being found within a $\Delta\eta \times \Delta\phi = 0.125 \times 0.300$ window around the center and having the same best-match track as the seed cluster. Satellite clusters are then added to the seed clusters to form the final superclusters. Once the electron superclusters have been formed, the ID tracks are then matched to the superclusters, using the same matching procedure described above for matching to the EM topo-clusters. Electron candidates are identified as a supercluster matched to good quality tracks.

To select prompt electron candidates and rejects tracks from pile-up events, requirements are placed on the impact parameters of the matching tracks. The significance of the longitudinal impact parameter d_0, defined as $|d_0|/\sigma(d_0)$, is required to be less than 5, while a cut on the transverse impact parameter of $|\Delta z_0 \sin\theta| < 0.5$ mm is imposed to select tracks originating from the hard scattering vertex [142].

Identification

Additional quality criteria are applied to distinguish prompt electrons from background sources such as electrons from photon conversion, electrons produced from heavy-flavor hadron decays, or energy deposits from hadronic jets (non-prompt electrons). Prompt electron identification is achieved through a likelihood-based algorithm that uses ID and calorimeter variables [143]. The variables contain discriminating information about the primary electron track, the shape of the electromagnetic shower, and the spatial compatibility between the track and the reconstructed EM cluster. Cuts on the likelihood discriminant define three working points for electron identification, *Loose*, *Medium*, and *Tight*, which are optimized for different $|\eta|$ and E_{T} bins to achieve predefined target efficiencies that are suitable for a wide range of analyses [142]. The working points are chosen to be increasingly more selective, providing increased background rejection at the expense of reduced identification efficiency. For typical electroweak processes the efficiency decreases, on average, from 93% to 88% to 80% for the *Loose*, *Medium*, and *Tight* selections, respectively, while the identification efficiencies increase gradually from low to high E_{T} [142].

Isolation

To improve the rejection of non-prompt electron backgrounds, electron candidates are required to be isolated from nearby tracks or energy deposits. Two types of isolation variables are defined, one using ID tracks and the other using calorimeter energy deposits [142]. The track-based isolation variable is defined by adding up the transverse momentum of ID tracks found within a cone of size ΔR around the electron, but excluding the electron track from the calculation. Since electrons produced from the decay of high p_{T} heavy particles are generally found in proximity to other decay products, the track-based isolation variable, labeled $p_{\mathrm{T}}^{\mathrm{varcone20}}$, is defined using a cone with a variable size that becomes smaller for larger electron p_{T}, $\Delta R = \min(10\ \mathrm{GeV}/p_{\mathrm{T}}, 0.2)$. The calorimeter-based isolation variable, labeled $E_{\mathrm{T}}^{\mathrm{cone20}}$, is defined by summing the transverse energy of clusters found within a cone of size $\Delta R = 0.2$ around the center of the electron cluster. The energy of the electron cluster is excluded from the calculation and a correction that removes contributions from pile-up events is also applied.

Cuts on the two isolation variables are used to define four electron isolation working points that can be used by ATLAS physics analyses [142]. Three of the working points are defined by applying fixed cuts on the isolation variables. The *Loose* and *Tight* working points use both calorimeter and track isolation variables. The *HighPtCaloOnly* working point uses only the calorimeter variable and requires $E_{\mathrm{T}}^{\mathrm{cone20}} < \max(0.015 \times p_{\mathrm{T}}, 3.5\ \mathrm{GeV})$. The fourth working point is designed to provide fixed efficiency for selected p_{T} values that is uniform in η, using both calorimeter and track isolation variables.

Calibration

The electron reconstruction, identification, and isolation efficiencies are measured in data and compared to predictions from simulation for samples of $Z \to e^+e^-$ and $J/\psi \to e^+e^-$ events. The efficiencies are measured to a precision ranging from 1% to 5%, with larger uncertainties obtained at large values of η and E_{T} [142]. To account for differences observed between data and simulation, scale factors are derived as a function of E_{T} and η and can be applied to simulated samples to correct for mismodelling. The scale factors are generally found to be close to unity [142].

4.3 Photons

As photons (γ) and electrons traveling through the ATLAS detector leave similar signatures in the electromagnetic calorimeter, their reconstructions strategies are closely related to each other. However, unlike electrons, photons produce electromagnetic showers that are not associated with tracks in the ID. The reconstruction of prompt photons within $|\eta| < 2.5$ proceeds using a strategy similar to the one used for electrons [142], and is described briefly in the following, as photons are not used for the analysis presented in Chapter 5.

Reconstruction

As described in Section 4.2, the algorithm begins with reconstructing the ID tracks and EM topo-clusters that will be used in later steps. The ID tracks are matched to the EM topo-clusters by using cuts on the angular separation between the extrapolated track and the cluster. The tracks are also used as inputs for reconstructing the conversion vertices, which are then matched to the topo-clusters. Starting from the matched topo-clusters, a dynamic clustering algorithm constructs the variable-size photon superclusters, which consist of seed clusters and their associated satellite clusters. Photon seed clusters are required to have $E_{\mathrm{T}} >$ 1.5 GeV, while satellite clusters are required to be found within a $\Delta\eta \times \Delta\phi = 0.075 \times 0.125$ window around the seed cluster. Once the photon superclusters have been formed, the conversion vertices are then matched to the superclusters. Based on the properties of the tracks and conversion vertices, the candidates are reconstructed as converted or unconverted photons. Converted photons correspond to the case where the photon decays to a pair of e^+e^- and are identified as clusters matched to a conversion vertex reconstructed from a pair of oppositely charged ID tracks that are likely to be electrons. Unconverted photons are identified as clusters that are not matched to any good quality tracks.

Identification

Prompt photons need to be identified from non-prompt photon signatures originating from background processes, such as the decay of neutral hadrons into photons or QCD jets that deposit a large amount of energy in the electromagnetic calorimeter. As prompt photons generally produce narrower showers and have a smaller leakage fraction into the hadronic calorimeter compared to background photons, identification is achieved by applying rectangular cuts on selected calorimeter variables that describe various characteristics of the electromagnetic shower. Three reference working points, *Loose*, *Medium*, and *Tight*, are defined using cuts on different sets of the discriminating variables [142]. *Loose* and *Medium* correspond to less restrictive selections and are used for the trigger algorithms, with *Loose* being the main trigger selection for data collected in 2015 and 2016 and *Medium* for data collected in 2017 and 2018. The primary identification working point is represented by the *Tight* selection, which is designed to select a subset of photon candidates that also pass the *Medium* selection and is optimized separately for converted and unconverted photons.

Isolation and Calibration

Photon isolation is defined using the transverse energy in a cone of size ΔR around the photon candidate axis and uses calorimeter-based and track-based information [142]. Different isolation selection criteria can be defined, with the most common choices using both calorimeter isolation and track isolation or using calorimeter isolation only. Each ATLAS analysis targeting photons in the final state must determine the appropriate choice of isolation criteria based on the presence of background sources, signal-to-noise ratio, and background rejection needs.

The photon reconstruction and identification efficiencies are measured in data and compared to the predictions from simulation for samples of $Z \to \ell\ell\gamma$ ($\ell = e, \mu$). The efficiencies are measured to a precision ranging from 1% to 12%, with larger uncertainties obtained at low E_{T} values [142]. Scale factors are derived and applied to simulated samples to correct for mismodelling.

4.4 Muons

Reconstructing muons ($\mu^{\pm}$) involves processing signals coming from all the ATLAS subdetectors, as muons leave hits in the ID and the Muon Spectrometer chambers and small energy deposits in the calorimeter. Muons are reconstructed in the pseudorapidity range $|\eta| < 2.7$, which corresponds to the acceptance of the MS [144].

Reconstruction

Muon reconstruction consists of first performing independent reconstructions in the sub-detectors, then combining the information to generate complete muon tracks that can be used by physics analyses. The reconstruction of ID tracks proceeds as outlined in Section 4.1. Muon reconstruction in the MS involves building tracks out of segments of hits found in each set of muon chambers. The segments are combined into track candidates by performing a χ^2 fit to hits from segments in different layers. The segments are selected based on criteria on hit multiplicity and fit quality and matched through their relative positions and angles.

The muon tracks from the ID and the MS are then combined with additional information from the calorimeter through different algorithms [144]. The algorithms define five types of reconstructed muons, depending on which sub-detector information is used:

- Combined muons use information from the ID and the MS. The combined muon track is obtained through a global fit to the hits from both sub-detectors. Muons are commonly reconstructed using an outside-in approach, by extrapolating from the MS track inward and matching it to an ID track. The majority of muons are reconstructed as combined muons and represent the category with the highest purity.

- Inside-out combined muons use a complementary inside-out approach, where ID tracks are extrapolated outward and matched to at least three loosely-aligned MS hits. As this method does not require a fully reconstructed MS track, is can be used to recover some efficiency for low p_{T} muons or in regions with limited MS coverage.

- MS extrapolated muons are reconstructed using only MS tracks. They are required to have information from at least two MS layers, except in the forward region where three layers are required. This method is used to reconstruct muons in the $2.5 < |\eta| < 2.7$ region that is outside the ID acceptance.

- Segment-tagged muons are reconstructed when an ID track is matched to at least one MS track segment. This reconstruction method is used for muons that interact with only one MS layer, due to either having low p_{T} or falling outside the MS acceptance.

- Calorimeter-tagged muons are reconstructed when an ID track is matched to a calorimeter energy deposit. Although it produces muons with the lowest purity, this method is used to recover acceptance in regions where the MS is only partially instrumented to allow for cables and services to the other sub-detectors.

Selections cuts are applied to the impact parameters of the muon tracks to reject background muons resulting from hadron decays, pile-up, or cosmic rays. A cut is applied to the d_0 significance, $|d_0|/\sigma(d_0)$, which is required to be less than 3 [144]. The uncertainty $\sigma(d_0)$ accounts for both the estimated d_0 resolution from the track fit and the beam width. The cut on the transverse impact parameter $|z_0| \sin\theta < 0.5$ mm selects muon tracks that are likely to have originated from the reconstructed primary vertex [144].

Identification

Muon identification applies quality cuts to select prompt muons with high efficiency while rejecting muons produced by background processes, primarily the decays of pions and kaons. A distinctive feature of background muons consists of the presence of a "kink" in the reconstructed track. Hence, the combined track for background muons is expected to have poor fit quality and the momenta of the individual ID and MS tracks are likely to be incompatible.

Based on this information, several variables are constructed that provide good discrimination between prompt and background muons [144]. An example of such a variable is the normalized χ^2 of the fit to the combined track, which reflects the poor quality of the fit for background muons. Using these discriminating variables, different muon identification working points are defined, in order to meet the wide needs of physics analyses targeting final states containing muons. Three standard working points (*Loose*, *Medium*, and *Tight*) are aimed to be suitable for the needs of most physics analyses, including analyses that target the Higgs boson decay to a four muon final state and those limited by non-prompt muon backgrounds – the working points are designed to select muons with progressively increasing purity, at the expense of decreasing selection efficiency (from 99% for the *Loose* working point to 90% for the *Tight* working point) [144]. An additional two working points are designed to provide optimal background rejection with high efficiency for the lowest p_{T} muons (*Low*-p_{T} working point) and optimal momentum resolution for muons with p_{T} greater than 100 GeV (*High*-p_{T} working point) [144].

Isolation

To further identify prompt muons, which are often produced isolated from other particles, from background muons from semileptonic decays, which are typically embedded in jets, specific criteria can be applied to muon isolation variables. The isolation variables can be constructed using track information, calorimeter information, or a combination of both track-based and calorimeter-based isolation [144]. Using the track-based isolation variable was found to be the most robust with respect to pile-up, as tracks from pile-up vertices or with large transverse impact parameters are rejected by the selections mentioned earlier. This variable is computed as the scalar sum of the transverse momenta of ID tracks found in a cone of size ΔR around the muon (excluding the muon track). Two versions of the track-based variable are available, one where the cone size ΔR is fixed to 0.2, labeled as $p_{\mathrm{T}}^{\mathrm{cone20}}$, and one where ΔR depends on the p_{T} of the muon as $\min(10\ \mathrm{GeV}/p_{\mathrm{T}}^{\mu}, 0.3)$, labeled as $p_{\mathrm{T}}^{\mathrm{varcone30}}$ [144]. Cuts on the isolation variables define isolation working points, which are chosen to provide different options to balance prompt muon acceptance against background muon rejection. For track-only isolation, only tracks with $p_{\mathrm{T}} > 1$ GeV are considered and two working points are defined, *HighPtTrackOnly* (which requires $p_{\mathrm{T}}^{\mathrm{cone20}} < 1.25$ GeV) and *TightTrackOnly* (which requires $p_{\mathrm{T}}^{\mathrm{varcone30}} < 0.6 \cdot p_{\mathrm{T}}^{\mu}$) [144].

Calibration

The muon reconstruction, identification, vertex association, and isolation efficiencies are measured in data and compared with the predictions from simulation for samples of $Z \to \mu^+\mu^-$ and $J/\psi \to \mu^+\mu^-$ events. The efficiencies are measured to a precision ranging from 0.1% to 1% [144]. Scale factors are derived to reduce the simulation mismodelling and are found to be close to unity [144].

4.5 Jets

Quarks and gluons are the most frequently produced particles in *pp* collisions at the LHC. As these particles carry the color charge, the color confinement theory dictates that quarks and gluons cannot be observed as isolated particles, as soon after their production they undergo fragmentation and hadronization to generate colorless, highly energetic hadrons. For sufficiently boosted partons, this results in highly collimated sprays of hadrons, which are observed in the ATLAS detector as tracks in the ID and energy deposits in the calorimeters. On the experimental side, these narrow cones of hadrons are referred to as *jets* and represent the most complicated ATLAS physics objects that need to be reconstructed. Ideally, a reconstructed jet should provide information about the parton that originated it [145]. This requires that jet reconstruction algorithms satisfy the property of infrared and collinear (IRC) safety, meaning that the jet definition is not affected by very low-energy and collinear emissions from the initial parton.

Reconstruction

Different types of jet reconstruction algorithms can be used to combine tracks or calorimeter clusters into jets. The most commonly used algorithm within the ATLAS experiment is the IRC safe anti-k_t algorithm [146]. To determine if two objects i and j should be clustered together, the anti-k_t algorithm computes the following distance measures:

$$d_{ij} = \min\left(\frac{1}{k_{t,i}^2}, \frac{1}{k_{t,j}^2}\right)\frac{\Delta R_{ij}^2}{R^2} \quad \text{and} \quad d_{iB} = \frac{1}{k_{t,i}^2}, \tag{4.3}$$

where $\Delta R_{ij} = \sqrt{(y_i - y_j)^2 + (\phi_i - \phi_j)^2}$ gives the angular separation between the objects, with y_i representing the rapidity and ϕ_i the azimuthal angle of object i. The parameter R (the jet radius) defines the maximum allowed size of the jet cone. $k_{t,i}$ represents the transverse momentum of object i and d_{iB} provides the distance between object i and the beam axis. The clustering procedure compares the two distances d_{ij} and d_{iB} to decide on the next step. If $d_{ij} < d_{iB}$, then objects i and j are combined and the algorithm proceeds to the next iteration. If $d_{ij} > d_{iB}$, object i is reconstructed as a jet and removed from the list of objects. The distances are then recomputed from the remaining objects and the entire procedure is repeated until no objects are left. As the distance measures depend inversely on the transverse momentum of the objects, the anti-k_t algorithm begins reconstruction with hard (high p_{T}) objects, to which it then adds soft (low p_{T}) objects. Consequently, anti-k_t reconstructed jets generally have round, regular shapes in the $y - \phi$ space, as shown in Figure 4.3.

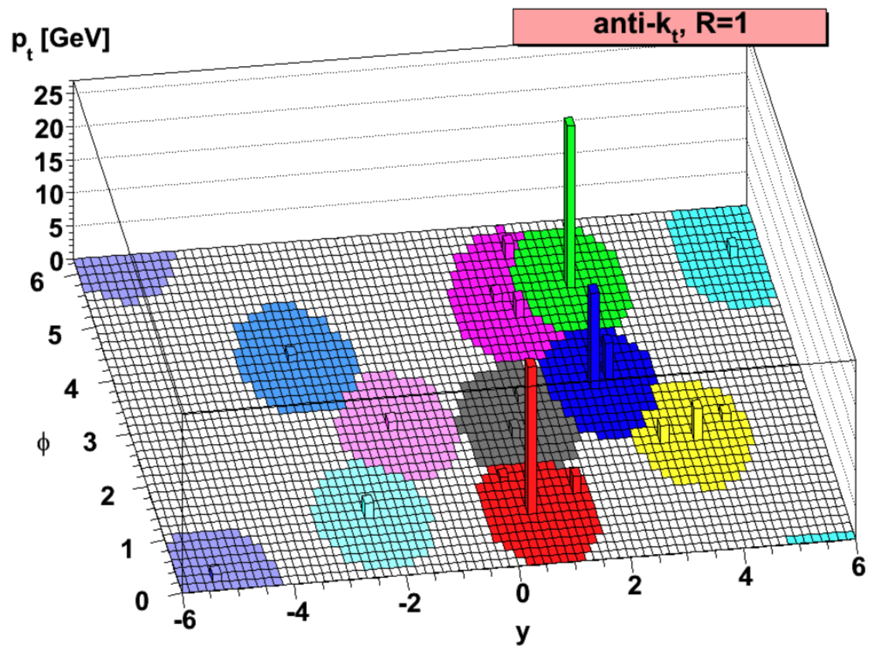

Figure 4.3: Simulation of jets reconstructed with the anti-k_t clustering algorithm using radius parameter $R = 1.0$ [146].

In ATLAS, the inputs to the anti-k_t jet reconstruction algorithm [146, 147] can consist of tracks, calorimeter energy deposits, or an algorithmic combination of tracks and calorimeter deposits known as particle flow [148] objects. Depending on the application, the value of the radius parameter R can be adjusted, resulting in three different categories of jets that can be used by physics analyses.

Jets originating from the hadronization of quarks and gluons are reconstructed as *small radius* (small-R) jets, using the anti-k_t algorithm with radius parameter $R = 0.4$. Small-R jet can be reconstructed using calorimeter-based energy information (*EMTopo* jets) or using particle flow objects (*PFlow* jets).

High momentum jets or those resulting from the decays of massive particles (e.g. the weak and Higgs bosons or the top quark) are reconstructed as *large radius* (large-R) jets, using the anti-k_t algorithm with radius parameter $R = 1.0$. The inputs for large-R jets consist of topological calorimeter-cell clusters that are calibrated using a local cell weighting procedure [141]. The jets undergo a grooming procedure that minimizes contamination from pile-up and underlying event contributions [149].

The radius parameter can also be defined as a function of the jet p_{T}, which results in so-called *variable radius* (VR) jets [150]. VR jets use tracks as inputs to the anti-k_t algorithm (VR track-jets). ID tracks with $p_{\mathrm{T}} > 0.5$ GeV and $|\eta| < 2.5$ are used as inputs to the track-jet clustering algorithm and are subject to standard tracking quality criteria. The radius parameter is given by $R(p_{\mathrm{T}}) = \rho/p_{\mathrm{T}}$, where ρ controls the rate at which the effective jet size decreases with increasing momentum, and lower (R_{min}) and upper (R_{max}) bounds are implemented as cut-offs. The track-jets are built using parameter values $\rho = 30$ GeV, $R_{\mathrm{min}} = 0.02$, and $R_{\mathrm{max}} = 0.4$, which were found to optimize the double b-tagging efficiency in boosted $H \to b\bar{b}$ decays [151].

Calibration

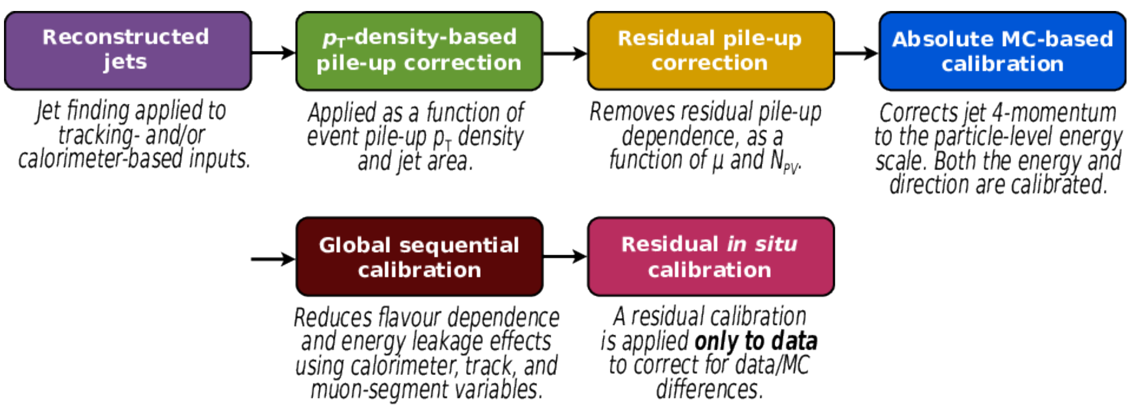

Figure 4.4: Schematic representation of the jet energy scale calibration chain [152].

The energy of reconstructed jets is calibrated to account for detector effects (such as different responses in the electromagnetic and hadronic calorimeters), reconstruction effects (such as energy deposited outside the jet cone), and pile-up contamination. Additionally, the calibration adjusts the jet energy scale (JES) of reconstructed jets to match the scale of simulated jets. This is achieved through a dedicated calibration chain that uses a combination of methods based on simulation and data-driven techniques [152]. The main calibration steps are shown schematically in Figure 4.4 and consist of:

- Origin correction: Since during reconstruction the jet axis points to the center of the detector, this step adjusts the direction of the jet to point towards the primary vertex, which improves η resolution.

- Pile-up corrections: This step aims to remove contributions from in-time (within the same bunch crossing) and out-of-time (during neighboring bunch crossings) pile-up interactions, which generate additional calorimeter energy deposits that could increase the jet energy. It consists of subtracting from the jet p_T first an overall correction, based on the average pile-up contribution, and then applying a residual correction that depends on the number of interactions per bunch crossing and the number of reconstructed primary vertices.

- Absolute JES calibration: This step adjusts the jet energy from the reconstruction scale to the particle-level (truth) scale used in simulation. The correction is derived by comparing reconstructed jets in data and truth jets and is applied as a function of E and η.

- Global Sequential Calibration: This correction accounts for fluctuations in the jet response due to energy leakage in the calorimeters. A four-momentum correction is derived as a function of p_T^{truth} and $|\eta|$ for five observables which depend on the shape and energy of the jet. This correction improves the distinction between jets initiated by quarks and gluons.

- In situ calibration: These corrections account for differences between data and simulation due to an imperfect modelling of the detector in simulation. An η-intercalibration is performed, in which well-measured jets in the central region $|\eta| < 0.8$ are used to derive a residual correction for jets in the forward region $0.8 < |\eta| < 4.5$ (generally less well-measured). Three other in situ calibrations are performed to correct for differences in the JES of central jets with respect to well-measured reference objects (Z bosons in the low p_T range $20 - 500$ GeV, photons in the intermediate p_T range $36 - 900$ GeV, and QCD multi-jet systems up to very high p_T of 2 TeV).

After calibration, the JES and its uncertainty are evaluated as a function of the jet p_T. The jet energy resolution (JER), defined as $\sigma(p_T)/p_T$, is also derived and calibrated in situ using di-jet events. The JES and JER are evaluated with a number of systematic uncertainties, which are primarily due to the data-driven calibration stages. The total uncertainty on the JES calibration varies from 5% for jets with very low p_T (20 GeV) to 1% for jets with high p_T (above 250 GeV and up to 2 TeV) and 3.5% at very high p_T (> 2.5 TeV) [152]. The uncertainty on the JER calibration varies from 3% at 20 GeV to less than 1% above 50 GeV [152].

As large-R jets are used to reconstruct massive particles such as the top quark, W, Z, or Higgs bosons into a single object, in addition to the jet energy, it is also important to calibrate the large-R jet mass. The large-R jets are passed through a chain of simulation-based calibration algorithms which correct the jet energy scale to the particle-level scale, account for any offset in pseudorapidity, and calibrate the jet mass scale (JMS) [153]. A comparison between data and simulation is used to validate the calibrations for the large-R JES and JMS. The uncertainty in the JES ratio between data and simulation is found to be $1\% - 2\%$ for jet p_T from 150 GeV to 2 TeV [154]. Over the same p_T range, the precision of the JMS varies from 2% to 10% [154]. The results for large-R JER and jet mass resolution

(JMR) obtained from simulation are also validated in situ. The agreement between the resolutions in simulation and data is found to be between 10% and 15% [154].

In the case of VR track-jets, as the tracks already have the correct momentum scale, no further residual jet calibration needs to be performed. However, the energy scale of track-jets is off by a factor of approximately[4] 1/3 compared to calorimeter jets, due to track-jets missing information from neutral jet constituents.

Pile-up Jet Suppression

Even with the pile-up corrections applied during calibration, it is still possible to have contributions from pile-up jets as a result of fluctuations in pile-up activity. To address this, a dedicated jet vertex tagging (JVT) algorithm is used to distinguish between hard scatter and pile-up jets, for jets with $|\eta| < 2.5$ [155]. Track, jet, and vertex variables are combined into a two-dimensional likelihood, from which a JVT discriminant (with values in the $[0, 1]$ range) can be derived. Cuts on the JVT discriminant are used to define the *Medium* (JVT > 0.2) and *Tight* (JVT > 0.5) working points [156]. The forward Jet Vertex Tagger (fJVT) is applied to suppress pile-up in jets in the $2.5 < |\eta| < 4.5$ region [157]. Cuts on the fJVT discriminant define *Loose* (fJVT < 0.4) and *Tight* (fJVT < 0.5) working points [156].

4.6 Flavor Tagging

Identifying the flavor of the quarks that initiate the jets provides crucial information that is needed to fully describe the hard scatter interaction. Specialized algorithms are used to identify jet flavor and the process is known as *flavor tagging*. This section summarizes the basic principles employed by the flavor tagging algorithms used by the ATLAS experiment during Run 2. Flavor tagging plays a key role in the analysis presented in this Chapter 5, and more details about the specific use of flavor tagging in the context of the analysis are provided in Section 5.3.2.

Flavor tagging uses the fact that reconstructed jets tend to have very different features, depending on the flavor of the partons that initiated them. As such, a distinction can be made between b-jets, c-jets, light-flavor jets (jets originating from u-, d-, s-quarks and gluons), and jets originating from hadronic decays of τ-leptons, which is shown schematically in Figure 4.5 and described in the following:

- b-jets are produced from the hadronization of b-quarks. Since b-hadrons have relatively long lifetimes (on the order of 1.5 ps [33]), they can travel distances of several mm inside the detector before decaying (the distance traveled depends on momentum and is ~ 5 mm for a 50 GeV hadron). As such, a displaced secondary vertex is expected to be found inside b-jets. Due to the large mass of ~ 5 GeV, b-hadrons contain $\sim 75\%$ of the jet momentum and decay into many particles (an average of ~ 5 charged particles

[4]This factor is 1/3 on average, but larger fluctuations can be observed on a jet-by-jet basis.

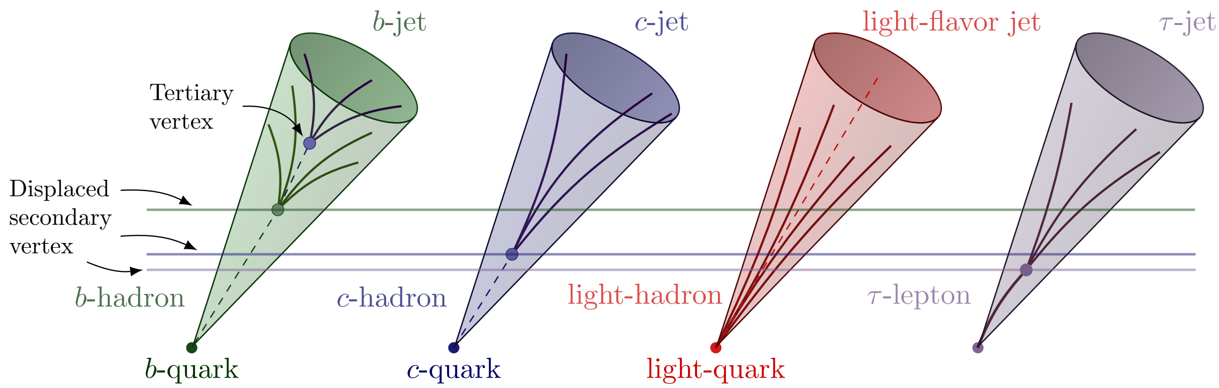

Figure 4.5: Illustration of the difference in features between jets initiated by b-quarks, c-quark, light-flavor quarks, and τ-leptons. Adapted from Ref. [158].

per decay). Additionally, due to the difference in the CKM matrix transition values $|V_{cb}|^2 > |V_{ub}|^2$, b-quarks decay primarily into c-quarks [50]. c-hadrons can also travel some distance before decaying in the detector, thus a tertiary vertex can be found inside b-jets.

- c-jets are produced from the hadronization of c-quarks. The most commonly produced c-hadron is the D-meson, which further decays into a kaon. The lifetime of the D-meson is shorter than that of b-hadrons, ranging between 0.2 and 1 ps [33]. Thus, D-mesons travel only a few mm before decaying (the distance is $\sim 1-3$ mm for a 50 GeV meson). The D-meson also has a smaller mass of ~ 2 GeV, hence it carries only $\sim 55\%$ of the jet momentum and decays into a smaller number of decay products (an average of ~ 2 charged particles per decay) compared to the b-hadron. The secondary vertex can still be measured, but its reconstruction is more complicated than for b-hadrons.

- Light-flavor jets are produced from the hadronization of u-, d-, s-quarks or gluons. For the light-flavor quarks, the hadronization occurs almost instantly, so there is no expected displaced vertex signature. Long-lived hadrons that are produced decay far away from the primary vertex, hence the secondary vertex signature cannot be reconstructed in the ID. Gluon initiated jets do not have a distinct secondary vertex either.

- τ-jets are produced in hadronic decays of τ-leptons. As the τ-lepton has a mass of 1.78 GeV and a lifetime of 0.29 ps [33], τ-jets have similar characteristics to c-jets, although τ-jets tend to be narrower. The dedicated procedures for reconstructing and identifying hadronically decaying τ-leptons are described in Section 4.7.

The ATLAS flavor tagging algorithms can be divided into two classes. The first class consists of *low-level taggers*, which distinguish between the different kinds of jets by using the ID tracks associated to the jets. The algorithms in this class use track properties, such as the impact parameters of the tracks or the presence of vertices, with dedicated algorithms being used to reconstruct secondary vertices and multi-vertex decay chains. The second class is represented by *high-level taggers*, which are machine learning algorithms that are trained using the discriminating information provided by the low-level taggers[5]. The high-level taggers provide the probabilities for a jet to be of a certain flavor type, which can be used to construct discriminants to primarily select a certain class of jets, e.g. b-tagging or c-tagging.

The performance of the flavor taggers is quantified in terms of the tagging efficiency for a particular jet flavor versus the misidentification rates for the other flavors[6]. The latter is commonly reported as the background rejection, which is defined as the inverse of the misidentification rate. These quantities are determined using simulated samples and are generally computed as a function of jet momentum.

Impact Parameter Based Algorithms

These algorithms use information about the track impact parameters d_0 and z_0. As b- and c- hadrons are relatively long-lived, their associated tracks generally have larger impact parameters than primary vertex tracks. Two different algorithms are used, referred to as `IP2D`, which uses only the transverse impact parameter, and `IP3D`, which uses both transverse and longitudinal impact parameters and the correlation between them [161]. Both algorithms make use of the signed[7] impact parameter significance[8], which is used to construct a log-likelihood ratio discriminant, shown in Figure 4.6 for a sample of simulated $t\bar{t}$ events.

A downside of the previously mentioned algorithms is that, by construction, they cannot exploit correlations between the impact parameters of different tracks. For example, in the decay of a b-hadron, particles produced at the secondary vertex can have large impact parameters, which are expected to be correlated[9] between tracks. Meanwhile, such a correlation is not expected in the absence of a displaced vertex, as is the case for light-flavor jets. The `IP3D` algorithm cannot take advantage of this correlation, as it assumes that the properties of any one track are independent of those of other tracks in the jet.

[5] The next generation ATLAS flavor taggers are based on graph neural networks (GNN), which can directly use information about charged particle tracks within a jet to predict the jet flavor, without the need for intermediate low-level taggers [159, 160]. The GNN-based flavor taggers are planned to be used during Run 3 and at the High-Luminosity LHC.

[6] For example, in the case of b-tagging, the efficiency is defined as the fraction of b-jets that are correctly identified as b-jets, while the misidentification rate for c-jets (light-flavor jets) is defined as the fraction of c-jets (light-flavor jets) that are incorrectly identified as b-jets.

[7] The impact parameters are assigned a positive sign if the track passes in front of the primary vertex with respect to the jet direction, and a negative sign if it passes behind the primary vertex.

[8] The significance is defined as the ratio between the impact parameter and its uncertainty: $d_0/\sigma(d_0)$ in the transverse plane and $z_0 \sin\theta/\sigma(z_0)$ in the longitudinal plane.

[9] The correlation is in the sense that if a track with large impact parameters is found, then it is more likely to also find a second track with large impact parameters.

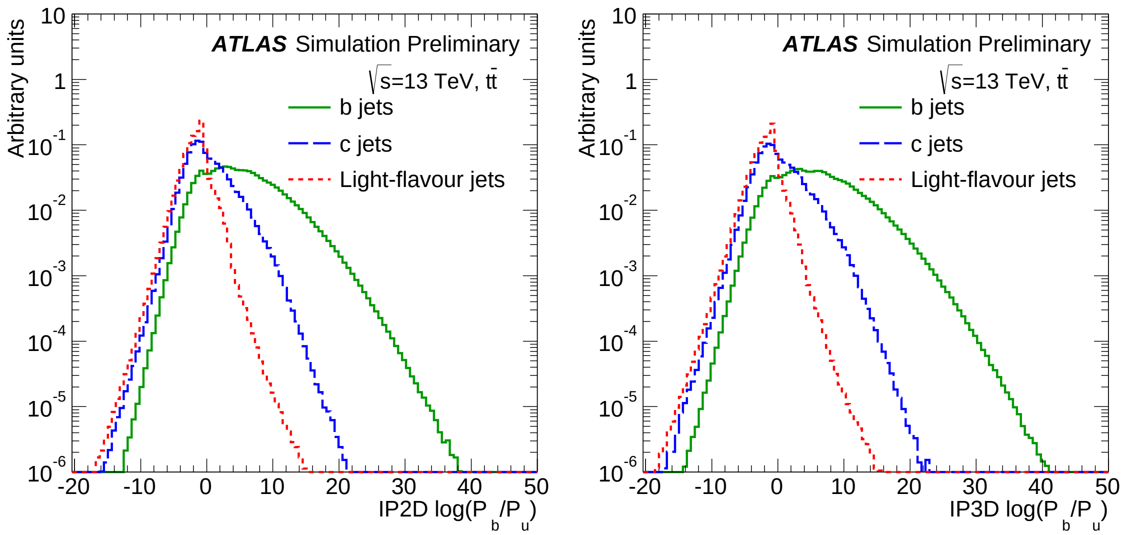

Figure 4.6: Log-likelihood ratio discriminant for the IP2D (left) and IP3D (right) algorithms [161]. The distribution of the discriminant is shown for b-jets (green), c-jets (blue), and light-flavor jets (red).

In order to address this limitation, an impact parameter based algorithm that uses recurrent neural networks (RNN) was developed [162]. RNNs are capable of directly learning the sequential dependencies between variables in an arbitrary length sequence, such as the tracks in a jet. The algorithm is referred to as RNNIP and it provides as output the probabilities that a jet is a b-jet, c-jet, light-jet, or τ-jet. The improvement gained by using the RNNIP algorithm consists in an approximately 2 (1.2) times increased rejection for light-jets (c-jets) compared to IP3D [162].

Secondary Vertex Algorithm

The purpose of the secondary vertex algorithm (SV) is to reconstruct a displaced secondary vertex within the jet [163]. In the first step, the algorithm attempts to reconstruct all two-track vertices, while also rejecting background tracks that originate from the decays of long-lived particles, photon conversions, or hadronic interactions with the detector material. In the second step, all the tracks that survived the previous selection are combined into a single secondary vertex, with outlier tracks removed iteratively. After the secondary vertex is reconstructed, different variables can be constructed to encode its properties, such as the reconstructed mass at the secondary vertex or the number of two-track vertex candidates reconstructed within the jet, shown in Figure 4.7. The set of secondary vertex variables is used as input for the high-level taggers.

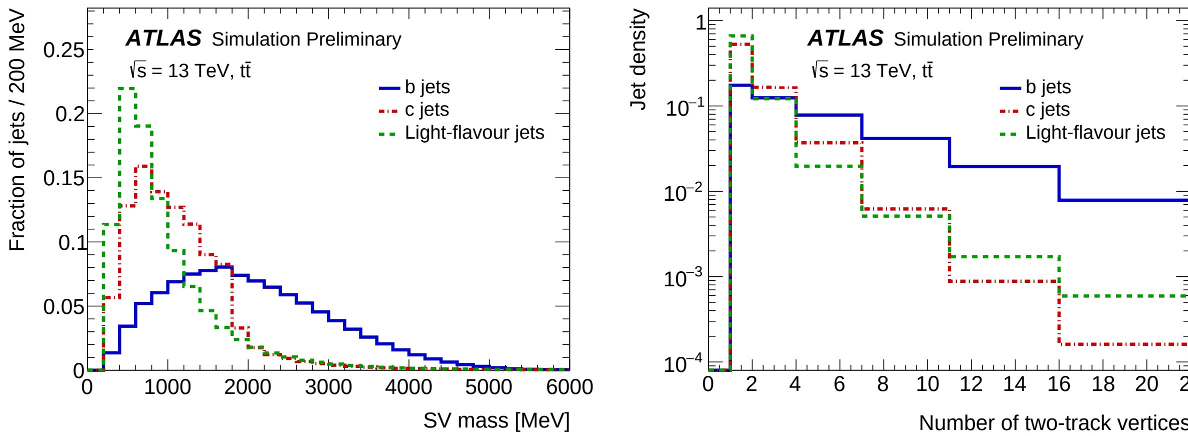

Figure 4.7: Normalized distributions of the secondary vertex mass (left) and the number of two-track vertices (right) reconstructed in the jet [163]. The distributions are shown for b-jets (blue), c-jets (red), and light-flavor jets (green).

Decay Chain Multi-Vertex Algorithm

`JetFitter` is a decay chain multi-vertex algorithm, which uses the topological structure of b- and c-hadron decays inside the jet to attempt to reconstruct the full decay chain from primary vertex to b-hadron to c-hadron [164]. The algorithm uses a Kalman filter to find a common line that passes through the primary, bottom, and charm vertices, which can approximate the flight path of the b-hadron. The positions of the vertices along the line are also determined. With this method, the b- and c-hadron vertices can be resolved even in the case where they are associated to a single track. A set of output variables is created, based on either the decay topology or the properties of the reconstructed vertices, which can be used as input for the high-level taggers.

High-Level Taggers

As mentioned earlier, the high-level taggers are algorithms that use machine learning techniques to combine the outputs from the low-level taggers into a final discriminant that is used to perform the jet flavor tagging. The high-level taggers consist of the `MV2` and `DL1` classes of algorithms, for which different variants exist, that differ in terms of architecture or training samples used [165, 166]. Generally, the high-level taggers use a combination of variables from the `IP2D`, `IP3D`, `SV1`, and `JetFitter` algorithms, as well as jet kinematic information. Table 4.1 provides a list of the input variables used by the `MV2` and `DL1` algorithms. Both classes of taggers are trained on a hybrid sample of $t\bar{t}$ and Z' events. The $t\bar{t}$ sample provides a significant number of b-jets, while the Z' sample is used to supplement with a uniform sample of all jet flavors up to high p_{T}.

Input	Variable	Description
Kinematics	p_{T}	Jet p_{T}
	η	Jet $\lvert\eta\rvert$
`IP2D/IP3D`	$\log(P_b/P_{\text{light}})$	Likelihood ratio between the b-jet and light-flavor jet hypotheses
	$\log(P_b/P_c)$	Likelihood ratio between the b-jet and c-jet hypotheses
	$\log(P_c/P_{\text{light}})$	Likelihood ratio between the c-jet and light-flavor jet hypotheses
`SV1`	$m(\text{SV})$	Invariant mass of tracks at the secondary vertex assuming pion mass
	$f_E(\text{SV})$	Energy fraction of the tracks associated with the secondary vertex
	$N_{\text{TrkAtVtx}}(\text{SV})$	Number of tracks used in the secondary vertex
	$N_{\text{2TrkVtx}}(\text{SV})$	Number of two-track vertex candidates
	$L_{xy}(\text{SV})$	Transverse distance between the primary and secondary vertex
	$L_{xyz}(\text{SV})$	Distance between the primary and secondary vertex
	$S_{xyz}(\text{SV})$	Distance between the primary and secondary vertex divided by its uncertainty
	$\Delta R(\vec{p_{\text{jet}}}, \vec{p_{\text{vtx}}})(\text{SV})$	ΔR between the jet axis and the direction of the secondary vertex relative to the primary vertex
`JetFitter`	$m(\text{JF})$	Invariant mass of tracks from displaced vertices
	$f_E(\text{JF})$	Energy fraction of the tracks associated with the displaced vertices
	$\Delta R(\vec{p_{\text{jet}}}, \vec{p_{\text{vtx}}})(\text{JF})$	ΔR between the jet axis and the vectorial sum of momenta of all tracks attached to displaced vertices
	$S_{xyz}(\text{JF})$	Significance of the average distance between the primary vertex and displaced vertices
	$N_{\text{TrkAtVtx}}(\text{JF})$	Number of tracks from multi-prong displaced vertices
	$N_{\text{2TrkVtx}}(\text{JF})$	Number of two-track vertex candidates (prior to decay chain fit)
	$N_{\text{1-trk vertices}}(\text{JF})$	Number of single-prong displaced vertices
	$N_{\geq\text{2-trk vertices}}(\text{JF})$	Number of multi-prong displaced vertices
`JetFitter` c-tagging	$L_{xyz}(2^{\text{nd}}/3^{\text{rd}}\text{ vtx})(\text{JF})$	Distance of 2^{nd} or 3^{rd} vertex from primary vertex
	$L_{xy}(2^{\text{nd}}/3^{\text{rd}}\text{ vtx})(\text{JF})$	Transverse displacement of the 2^{nd} or 3^{rd} vertex
	$m_{\text{Trk}}(2^{\text{nd}}/3^{\text{rd}}\text{ vtx})(\text{JF})$	Invariant mass of tracks associated with 2^{nd} or 3^{rd} vertex
	$E_{\text{Trk}}(2^{\text{nd}}/3^{\text{rd}}\text{ vtx})(\text{JF})$	Energy fraction of the tracks associated with 2^{nd} or 3^{rd} vertex
	$f_E(2^{\text{nd}}/3^{\text{rd}}\text{ vtx})(\text{JF})$	Fraction of charged jet energy in 2^{nd} or 3^{rd} vertex
	$N_{\text{TrkAtVtx}}(2^{\text{nd}}/3^{\text{rd}}\text{ vtx})(\text{JF})$	Number of tracks associated with 2^{nd} or 3^{rd} vertex
	$Y_{\text{trk}}^{\text{min}}, Y_{\text{trk}}^{\text{max}}, Y_{\text{trk}}^{\text{avg}}(2^{\text{nd}}/3^{\text{rd}}\text{ vtx})(\text{JF})$	Min., max., and avg. track rapidity of tracks at 2^{nd} or 3^{rd} vertex

Table 4.1: Input variables used by the `MV2` and `DL1` flavor tagging algorithms [165]. The `JetFitter` c-tagging variables are used in the case of the `DL1` algorithm only.

Relevant to the analysis in Chapter 5 is the DL1 class of algorithms, which is based on a deep feed-forward neural network architecture and provides multidimensional outputs corresponding to the probabilities that a jet is a b-jet, c-jet, or light-flavor jet, respectively. As a result, the DL1 outputs can be used to construct discriminants for both b- and c-tagging:

$$DL_{1,b} = \ln \frac{p_b}{f_c p_c + (1 - f_c) p_u} \quad \text{and} \quad DL_{1,c} = \ln \frac{p_c}{f_b p_b + (1 - f_b) p_u}, \tag{4.4}$$

with p_b, p_c, and p_u representing the probability of being a b-jet, c-jet, or light-flavor jet, respectively. While the parameters f_c and f_b are tunable, the standard definition for the b-tagging discriminant uses $f_c = 0.08$. Cuts are placed on the DL1 output discriminants to provide different efficiency working points for b-tagging and/or c-tagging. A variant of the DL1 algorithm is the DL1r tagger, which in addition to the input variables listed in Table 4.1 also uses the output probabilities from the RNNIP low-level tagger [167]. The use of DL1r to perform simultaneous b- and c-tagging within the context of the analysis is discussed further in Section 5.3.2.

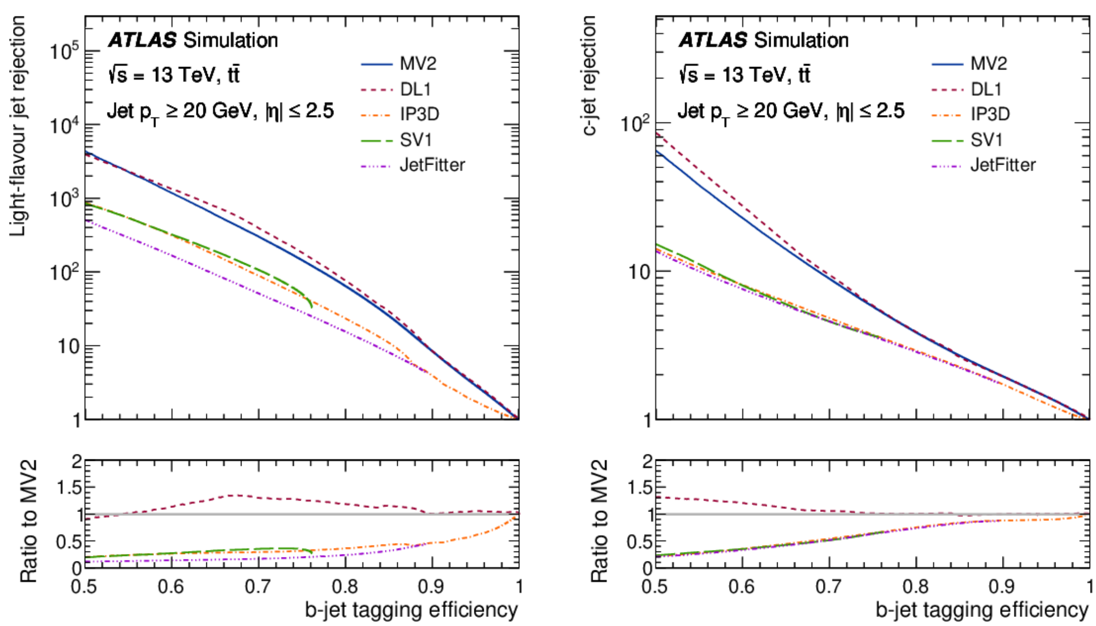

Figure 4.8: Light-flavor jet (left) and c-jet (right) rejection versus b-tagging efficiency for the low- and high-level flavor tagging algorithms [165]. The results are evaluated on a sample of $t\bar{t}$ events and shown for the IP3D, SV1, JetFitter, MV2, and DL1 algorithms.

Figure 4.8 compares the c-jet and light-flavor jet rejection factors as a function of the b-jet tagging efficiency for the low-level and high-level taggers. For the same b-tagging efficiency, the high-level taggers achieve up to approximately an order of magnitude higher levels of background rejection compared to the low-level taggers, demonstrating the benefit of combining all the information provided by the low-level taggers. Additionally, the neural-network based `DL1` algorithm provides better background rejection than the BDT based `MV2` tagger, as the neural network architecture can better exploit correlations between the different input variables.

Flavor Tagging Calibration

Flavor tagging working points (WPs) are defined by placing cuts on the distribution of the `DL1` discriminant, and all jets with a score above the WP threshold are considered to be tagged at the WP's level. For b-tagging, the WPs are chosen to achieve 85%, 77%, 70%, and 60% efficiency on b-jets, and show increasingly higher rejection for c-jets, τ-jets, and light-flavor jets [165]. The flavor tagging WPs are calibrated to account for any differences between the tagging efficiencies in data and in simulation, and the scale factors (SFs) are defined as:

$$\mathrm{SF} = \frac{\epsilon_{\mathrm{data}}}{\epsilon_{\mathrm{MC}}}, \tag{4.5}$$

where ϵ_{MC} and ϵ_{data} represent the tagging efficiency in simulation and in data, respectively. The calibration is performed separately for each jet flavor and the SFs and their uncertainties are derived as a function of jet p_{T} using samples of $t\bar{t}$ events. The SFs are generally found to be close to unity, with an uncertainty that ranges from 1% to 17% [165, 168].

4.7 Tau Leptons

The tau ($\tau^{\pm}$) is the heaviest of the leptons. As a result of having a lifetime of only 2.9×10^{-13} s, τ-leptons travel only a small average distance before decaying. This prevents them from being directly detected with the ATLAS detector, and instead they must be identified from their decay signature, similar to the way in which heavy-flavor quarks are identified.

The τ-leptons can decay either leptonically (35% of the time) or hadronically (65% of the time). The τ reconstruction described in this section focuses on the hadronic decay modes, where the final state products can be observed as a combination of narrow jets in the calorimeter and tracks in the ID [169]. The most common hadronic decay modes contain in the final state charged pions, either one (1-prong, 75% of the time) or three (3-prong, 22% of the time), and on occasion can also contain one or two neutral pions which decay to a pair of photons.

The τ reconstruction algorithm uses jets formed using the anti-k_t algorithm with a radius parameter $R = 0.4$, which are also required to pass selection cuts of $p_{\mathrm{T}} > 20$ GeV and $|\eta| < 2.5$ (excluding the transition region $1.37 < |\eta| < 1.52$ between the barrel and forward calorimeters) [169]. To increase the reconstruction efficiency and reduce effects from pile-up, the vertex at which the τ-lepton is produced is identified. Possible τ candidates are required to have one or three tracks associated with the τ production vertex. The tracks are required to be found in the core region around the τ axis and to pass selection cuts on p_{T}, the number of hits in the ID, and the transverse and longitudinal impact parameters with respect to the τ vertex.

As the τ reconstruction algorithm provides little to no rejection of QCD jets, dedicated algorithms are used to identify the τ-jets by exploiting characteristics such as low track multiplicity, collimated energy deposits, and the displacement of the vertex. This is achieved by training a boosted decision tree (BDT) on a set of discriminating variables for τ-jets. The BDT is trained on simulated samples containing τ decays from $Z/\gamma^* \to \tau\tau$ events, with separate trainings being performed for the 1-prong and 3-prong decay modes [170]. The output score of the BDT is used to define three working points (*Loose*, *Medium*, and *Tight*), which correspond to different efficiency values for the τ identification. A more recent version of the τ identification algorithm replaces the BDT with a recurrent neural network, which provides two times better background rejection than the BDT classifier for the same signal efficiency [171]. The RNN-based τ identification defines four working points (*Very Loose*, *Loose*, *Medium*, and *Tight*) that can be used by physics analyses.

The uncertainties on the τ reconstruction and identification efficiencies are evaluated using simulated $Z/\gamma^* \to \tau\tau$ events and found to be between 2% and 18% [169].

4.8 Missing Transverse Momentum

Not all particles interact with the ATLAS detector and thus cannot be directly detected. An example of this consists of the neutrinos, as well as possible beyond the Standard Model particles, such as dark matter candidates. The presence of such particles has to be instead inferred from the momentum imbalance in the transverse plane of the detector. As the initial particles are travelling entirely along the beam axis, conservation of momentum requires that the total momentum of the final state particles has to be zero in the transverse plane.

The momentum imbalance in the transverse plane, referred to as the missing transverse momentum, is determined as [172]:

$$\begin{aligned}\vec{E}_{\mathrm{T}}^{\mathrm{miss}} &= -\left(\sum_{\mathrm{hard}} \vec{p_{\mathrm{T}}} + \sum_{\mathrm{soft}} \vec{p_{\mathrm{T}}}\right) \\ &= -\left(\sum_{e} \vec{p_{\mathrm{T}}} + \sum_{\gamma} \vec{p_{\mathrm{T}}} + \sum_{\tau} \vec{p_{\mathrm{T}}} + \sum_{\mu} \vec{p_{\mathrm{T}}} + \sum_{\mathrm{jets}} \vec{p_{\mathrm{T}}} + \sum_{\mathrm{unused\ tracks}} \vec{p_{\mathrm{T}}}\right)\end{aligned} \tag{4.6}$$

The missing transverse momentum formula contains a hard term and a soft term. The hard term accounts for the momenta of all the fully reconstructed and calibrated objects, corresponding to particles (e.g. electron, muons, τ-leptons, and photons) and jets. The particles and jets that are used to compute the hard term are reconstructed with the methods described in the previous sections and have to pass specific selection cuts. As the (same) signals from the different sub-detectors can be used to reconstruct different physics objects, the $\vec{E}_{\mathrm{T}}^{\mathrm{miss}}$ reconstruction method avoids possible double counting by using an ambiguity resolution procedure to reject already used signals when adding up the $\vec{E}_{\mathrm{T}}^{\mathrm{miss}}$ contributions.

This is achieved by prioritizing the reconstruction of electrons, followed, in order, by photons, hadronically decaying τ-leptons, and jets. Muons have little or no signal overlap with other particles as they are primarily reconstructed from ID and MS tracks. The soft term includes any charged particle tracks that are associated with the primary vertex, but not with any of the reconstructed objects. It is computed using only ID tracks associated with the primary vertex.

The performance of the $\vec{E}_{\mathrm{T}}^{\mathrm{miss}}$ reconstruction with the ATLAS detector is determined from data and simulation samples, using selected events with expected $\vec{E}_{\mathrm{T}}^{\mathrm{miss}} = 0$ (e.g. leptonic Z boson decays) and events with expected missing transverse momentum from neutrinos (e.g. leptonic W boson or $t\bar{t}$ semileptonic decays) [172]. The systematic uncertainties on the $\vec{E}_{\mathrm{T}}^{\mathrm{miss}}$ scale and resolution are determined by considering the uncertainties in the reconstruction of the physics objects that make up the hard and soft term. The $\vec{E}_{\mathrm{T}}^{\mathrm{miss}}$ scale and resolution uncertainties are found to range between 5% and 10% [172].

Chapter 5

Measurement of $WH(H \to b\bar{b}/c\bar{c})$ Decays

The existence of the Higgs boson was confirmed by the ATLAS and CMS collaborations in July 2012 [81, 82]. Since then, many properties of the Higgs boson have been measured and found to be in agreement with the predictions of the Standard Model. However, the coupling of the Higgs boson to all SM fermions is still to be shown experimentally. As the coupling is stronger for heavier fermions, the Higgs decays to third generation fermions are more accessible than those to lower generation fermions. For example, the couplings of the Higgs boson to the τ-lepton (through the $H \to \tau\tau$ decay [173]) and the top quark (through the ttH production mode [174, 175]) have been measured. The coupling to the bottom quark was also observed, using the VH production mode together with the $H \to b\bar{b}$ decay mode [176, 177]. The VH mode was chosen because the leptonic decays of the vector bosons provide a clean signature that can be used to suppress the large QCD multi-jet backgrounds that make the $H \to b\bar{b}$ decay challenging to measure. After observation of the $VH(H \to b\bar{b})$ mode, additional analyses have focused on performing precision measurements, with the ATLAS collaboration publishing three results. The first two focused on the search for Higgs boson decays at low transverse momenta (the *resolved* regime) [178] and at high transverse momenta (the *boosted* regime) [179], respectively. The third analysis performed a combination of the resolved and boosted $VH(H \to b\bar{b})$ analyses [180]. The CMS collaboration also performed an analysis that targeted the combination of the resolved and boosted $VH(H \to b\bar{b})$ regimes [181].

The coupling of the Higgs boson to first and second generation fermions is yet to be firmly established. For the decay of the Higgs boson into muons, the CMS collaboration reported a 3σ excess [182] while the ATLAS collaboration found a 2σ excess over the background-only hypothesis [183]. No evidence was found in direct searches for $H \to c\bar{c}$ [184, 185] or $H \to e^+e^-$ decays [186, 187], or measurements of exclusive decays of the Higgs boson to light mesons [188, 189] (which can probe the Higgs coupling to light quarks) or to heavy vector quarkonium states [190] (which can probe the b- and c-quark Yukawa couplings). However, these analyses can still place upper limits on the Higgs coupling to c-quarks, electrons, and light-flavor (u, d, s) quarks. Such measurements are important to perform as they can limit the range of beyond the SM theories that predict modifications to the Higgs boson couplings to lower generation fermions [191, 192].

The decay of the Higgs boson into a pair of charm quarks provides the most promising avenue to investigate the Higgs coupling to lower generation quarks, as it is the most common decay mode that has yet to be observed, with a branching ratio of 2.89% [193]. In particular, direct searches for Higgs to charm decays in the VH production mode have been able to place upper limits on the cross section times branching fraction for the $VH(H \to c\bar{c})$ process. The ATLAS collaboration measured an upper limit of 26 times the SM predicted cross section times branching fraction (26× SM, with an expected limit of 31× SM) [194], while the CMS collaboration measured an upper limit of 14.4× SM (with an expected limit of 7.6× SM) [195]. As the $VH(H \to c\bar{c})$ decays have a similar final state signature to $VH(H \to b\bar{b})$ decays, studying the two decay modes together can be advantageous, and a combined $VH(H \to b\bar{b}/c\bar{c})$ analysis would allow for a coherent treatment of the two decay modes. This could provide better constraints on the shared main backgrounds (vector bosons produced in association with jets and top quark processes) and allow for a proper treatment of correlations in the theory systematic uncertainties, as well as the ability to simultaneously measure the $VH(H \to b\bar{b})$ and $VH(H \to c\bar{c})$ decays.

This chapter presents a combined measurement of Higgs boson decays to bottom and charm quarks with the ATLAS detector at the LHC. The measurement is performed in the VH production mode and focuses specifically on the case where the vector boson is a W boson decaying leptonically: $WH \to \ell\nu q\bar{q}$ where ℓ is an electron, muon, or hadronically decaying τ-lepton and $q \in \{b, c\}$. The analysis uses the full dataset of pp collisions collected by the ATLAS detector during Run 2 of the LHC, which corresponds to an integrated luminosity of 140 fb^{-1} collected at a center-of-mass energy of 13 TeV. The goal of this analysis is to perform a coherent and improvement measurement of $WH(H \to b\bar{b})$ and $WH(H \to c\bar{c})$ decays simultaneously, by employing a common analysis strategy optimized for both decay channels.

The chapter is structured as follows: Section 5.1 provides an overview of the analysis strategy. The data and simulated samples used in this analysis are described in Section 5.2. Section 5.3 introduces the object and event selections and event categorizations. The experimental uncertainties are presented in Section 5.5, while Section 5.6 discusses the theoretical uncertainties related to signal and background modelling. Section 5.7 covers the details of the statistical analysis performed, while results for the $WH(H \to b\bar{b}/c\bar{c})$ measurement are presented in Section 5.8. Section 5.9 provides the conclusions.

5.1 Analysis Overview

The $VH(H \to b\bar{b}/c\bar{c})$ analysis aims to measure the Higgs boson decays into heavy-flavor (bottom and charm) quarks. It targets Higgs bosons produced in association with a vector boson (the VH production mode), as selecting the leptonic decays of the vector bosons, which are characterized by high p_{T} leptons or large $E_{\mathrm{T}}^{\mathrm{miss}}$, can significantly reduce the large background from QCD events. Based on the number of directly observable leptons that the vector boson decays into, the targeted events can generally be categorized as belonging to the *0-lepton* ($ZH \to \nu\nu q\bar{q}$), *1-lepton* ($WH \to \ell\nu q\bar{q}$), or *2-lepton* channels ($ZH \to \ell\ell q\bar{q}$).

Based on the decay of the Higgs boson, the events can be categorized as belonging to the $VH(H \to b\bar{b})$ regime (which is further divided into resolved and boosted regions with a cut on the momentum of the vector boson at $p_{\mathrm{T}}^{V} = 400$ GeV) or the $VH(H \to c\bar{c})$ regime (which is not split into separate resolved and boosted regions due to the limited statistics at large p_{T}^{V}). The $VH(H \to c\bar{c})$ and $VH(H \to b\bar{b})$ regimes are separated by requiring the presence of jets flavor tagged as c- or b-jets, respectively. The flavor tagging is implemented using a scheme which allows for a simultaneous and coherent definition and calibration of b-tagged and c-tagged jets. In the boosted $VH(H \to b\bar{b})$ regime, the flavor tagging is implemented using a b-tagging only scheme [165]. More details on the flavor tagging strategies employed by this analysis are provided in Section 5.3.2. Figure 5.1 provides an illustration of the three analysis regimes.

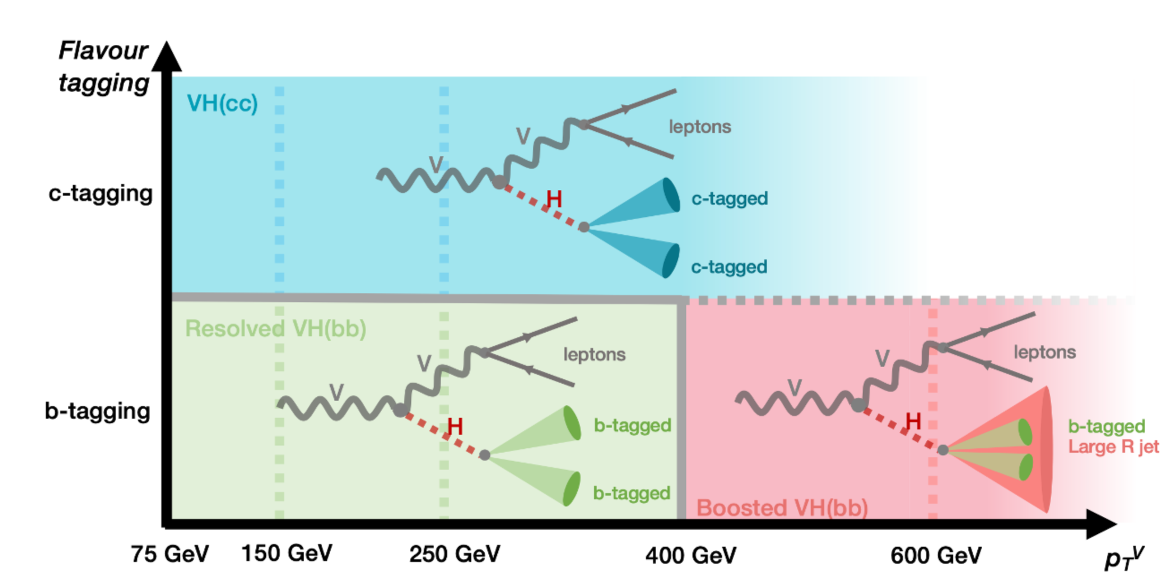

Figure 5.1: Analysis regimes targeted by the $VH(H \to b\bar{b}/c\bar{c})$ analysis [196]. The $VH(H \to c\bar{c})$ and $VH(H \to b\bar{b})$ regimes are separated by requiring that the jets be flavor tagged as c- or b-jets, respectively. The resolved and boosted $VH(H \to b\bar{b})$ regimes are separated with a 400 GeV cut on the p_{T} of the vector boson.

The analysis regions are defined using jet flavor tagging requirements and selections on other kinematic variables. *Signal regions* (SRs) are chosen to maximize the sensitivity to the $VH(H \to b\bar{b})$ and $VH(H \to c\bar{c})$ processes, respectively. In general, the SRs require the presence of b- or c-tagged jets, and are defined in different bins based on p_{T}^{V} and jet multiplicity to account for differences in the signal-to-background ratio. *Control regions* (CRs) are used to constrain the background processes using data events. The CRs are orthogonal to the SRs and are defined by using cuts on the angular separation ΔR between jets or requiring the presence of specific combinations of flavor tagged jets. Dedicated CRs exist to estimate the background contribution from events where vector bosons are produced in association with jets ($V+$jets) and from top quark processes, such as $t\bar{t}$. The CRs are divided into the same p_{T}^{V} and jet multiplicity bins as the SRs and the two regions are treated similarly in the statistical fit. In total, the analysis includes 20 signal regions and 42 control regions.

The sensitivity of the measurement is enhanced by using multi-variate analysis (MVA) techniques in all three regimes considered. Three dedicated boosted decision trees (BDTs) are individually trained to distinguish between the relevant ($VH(H \to b\bar{b})$ or $VH(H \to c\bar{c})$) signal and background in each of the analysis regions. The BDTs use different sets of input variables that are optimally chosen for that particular analysis regime. The output of the BDTs is used as the discriminating variable in the SRs in the statistical analysis. In the CRs, the distribution of the invariant mass of the Higgs candidate or the distribution of the vector boson transverse momentum (p_{T}^{V}) are used, depending on the composition of the CR.

A *binned likelihood fit* is performed to the distribution of the BDT output scores. The fit model is designed to incorporate the $VH(H \to b\bar{b})$ and $VH(H \to c\bar{c})$ regimes in a coherent way and the measurements are extracted from a simultaneous fit to all the $VH(H \to b\bar{b})$ and $VH(H \to c\bar{c})$ analysis regions. The extracted measurements consist of the $VH(H \to b\bar{b})$ signal strength and its significance and the $VH(H \to c\bar{c})$ signal strength and its upper limit at the 95% CL. The $VH(H \to b\bar{b}/c\bar{c})$ measurements can also be interpreted using the kappa (κ) framework, which allows for an extraction of direct constraints on the Higgs-bottom (κ_b) and Higgs-charm (κ_c) Yukawa coupling modifiers and on their ratio κ_b/κ_c, performed coherently within a single analysis. More details about the κ framework interpretation are provided in Section 5.7.3. The analysis can also be performed with an alternative setup, where the targeted signal consists of the diboson processes $VZ(Z \to b\bar{b}/c\bar{c})$. The results of the diboson measurement are used as a validation cross-check of the analysis strategy.

As previously mentioned, the analysis presented in this chapter is targeting only $H \to b\bar{b}/c\bar{c}$ decays where the Higgs boson originates from the WH production mode. As a result, the remaining sections in the chapter will focus only on details relevant to the 1-lepton channel of the $VH(H \to b\bar{b}/c\bar{c})$ analysis. The full analysis targeting all three lepton channels will be presented in a future ATLAS publication.

5.2 Data and Simulated Samples

The analysis uses data collected by the ATLAS detector during Run 2 of the LHC, which corresponds to a total luminosity of 140 fb^{-1} at a center-of-mass energy of $\sqrt{s} = 13$ TeV [101]. In the 1-lepton channel, the data was collected using $E_{\mathrm{T}}^{\mathrm{miss}}$ and single lepton triggers. The $E_{\mathrm{T}}^{\mathrm{miss}}$ triggers are used to obtain high trigger efficiency in the single muon channel, due to the

Process	ME Generator	ME PDF Set	PS Generator	Cross-section Order	$\sigma \times$ BR [pb]
$qq \to WH \to \ell\nu b\bar{b}$	Powheg Box v2 [63, 64] + GoSam [197] + MiNLO [203]	NNPDF3.0NLO [198]	Pythia 8.245 [58]	NNLO(QCD)+NLO(EW) [199–202]	2.69×10^{-1}
$qq \to WH \to \ell\nu c\bar{c}$	Powheg Box v2 + GoSam + MiNLO	NNPDF3.0NLO	Pythia 8.245	NNLO(QCD)+NLO(EW)	1.34×10^{-2}
$W+$jets	Sherpa 2.2.11 [61, 204–207]	NNPDF3.0NNLO [198]	Sherpa 2.2.11 [208, 209]	NLO [210]	60200
$t\bar{t}$	Powheg Box v2 [62, 211]	NNPDF3.0NLO	Pythia 8.230	NNLO+NNLL [212–218]	832
single-top (s)	Powheg Box v2 [219]	NNPDF3.0NLO	Pythia 8.230	NLO [220, 221]	3.35
single-top (t)	Powheg Box v2	NNPDF3.0NLO	Pythia 8.230	NLO	70.4
single-top (Wt)	Powheg Box v2 [222]	NNPDF3.0NLO	Pythia 8.230	Approx. NNLO [223, 224]	71.7
$qq \to WW$	Sherpa 2.2.11	NNPDF3.0NNLO	Sherpa 2.2.11	NLO	45.7
$qq \to WZ$	Sherpa 2.2.11	NNPDF3.0NNLO	Sherpa 2.2.11	NLO	21.7
$gg \to VV$	Sherpa 2.2.2	NNPDF3.0NNLO	Sherpa 2.2.2	NLO	3.09

Table 5.1: Monte Carlo generators used to simulate the signal and background processes relevant for the $VH(H \to b\bar{b}/c\bar{c})$ 1-lepton channel analysis and the process cross sections at $\sqrt{s} = 13$ TeV [196]. Different generators are used for matrix element (ME) and parton shower (PS) calculations. The order of the cross-section calculation used for process normalization in QCD is either next-to-leading order (NLO), next-to-next-to-leading order (NNLO), or next-to-next-to-leading log (NNLL).

fact that the trigger is based on calorimeter $E_{\mathrm{T}}^{\mathrm{miss}}$, where most of the muon momentum would be counted at trigger level. The data is subject to a set of good quality requirements, which selects only data events that were collected during periods when all detector components were operating as expected.

The signal and most background processes relevant to the analysis are simulated using Monte Carlo (MC) generators. Table 5.1 lists the MC generators used to simulate the nominal samples for the signal and background processes relevant in the 1-lepton channel. The exception consists of the QCD multi-jet background, which is estimated using data-driven techniques. All simulated samples are passed through the ATLAS detector simulation [72] (based on Geant4 [73]) and then reconstructed using the ATLAS offline reconstruction software.

Signal

The $VH(H \to b\bar{b})$ and $VH(H \to c\bar{c})$ signals relevant to the analysis presented in this chapter consist of the process $q\bar{q} \to WH \to \ell\nu q\bar{q}$, where the final state q is a b- or c-quark, for which the leading-order Feynman diagram is show in Figure 5.2. For both signals, the matrix element calculation is performed using the Powheg Box v2 generator [63, 64] interfaced with the NNPDF3.0NLO PDF set [198]. The parton shower, underlying event, and multiple parton interactions are simulated using Pythia 8.245 [58]. The samples are generated assuming that the mass of the Higgs boson is $m_H = 125$ GeV [225]. Additional samples are generated using Powheg+Herwig 7 (where Herwig 7.0 [226] is used to simulate the parton shower, underlying event, and multiple parton interactions) and are used to assess the signal modelling uncertainties.

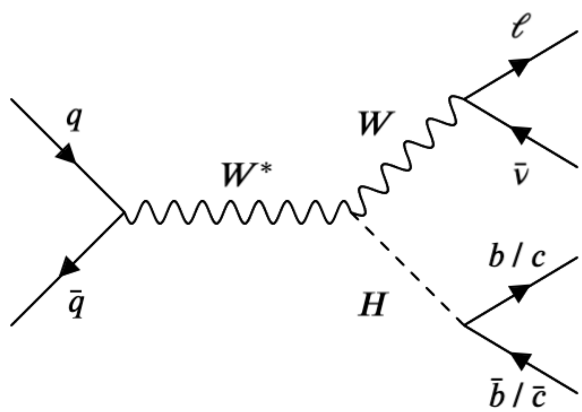

Figure 5.2: Leading-order Feynman diagram for the $WH(H \to b\bar{b}/c\bar{c})$ signal process.

$V+$jets Background

One of the largest backgrounds for this analysis is represented by the production of a vector boson in association with additional jets ($V+$jets). For the 1-lepton channel, this background is composed primarily of $W+$jets events, with the $Z+$jets contribution being almost negligible. The additional jets can result from gluon splitting, in which case two same flavor jets are produced, or from other diagrams that have different flavor jets in the final state. The $V+$jets processes are simulated with Sherpa 2.2.11 [204] interfaced with the NNPDF3.0NNLO PDF set [198] for matrix element [61, 205–207] and parton shower and hadronization [208, 209]. The $V+$jets samples are generated following the standard Sherpa prescription [210] and different filters are applied to select a particular flavor composition for the jets produced in association with the vector boson (for example, samples enriched in $V+bb$ or $V+cc$ events). This ensures that the simulated samples have enough statistics to provide a robust prediction to be compared to the data in the heavy-flavor enriched phase space of the analysis.

Additional simulated samples are considered for the derivation of systematic modelling uncertainties. These samples are generated using MadGraph5_aMC@NLO 2.6.5 [66] for matrix element calculation, Pythia 8.240 [58] for parton shower and hadronization, and the FxFx NLO matrix element and parton shower merging prescription [71]. Furthermore, it is known that, when compared to data, the Sherpa 2.2.11 generator shows a larger amount of mismodelling of the p_{T}^{V} distribution than does the Sherpa 2.2.1 generator [59, 210]. To account for this, Sherpa 2.2.1 samples are used to derive uncertainties on the mismodelling of the p_{T}^{V} distribution.

Top quark Backgrounds

Top quark pair production ($t\bar{t}$) represents another dominant background for the $VH(H \to b\bar{b}/c\bar{c})$ analysis. In the 1-lepton channel, the vector boson system is reconstructed from the leptonic decay products of one of the W bosons produced from the $t\bar{t}$ decay. The $t\bar{t}$ process is simulated using the POWHEG NLO [62, 211] generator for matrix element calculation, interfaced to PYTHIA 8.230 [58] with the NNPDF3.0NLO PDF set [198] for parton shower, hadronization, and underlying event simulation. As for the $V+$jets samples, filtering is applied in order to increase the available statistics.

Alternative $t\bar{t}$ samples are considered to assess the impact of systematic modelling uncertainties. A POWHEG+HERWIG 7 sample is generated that uses same setup for POWHEG as the nominal sample, but simulates the parton shower, hadronization, and underlying event using the HERWIG 7.0 [226] generator. This sample is used to determine the uncertainties related to using a different parton shower model. A MADGRAPH5_aMC@NLO+PYTHIA 8.2 sample is produced that uses the MADGRAPH5_aMC@NLO [66] generator for the matrix element calculation at NLO precision and the PYTHIA 8.2 generator for the simulation of the parton shower, hadronization, and underlying event. This sample is used to study systematic variations due to having a different matrix element prediction. Samples with different settings for the POWHEG+PYTHIA 8 generator are also considered as additional sources of systematic uncertainties to account for effects from initial (ISR) and final state radiation (FSR). The samples use different values for the QCD renormalization and factorization scales (for ISR and FSR) and different variations for the PYTHIA 8 shower tune (for ISR only) compared to the nominal POWHEG+PYTHIA 8 generator.

Single-top quark processes contribute as a minor background in the analysis and are simulated separately for the s-channel, t-channel, and Wt-channel. The samples are generated using POWHEG for the matrix element calculation with the NNPDF3.0NLO PDF set interfaced with PYTHIA 8.230 for the parton shower, hadronization, underlying event, and multiple parton interactions simulation. Alternative samples are considered for the t-channel and Wt-channel processes. HERWIG 7.0 samples are used to evaluate uncertainties due to different parton shower models, while MADGRAPH5_aMC@NLO+PYTHIA 8 samples are used to evaluate uncertainties due to different matrix element predictions. An additional sample is used to account for two different treatments[1] of the overlap between $t\bar{t}$ and Wt events, namely diagram subtraction (DS, used for the nominal sample) and diagram removal (DR, used for the alternative sample) [227].

Diboson Background

Diboson final states arising from WW, WZ, and ZZ events represent a minor background in the analysis, which nonetheless must be treated carefully as the peak in the mass distribution is located close to the VH mass peak. Diboson events can be initiated by quarks or gluons

[1]The diagram subtraction scheme removes the interference at cross section level, while the diagram removal scheme removes the resonant $t\bar{t}$ diagrams at amplitude level.

(via quark loops). These events can have a final state signature that is very similar to the VH signal when one of the vector bosons decays leptonically and the other decays hadronically. The diboson samples are simulated using the Sherpa 2.2.11 generator for the $qq \to VV$ processes and the Sherpa 2.2.2 generator for the $gg \to VV$ processes. The Sherpa generator with the NNPDF3.0NNLO PDF set is used for both matrix element calculation and parton shower simulation. Additional samples are used to assess systematic modelling uncertainties. Uncertainties in the matrix element calculation and the parton shower model are derived using a Powheg+Pythia 8 sample which uses Powheg v2 for the matrix element interfaced with Pythia 8 for the parton shower, while Sherpa 2.2.1 samples are used to derive uncertainties due to the choice of parameters used for the Sherpa 2.2.11 fragmentation function.

QCD Multi-jet Background

The QCD multi-jet background represents a minor background in the 1-lepton channel. The sources of this background are real muons or electrons from semileptonic decays of heavy-flavor hadrons or jets that fake leptons, which would pass the lepton triggers. Such "fake" leptons are known to be modelled by simulation with poor accuracy. Additionally, only a small (but non-negligible) fraction of these leptons are expected to pass the lepton isolation requirements, resulting in limited statistics. As modelling this background using MC simulation is difficult to achieve, the QCD multi-jet background is instead derived using a data-driven approach in a multi-jet enriched region. This background is considered only for the resolved $VH(b\bar{b})$ and $VH(c\bar{c})$ regimes, as the multi-jet contribution in the boosted $VH(b\bar{b})$ regime was found to be negligible (less than 2×10^{-5} events).

5.3 Event Selection and Categorization

This section introduces the physics objects and the flavor tagging schemes that are relevant to the $VH(H \to b\bar{b}/c\bar{c})$ 1-lepton channel analysis, followed by the event selection and event categorization used in the analysis.

5.3.1 Object Selection

This section summarizes the object definitions that are specific to the analysis presented in this chapter. A general overview of the ATLAS algorithms used for the reconstruction and calibration of physics objects is provided in Chapter 4.

Electrons

As a baseline, the analysis considers electrons with $p_{\mathrm{T}} > 7$ GeV and for which the electron cluster falls within the $|\eta| < 2.47$ range (VH-loose selection). Electrons likely to originate from the WH process are selected by applying a tighter p_{T} cut of $p_{\mathrm{T}} > 27$ GeV (WH-signal selection), which is motivated by the trigger thresholds. Tight lepton selections are also applied to suppress the QCD multi-jet background in the 1-lepton channel. Electrons are required to pass the *Tight* identification working point and the *HighPtCaloOnly* isolation criterion using calorimeter-based isolation.

Muons

Muons used in this analysis are required to have $p_{\mathrm{T}} > 7$ GeV and $|\eta| < 2.5$ (VH-loose selection). Signal originating muons with $p_{\mathrm{T}} > 25$ GeV are required in the $p_{\mathrm{T}}^{V} > 150$ GeV region, while in the $p_{\mathrm{T}}^{V} < 150$ GeV the p_{T} threshold is increased to 27 GeV to satisfy the single-muon trigger threshold criteria (WH-signal selection). Tight lepton selections are applied to suppress the QCD multi-jet background. Muons are required to pass the *Medium* working point for muon identification and a tight track-based isolation criteria (*HighPtTrackOnly* working point).

τ-leptons

Hadronically decaying τ-leptons are required to have $p_{\mathrm{T}} > 20$ GeV, $|\eta| < 2.5$ (excluding the $1.37 < |\eta| < 1.52$ transition region between the barrel and end-cap of the EM calorimeter), and 1 or 3 tracks. The τ-leptons are required to pass the *Loose* working point of the RNN-based τ identification algorithm.

Jets

Jets play an important role in the analysis, as they are crucial for the identification of event topologies and kinematics consistent with the $VH(H \to b\bar{b}/c\bar{c})$ signal processes. All three jet types introduced in Section 4.5 are considered in this analysis.

Small-R Jets Small-R *PFlow* jets are used in the resolved $VH(H \to b\bar{b})$ and $VH(H \to c\bar{c})$ regimes. The jets are classified as either *signal* or *forward* jets. Signal jets are required to have $p_{\mathrm{T}} > 20$ GeV and $|\eta| < 2.5$. Suppression of pile-up jets is achieved by applying the *Tight* JVT selection to signal jets with $p_{\mathrm{T}} < 60$ GeV. Forward jets must have $p_{\mathrm{T}} > 30$ GeV and $2.5 \leq |\eta| < 4.5$. The *Loose* fJVT selection is applied to forward jets with $p_{\mathrm{T}} < 120$ GeV to reduce contributions from pile-up.

As signal jets contain tracking information, they are used for flavor tagging and the subsequent reconstruction of the Higgs boson candidate, as well as for event categorization. The forward jets are considered for the determination of the jet multiplicity used in the event categorization. Both signal and forward jets are considered in the reconstruction of missing transverse momentum.

Large-R Jets Large-R jets are used in the $VH(H \to b\bar{b})$ boosted regime only, where the goal is to reconstruct the full $H \to b\bar{b}$ decay using a single jet. The large-R jets are required to pass cuts of $p_{\mathrm{T}} > 250$ GeV and $|\eta| < 2.0$. The p_{T} cut represents the point where the two b-quarks are geometrically separated by an angular distance of $\Delta R \sim 1.0$.

Variable-*R* Track-jets VR track-jets are used as b-tagging inputs to identify jets originating from the $H \to b\bar{b}$ decay in the boosted regime. The track-jets are required to have $p_{\mathrm{T}} > 10$ GeV and $|\eta| < 2.5$.

Missing Transverse Momentum

The missing transverse momentum $\vec{E}_{\mathrm{T}}^{\mathrm{miss}}$ plays an important role in the 1-lepton channel, as it is used as a proxy for the p_{T} of the neutrino from the W boson decay. Hence, $\vec{E}_{\mathrm{T}}^{\mathrm{miss}}$ enters the calculation of the transverse momentum of the vector boson.

5.3.2 Flavor Tagging

As this analysis probes the decay of the Higgs boson into heavy-flavor quarks, flavor tagging is used to peform both b-tagging and c-tagging. The analysis uses the `DL1r` algorithm [167] to perform the jet flavor tagging, and both b-tagging and c-tagging discriminants (scores) from Eqn. 4.4 are used. Two different tagging schemes are used for the resolved regime (resolved $VH(H \to b\bar{b})$ and $VH(H \to c\bar{c})$) and for the boosted $VH(H \to b\bar{b})$ regime.

Flavor Tagging Schemes

In the resolved regime, a pseudo-continuous[2] flavor tagging (PCFT) scheme is used. The PCFT scheme, which is used to simultaneously perform both b- and c-tagging, is schematically represented in Figure 5.3. The 2-D plane formed from the `DL1r` b- and c-tagging scores is divided into five exclusive bins by defining two b-tagging WPs and two c-tagging WPs. Based on its b- and c-tagging scores, each jet is assigned to exactly one bin:

- b-tagged with 60% WP (red, label B)
- b-tagged with 70% WP (blue, label B, does not include jets from the 60% WP bin)
- tight c-tagged (green, label T)
- loose c-tagged (light green, label L)
- not tagged / untagged (gray, label N)

[2]The flavor tagging scheme is referred to as pseudo-continuous because the space spanned by the tagging discriminant(s) is divided into discrete bins which are used to decide the tagging categories. Using a fully continuous tagging scheme is not feasible due to the computational challenges associated with calibrating such a scheme.

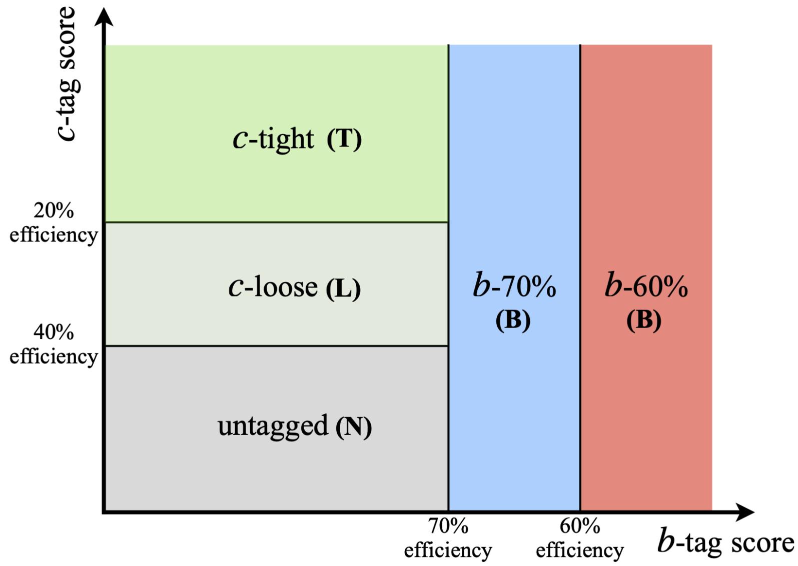

Figure 5.3: Pseudo-continuous flavor tagging scheme for the `DL1r` tagger used in the resolved $VH(H \to b\bar{b})$ and $VH(H \to c\bar{c})$ regimes [196].

PCFT Bin Name	Jet Tagging Efficiency			
	b-jet	c-jet	light-flavor jet	τ-jet
b-60%	58%	2.65%	0.051%	0.49%
b-70%	11.2%	5.2%	0.13%	1.7%
c-tight	4.8%	24.2%	0.9%	19.5%
c-loose	11.5%	20.5%	6.5%	18.5%

Table 5.2: Tagging efficiencies for b-jets, c-jets, light-flavor jets, and τ-jets in the PCFT scheme [196]. The efficiencies are measured using simulated $t\bar{t}$ events.

The 70% and 60% b-tagging WPs follow the official ATLAS recommendations for `DL1r` [167], while the tight and loose c-tagging WPs have been optimized specifically for the $VH(H \to b\bar{b}/c\bar{c})$ analysis. Table 5.2 shows the resulting tagging efficiencies for b-, c-, light-flavor, and τ-jets for the PCFT bins. For the combined tight and loose c-tag bins, about 45% of jets originating from c-quark are correctly tagged as c-jets.

In the boosted $VH(H \to b\bar{b})$ regime, only b-tagging is applied, using a pseudo-continuous b-tagging (PCBT) scheme, which defines four WPs using cuts on the distribution of the `DL1r`

b-tagging score. The WPs are defined to provide b-tagging efficiencies of 60%, 70%, 77%, or 85% [167]. The b-tagging is performed on the track-jets inside the large-R jet. Considering that the boosted regime has limited statistics, the loosest 85% b-tagging WP (which has an inclusive efficiency of 83% for b-jets in the $400 < p_{\mathrm{T}} < 1000$ GeV range [167]) is used in order to maximize the signal yield.

Calibration

The tagging efficiencies and the SFs and their uncertainties are derived using the calibration methods recommended by the ATLAS flavor tagging (FTAG) group [165, 168]. The calibrations are derived separately for each jet flavor. For b-jets and c-jets, the calibrations are derived using dileptonic and semileptonic $t\bar{t}$ events, respectively. The calibration for light-flavor jets is derived using $Z+$jets events. As the 60% b-tagging WP has a very low efficiency for light-flavor jets (0.051%, see Table 5.2), the light-jet scale factor is set to 1 and the uncertainties from the 70% b-tagging WP are used. For τ-jets, the same calibrations are used as for c-jets.

In the resolved regime (resolved $VH(H \to b\bar{b})$ and $VH(H \to c\bar{c})$), the tagging efficiencies and SFs are derived simultaneously in all five bins of the PCFT scheme. The derived scale factors and their uncertainties for the PCFT scheme are shown in Figure 5.4. For b-jets, the uncertainties are on the order of 5%, except for the untagged bin where they are $\sim 10\%$. For c-jets (and τ-jets), the uncertainties range between 5% and 10%, with larger uncertainties found in the 60% b-tagging and 70% b-tagging bins. The SF uncertainties for light-flavor jets are $\sim 10\%$ in the c-tight and c-loose bins and $\sim 20\%$ in the 60% b-tagging and 70% b-tagging bins.

In the boosted $VH(H \to b\bar{b})$ regime, the efficiencies and SFs in the five tagging score regions that correspond to the PCBT working points are available from the official calibrations provided by the ATLAS FTAG group [167]. However, official calibration uncertainties are available only up to jet p_{T} of 300 GeV, which is lower that the p_{T} range probed in the boosted regime. To address this, an extrapolation of the flavor tagging uncertainties from the last calibrated bin to higher p_{T} values is performed specifically within the context of the $VH(H \to b\bar{b}/c\bar{c})$ analysis. Figure 5.5 shows the SFs and their uncertainties as a function of jet p_{T} for the 85% b-tagging WP of the PCBT scheme. The uncertainties are found to get larger with increasing jet p_{T}, and range between $5\% - 10\%$ for b-jets, c-jets, and τ-jets and $15\% - 20\%$ for light-flavor jets.

Direct and Truth Tagging Strategies

As described previously, the standard way of applying flavor tagging consists of defining a WP cut on the tagging score and tagging all jets with scores larger than the WP threshold – this method is known as *direct tagging*. Considering the limited tagging efficiency of the WPs used in the analysis, a sizeable fraction of the MC events end up being discarded if direct tagging is used. This results in regions of the analysis phase space not having enough

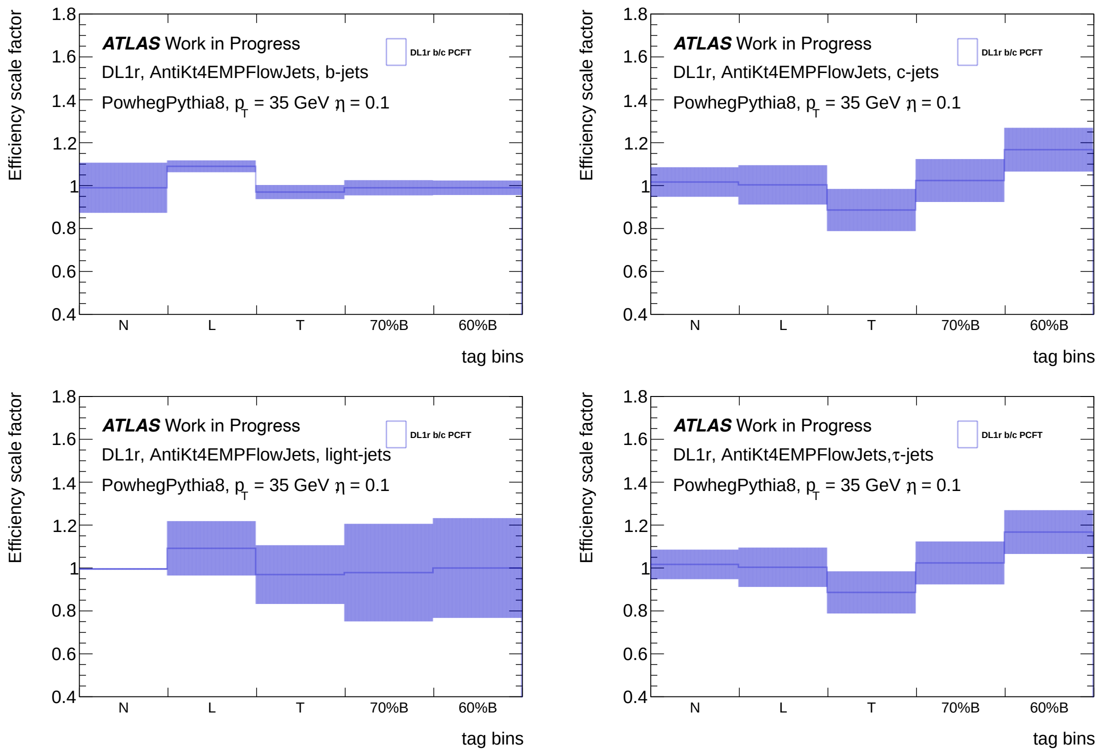

Figure 5.4: Flavor tagging calibration scale factors for the `DL1r` PCFT scheme used in the resolved $VH(H \to b\bar{b})$ and $VH(H \to c\bar{c})$ regimes [196]. The scale factors are derived using $t\bar{t}$ and $Z+$jets events.

events to properly model the backgrounds, which leads to large statistical uncertainties on the simulated background samples.

An alternative tagging strategy which does not result in limited statistics can be used instead, which is known as *truth tagging*. In truth tagging, the flavor tagging efficiency is parametrized such that a probability to pass a given WP can be derived for every event. With this method, all the available MC events can be used, and each event is weighted by a truth tagging weight, which is defined as the product between the tagging efficiency (ϵ_j) for all tagged jets and the tagging inefficiency ($1 - \epsilon_j$) for all untagged jets in the event. Truth tagging is applied using a graph neural network (GNN), which is well-suited to handle many input features and can properly account for correlations between the features [228]. In the GNN, each node represents a jet, while the node features consists of jet-level and event-level features, as shown in Table 5.3. The GNN is trained to obtain the appropriate truth tagging weights for each event.

The performance of truth tagging can be evaluated by comparing the truth tagged distributions to those obtained using direct tagging. For accurate truth tagging results, the shapes of the distributions obtained with the two tagging methods are expected to be sim-

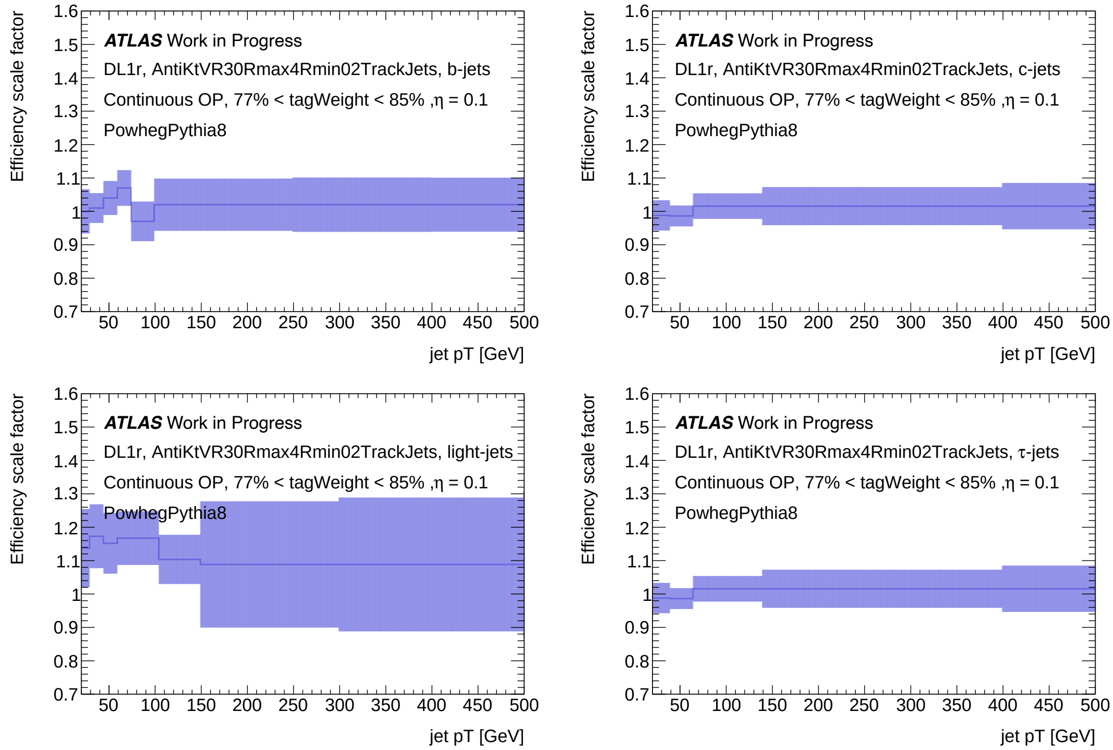

Figure 5.5: Flavor tagging calibration scale factors for the `DL1r` PCBT scheme used in the boosted $VH(H \to b\bar{b})$ regime [196]. The scale factors are derived using $t\bar{t}$ and $Z+$jets events.

ilar (within the statistical fluctuations of the direct tagged distribution). However, truth tagging can produce smoother shapes with less statistical fluctuations, as can be seen in Figure 5.6.

In the analysis, different tagging strategies are used in the different regimes and between the different simulated samples. The resolved $VH(H \to b\bar{b})$ and $VH(H \to c\bar{c})$ regimes use direct tagging for all samples. The boosted $VH(H \to b\bar{b})$ regime uses GNN truth tagging for all samples in order to maximize the amount of available statistics, except for signal which already has sufficient statistics with direct tagging.

5.3.3 Event Selection

This section outlines the cuts used to determine which events will be used in the analysis and which events will be discarded (event selection), while Section 5.3.4 will describe the criteria used to define the signal and control regions (event categorization).

The resolved $VH(H \to b\bar{b})$ and $VH(H \to c\bar{c})$ regimes use the same set of event selection cuts, except for the flavor tagging requirement which differentiates between b-jets and c-jets.

Input Feature	Feature Type
Jet p_{T}	
Jet η	
Jet ϕ	
Jet flavor label	Jet-level variable
Mass of leading p_{T} b or c hadron in the jet	
p_{T} of leading p_{T} b or c hadron in the jet	
η of leading p_{T} b or c hadron in the jet	
ϕ of leading p_{T} b or c hadron in the jet	
Average number of interactions per event, $\langle\mu\rangle$	Event-level variable
Angular separation between two jets, ΔR	Jet-pair variable

Table 5.3: Input features used for GNN truth tagging [196].

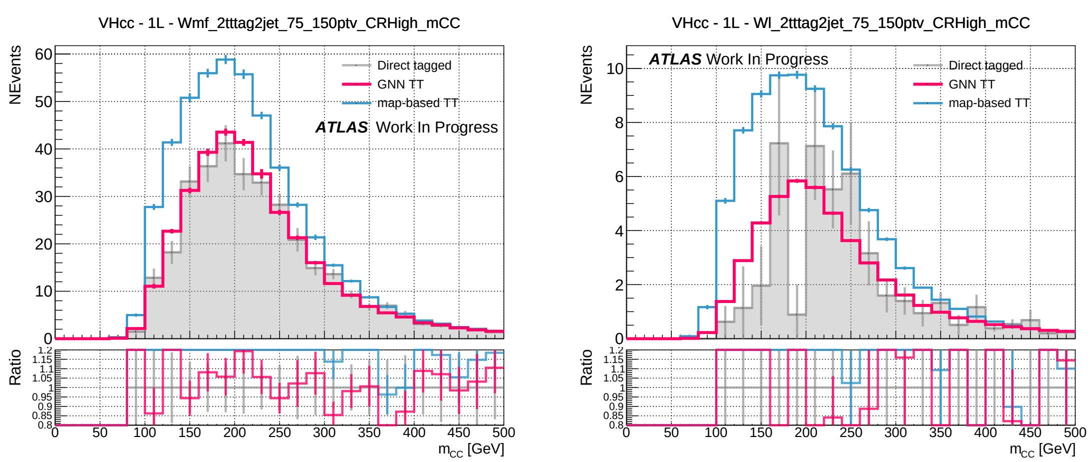

Figure 5.6: Comparison between GNN truth tagged (red) and direct tagged (gray) distributions for $W+$jets samples in the 1-lepton channel [196].

The boosted $VH(H \to b\bar{b})$ regime follows a different event selection due to using a different reconstruction strategy for the Higgs boson. The event selection cuts used in the analysis are summarized in Table 5.4 for the resolved regime and in Table 5.5 for the boosted regime.

Common Selections	
Jets	≥ 2 signal jets
Candidate jets tagging	2 b-tags ($VH(H \to b\bar{b})$), ≥ 1 T-tag ($VH(H \to c\bar{c})$)
Leading Higgs candidate jet p_{T}	> 45 GeV
Sub-leading Higgs candidate jet p_{T}	> 20 GeV
m_{jj}	> 50 GeV (before correction)
ΔR(jet1, jet2)	Upper cut $\Delta R < \pi$
1-lepton Channel Selections	
Trigger	e channel: single electron trigger μ channel: single muon trigger ($p_{\mathrm{T}}^V < 150$ GeV) and $E_{\mathrm{T}}^{\mathrm{miss}}$ triggers ($p_{\mathrm{T}}^V > 150$ GeV)
Jets	≤ 3 jets
Additional jets tagging	no T-tag ($VH(H \to b\bar{b})$), no b-tag ($VH(H \to c\bar{c})$)
Hadronic τ	no hadronic τ
Leptons	1 WH-signal lepton > 1 VH-loose lepton veto
$E_{\mathrm{T}}^{\mathrm{miss}}$	> 30 GeV (e channel)
S_{T}	> 120 (2 jets), > 150 GeV (3 jets) (μ channel with single muon trigger)
m_{T}^W	> 20 GeV ($75 < p_{\mathrm{T}}^V < 150$ GeV only)

Table 5.4: Summary of the signal event selection used in the 1-lepton channel for the resolved $VH(H \to b\bar{b})$ and $VH(H \to c\bar{c})$ regimes [196]. Here, b-tag denotes that a jet is either b-tagged with 60% WP or b-tagged with 70% WP, while T-tag denotes that a jet is tight c-tagged, according to the PCFT scheme described in Section 5.3.2.

Trigger Selection

In the 1-lepton channel, events can be triggered by the presence of an electron or a muon. Single electron events must be triggered by at least one of the lowest un-prescaled single electron triggers. The trigger thresholds vary between 24 GeV and 300 GeV. Single muon events are selected using different triggers, depending on the value of the p_{T}^V. For $p_{\mathrm{T}}^V < 150$ GeV events, single muon trigger are used, with thresholds varying between 20 GeV and 50 GeV. For $p_{\mathrm{T}}^V > 150$ GeV events, the lowest un-prescaled $E_{\mathrm{T}}^{\mathrm{miss}}$ triggers are used to obtain high trigger efficiencies for high p_{T} muons. The $E_{\mathrm{T}}^{\mathrm{miss}}$ trigger thresholds vary between 70 GeV and 110 GeV.

Common Selections	
p_{T}^{V}	> 400 GeV
Large-R jet	at least one large-R jet, $p_{\mathrm{T}} > 250$ GeV, $\lvert\eta\rvert < 2$
Track-jets	at least two track-jets, $p_{\mathrm{T}} > 10$ GeV, $\lvert\eta\rvert < 2.5$, matched to the leading large-R jet
b-jets	leading two track-jets matched to the leading large-R jet must be b-tagged
m_J	> 50 GeV
1-lepton Channel Selections	
Trigger	e channel: single electron trigger μ channel: $E_{\mathrm{T}}^{\mathrm{miss}}$ triggers
Leptons	1 WH-signal lepton no VH-loose lepton no hadronic τ
$E_{\mathrm{T}}^{\mathrm{miss}}$	> 50 GeV (e channel)

Table 5.5: Summary of the signal event selection used in the 1-lepton channel for the boosted $VH(H \to b\bar{b})$ regime [196].

Vector Boson Selection

In the 1-lepton channel, the signal process is considered to be either the $WH \to \ell\nu b\bar{b}$ or the $WH \to \ell\nu c\bar{c}$ process. As such, the 1-lepton channel considers only events with exactly one WH-signal lepton (electron or muon) and no additional VH-loose leptons. The transverse momentum of the vector boson (p_{T}^{V}) is reconstructed as the vector sum of the lepton transverse momentum and the missing transverse momentum $\vec{E}_{\mathrm{T}}^{\mathrm{miss}}$. Only events with p_{T}^{V} greater than 75 GeV are considered in the analysis.

A special treatment is required for WH signal events where $W \to \tau\nu_{\tau}$, and the τ-lepton decays hadronically, which get categorized into the 0-lepton channel, due to the lack of a reconstructed lepton in the final state. Formally, such events do not belong in the 0-lepton channel as they represent decays of the W boson, whereas the 0-lepton channel targets events from $ZH \to \nu\nu q\bar{q}$ decays. To account for this, a hadronic τ split is applied to such events, which are divided, based on the number of hadronic τ-jets[3], into events that have no hadronic τ-jets and events with more than one hadronic τ-jet. When generating inputs for the statistical fit, events with more than one hadronic τ-jet are then assigned to the 1-lepton channel and considered together with the nominal 1-lepton channel events[4]. An additional $m_{\mathrm{T}}^{W} > 10$ GeV cut is applied to the events with at least one hadronic τ-jet in order to remove any fake τ contamination.

[3] The hadronic τ-jets are identified using the RNN-based τ identification algorithm mentioned in Section 4.7.

[4] For technical reasons, this step has to performed after the event selection is performed for both the 0-lepton and 1-lepton channels.

Jet, $E_{\mathrm{T}}^{\mathrm{miss}}$, and Hadronic τ Selections

In the resolved regime, only events with at most 3 jets are considered in order to reduce contributions from the top quark background. In the 3 jets case, the additional non-Higgs candidate jet is required to not be tight c-tagged in $VH(H \to b\bar{b})$ and not b-tagged in $VH(H \to c\bar{c})$. For events in the electron channel, a cut of $E_{\mathrm{T}}^{\mathrm{miss}} > 30$ GeV is applied to suppress the QCD multi-jet background. A requirement is also applied to the scalar sum of jet p_{T}, S_{T}, which must be greater than 120 GeV (150 GeV) for events with 2 jets (3 jets). This cut removes a region that is mismodelled in simulation due to a complex dependence of the $E_{\mathrm{T}}^{\mathrm{miss}}$ trigger efficiency on the jet activity. The transverse mass[5] of the W boson candidate, m_{T}^{W}, is required to be larger than 20 GeV in the 75 GeV $< p_{\mathrm{T}}^{V} <$ 150 GeV region to further suppress the multi-jet background. An additional veto on the presence of hadronic τ-leptons is used to suppress contributions from $t\bar{t}$ events where the W boson (from the top quark decay) decays to a neutrino and a τ lepton, and the τ-lepton further decays hadronically.

In the boosted regime, a $E_{\mathrm{T}}^{\mathrm{miss}} > 50$ GeV cut is applied in the electron channel only, to reduce contributions from the multi-jet background, which is much larger in the electron channel than in the muon channel. Similarly to the resolved regime, a hadronic τ-lepton veto is applied to suppress contributions from the $t\bar{t}$ background.

5.3.4 Event Categorization

This section describes the criteria used to define the signal and control regions used in the analysis, which are defined after the event selection procedure described in Section 5.3.3 is applied. The analysis regions are generally constructed based on the flavor tagging information for the signal jets used to reconstruct the Higgs boson candidate (two small-R jets in the resolved $VH(H \to b\bar{b})$ and $VH(H \to c\bar{c})$ regimes and a large-R jet in the boosted $VH(H \to b\bar{b})$ regime). More details about the strategies used to reconstruct the Higgs boson candidate are provided in Section 5.3.5.

Resolved $VH(H \to b\bar{b})$ and $VH(H \to c\bar{c})$ Categorization

The total number of selected jets, signal and forward jets, is used to define exclusive categories of events (jet multiplicity bins). In the 1-lepton channel, only events containing two jets (2-jet category) and three jets (3-jet category) are considered in the resolved regime. Events with four or more jets are rejected due to high contamination from $t\bar{t}$ events.

The transverse momentum of the vector boson is also used to define exclusive categories of events (p_{T}^{V} bins). In the 1-lepton channel, three p_{T}^{V} bins are included: $75 < p_{\mathrm{T}}^{V} < 150$ GeV, $150 < p_{\mathrm{T}}^{V} < 250$ GeV, and $250 < p_{\mathrm{T}}^{V} < 400$ GeV. In the $VH(H \to c\bar{c})$ regime, the highest p_{T}^{V} bin also includes events with $p_{\mathrm{T}}^{V} > 400$ GeV (e.g. the $p_{\mathrm{T}}^{V} > 250$ GeV bin), as the overlap with events falling into the boosted $VH(H \to b\bar{b})$ regime was found to be minimal.

[5] $m_{\mathrm{T}}^{W} \equiv \sqrt{2 p_{\mathrm{T}}^{\ell} E_{\mathrm{T}}^{\mathrm{miss}} (1 - \cos(\Delta\phi(\ell, E_{\mathrm{T}}^{\mathrm{miss}})))}$

Signal Regions

The signal regions are defined using flavor tagging information and cuts on the angular separation between the two relevant signal jets in the event, ΔR (jet1, jet2). In total, 18 SRs are used in the resolved $VH(H \to b\bar{b})$ and $VH(H \to c\bar{c})$ regimes and are schematically shown in Figure 5.7.

Figure 5.7: Signal regions used in the 1-lepton channel of the resolved $VH(H \to b\bar{b})$ and $VH(H \to c\bar{c})$ analysis regimes.

The $VH(H \to b\bar{b})$ SRs contain events that have exactly two b-tagged jets. In the $VH(H \to c\bar{c})$ SR, events are required to have at least one tight c-tagged jet. Separate SRs are considered for events with one tight c-tag and one untagged jet (the TN region) and for events with either one tight c-tag and one loose c-tag or two tight c-tags (the LT and TT regions, respectively, which are considered together as the XT region).

Continuous cuts on ΔR (jet1, jet2) as a function of p_{T}^{V} are applied to the different jet multiplicity bins to separate out events that are assigned to the SRs. The functional form of the ΔR cuts is listed in Table 5.6. The upper ΔR cut is defined such that $> 95\%$ (85%) of events in the 2-jet (3-jet) category fall bellow this threshold. An additional upper cut at $\Delta R = \pi$ is applied to account for mismodelling observed at high ΔR values. The lower cut on ΔR is applied only in the resolved $VH(H \to b\bar{b})$ regime, to ensure orthogonality with the low ΔR CR described below.

Control Regions

Control regions are used to constrain the modelling of the background processes relevant to the analysis. In order to constrain all the backgrounds that are relevant to the SRs, the control regions are defined in the same flavor tagging regions as the signal regions (e.g. BB, TN, LT, TT), as well as in different tagging regions (BT, LN) which are pure in a

Jet Multiplicity	Lower Cut on ΔR ($VH(H \to b\bar{b})$ only)	Upper Cut on ΔR
2-jet	$0.41 + e^{0.818-0.01056\times p_{\mathrm{T}}^{V}} < \Delta R$	$\Delta R < 0.787 + e^{1.387-0.007\times p_{\mathrm{T}}^{V}}$
3-jet	$0.43 + e^{0.399-0.00931\times p_{\mathrm{T}}^{V}} < \Delta R$	$\Delta R < 0.684 + e^{1.204-0.006\times p_{\mathrm{T}}^{V}}$

Table 5.6: Kinematic selections used to define the signal regions [196].

specific background process. Figure 5.8 illustrates the CRs included in the analysis and the variables fit in each region. A total of 40 CRs are defined across the resolved $VH(H \to b\bar{b})$ and $VH(H \to c\bar{c})$ regimes. More details about the different types of CRs are provided below.

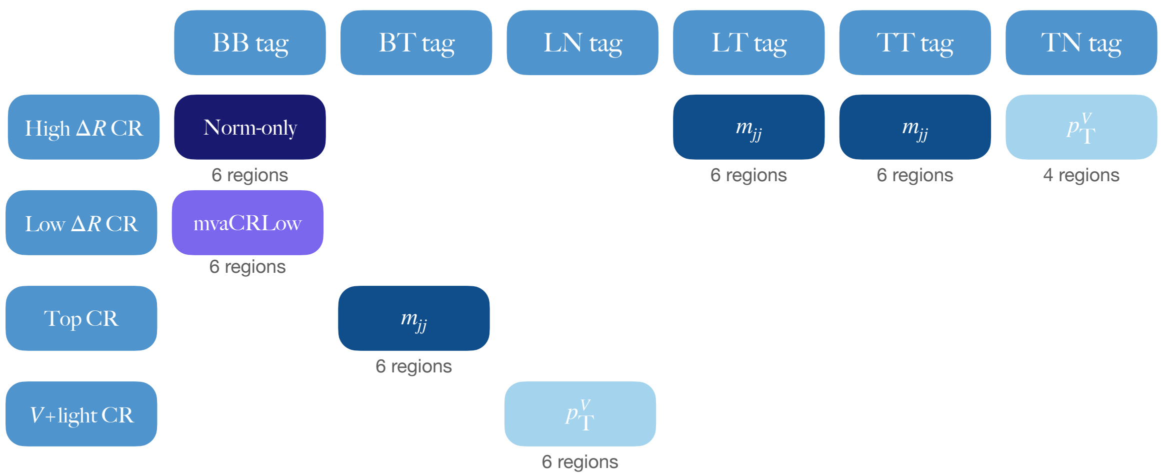

Figure 5.8: Control regions used in the 1-lepton channel of the resolved $VH(H \to b\bar{b})$ and $VH(H \to c\bar{c})$ analysis regimes and the variables used for the statistical fit in each region.

High ΔR Control Region

The high ΔR control region is used to constrain the normalization and shape for the $V+$jets and $t\bar{t}$ backgrounds. A continuous cut on ΔR (jet1, jet2) as a function of p_{T}^{V} is applied to the different jet multiplicity bins to separate out events that are assigned to the high ΔR CRs. The functional form of the ΔR cut is listed in Table 5.7. An additional upper cut at $\Delta R = \pi$ is applied to account for mismodelling observed at high ΔR values. In the high ΔR CR, the LT and TT regions are kept separate as this provides better constraints on the $V+$jets background components containing mixed-flavor and heavy-flavor jets, respectively, compared to using the inclusive XT region. The fit variable is the mass of the Higgs candidate, m_{jj}, in the LT and TT regions and p_{T}^{V} in the TN region.

Jet Multiplicity	Cut on ΔR
2-jet	$\Delta R > 0.787 + e^{1.387-0.007\times p_{\mathrm{T}}^{V}}$
3-jet	$\Delta R > 0.684 + e^{1.204-0.006\times p_{\mathrm{T}}^{V}}$

Table 5.7: Selections used to define the high ΔR control regions [196].

Low ΔR Control Region

A low ΔR control region is considered in the resolved $VH(H \to b\bar{b})$ 1-lepton channel only. This region is enriched in $W+$jets events containing heavy-flavor jets, allowing for a better constraint on this background. The functional form of the ΔR cut is listed in Table 5.8. The fit variable is the output score (`mvaCRLow`) of a BDT[6] trained to differentiate between $W+$jets (as signal) and $t\bar{t}$ events, providing a better constrain on the $W+$jets background.

Jet Multiplicity	Cut on ΔR
2-jet	$\Delta R < 0.41 + e^{0.818-0.01056\times p_{\mathrm{T}}^{V}}$
3-jet	$\Delta R < 0.43 + e^{0.399-0.00931\times p_{\mathrm{T}}^{V}}$

Table 5.8: Selections used to define the low ΔR control region used in $VH(H \to b\bar{b})$ 1-lepton channel [196].

Top Control Region

The control regions are used to constrain the backgrounds originating from top quark processes ($t\bar{t}$ and single-top). In the case where the top decay results in two b-jets (Top(bb) component), a constraint can be obtained from the $VH(b\bar{b})$ high ΔR CRs, which are enriched in the Top(bb) component. For the Top(bc) and Top(bl) component, dedicated top control regions are defined by selecting events with at least one b-tag and at least one tight c-tag (BT region). The BT region is, by construction, orthogonal to the $VH(H \to b\bar{b})$ and $VH(H \to c\bar{c})$ SRs. The fit variable used in the top CR is the mass of the Higgs candidate, m_{jj}.

V + light Control Region

This control region is used to constrain the $V+$jets background component containing light-flavor jets (V + light). Events entering this region are required to have one loose c-tagged

[6] The `mvaCRLow` BDT is described further in Section 5.4.

jet and one untagged jet (LN region). In the 1-lepton channel, this results in a region composed of 60% W + light events. The fit variable in the V + light CR is p_{T}^{V}. This is used to better constrain the p_{T}^{V} shape for the V + jets samples, given that the SHERPA 2.2.11 V + jets samples are known to mismodel the shape of the p_{T}^{V} distribution compared to data.

Boosted $VH(H \to b\bar{b})$ Categorization

Regions in the boosted regime contain only events where the transverse momentum of the vector boson is larger than 400 GeV, in order to avoid any overlap with the resolved $VH(H \to b\bar{b})$ regime. Events in the boosted regime are further divided into two p_{T}^{V} bins, $400 < p_{\mathrm{T}}^{V} < 600$ GeV and $p_{\mathrm{T}}^{V} > 600$ GeV.

The boosted $VH(H \to b\bar{b})$ signal region is defined by selecting events that have exactly two b-tagged track-jets associated with the large-R jet. A dedicated control region is constructed to constrain the $t\bar{t}$ background by selecting events that have at least one additional b-tagged track-jet outside the jet. This accounts for the fact that $t\bar{t}$ decays can result in at least one b-quark outside the large-R jet. For example, one of the top quarks could decay into a b-quark and a hadronically decaying W boson, and thus get reconstructed as the large-R jet. Meanwhile, the other top quark could decay into a b-quark and a leptonically decaying W boson, resulting in an additional b-tagged track-jet outside the large-R jet. The fit variable in the top CR is the mass of the large-R jet, m_J.

The boosted $VH(H \to b\bar{b})$ 1-lepton channel contains a total of four regions: two SRs (one for each p_{T}^{V} bin) and two top CRs (one for each p_{T}^{V} bin).

5.3.5 Higgs Candidate Reconstruction

Due to the fact that the resolved (resolved $VH(H \to b\bar{b})$ and $VH(H \to c\bar{c})$) and boosted $VH(H \to b\bar{b})$ regimes use different types of jets and flavor tagging schemes, separate strategies must be used for reconstructing the Higgs boson candidate.

In the resolved regime, it is important to ensure that the same event does not get categorized in both the $VH(H \to b\bar{b})$ and $VH(H \to c\bar{c})$ signal regions. This is achieved by identifying events that have both b-tagged and tight c-tagged jets, which are moved to the dedicated top background control region (BT region) introduced in the previous section, which is shared between resolved $VH(H \to b\bar{b})$ and $VH(H \to c\bar{c})$. In this region, the Higgs candidate is formed from the b-tagged jet with the highest p_{T} (if multiple b-tagged jets exist) and the tight c-tagged jet with the highest p_{T} (if multiple tight c-tagged jets exist).

For the remaining events, the Higgs candidate is reconstructed by considering all the signal jets in each event, as follows. In the resolved $VH(H \to b\bar{b})$ regime, the two jets that are b-tagged are used to reconstruct the Higgs candidate. In the $VH(H \to c\bar{c})$ regime, the jets are first ordered by which c-tagging bin they are assigned to, with tight c-tagged jets being considered first, followed by loose c-tagged jets, and finally untagged jets. If two or more jets are assigned to the same c-tagging bin, then they will be considered in order of decreasing p_{T}. The Higgs candidate is then reconstructed from the two highest ordered jets, first by c-tagging bin, then by p_{T}. As an example, consider an event with three jets, where one jet is tight c-tagged, and the other two are loose c-tagged. The tight c-tagged jet has a lower p_{T} than either of the loose c-tagged jets. In this case, the Higgs candidate jets consist of the tight c-tagged jet and the jet with the highest p_{T} between the two loose c-tagged jets. This event would be categorized into the LT tag SR or LT tag high ΔR CR, depending on the value of the ΔR between the two jets.

After the two Higgs candidate jets are chosen, they are sorted by their p_{T}. The jet with the highest p_{T} is considered the leading jet, while the other jet is the sub-leading jet. The other jets in the event are also sorted in order of decreasing p_{T}. The leading Higgs candidate jet must have $p_{\mathrm{T}} > 45$ GeV, while the other jets must pass a p_{T} cut of 20 GeV. A cut on the invariant mass of the Higgs candidate di-jet system, $m_{jj} > 50$ GeV, is applied to account for the known mismodelling of $V+$jets in the low Higgs mass regime.

In the boosted $VH(H \to b\bar{b})$ regime, the large-R jet with the highest p_{T} is chosen as the Higgs candidate. The large-R jet is required to be matched to at least two track-jets; the first three track-jets in decreasing p_{T} order are considered for flavor tagging. In the signal region, exactly two of the three track-jets are required to be b-tagged. The Higgs candidate mass is given by the invariant mass of the leading large-R jet, m_J. A cut of $m_J > 50$ GeV is applied as calibrations are not available for this low mass region.

After the Higgs candidate has been determined, the momentum resolution of the candidate jets is improved by applying two types of jet corrections. The *muon-in-jet* correction is applied to recover any energy loss in the calorimeter due to semileptonic decays of b- or c-hadrons that contain muons in the final state, and is applied to all events. The *PtReco* correction is applied to account for the fact that jet decay products can go outside the nominal cone size used by the jet reconstruction algorithm (out-of-cone effect). This is more likely to affect b-jets than c-jets, due to b-jets having a secondary vertex and the large b-hadron mass. Hence, the *PtReco* correction is applied only in the resolved $VH(H \to b\bar{b})$ regime.

5.4 Multi-Variate Analysis

Multi-variate analysis methods are used to improve the separation between signal and background events, leading to increased signal purity and background rejection. For this purpose, the analysis uses Boosted Decision Trees, trained on a set of discriminating event input features, that output a one dimensional score which is later used as the fit variable in the SRs of the analysis.

Dedicated BDTs are used in each of the resolved $VH(H \to b\bar{b})$, boosted $VH(H \to b\bar{b})$, and $VH(H \to c\bar{c})$ analysis regions, and are trained on events categorized in the signal and ΔR control regions to increase the available training statistics and improve stability[7]. For these VH BDTs, the signal consists of $VH(H \to b\bar{b})$ samples in the $VH(H \to b\bar{b})$ regions and $VH(H \to c\bar{c})$ samples in the $VH(H \to c\bar{c})$ regions. In both $VH(H \to b\bar{b})$ and $VH(H \to c\bar{c})$

[7] Training using only events from the signal region was found to introduce significant overtraining issues.

regions the background consists of the $V+$jets, $t\bar{t}$, single-top, and diboson samples. The $VH(H \to b\bar{b})$ events are not considered as a background when training the $VH(H \to c\bar{c})$ BDTs, or vice versa, as this was found to worsen the performance of the BDTs. However, the BDTs still exhibit some level of $VH(H \to b\bar{b})$ versus $VH(H \to c\bar{c})$ discriminating power since flavor tagging information is used as an input feature during training.

In addition, in each of the three analysis regimes, a separate BDT is trained using diboson samples as the signal [8]. The VZ BDTs are used to cross-check the performance of the BDT method and of the analysis strategy in general. In Section 5.7, a statistical fit is performed to measure the $VZ(Z \to b\bar{b})$ and $VZ(Z \to c\bar{c})$ processes, using the output score of the VZ BDTs as the fit discriminating variable.

The full set of input variables used for the training of the BDTs is shown in Table 5.9. This includes variables such as the invariant mass of the Higgs candidate and the angular separation between the two jets (track-jets in the boosted regime) that make up the Higgs candidate. These variables are expected to have good discriminating power between signal and background, as can be seen from the distributions for the VH signal and the background shown in Figure 5.9. The $m_{j_1 j_2}$ and $\Delta R(j_1, j_2)$ variables are generally found to have the highest importance for the BDT training in all analysis regimes. The transverse momentum of the vector boson, p_{T}^{V}, also has a sizeable importance in the BDT training.

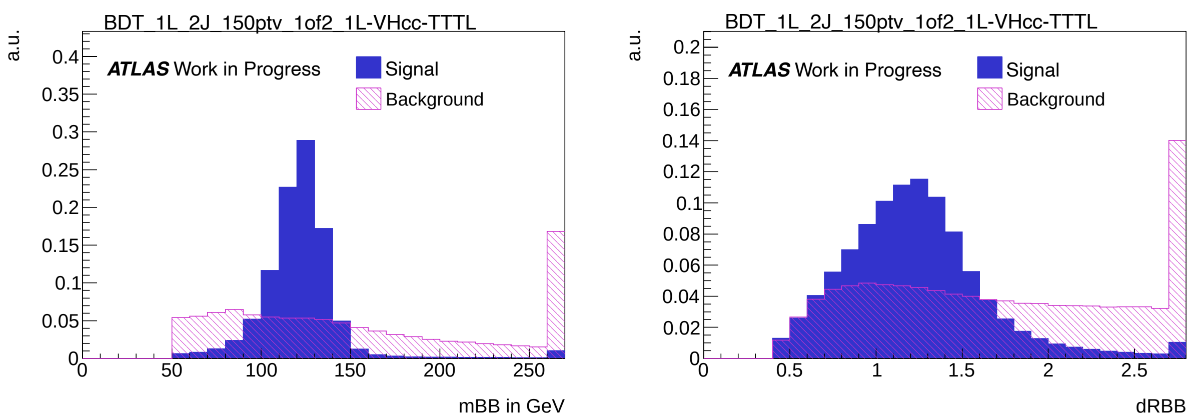

Figure 5.9: Distribution of input variables used for the BDT training in the $VH(H \to c\bar{c})$ regime: invariant mass $m_{j_1 j_2}$ (left) and angular separation $\Delta R(j_1, j_2)$ (right) of the two Higgs candidate jets [196]. Both signal and background distributions are normalized to unit area and the last bin contains the overflow.

All nominal MC samples considered in the analysis are used to train the BDTs. The BDT hyperparameters are optimized separately in each of the three analysis regimes and

[8] In the $VH(H \to b\bar{b})$ regimes, $VZ(Z \to b\bar{b})$ samples are used as signal, $VZ(Z \to c\bar{c})$ samples are excluded from training, and the rest of the samples form the background. Similarly, in the $VH(H \to c\bar{c})$ regime, $VZ(Z \to c\bar{c})$ is the signal, $VZ(Z \to b\bar{b})$ is excluded, and the rest of the samples form the background.

Variable	Description	Resolved Regime	Boosted Regime
$m_{j_1 j_2}$ or m_J	Invariant mass of the Higgs candidate system	×	×
$m_{j_1 j_2 j_3}$	Invariant mass of the Higgs candidate jets and the remaining jet with highest p_{T}	×	
$p_{\mathrm{T}}^{j_1}$ or $p_{\mathrm{T}}^{j_1,\mathrm{trk}}$	Transverse momentum of the leading p_{T} Higgs candidate jet (or track-jet)	×	×
$p_{\mathrm{T}}^{j_2}$ or $p_{\mathrm{T}}^{j_2,\mathrm{trk}}$	Transverse momentum of the subleading p_{T} Higgs candidate jet (or track-jet)	×	×
$p_{\mathrm{T}}^{j_3,\mathrm{trk}}$	Transverse momentum of the leading non b-tagged track-jet		×
$\sum_{i\neq 1,2} p_{\mathrm{T}}^{j_i}$	p_{T} sum of non Higgs candidate jets with $p_{\mathrm{T}} > 20$ GeV	×	
$\Delta R(\vec{j_1}, \vec{j_2})$ or $\Delta R(\vec{j_{1,\mathbf{trk}}}, \vec{j_{2,\mathbf{trk}}})$	Angular distance between the two Higgs candidate jets (or track-jets)	×	×
$\mathrm{bin}_{\mathrm{DL1r}}(j_1)$ or $\mathrm{bin}_{\mathrm{DL1r}}(j_1, \mathrm{trk})$	Tagging bin for the leading Higgs candidate jet (or track-jet)	×	×
$\mathrm{bin}_{\mathrm{DL1r}}(j_2)$ or $\mathrm{bin}_{\mathrm{DL1r}}(j_2, \mathrm{trk})$	Tagging bin for the sub-leading Higgs candidate jet (or track-jet)	×	×
p_{T}^{V}	Transverse momentum of the vector boson	×	×
$E_{\mathrm{T}}^{\mathrm{miss}}$	Missing transverse energy	×	×
$\lvert\Delta y(\vec{V}, \vec{H_{\mathrm{cand}}})\rvert$	Rapidity difference between the vector boson and the Higgs candidate	×	×
$\lvert\Delta \phi(\vec{V}, \vec{H_{\mathrm{cand}}})\rvert$	Azimuthal distance between the vector boson and the Higgs candidate	×	×
$\min[\Delta\phi(\vec{\ell}, \vec{j_1}$ or $\vec{j_2})]$	Azimuthal distance between the lepton and the closest b- or c-tagged jet	×	
m_{T}^{W}	Transverse mass of the W boson candidate	×	
m_{top}	Reconstructed mass of the leptonically decaying top quark	×	
$(p_{\mathrm{T}}^{\ell} - E_{\mathrm{T}}^{\mathrm{miss}})/p_T^W$	Proxy for p_{T} imbalance between charged lepton and neutrino from W boson decay		×
p_{T}^{ℓ}	Transverse momentum of the lepton		×
N(track-jets in J)	Number of track-jets matched to the large-R jet		×
N(add. small R-jets)	Number of additional small-R jets not matched to the large-R jet		×
Color	Variable that exploits color-flow difference between gluon splitting and QCD singlet state decays		×
$\min\{\Delta R(j_1$ or $j_2, j)\}$	Angular distance between the closest b- or c-tagged jet and the third additional jet	×	

Table 5.9: Summary of the input variables used in the 1-lepton channel for the training of the BDTs for the resolved $VH(H \rightarrow b\bar{b}/c\bar{c})$ and the boosted $VH(H \rightarrow b\bar{b})$ regimes [196].

are chosen to maximize the discriminating performance of the BDT output score. The final hyperparameter settings for all the BDTs used in the analysis are summarized in Table 5.10. In the resolved regimes, the BDTs are trained separately in jet multiplicity (2-jet and 3-jet) and p_{T}^{V} categories ($75 < p_{\mathrm{T}}^{V} < 150$ GeV and $p_{\mathrm{T}}^{V} > 150$ GeV.), for a total of 4 training regions. In the boosted regime, a single, inclusive training is performed. The trainings are performed using a k-fold cross-validation method. For each training region, $k = 2$ sub-trainings are considered. In one sub-training, the even event-numbered MC events are used for training and the model is evaluated on the odd numbered events. In the other sub-training, the odd numbered MC events are used for training and the model is evaluated on the even numbered events. The final discriminant is then constructed as the sum of the discriminants for the even and odd events[9].

	Resolved $VH(\to b\bar{b})$ and $VZ(\to b\bar{b})$	Boosted $VH(\to b\bar{b})$ and $VZ(\to b\bar{b})$	$VH(\to c\bar{c})$	$VZ(\to c\bar{c})$
Boost type	Gradient Boost	Adaboost	Gradient Boost	Adaboost
Number of trees	600	800	600	200
Maximum depth	4	3	4	4
Learning rate (β)	0.5	0.35	0.5	0.15
Number of cuts	100	60	100	100
Minimum node size	5%	2%	5%	5%
Separation method	Gini index	Gini index	Gini index	Gini index
Pruning method	No pruning	No pruning	No pruning	No pruning

Table 5.10: Hyperparameter settings for the VH and VZ BDTs used in the resolved $VH(H \to b\bar{b})$, boosted $VH(H \to b\bar{b})$, and $VH(H \to c\bar{c})$ regimes in the 1-lepton channel [196].

A well-known issue that can affect machine learning based techniques is that of overtraining, which occurs when a model achieves excellent performance on the training set, but fails to generalize the learned trends to new data. In the analysis, overtraining checks are performed to ensure that the BDT performance is generally optimal. For each sub-training, the BDT output score for the training and test sets are compared using a Kolmogorov-Smirnov (KS) similarity test. The performance of the BDTs on the training and test sets are also compared using receiver operating characteristic (ROC) curves. The VH and VZ BDTs do not exhibit any significant overtraining and demonstrate good separation power between signal and background, as can be seen from Figure 5.10.

One additional BDT is used in the analysis. This BDT (denoted `mvaCRLow`) is considered only in the low ΔR control region of the resolved $VH(H \to b\bar{b})$ regime, where it used to distinguish $W + bb$ events from the large $t\bar{t}$ contribution, especially in regions with low p_{T}^{V}. The `mvaCRLow` BDT is trained using events with exactly two b-tagged jets that get categorized into the low ΔR CR and the $W+$jets samples are used as the signal. The same input features for the resolved $VH(H \to b\bar{b})$ regime are used and the 2-fold cross-validation method is also applied in the same manner as for the VH BDTs. The `mvaCRLow` ouput score is used as the fit variable for the low ΔR control region.

Finally, the distribution of the BDT output scores undergoes a transformation designed to optimize the final sensitivity of the discriminant[10]. This is motivated by the fact that bins

[9] The MC event number is a randomly assigned identifier and no physics difference is expected between even and odd numbered MC events.

[10] The transformation of the BDT output score was first used in the resolved $VH(H \to b\bar{b})$ analysis [178]. In the $VH(H \to b\bar{b}/c\bar{c})$ analysis, its use is also extended to the boosted $VH(H \to b\bar{b})$ and $VH(H \to c\bar{c})$ regimes.

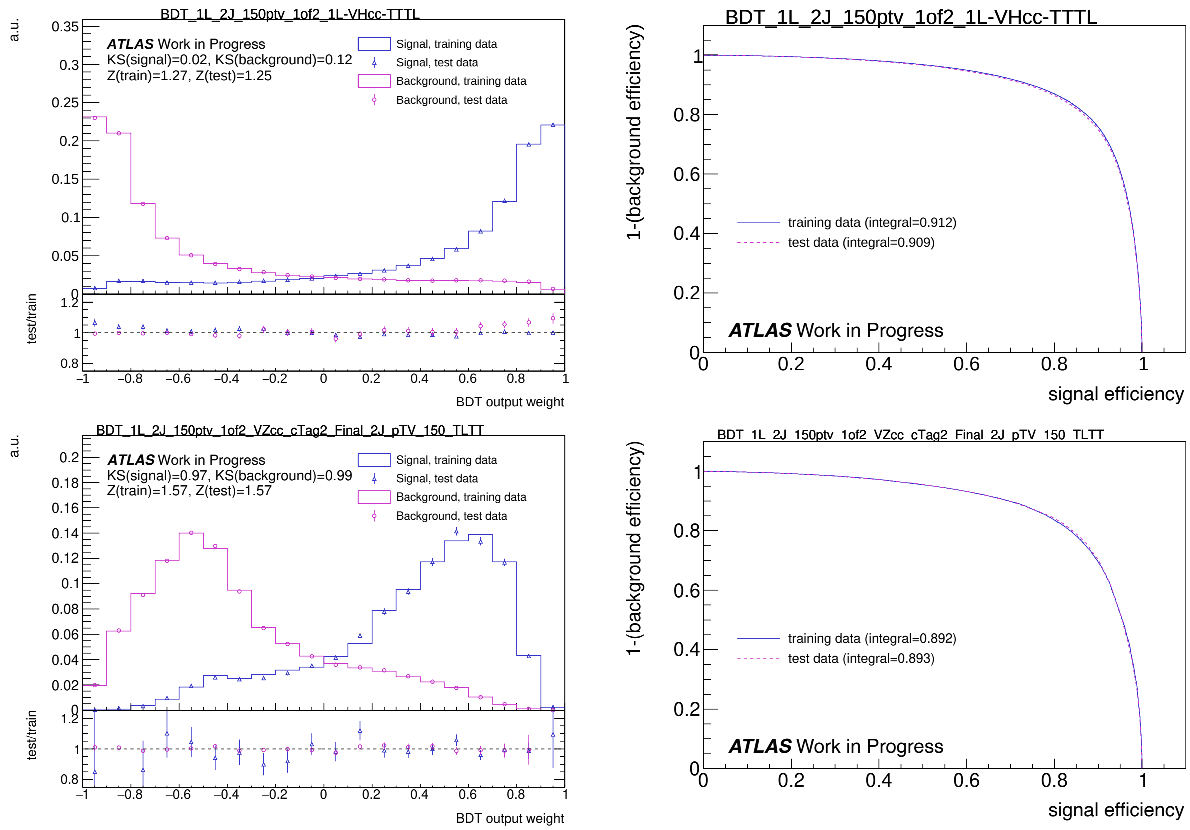

Figure 5.10: Overtraining checks for the VH (top) and VZ (bottom) BDTs used in the $VH(H \to c\bar{c})$ regime of the 1-lepton channel [196]. The left side plots compare the distribution of the BDT output scores, while the right side plots compared the ROC curves between the training and test sets.

at low BDT scores contain almost entirely background events, while bins at high BDT scores have good signal-to-background ratio, as can be seen in Figure 5.10. As such, the default equidistant and fine binning of the BDT distribution does not necessarily achieve optimal sensitivity. After the transformation, the BDT output distributions usually have smoother shapes, for both signal and background, with finer bins in the signal-enriched region at high BDT scores and coarser bins in the background dominated regions at low BDT scores. The transformation also ensures that the statistical uncertainty in each bin is smaller than 20%.

5.5 Experimental Uncertainties

The analysis considers experimental uncertainties related to detector performance, trigger efficiency, physics object reconstruction, and flavor tagging. The uncertainties that are considered in the resolved $VH(H \to b\bar{b})$, boosted $VH(H \to b\bar{b})$, and $VH(H \to c\bar{c})$ regimes depend on the physics objects that are used in each. The experimental uncertainties are assessed following the prescriptions provided by the ATLAS Combined Performance (CP) groups[11]. In general, a full set of systematic uncertainties can consist of up to $\mathcal{O}(100)$ variations. Reduced sets of systematic uncertainties are also derived by performing principal component analysis, which reduces the number of variations by combining them in a way that preserves the original correlations. Table 5.11 provides a list of all the experimental uncertainties considered in this analysis.

Luminosity and Pile-up

The uncertainty on the combined integrated luminosity in the Run 2 data taking period (between 2015 and 2018) was measured to be 0.83%, obtained using the LUCID-2 detector [229] following the methodology outlined in Ref. [101].

The uncertainty on the pile-up distribution in simulated events is obtained by considering variations in the nominal data rescaling factor, which has a value of 1.0/1.03. This factor is used to rescale the μ values in data to compute pile-up weights [230]. The rescaling is necessary because MC simulated events at a given μ are better at simulating data events at a higher μ value. The systematic uncertainty is computed by varying the value of the nominal rescaling factor to 1.0/0.99 and 1.0/1.07, respectively.

Trigger

Lepton and $E_{\mathrm{T}}^{\mathrm{miss}}$ triggers are used to identify events in the 1-lepton channel. For the lepton triggers, the analysis considers systematic uncertainties related to the trigger efficiency. For electrons, this consists of a single uncertainty that combines the statistical and systematic uncertainties. The statistical and systematic uncertainties are considered separately for the muon trigger. For the $E_{\mathrm{T}}^{\mathrm{miss}}$ trigger, scale factors that account for the efficiency turn-on are derived using $W(\mu,\nu)+\text{jets}$ events [231]. The analysis considers three different systematic uncertainties on these SFs: the statistical uncertainty on the data used to derive the SFs, a systematic uncertainty derived using different processes ($Z+\text{jets}$ and $t\bar{t}$) to derive the SFs, and an uncertainty that accounts for the kinematic dependence of the trigger efficiency on the scalar sum of all final state jets within the event (`SumPt`).

Lepton and $E_{\mathrm{T}}^{\mathrm{miss}}$ reconstruction

The analysis considers systematic uncertainties related to the reconstruction of leptons and $E_{\mathrm{T}}^{\mathrm{miss}}$. These uncertainties are derived in the respective calibration analyses for these physics objects.

[11] The experimental uncertainties are not guaranteed to be derived consistently between the various categories, as they are estimated separately by different ATLAS CP groups.

Category	Uncertainty Name	Description	Analysis Regime
Event	LUMI_2015_2018	Uncertainty on total integrated luminosity	all
	PRW_DATASF	Uncertainty on pile-up modelling	all
e Trigger	EL_EFF_Trigger_TOTAL	Trigger efficiency total (statistical + systematic) uncertainty	all
μ Trigger	MUON_EFF_TrigStat(Syst)Uncertainty	Trigger efficiency statistical (systematic) uncertainty	all
$E_{\mathrm{T}}^{\mathrm{miss}}$ Trigger	METTrigStat	Statistical uncertainty on the $W(\mu,\nu)+$jets events used to derive the SFs	resolved
	METTrigTop	Uncertainty on the SF measurements for different process ($t\bar{t}$)	resolved
	METTrigZ	Uncertainty on the SF measurements for different process ($Z+$jets)	resolved
	METTrigSumpt	Uncertainty on the kinematic dependence on SumPt	resolved
e Reconstruction	EL_EFF_Reco_TOTAL	Reconstruction efficiency total uncertainty	all
	EL_EFF_ID_TOTAL	Identification efficiency total uncertainty	all
	EL_EFF_Iso_TOTAL	Isolation efficiency total uncertainty	all
	EG_SCALE_ALL	Energy scale uncertainty	all
	EG_RESOLUTION_ALL	Energy resolution uncertainty	all
μ Reconstruction	MUON_EFF_RECO_STAT(SYS)	Reconstruction and ID efficiency statistical (systematic) uncertainty for muons with $p_{\mathrm{T}} > 15\,\mathrm{GeV}$	all
	MUON_EFF_RECO_STAT(SYS)_LOWPT	Reconstruction and ID efficiency statistical (systematic) uncertainty for muons with $p_{\mathrm{T}} \leq 15\,\mathrm{GeV}$	all
	MUON_EFF_ISO_STAT(SYS)	Isolation efficiency statistical (systematic) uncertainty	all
	MUON_EFF_TTVA_STAT(SYS)	Track-to-vertex association efficiency statistical (systematic) uncertainty	all
	MUON_SCALE	Momentum scale uncertainty	all
	MUON_SAGITTA_RHO(REBIAS)	Momentum scale uncertainty to cover charge-dependent local misalignment effects	all
	MUON_ID	Momentum resolution uncertainty of the Inner Detector	all
	MUON_MS	Momentum resolution uncertainty of the Muon Spectrometer	all
τ Reconstruction	TAUS_TRUEHADTAU_EFF_RECO_TOTAL	Reconstruction efficiency uncertainty	all
	TAUS_TRUEHADTAU_EFF_RNNID	RNN-based identification efficiency uncertainty	all
	TAUS_TRUEHADTAU_SME_TES	In situ tau energy scale correction	all
	TAUS_TRUEELECTRON_EFF_ELEBDT_STAT(SYS)	Electron veto efficiency statistical (systematic) uncertainty	all
$E_{\mathrm{T}}^{\mathrm{miss}}$ Reconstruction	MET_SoftTrk_ResoPara(Perp)	'Soft term'-related longitudinal (transverse) resolution uncertainty	all
	MET_SoftTrk_Scale	'Soft term'-related scale uncertainty	all
	MET_JetTrk_Scale	$E_{\mathrm{T,\,trk}}^{\mathrm{miss}}$ scale uncertainty	all
Small-R Jets	JET_CR_BJES_Response	Energy scale uncertainties for b-jets	all
	JET_CR_EffectiveNP_Detector{1-2}	Energy scale uncertainties due to in situ calibration	all
	JET_CR_EffectiveNP_Mixed{1-3}	Energy scale uncertainties due to in situ calibration	all
	JET_CR_EffectiveNP_Modelling{1-4}	Energy scale uncertainties due to in situ calibration	all
	JET_CR_EffectiveNP_Statistical{1-6}	Energy scale uncertainties due to in situ calibration	all
	JET_CR_EtaIntercal_Modelling	Energy scale uncertainties to cover η-intercalibration non-closure	all
	JET_CR_EtaIntercal_NonClosure_highE	Energy scale uncertainties to cover η-intercalibration non-closure	all
	JET_CR_EtaIntercal_NonClosure_negEta	Energy scale uncertainties to cover η-intercalibration non-closure	all
	JET_CR_EtaIntercal_NonClosure_posEta	Energy scale uncertainties to cover η-intercalibration non-closure	all
	JET_CR_EtaIntercal_TotalStat	Energy scale uncertainties to cover η-intercalibration non-closure	all
	JET_CR_Flav_Comp(Response)	Energy scale uncertainty related to flavour composition (response)	all
	JET_PU_{OffsetMu(NPV),PtTerm,RhoTopology}	Energy scale uncertainties due to pile-up effects	all
	JET_CR_PunchTroughMC16	Energy scale uncertainty for 'punch-through'	all
	JET_CR_SingleParticle_HighPt	Energy scale uncertainty for the behavior of high-p_{T} jets	all
	JET_JvtEfficiency	JVT efficiency uncertainty	all
	JET_CR_JER_DataVsMC	Energy resolution uncertainty	all
	JET_CR_JER_EffectiveNP_{1-6,7restTerm}	Energy resolution uncertainties	all
Large-R Jets	FJ_JMSJES_Baseline_Kin	Energy and mass scale uncertainty due to basic data-simulation differences	boosted
	FJ_JMSJES_Modelling_Kin	Energy and mass scale uncertainty due to simulation differences	boosted
	FJ_JMSJES_Tracking_Kin	Energy and mass scale uncertainty on reference tracks	boosted
	FJ_JMSJES_TotalStat_Kin	Energy and mass scale uncertainty from statistical uncertainty on the measurement	boosted
	FJ_JER	Energy resolution uncertainty	boosted
	FJ_JMR	Mass resolution uncertainty	boosted
Flavor tagging: PFlow Jets	FT_EFF_PFlow_Eigen_B_{0-44}	b-tagging efficiency uncertainties for b-jets	resolved
	FT_EFF_PFlow_Eigen_C_{0-19}	b-tagging efficiency uncertainties for c-jets	resolved
	FT_EFF_PFlow_Eigen_Light_{0-19}	b-tagging efficiency uncertainties for light-flavor jets	resolved
	FT_EFF_PFlow_extrapolation	b-tagging efficiency uncertainty for high-p_{T} jets	resolved
Flavor tagging: VR Track-jets	FT_EFF_VR_Eigen_B_{0-4}	b-tagging efficiency uncertainties for b-jets	boosted
	FT_EFF_VR_Eigen_C_{0-3}	b-tagging efficiency uncertainties for c-jets	boosted
	FT_EFF_VR_Eigen_Light_{0-3}	b-tagging efficiency uncertainties for light-flavor jets	boosted
	FT_EFF_VR_extrapolation	b-tagging efficiency uncertainty for high-p_{T} jets	boosted

Table 5.11: List of experimental systematic uncertainties considered in the $VH(H \to b\bar{b}/c\bar{c})$ analysis [196].

The electron reconstruction, identification, and isolation efficiencies are measured in data and compared to predictions from simulation for samples of $Z \to e^+e^-$ and $J/\psi \to e^+e^-$ events. Uncertainties related to the reconstruction efficiency SFs, the identification efficiency SFs, and the isolation efficiency SFs are derived [142]. For the electron energy scale, the full calibration considers 60 different systematic uncertainties. As these uncertainties do not represent dominant systematic sources for the $VH(H \to b\bar{b}/c\bar{c})$ analysis, only two uncertainties related to the energy scale and resolution are considered, which group together the large number of original variations.

The SFs for muon reconstruction are derived using samples of $Z \to \mu^+\mu^-$ and $J/\psi \to \mu^+\mu^-$ samples using the Run 2 dataset [144]. Systematic uncertainties related to the reconstruction, isolation, and track-to-vertex association SFs are provided. Separate reconstruction uncertainties are available for low p_{T} muons[12], where the J/ψ measurement is more important, and for high p_{T} muons, where the Z measurement is more accurate. Uncertainties related to the muon energy scale and resolution are also available and included in this analysis.

The SFs for hadronic τ-lepton reconstruction are derived using $Z \to \tau\tau$ events and four sources of systematic uncertainties are considered (leptonic τ decays are already covered by the electron and muon reconstruction uncertainties) [169]. One systematic uncertainty is used for the τ reconstruction efficiency. The uncertainty for the RNN-based identification efficiency is estimated separately for 1-prong and 3-prong τ leptons and parameterized as a function of p_{T} [170, 171]. Uncertainties for the in situ τ-jet energy scale correction are also derived separately for 1-prong and 3-prong τ-leptons. The electron veto efficiency uncertainty is provided for 1-prong τ-leptons and has a statistical component and a systematic component, which are considered separately.

The analysis also considers systematic uncertainties related to the $E_{\mathrm{T}}^{\mathrm{miss}}$ scale and resolution [172].

Small-*R* Jets

The largest sources of jet-related uncertainty originate from the uncertainties for the jet energy scale (JES) and jet energy resolution (JER), which are included in this analysis [152]. The full set of jet-related systematic uncertainties consists of $\mathcal{O}(100)$ systematic variations, but the analysis uses a reduced set of uncertainties. The uncertainties are related to in situ analyses, η-intercalibration, high p_{T} jets, pile-up, flavor composition, flavor response, b-jets, and punch-through jets. Uncertainties on the JVT and fJVT efficiency SFs are also considered [155].

[12] Systematic uncertainties on low p_{T} muons are less relevant in the 1-lepton channel, where the low p_{T} muons are used to veto events with more than one lepton.

Large-R Jets

A full set of in situ derived systematic uncertainties [154] for jet energy scale, jet energy resolution, jet mass scale (JMS), and jet mass resolution (JMR) is available, consisting of $\mathcal{O}(200)$ variations across the four categories. The analysis uses a reduced set of uncertainties for JES, JER, JMS and the full set of uncertainties for JMR.

Flavor Tagging

The full set of flavor tagging systematic uncertainties [165, 166] consists of ~ 160 variations across the four jet flavor categories (b-, c-, τ-, and light-flavor jets), but the analysis makes use of a reduced set of uncertainties. As the tagging efficiencies for c- and τ-jets are similar, the same SFs and systematic uncertainties are applied to both c-jets and τ-jets. Given that the calibrations have limited reach in jet p_{T}, the uncertainties have to be extrapolated beyond the last calibrated bin for jets with high p_{T}. An additional uncertainty is included to account for this high-p_{T} extrapolation.

5.6 Signal and Background Modelling Uncertainties

This section provides an overview of the theoretical uncertainties that are considered for the signal and background processes relevant to the 1-lepton channel $VH(H \to b\bar{b}/c\bar{c})$ analysis. For this analysis, both $VH(H \to b\bar{b})$ and $VH(H \to c\bar{c})$ represent signal processes. The main background contributions in the 1-lepton channel arise from $W+$ jets and top quark processes ($t\bar{t}$ and single-top). Diboson and QCD multi-jet events provide minor contributions to the total background.

5.6.1 Derivation of Modelling Uncertainties

The signal and background processes in the $VH(H \to b\bar{b}/c\bar{c})$ 1-lepton channel analysis are primarily modelled using simulated MC samples, except for the QCD multi-jet background. In the latter case, the modelling of such events in simulation is known to not be accurate, thus this background is modelled using a data-driven approach. The simulated samples are used to derive the expected signal and background yields, as well as the distributions of relevant kinematic variables in the analysis phase space.

To assess the uncertainty on the prediction of the MC samples, *nominal samples* are compared to *alternative samples*. The nominal samples are generated using the MC generators that describe a particular process with the best precision. Alternative samples are used to account for systematic uncertainties stemming from, for example, differences in matrix element generation, parton shower generation, or perturbation theory corrections. The alternative samples include both samples that are generated using different MC generators and samples generated with the nominal generators but with different parameter values, such as samples used to estimate initial state radiation and/or final state radiation effects. Depending on the process, the latter can also correspond to variations in the QCD renormalization and factorization scales (μ_R and μ_F), different parton distribution function (PDF) sets, or different electroweak corrections.

Table 5.12 provides a summary of the nominal generators, the alternative generators, and the sources of theoretical uncertainties considered for the simulated samples used in the analysis. When performing the comparison between the nominal and alternative generators, different types of uncertainties can be derived, as described in the following subsections. The uncertainties are derived separately in the resolved and boosted regimes.

Sample	Nominal	Alternative	Theory Systematic Variations
$VH(H \to b\bar{b})$	Powheg+Pythia 8	Powheg+Herwig 7	μ_R and μ_F, PDF, ISR/FSR
$VH(H \to c\bar{c})$	Powheg+Pythia 8	Powheg+Herwig 7	μ_R and μ_F, PDF, ISR/FSR
V + jets	Sherpa 2.2.11	MadGraph5_aMC@NLO+Pythia 8 with FxFx merging, Sherpa 2.2.1	μ_R and μ_F, PDF, electroweak corrections
$t\bar{t}$ and single-top	Powheg+Pythia 8	Powheg+Herwig 7, MadGraph5_aMC@NLO+Pythia 8	Additional ISR/FSR, DS/DR (single-top Wt)
Diboson	Sherpa 2.2.11	Powheg+Pythia 8, Sherpa 2.2.1	μ_R and μ_F, PDF, electroweak corrections

Table 5.12: Samples used in the $VH(H \to b\bar{b}/c\bar{c})$ analysis with their nominal and alternative MC generators and the systematic variations used to derive the theory modelling uncertainties [196].

Normalization Uncertainties

The overall normalizations for the background processes are either measured from data (the preferred approach whenever possible), in which case the normalizations are left freely floating in the fit, or they are derived from simulated samples. In the latter case, generator comparisons are performed in order to derive the associated normalization uncertainties, which are computed as an overall uncertainty on the yields of different processes. A summary of the normalizations uncertainties for the backgrounds relevant to the $VH(H \to b\bar{b}/c\bar{c})$ 1-lepton channel analysis is shown in Table 5.13.

Acceptance Ratio Uncertainties

In the fit model, the floating normalizations can be correlated across different analysis regions, such as regions with different p_T^V, jet multiplicity, flavor composition, or signal and control regions. In such cases, the floating normalization would be determined from the

Modelling Systematic Uncertainty	Resolved $VH(H \to b\bar{b}/c\bar{c})$	Boosted $VH(H \to b\bar{b})$
$W+$jets		
$W+hf$ normalization	Floating	Floating
$W+mf$ normalization	Floating	36%
$W+lf$ normalization	Floating	38%
$W+hf$ flavor composition ratios	4% – 20%	11%
$W+mf$ flavor composition ratios	12% – 29%	9% – 15%
High/Low ΔR CR-SR acceptance ratios	2% – 65%	–
top CR-SR acceptance ratio	–	16% – 27%
$W+mf$ p_T^V acceptance ratio	–	3%
$W+lf$ p_T^V acceptance ratio	–	3%
Top ($t\bar{t}$ and single-top Wt-channel)		
Top(bb) normalization	Floating	–
Top(others) normalization	Floating	–
Top normalization	–	Floating
Top(others) flavor composition ratios	5% – 10%	–
$Wt/t\bar{t}$ composition ratio	12% – 18%	22% – 36%
High/Low ΔR CR-SR acceptance ratios	2% – 10%	–
top CR-SR acceptance ratio	–	14% – 19%
Single-top s-/t-channel		
Normalization	5% – 17%	–
High/Low ΔR CR-SR acceptance ratios	3% – 17%	–
p_T^V acceptance ratios	7% – 15%	–
N_{jet} acceptance ratio	15%	–
Diboson		
WW/WZ normalization	16%/19%	16%/27%
$ggVV$ normalization	30%	30%
N_{jet} acceptance ratio	10% – 22%	–
p_T^V acceptance ratios	2% – 10%	7% – 30%
High/Low ΔR CR-SR acceptance ratios	11% – 50%	–
$p_T^V \times N_{\text{jet}}$ acceptance uncertainty from QCD scales	2% – 19%	2% – 10%
Multi-jet		
Normalization	5% – 100%	–

Table 5.13: Background modelling uncertainties considered in the $VH(H \to b\bar{b}/c\bar{c})$ 1-lepton channel only analysis. The values provided quantify the size of the uncertainty affecting the yield for each background. Uncertainties in the shapes of the fitted distributions are also considered for all backgrounds.

statistically dominant region. Any residual differences in the number of predicted events between the regions that are treated as correlated are implemented through acceptance uncertainties. These uncertainties account for the fact that different MC generators can predict different yields in different analysis regions, which in practice results in a change in the ratio between the number of events across different analysis regions.

The acceptance uncertainty is computed as the double ratio of the yields in two different regions A and B, as predicted by the nominal and alternative generators, according to the following formula:

$$\text{Acceptance ratio} = \sqrt{\sum_{\text{var}_i} \left(\frac{(\frac{n_B}{n_A})_{\text{var}_i}}{(\frac{n_B}{n_A})_{\text{nominal}}} - 1 \right)^2} \tag{5.1}$$

In Eqn. 5.1, $(\frac{n_B}{n_A})_{\text{nominal}}$ denotes the ratio computed using the predictions of the nominal MC generator, while $(\frac{n_B}{n_A})_{\text{var}_i}$ gives the ratio predicted by the alternative generator or other variations of the nominal generator, denoted var_i. Region A represents the region with the highest purity or statistics for a particular process, while Region B has lower purity / statistics. Generally, multiple sources of uncertainty are considered (as shown in Table 5.12) and the final acceptance uncertainty is obtained by adding the uncertainty of each source in quadrature. The total acceptance uncertainty is then applied to region B.

If it is necessary to extrapolate across three different regions A, B, and C, two types of acceptance uncertainties are considered. First, an acceptance ratio is computed between one region and the combined other two regions, i.e. A $\to$ B+C, which is applied to regions B and C, or B+C $\to$ A applied to region A. Then, a second acceptance ratio is computed between the two grouped regions, i.e. B $\to$ C or C $\to$ B. Table 5.13 contains a summary of the acceptance uncertainties considered for the $VH(H \to b\bar{b}/c\bar{c})$ 1-lepton channel analysis, while Table 5.14 shows the SR/CR extrapolations in the resolved $VH(H \to b\bar{b})$ regime, where the extrapolation must be done between the SR, high ΔR CR, and low ΔR CR. In the $VH(H \to c\bar{c})$ regime, the extrapolation is derived between the SR and the high ΔR CR, while in the boosted $VH(H \to b\bar{b})$ regime it is derived between the SR and the top CR.

Shape Uncertainties

Differences in the shape of variables used in the statistical fit (such as the MVA discriminant in the SR) between different MC generators are quantified through shape systematic uncertainties. For most samples, these shape uncertainties are derived using the Calibrated Likelihood Ratio Estimator (CARL) algorithm [232]. The CARL method consists of training a deep neural network (NN) to distinguish between the nominal and the alternative samples. The NN is trained on the same set of kinematic variables used for the BDTs described in Section 5.4. The output of the CARL NN consists of an estimator $r^*(\mathbf{x})$ for the ratio:

$$r(\mathbf{x}) = \frac{q(\mathbf{x}; \theta_A)}{p(\mathbf{x}; \theta_N)}, \tag{5.2}$$

Background	A → (←)B+C	B → C
$W + hf$	$\mathrm{CR_{Low}} + \mathrm{SR} \to \mathrm{CR_{High}}$	$\mathrm{CR_{Low}} \to \mathrm{SR}$
Top(bb)	$\mathrm{CR_{High}} \to \mathrm{SR} + \mathrm{CR_{Low}}$	$\mathrm{SR} \to \mathrm{CR_{Low}}$
Top(others)	$\mathrm{SR} + \mathrm{CR_{Low}} \to \mathrm{CR_{High}}$	$\mathrm{SR} \to \mathrm{CR_{Low}}$
Single-top, $75 < p_{\mathrm{T}}^{V} < 150$ GeV	$\mathrm{SR} \to \mathrm{CR_{High}} + \mathrm{CR_{Low}}$	$\mathrm{CR_{High}} \to \mathrm{CR_{Low}}$
Single-top, $p_{\mathrm{T}}^{V} > 150$ GeV	$\mathrm{CR_{High}} \to \mathrm{SR} + \mathrm{CR_{Low}}$	$\mathrm{SR} \to \mathrm{CR_{Low}}$
Diboson	$\mathrm{SR} + \mathrm{CR_{Low}} \to \mathrm{CR_{High}}$	$\mathrm{SR} \to \mathrm{CR_{Low}}$

Table 5.14: High/Low ΔR CR-SR extrapolations derived in the resolved $VH(H \to b\bar{b})$ regime. $\mathrm{CR_{Low}}$ and $\mathrm{CR_{High}}$ denote the low ΔR CR and high ΔR CR, respectively.

where $p(\mathbf{x}; \theta_N)$ represents the distribution of the kinematic variable $\mathbf{x}$ as predicted by the nominal generator and $q(\mathbf{x}; \theta_A)$ represents the distribution predicted by the alternative generator. θ_N and θ_A represent internal parameters characterizing the nominal and alternative MC generators, respectively.

Using techniques inspired from generative AI, the CARL algorithm can produce a sample which follows the shape of the alternative sample, but inherits the increased statistics of the nominal sample, which in turn reduces the amount of statistical fluctuations – this sample is denoted as the CARL-reweighted sample. Note that, due to the often limited training statistics available for the alternative sample compared to the nominal one, it is possible to introduce bias in the CARL-reweighted distribution. Hence, checks must be performed to ensure that the CARL-reweighted sample is not biased towards resembling the nominal distribution. The shape uncertainties are then derived by taking the ratio of the (normalized) distribution between the CARL-reweighted sample and the nominal sample.

Additional shape uncertainties are considered, for example, by comparing the nominal sample to samples with variations in the QCD scale parameters μ_R and μ_F. For signal samples, the shape uncertainties are derived using the alternative parton shower generator. For single-top Wt samples, DS/DR shape uncertainties are derived from the DR samples. For $V +$jets samples, shape uncertainties are also included to account for the fact that, in certain p_{T}^{V} regions, the Sherpa 2.2.11 p_{T}^{V} distribution shows more disagreement with the data compared to the Sherpa 2.2.1 distribution [210].

5.6.2 Signal Modelling

The modelling of the signal process is affected by two distinct sources: uncertainties on the VH production cross section and uncertainties on the $H \to b\bar{b}$ and $H \to c\bar{c}$ decays. The final $VH(H \to b\bar{b}/c\bar{c})$ analysis (i.e. combining all three lepton channels) will implement a complete set of normalization, acceptance, and shape uncertainties to account for these sources and the uncertainties will be derived within the context of that analysis (including using the CARL reweighting method for deriving shape uncertainties). The $VH(H \to$

$b\bar{b}/c\bar{c}$) 1-lepton channel analysis presented in this chapter considers only a simplified set of modelling uncertainties for the signal processes, as described in the following paragraphs and summarized in Table 5.15, making use of the uncertainties that were previously derived for the individual $VH(H \to b\bar{b})$ [178, 179] and $VH(H \to c\bar{c})$ [194] analyses.

Modelling Systematic Uncertainty	Resolved $VH(H \to b\bar{b}/c\bar{c})$	Boosted $VH(H \to b\bar{b})$
$H \to b\bar{b}$ branching ratio	1.6%	
$H \to c\bar{c}$ branching ratio	+5.5% / -2.0%	–
WH cross section uncertainty ($VH(H \to c\bar{c})$ only)	2.0%	–
Phase space acceptance uncertainty	6.2%	–
N_{jet} acceptance ratio	11%	–
Uncertainty due to PS, hadronization, and UE modelling	–	4.4%

Table 5.15: Signal modelling uncertainties considered in the $VH(H \to b\bar{b}/c\bar{c})$ 1-lepton channel only analysis. The values provided quantify the size of the uncertainty affecting the yield for the signal processes. Uncertainties in the shapes of the fitted distributions are also considered.

Normalization Uncertainties

The analysis considers theoretical uncertainties on the value of the branching ratios for the $H \to b\bar{b}$ and $H \to c\bar{c}$ decays, as well as on the WH production cross section, following the guidelines provided in Ref. [79]. Additionally, comparisons between the nominal and alternative generators for the signal processes are performed to derive uncertainties on the phase space acceptance.

Acceptance Uncertainties

An acceptance uncertainty is implemented to account for migrations between the 2-jet and 3-jet categories. In addition, uncertainties that account for differences in the parton shower, hadronization, and underlying event model are derived from comparisons between the nominal Powheg+Pythia 8 and the alternative Powheg+Herwig 7 generators and applied in the boosted regime.

Shape Uncertainties

Shape uncertainties are considered to account for the effect of variations in the QCD renormalization and factorization scales μ_R and μ_F. These represent the most important uncertainties for the prediction of the VH cross section. Additionally, uncertainties due to the NLO EW corrections are considered to account for effects on the shape of the p_{T}^{V} distribution.

5.6.3 $W+$jets Background Modelling

The largest background in the $VH(H \to c\bar{c})$ regime of the analysis is represented by $V+$jets events. $W+$jets events represent the dominant background contribution in the 1-lepton channel, where the W boson decays to a lepton (electron or muon) and a neutrino. Events where the W boson decays to a τ-lepton and a neutrino, and the τ-lepton further decays hadronically and is misidentified as a jet, represent a non-negligible contribution that gets categorized in the 0-lepton channel due to the lack of a reconstructed lepton in the final state. Formally, such events should not be categorized in the 0-lepton channel as they represent decays of the W boson, whereas the 0-lepton channel targets events from $ZH \to \nu\nu q\bar{q}$ decays. To account for this, a hadronic τ split is applied to the events in the 0-lepton channel, which are divided, based on the number of hadronic τ-jets, into events that have no hadronic τ-jets and events with more than one hadronic τ-jet. For the purposes of modelling the $W+$jets background, events with more than one hadronic τ-jet are assigned to the 1-lepton channel and considered together with the nominal 1-lepton channel events for the derivation of the systematic uncertainties. $Z+$jets events represent a negligible contribution in the 1-lepton channel, hence dedicated modelling uncertainties, such as normalization or acceptance ratios, are not derived for this process.

The $W+$jets background can be divided into six different components based on the flavor composition of the Higgs candidate di-jet system: $W+bb$, $W+bc$, $W+bl$, $W+cc$, $W+cl$, and $W+l$. The strategy for configuring the statistical fit, and implicitly deriving the $W+$jets modelling uncertainties, is to group similar processes together, as different flavor compositions that originate from the same physics process should be subject to similar modelling issues.

The heavy-flavor ("hf") category consists of heavy-flavor jets produced in association with a W boson, which are generated as a result of gluon splitting and the fusion of b/c-quarks. As the modelling of these processes is known to be problematic, the components are grouped into a single $W+hf(bb,cc)$ category. The mixed-flavor ("mf") category corresponds to cases where the jets represent a mixture of b- and c-jets or a mixture of heavy- and light-flavor jets. As these combinations produce a similar shape for the di-jet invariant mass, the components are merged together as $W+mf(bc,bl,cl)$. Events with light-flavor jets only are considered separately as a $W+lf(l)$ category.

For deriving the acceptance ratios, only the most dominant component in each category is used (which can be different between the $VH(H \to b\bar{b})$ and $VH(H \to c\bar{c})$ regimes), while for deriving the shape uncertainties, all the components in each category are considered. Tables 5.16-5.17 provide the fraction that each of the $W+$jets subcomponents contribute to the total $W+$jets background, as predicted by the nominal generator Sherpa 2.2.11, in the signal region and high ΔR control region of the $VH(H \to c\bar{c})$ regime. The dominant component in the $W+hf$ category is represented by $W+cc$ events, while the dominant component in the $W+mf$ category consists of $W+cl$ events.

As can be seen in the tables, the not tagged-tight c-tag (NT) category is largely dominated by the $W+cl$ and $W+l$ components. The loose-tight c-tag (LT) category has significant

SR, Sherpa 2.2.11		NT tag		LT tag		TT tag	
p_T^V region	Process	2-jet	3-jet	2-jet	3-jet	2-jet	3-jet
$75 < p_T^V < 150$ GeV	$W + bb$	0.1 %	0.1 %	0.5 %	0.7 %	0.7 %	1.1 %
	$W + bc$	0.4 %	0.4 %	2.0 %	1.8 %	3.5 %	3.2 %
	$W + bl$	1.3 %	1.7 %	1.4 %	1.8 %	0.9 %	1.0 %
	$W + cc$	3.8 %	4.5 %	17.9 %	19.7 %	55.6 %	60.9 %
	$W + cl$	75.7 %	72.7 %	63.2 %	60.1 %	33.9 %	29.4 %
	$W + l$	18.8 %	20.6 %	14.9 %	15.9 %	5.4 %	4.3 %
$p_T^V > 150$ GeV	$W + bb$	0.2 %	0.2 %	1.1 %	1.2 %	1.6 %	1.5 %
	$W + bc$	0.3 %	0.3 %	1.8 %	1.6 %	2.2 %	2.5 %
	$W + bl$	1.5 %	1.9 %	1.6 %	1.9 %	0.9 %	0.9 %
	$W + cc$	5.1 %	5.9 %	21.9 %	23.9 %	63.5 %	63.5 %
	$W + cl$	70.3 %	67.6 %	56.6 %	52.3 %	26.5 %	25.4 %
	$W + l$	22.6 %	24.0 %	17.0 %	19.0 %	5.3 %	6.1 %

Table 5.16: Contributions to the total background of the individual $W+$jets flavor components, as predicted by the nominal generator, in the signal region of the $VH(H \rightarrow c\bar{c})$ regime in the 1-lepton channel.

High ΔR CR, Sherpa 2.2.11		NT tag		LT tag		TT tag	
p_T^V region	Process	2-jet	3-jet	2-jet	3-jet	2-jet	3-jet
$75 < p_T^V < 150$ GeV	$W + bb$	0.0 %	0.1 %	0.3 %	0.3 %	0.5 %	0.6 %
	$W + bc$	0.4 %	0.4 %	2.1 %	2.1 %	4.4 %	4.0 %
	$W + bl$	1.6 %	1.9 %	1.8 %	1.9 %	1.4 %	1.2 %
	$W + cc$	3.3 %	3.6 %	15.2 %	15.8 %	51.0 %	51.6 %
	$W + cl$	75.0 %	73.5 %	64.5 %	62.9 %	37.1 %	36.9 %
	$W + l$	19.6 %	20.6 %	16.2 %	16.9 %	5.6 %	5.7 %
$p_T^V > 150$ GeV	$W + bb$	0.1 %	0.1 %	0.4 %	0.5 %	0.8 %	0.8 %
	$W + bc$	0.4 %	0.3 %	1.9 %	1.8 %	3.4 %	3.5 %
	$W + bl$	1.9 %	2.3 %	2.3 %	2.3 %	1.6 %	1.4 %
	$W + cc$	3.4 %	3.7 %	15.3 %	15.7 %	47.8 %	51.3 %
	$W + cl$	69.4 %	68.4 %	60.2 %	58.8 %	38.6 %	35.8 %
	$W + l$	24.9 %	25.2 %	19.9 %	20.8 %	7.9 %	7.1 %

Table 5.17: Contributions to the total background of the individual $W+$jets flavor components, as predicted by the nominal generator, in the high ΔR control region of the $VH(H \rightarrow c\bar{c})$ regime in the 1-lepton channel.

contributions from $W + cl$, $W + cc$ and $W + l$, while the tight-tight c-tag (TT) category is dominated by $W + cc$ and $W + cl$. The $W + bb$, $W + bc$, and $W + bl$ components are found to be sub-dominant in all three tag regions, with a less than $\sim 5\%$ combined contribution to the $W+$jets background. These trends are found to be consistent between the 2-jet and 3-jet categories.

In the $VH(H \to b\bar{b})$ regimes, the dominant contribution in the two b-tag (BB) region is represented by the $W + hf$ category, which contributes $\sim 85\%$ of the total $W+$jets background in the resolved regime ($\sim 75\%$ in the boosted regime) [196]. As expected from the flavor tagging selection, the dominant component in the $W + hf$ category consists of $W + bb$ events. The $W + mf$ and $W + lf$ categories are found to represent sub-dominant contributions to the background composition.

Sources of Systematic Uncertainties

The systematic uncertainties related to the modelling of the $W+$jets backgrounds are derived by comparing the nominal Sherpa 2.2.11 samples to alternative samples generated with MadGraph5_aMC@NLO+Pythia with the FxFx merging prescription (for simplicity, referred to as MadGraph FxFx). The MadGraph FxFx samples are used to estimate uncertainties in the nominal prediction due to using a different matrix element and parton shower calculation. Figure 5.11 illustrates the distributions of the Higgs candidate invariant mass and the transverse momentum of the W boson for $W + cl$ events in the $VH(H \to c\bar{c})$ regime, comparing the predictions between the nominal and alternative generator. The MadGraph FxFx predicted distributions show both normalization and shape differences from the nominal predictions, both of which are considered for the derivation of systematic uncertainties as described in the following sections.

Alternative Sherpa 2.2.11 samples generated with setups different from the nominal are also considered for assessing systematic uncertainties. As shown in Table 5.12, the Sherpa 2.2.11 alternative samples are used to estimate systematic variations due to:

- differences in the QCD renormalization (μ_R) and factorization (μ_F) scales
- the choice of PDF
- the effects of the electroweak corrections

For estimating the impact of the QCD scales, the Sherpa 2.2.11 samples contain alternative event weights that correspond to the 7-point variations in the renormalization and factorization scales, which are evaluated coherently in the matrix element and the parton shower calculations [233]. The values for μ_R and μ_F are varied independently by factors of 0.5 and 2, avoiding cases where the variations are in opposite directions (i.e. $(\mu_R, \mu_F) = (0.5, 2), (2, 0.5)$ are not considered). The QCD scale uncertainty is taken to be the maximum difference in the envelope of the variations with respect to the nominal value $\mu_R = 1, \mu_F = 1$. A representative example of the effects of the QCD scale variations is provided in Figure 5.12, which

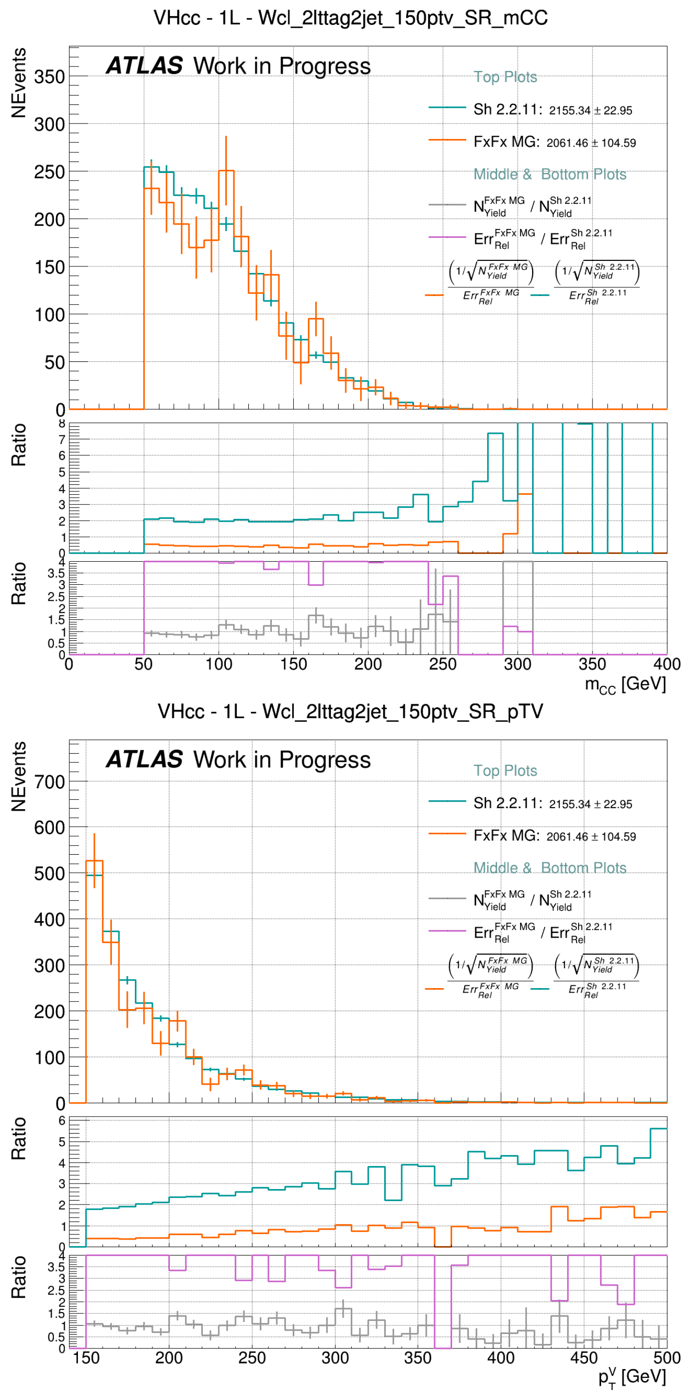

Figure 5.11: Distribution of the Higgs candidate invariant mass (top) and the W boson transverse momentum (bottom) for $W + cl$ events in the phase space of the $VH(H \to c\bar{c})$ regime, comparing the nominal and alternative generators. The cyan line shows the prediction of the nominal generator Sherpa 2.2.11, while the orange line corresponds to the prediction of the MadGraph FxFx alternative generator.

illustrates the p_{T}^{V} distribution for $W + mf$ events in the $VH(H \to c\bar{c})$ regime. On average, the QCD scale uncertainty is found to be $\mathcal{O}(10\%)$.

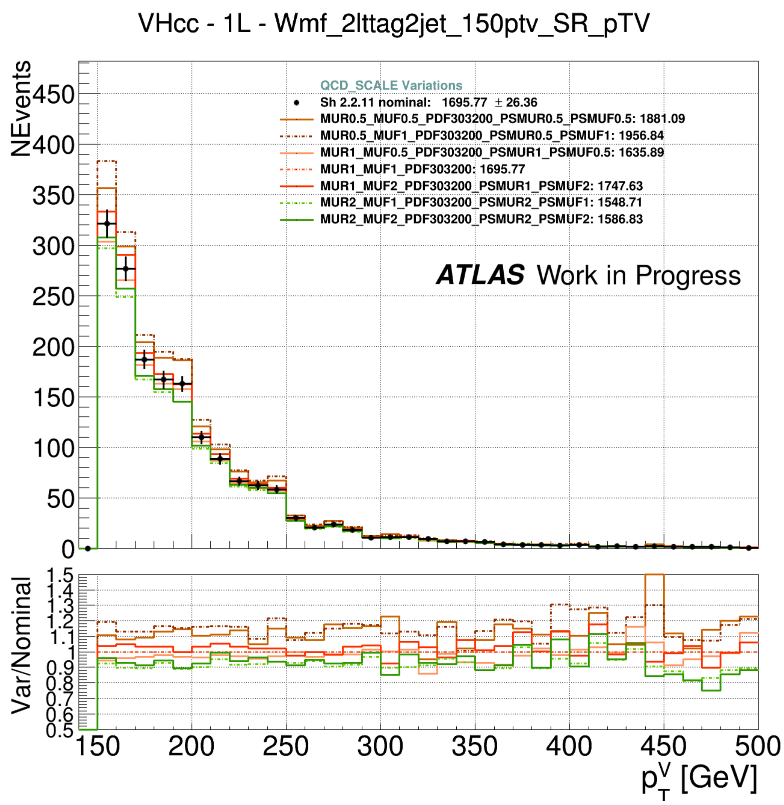

Figure 5.12: Distribution of the W boson transverse momentum for $W + mf$ events in the phase space of the $VH(H \to c\bar{c})$ regime, showing the effects of the QCD scale variations. The QCD scales μ_R and μ_F are varied independently by factors of 0.5 and 2. The brown solid line denotes the $\mu_R = 0.5, \mu_F = 0.5$ combination, and the green solid line denotes the $\mu_R = 2, \mu_F = 2$ variation. The nominal SHERPA 2.2.11 prediction is shown with black dots.

Uncertainties related to the choice of the NNPDF3.0NNLO nominal parton distribution function are estimated by considering the Hessian eigenvector set and variations in the value of the strong coupling constant ($\alpha_S = 0.117$ and $\alpha_S = 0.119$). The PDF uncertainties are derived using the Hessian eigenvector set according to the method described in Ref. [55] using the `LHAPDF` tool [234]. Briefly, this consists of generating $N = 100$ additional distributions, which correspond to the eigenvectors of the Hessian matrix used to characterize the PDF uncertainty by varying the PDF parameters. The PDF uncertainty on the nominal yield

$\sigma^{(0)}$ is computed as

$$\delta^{\text{pdf}}\sigma = \sqrt{\sum_{i=1}^{N}(\sigma^{(i)} - \sigma^{(0)})^2} \tag{5.3}$$

and represents a 68% confidence level. An example of the effects of the PDF variations can be seen in Figure 5.13, which shows the distribution of the Higgs candidate invariant mass for $W + hf$ events in the $VH(H \to c\bar{c})$ regime. The PDF uncertainty is found to be, on average, on the order of a few percent.

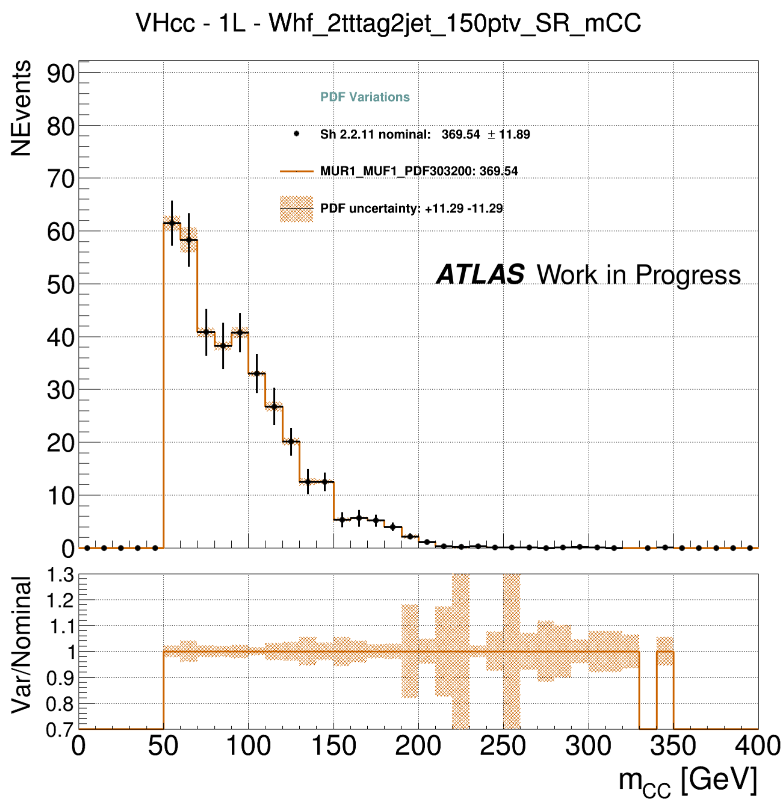

Figure 5.13: Distribution of the invariant mass of the Higgs candidate for $W + hf$ events in the phase space of the $VH(H \to c\bar{c})$ regime, showing the effects of the PDF uncertainty. The brown hashed area shows the envelope of the 100 different configurations of the PDF, which is considered as the PDF systematic uncertainty. The nominal SHERPA 2.2.11 prediction is shown with black dots.

Higher-order electroweak corrections to single boson production must also be considered for accurate modelling of single vector bosons, particularly in regions of phase space where the boson is produced with large p_{T}. The NLO electroweak calculations for $V +$jets production contain contributions from both virtual loops and real emissions of vector bosons, however, the Sherpa 2.2.11 samples used by the analysis are generated considering only the virtual loop contributions ($\mathrm{EW_{virt}}$)[13] [210]. The corrections to the LO cross section due to the NLO EW virtual calculations can be combined with the NLO QCD only corrections in three different ways:

- additive scheme: $\sigma^{\mathrm{NLO}}_{\mathrm{QCD+EW_{virt}}} = \sigma^{\mathrm{LO}} + \Delta\sigma^{\mathrm{NLO}}_{\mathrm{QCD}} + \Delta\sigma^{\mathrm{NLO}}_{\mathrm{EW_{virt}}}$
- multiplicative scheme: $\sigma^{\mathrm{NLO}}_{\mathrm{QCD\times EW_{virt}}} = (\sigma^{\mathrm{LO}} + \Delta\sigma^{\mathrm{NLO}}_{\mathrm{QCD}}) \times (1 + \Delta\sigma^{\mathrm{NLO}}_{\mathrm{EW_{virt}}})$
- exponentiated scheme: $\sigma^{\mathrm{NLO}}_{\mathrm{QCD\times e^{EW_{virt}}}} = (\sigma^{\mathrm{LO}} + \Delta\sigma^{\mathrm{NLO}}_{\mathrm{QCD}}) \times e^{\Delta\sigma^{\mathrm{NLO}}_{\mathrm{EW_{virt}}}}$

The NLO EW correction is applied according to the recommendations of the ATLAS Physics Modelling Group: the correction scheme that is closest to the NLO QCD only prediction is chosen to modify the nominal Sherpa 2.2.11 predictions, while the other two schemes are considered as sources of systematic uncertainty. For the $W+$jets samples considered by the $VH(H \to b\bar{b}/c\bar{c})$ analysis, the additive correction scheme was found to be closest to the NLO QCD only predictions, as can be seen from Figure 5.14. The differences between the additive correction and the multiplicative and exponentiated ones are taken as uncertainties due to missing higher order terms from mixed QCD-EW contributions. These EW correction uncertainties are generally found to be at or less than the percent level.

Normalizations

In the resolved regimes, the three $W+$jets background components ($W + hf$, $W + mf$, $W + lf$) are left freely floating in the fit. The $W + lf$ background is constrained using a dedicated control region, corresponding to the loose c-tag-not tagged (LN) category in the $VH(H \to c\bar{c})$ regime. Six such control regions are introduced in the fit, split by p_{T}^{V} ($75 < p_{\mathrm{T}}^{V} < 150$ GeV, $150 < p_{\mathrm{T}}^{V} < 250$ GeV, and $p_{\mathrm{T}}^{V} > 250$ GeV) and jet multiplicity (2-jet and 3-jet). Each control region has an associated floating normalization, i.e. decorrelated for each p_{T}^{V} and jet multiplicity bin.

The $W + hf$ and $W + mf$ backgrounds are constrained from the ΔR control regions and the signal regions. In the $VH(H \to c\bar{c})$ regime, $W + hf$ is dominated by the $W + cc$ component, and is constrained by the TT regions. $W + mf$ is mostly composed of $W + cl$ events, and is thus constrained by the LT and NT regions. In the $VH(H \to b\bar{b})$ regime, $W + hf$ is dominated by the $W + bb$ component and constrained by the BB regions, while $W + mf$ and $W + lf$ represent negligible background contributions. The floating normalizations for $W + hf$ and $W + mf$ are also decorrelated between the different p_{T}^{V} ($75 < p_{\mathrm{T}}^{V} < 150$ GeV, $150 < p_{\mathrm{T}}^{V} < 250$ GeV, and $p_{\mathrm{T}}^{V} > 250$ GeV) and jet multiplicity (2-jet and 3-jet) categories.

In the boosted $VH(H \to b\bar{b})$ regime, the $W + hf$ component is found to be dominant and is assigned freely floating normalizations, decorrelated between the $400 < p_{\mathrm{T}}^{V} < 600$ GeV

[13] The real emission of vector bosons is neglected for both simplicity and because its inclusion would lead to a different experimental signature that is usually generated with separate samples.

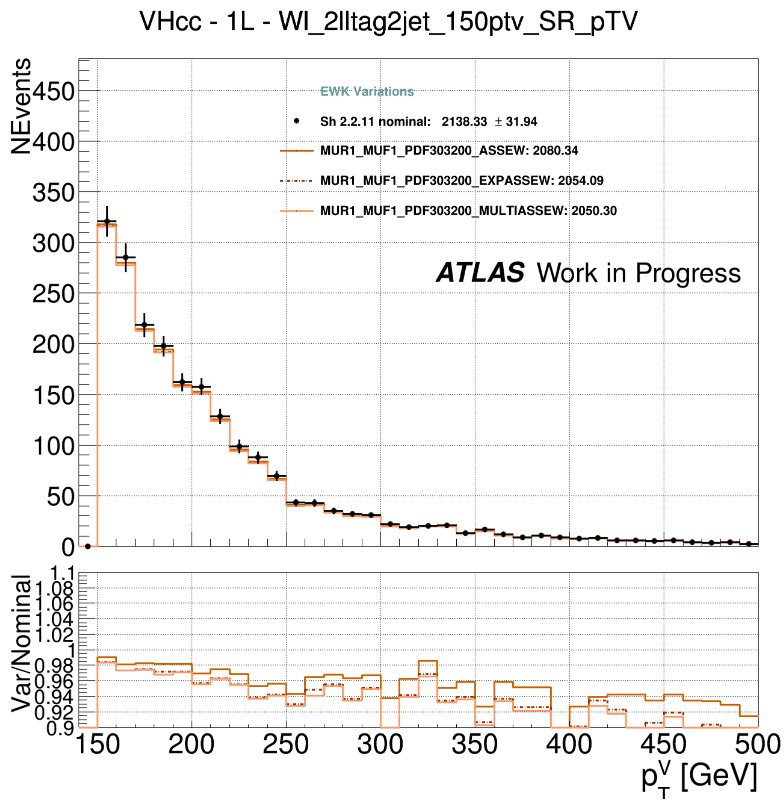

Figure 5.14: Distribution of the W boson transverse momentum for $W + lf$ events in the phase space of the $VH(H \to c\bar{c})$ regime, showing the effects of the NLO EW corrections. The distribution obtained by applying the additive EW correction scheme (brown solid line) is found to be closest to the SHERPA 2.2.11 NLO QCD only prediction (black dots). The predictions obtained with the exponentiated (dotted line) and multiplicative schemes (orange solid line) are similar to each other and show the largest deviation from the NLO QCD only prediction.

and $p_{\mathrm{T}}^{V} > 600$ GeV regions. The $W + mf$ and $W + lf$ components are sub-dominant and are assigned normalization uncertainties of 36% and 38% of their nominal MC predictions, respectively.

Acceptance Uncertainties

As previously mentioned, the acceptance ratio uncertainties are derived by considering differences in the predicted yields between the nominal generator and the alternative generator, as well as the variations corresponding to different QCD scales μ_R and μ_F, uncertainty in the PDF, different α_S values, and alternative NLO EW correction schemes. Table 5.18 provides an example of the individual contributions of these uncertainty sources to the total acceptance uncertainty derived to account for differences in the flavor composition of the $W + mf$ component in $VH(H \to c\bar{c})$. Generally for $W+$jets, the total acceptance ratio uncertainty tends to be dominated by the difference in predictions between the nominal generator SHERPA 2.2.11 and the alternative generator MADGRAPH FXFX. The variations in the QCD scales and the uncertainty in the PDF tend to be the second-largest uncertainty sources. The uncertainties due to different α_S values and the alternative NLO EW correction schemes (exponentiated and multiplicative relative to additive) represent minor contributions.

For the $W+$jets background, acceptance ratios are estimated for both the signal and control regions and computed between regions with different flavor compositions, p_{T}^{V} ranges, and between signal and control regions. As the floating normalizations are decorrelated in p_{T}^{V} and/or jet multiplicity, no acceptance ratios are applied between p_{T}^{V} or jet multiplicity categories. In $VH(H \to c\bar{c})$, the acceptance ratio uncertainties are computed inclusively using the yields in the NT, LT, and TT categories, while in $VH(H \to b\bar{b})$ they are computed separately using the BB category. When the numbers are found to be compatible, the acceptance ratios are also computed inclusively by combining SR and CR, jet multiplicity regions, and/or the $150 < p_{\mathrm{T}}^{V} < 250$ GeV and $p_{\mathrm{T}}^{V} > 250$ GeV regions, in order to reduce statistical fluctuations.

To account for the complex flavor composition of the $W+$jets background, dedicated acceptance ratio uncertainties are derived for the groups floated together in the fit, namely $W+hf(bb, cc)$ and $W+mf(bc, bl, cl)$. For the $W+hf$ group, this uncertainty is computed as the yield ratio between the two subcomponents, $W+cc/W+bb$. The size of this uncertainty ranges between 4% and 20% when taking into account trends with jet multiplicity and p_{T}^{V}. For the $W + mf$ group, separate acceptance uncertainties are derived as the ratio between each of the $W+mf$ sub-dominant components and the $W+mf$ dominant component, with the latter consisting of $W + cl$ in the resolved regimes and $W + bc$ in the boosted regime. These uncertainties are found to range between 9% and 29%.

The acceptance effect between the signal and control regions is treated with explicit acceptance uncertainties for each of the $W+$jets groups. In the resolved regimes, the $W+hf$ component is primarily constrained from the BB tag category of the SR and low ΔR CR, the $W+mf$ component is constrained by the NT tag and LT tag categories of the high ΔR

Categorisation	Variation Type	Variation	$\frac{W+bc}{W+cl}$	$\frac{W+bl}{W+cl}$
SR + High ΔR CR, NT+LT+TT tags, $150 < p_{\mathrm{T}}^{V} < 250$ GeV, 2-jet	Alternative Generator	MGPy8_FxFx	**-22.7** ± 2.4 %	**-28.8** ± 1.2 %
	QCD Scales μ_R and μ_F	MUR0.5_MUF0.5	**-5.1** %	**-3.7** %
		MUR0.5_MUF1	-3.9 %	-0.4 %
		MUR1_MUF0.5	-1.9 %	-3.1 %
		MUR1_MUF1	0.0 %	0.0 %
		MUR1_MUF2	1.7 %	1.6 %
		MUR2_MUF1	-2.0 %	-1.1 %
		MUR2_MUF2	0.5 %	0.7 %
	PDF Uncertainty	PDF303200_up	4.9 %	-0.1 %
		PDF303200_down	**-5.2** %	**0.1** %
	α_S Variations	PDF270000	**1.5** %	-0.2 %
		PDF269000	-0.9 %	**-1.4** %
	NLO EW Corrections	PDF303200_ASSEW	0.0 %	0.0 %
		PDF303200_EXPASSEW	**-0.3** %	**-0.4** %
		PDF303200_MULTIASSEW	**-0.3** %	**-0.5** %
		Total	**23.9** %	**29.1** %

Table 5.18: Flavor composition acceptance ratios for the $W{+}mf$ component in $VH(H \to c\bar{c})$, derived from comparisons to MadGraph FxFx and Sherpa 2.2.11 internal variations, in the $150 < p_{\mathrm{T}}^{V} < 250$ GeV, 2-jet category. The internal variations considered consist of the 7-point QCD scale μ_R and μ_F variations, up and down uncertainties in the PDF, different α_S values, and alternative NLO EWK corrections schemes (EXPASSEW, MULTIASSEW) relative to nominal (ASSEW). The maximum acceptance uncertainties computed for each variation group (bold numbers) are summed in quadrature to obtain the final acceptance priors shown in the Total row.

CR, and the $W + lf$ component is constrained from the LN tag category of the SR. These constraints are taken into account when deriving the relevant acceptance uncertainties. For $W + hf$, the extrapolation is performed between the SR, high ΔR CR, and low ΔR CR (the latter only in the $VH(H \to b\bar{b})$ regions). For $W + mf$ and $W + lf$, as they are constrained from $VH(H \to c\bar{c})$ regions, the extrapolation is performed between the SR and the high ΔR CR. The size of these acceptance uncertainties is found to range between 2% and 65%. In the boosted regime, the extrapolation is performed between the SR and the top CR, with the size of the uncertainties ranging from 16% to 27%.

In the boosted $VH(H \to b\bar{b})$ regime only, an acceptance ratio uncertainty is derived to extrapolate between the two $400 < p_{\mathrm{T}}^{V} < 600$ GeV and $p_{\mathrm{T}}^{V} > 600$ GeV regions. This uncertainty is found to be $\sim 3\%$ and is applied to the $W + mf$ and $W + lf$ background components.

Shape Uncertainties

Differences in the modelling of $W+$jets kinematic variables between the nominal generator Sherpa 2.2.11 and the alternative generator MadGraph FxFx are accounted for with dedicated shape uncertainties derived using the CARL reweighting method. The CARL method is used to generate an alternative CARL-reweighted sample, which follows the shape predicted by the MadGraph FxFx generator, but benefits from the larger statistics of the Sherpa 2.2.11 sample. Additionally, given the neural network nature of CARL, this method can simultaneously account for correlations between all the kinematic variables used during training.

As with any machine learning method, dedicated checks are performed to verify the validity of the trainings. In the limit of a perfect training, the CARL-reweighted distribution would be identical to the alternative distribution. However, this is not guaranteed to be the case in the typical use cases of the CARL method, which are limited by practical factors such as finite computational resources and limited training sample sizes. Hence, for the CARL method, the most relevant metric to check is the agreement between the CARL-reweighted and the alternative predicted distributions. An example is provided by the closure plots shown in Figure 5.15, which highlight the performance of the dedicated CARL training for the $VH(H \to c\bar{c})$ regime.

For $W+$jets, good closure is generally found between the CARL-reweighted and the alternative distributions, as shown in the top plot of Figure 5.15 for the invariant mass distribution. This can be seen both by comparing the two distributions in the top panel and by looking at the ratio between the distributions in the middle panel, where the black line denoting the ratio is generally close to 1.0 and within the one standard deviation band of MC statistical uncertainty. For variables where the nominal and alternative distributions are similar in shape, as in the case of p_{T}^{V} shown in the bottom plot of Figure 5.15, the CARL-reweighted distribution still has the advantage of providing a smoother shape with fewer statistical fluctuations. This can be seen in the bottom panel of the plot, where the black line denotes the residuals between the CARL-reweighted and the alternative distributions. The residuals between CARL-reweighted and alternative are found to be much closer to 0 (generally within 1σ) than the residuals between nominal and alternative (light blue line), especially at higher p_{T}^{V} values.

Separate CARL trainings are performed in each of the resolved $VH(H \to b\bar{b})$, $VH(H \to c\bar{c})$, and boosted $VH(H \to b\bar{b})$ regimes. Within each regime, the CARL training is generally performed inclusively (e.g. by combining jet multiplicity, p_{T}^{V}, and/or SR and CR regions) in order to increase the available statistics and improve the training performance. However, the CARL-reweighted distributions are generated for the more exclusive analysis regions used in the statistical fit. The performance of the CARL method is also validated in these exclusive regions, where good closure is generally found. A representative example for the distribution of the $VH(H \to c\bar{c})$ BDT output score is shown in Figure 5.16. The agreement between the CARL-reweighed and the alternative distributions is quantified through a χ^2 test. In the case of good closure, the χ^2/n.d.f value is expected to be close to ≈ 1.0, as can be seen in

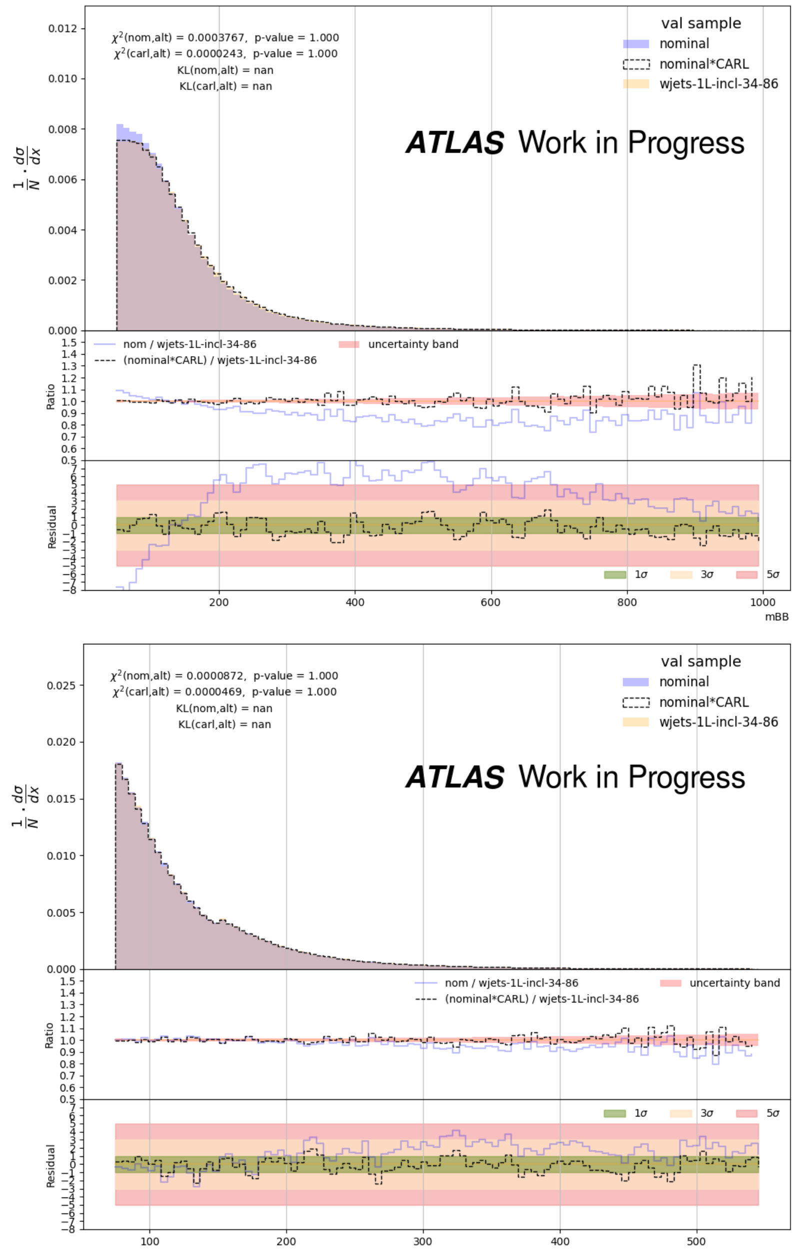

Figure 5.15: Closure plots for the CARL training for $W+$jets in the $VH(H \to c\bar{c})$ regime, showing the distribution of the Higgs candidate invariant mass (top) and vector boson transverse momentum (bottom). The top panel compares the distributions between the nominal (blue), alternative (yellow), and CARL-reweighted samples (dashed black line). The middle panel shows the ratio between nominal and alternative (blue line) and between CARL-reweighted and alternative (dashed black line). The residual shown in the bottom panel is computed as the difference between two distributions divided by the total statistical uncertainty.

Figure 5.16.

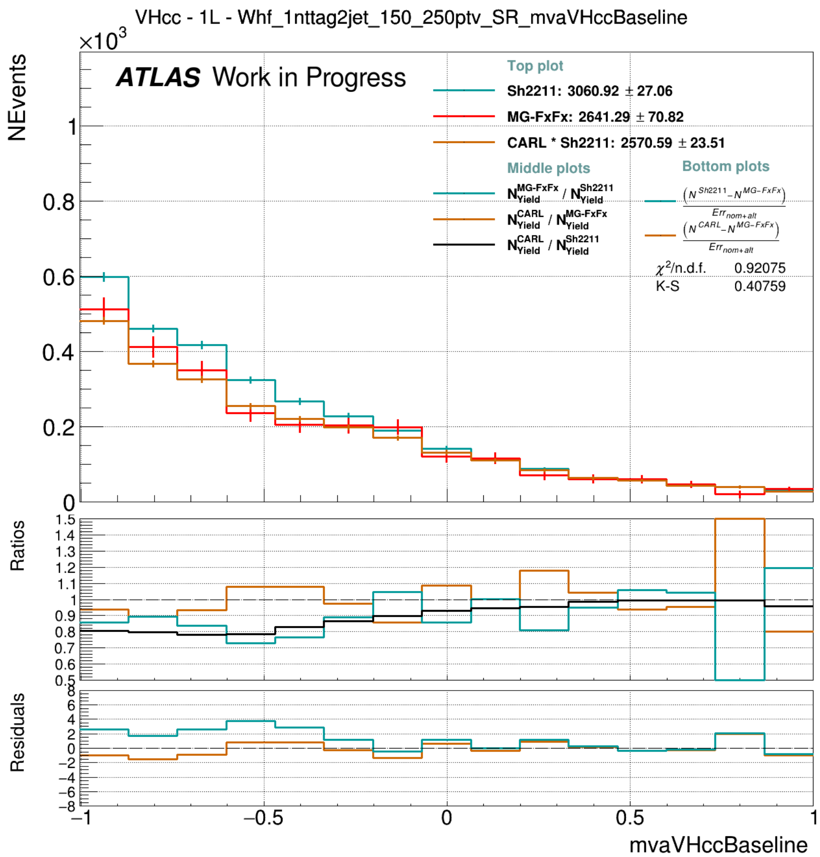

Figure 5.16: CARL closure plot for the distribution of the $VH(H \to c\bar{c})$ BDT output score for $W + hf$ in the NT tag, 2-jet, $150 < p_{\mathrm{T}}^{V} < 250$ GeV category of the SR. In the top panel, the CARL-reweighted distribution (brown line) is compared to the alternative (red line) and nominal (teal line) distributions. Good closure can be observed between the CARL-reweighed and alternative distributions, with $\chi^2/\mathrm{n.d.f} = 0.92$.

Shape uncertainties are also derived to account for variations due to the QCD scales and the NLO EW corrections. From the 7-point QCD scales variations, the variation corresponding to $\mu_R = 2$ and $\mu_F = 2$ is chosen as it tends to provide the largest uncertainties compared to the nominal prediction. The multiplicative EW correction scheme is formally considered as an additional source of shape uncertainty, as it provides the largest differences from the additive correction scheme (with the latter chosen to correct to NLO QCD only Sherpa 2.2.11 predictions). However, the EW shape uncertainties are generally found to be quite small, on the order of a percent or less.

Finally, Sherpa 2.2.1 samples are used to derive shape uncertainties for the p_{T}^{V} distribution only. This distribution was found to show more discrepancy when comparing the SHERPA 2.2.11 samples to the observed data than when performing the same comparison with SHERPA 2.2.1. Thus, the p_{T}^{V} shape uncertainties are derived by reweighting the SHERPA 2.2.11 distribution to resemble the SHERPA 2.2.1 one. This is achieved by fitting a reweighting polynomial to the ratio of the two p_{T}^{V} distributions. The polynomial fit is performed separately for each of the $W+$jets flavor groups, $W+hf$, $W+mf$, and $W+lf$, and the results can be seen in Figure 5.17. The shape uncertainties are then computed from the ratio of the reweighted SHERPA 2.2.11 distribution to the nominal one.

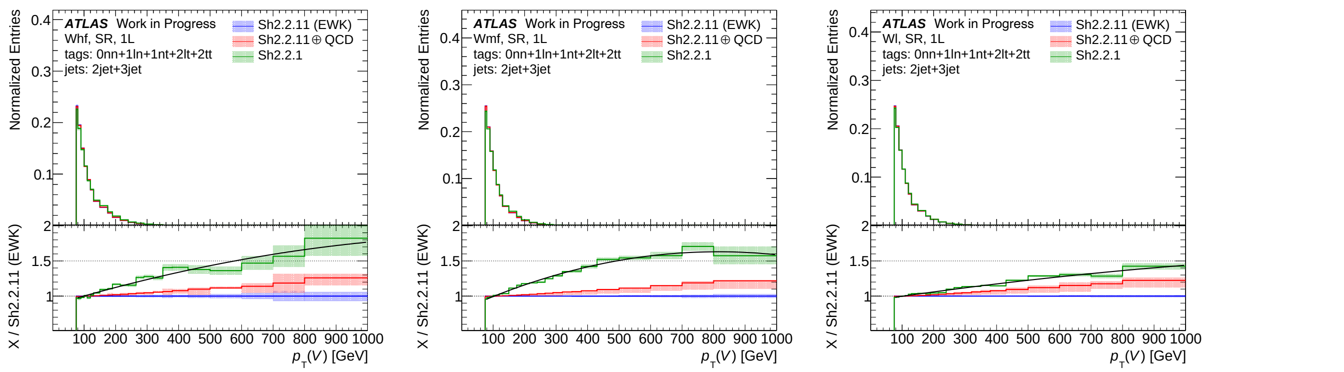

Figure 5.17: p_{T}^{V} shape uncertainties for $W+$jets derived from a comparison of the p_{T}^{V} distributions between SHERPA 2.2.11 and SHERPA 2.2.1 [196]. The reweighting polynomials (black line in the bottom panels) are fitted to the ratio between the two p_{T}^{V} distributions and derived separately for $W+hf$ (left), $W+mf$ (middle), and $W+lf$ (left).

5.6.4 Modelling of Other Backgrounds

Top Quark Processes

The dominant background contribution in the resolved and boosted $VH(H \to b\bar{b})$ regimes originates from the decays of top quarks, namely $t\bar{t}$ and single-top production. The single-top processes are divided into s-, t-, and Wt-channels, with the latter having the highest contribution to the single-top yields.

The systematic uncertainties considered for the modelling of the top quark background account for:

- differences between the predictions of the nominal and the alternative generators, which cover the effect of varying the matrix element and parton shower calculations
- variations in ISR and FSR contributions

Normalizations To minimize the sensitivity to interference effects, the $t\bar{t}$ and single-top Wt processes are floated together as a single Top process. In the resolved regimes, based on the flavor composition of the di-jet system, two categories are considered: Top(bb) and Top(others), where others include the bc, bl, cc, cl and ll di-jet compositions. These categories are assigned separate floating normalizations, which are constrained by the $VH(H \to b\bar{b})$ high ΔR CR and the top CR, respectively. Normalization uncertainties are derived for the single-top s- and t-channel contributions. In the boosted regime, the Top background is assigned a single floating normalization.

Acceptance Uncertainties In the resolved regimes, acceptance ratio uncertainties are derived to account for the different flavor components of the Top(others) category and to extrapolate between the SR and the high and low ΔR CRs. As the $t\bar{t}$ and Wt-channel processes are floated together, an additional acceptance uncertainty is derived to allow for a difference in the relative composition between the two processes. For the single-top t-channel contribution, acceptance uncertainties are considered for extrapolating between SR and high/low ΔR CRs, between different p_{T}^{V} regions, and between jet multiplicity regions. The single-top s-channel represents a small background contribution, so no acceptance uncertainties are considered for this process. In the boosted regime, acceptance uncertainties are derived between the SR and the top CR for the Top background. An additional uncertainty is derived to allow for a difference in composition between the $t\bar{t}$ and Wt-channel processes.

Shape Uncertainties The CARL reweighting method is used to derive shape uncertainties to account for differences in the distributions of kinematic variables between the nominal generator POWHEG+PYTHIA 8 and the alternative generators. A POWHEG+HERWIG 7 sample is used to derive uncertainties due to a different parton show model, while a MADGRAPH5_aMC@NLO+PYTHIA 8 is used for matrix element differences. Shape uncertainties due to differences in ISR and FSR are evaluated by using samples generated with the nominal generator POWHEG+HERWIG 8, but with different values for the renormalization scale, factorization scale, and PYTHIA 8 shower tune. These uncertainties are derived separately for the $t\bar{t}$, single-top Wt-channel, and single-top t-channel processes. An additional shape uncertainty is considered for the single-top Wt-channel process to estimate the effects of different treatments (DS and DR) of the overlap between $t\bar{t}$ and Wt events. The DS-DR uncertainty is derived as the difference between the nominal POWHEG+PYTHIA 8 DS sample and the alternative POWHEG+PYTHIA 8 DR sample. This uncertainty incorporates both normalization and shape effects in order to account for a large phase difference between the DS and DR samples.

Diboson

Diboson processes represent a small, but significant background in the analysis, as these events can have a similar signature to the VH signal (i.e. $VZ(Z \to b\bar{b}/c\bar{c})$) and can be used to validate the analysis strategy; however, the peak of the di-jet invariant mass distribution for VZ is located at a slightly lower mass than for the VH signal process. In the 1-lepton channel, the dominant diboson components consist of $W_{\mathrm{l}}Z_{\mathrm{h}}$ (where the W boson decays leptonically and the Z boson decays hadronically, relevant in the $VH(H \to b\bar{b})$ regime) and WW (where one W boson decays leptonically and the other decays hadronically, relevant in the $VH(H \to c\bar{c})$ regime). A small contribution can also arise from failed reconstruction of leptons, in the case of $W_{\mathrm{h}}Z_{\mathrm{l}}$ events where the W boson decays hadronically and the Z boson decay leptonically.

Based on the flavor composition of the di-jet system, these events can be categorized into a signal-like component ($WZ(Z \to b\bar{b}/c\bar{c})$) and a background component (consisting of WW, $W_{\mathrm{l}}Z_{\mathrm{h}}$ with Z decaying to light-flavor quarks, and $W_{\mathrm{h}}Z_{\mathrm{l}}$). The $WZ(Z \to b\bar{b}/c\bar{c})$ events are used as signal in the cross-check of the $VH(H \to b\bar{b}/c\bar{c})$ analysis strategy.

The sources of systematic uncertainties related to the modelling of the diboson background consist of:

- differences between the predictions of the nominal generator Sherpa 2.2.11 and the alternative generators (Powheg+Pythia 8 and Sherpa 2.2.1)
- variations in the QCD renormalization and factorization scales μ_R and μ_F
- the effects of alternative electroweak corrections
- variations in the PDF set used and in the value of α_S

Normalization Uncertainties Normalization uncertainties are derived separately for the WZ, WW, and $ggVV$ diboson components and also separately in the resolved and boosted regimes.

Acceptance Uncertainties Acceptance ratio uncertainties are derived for the signal-like WZ component and for the background-like diboson component, separately in the resolved and boosted regimes. The acceptance uncertainties are derived between jet multiplicity categories (2-jet to 3-jet), between p_{T}^{V} regions, and between the SR and the high/low ΔR CRs. For the WZ component only, acceptance uncertainties between different jet multiplicity $\times$ p_{T}^{V} regions are derived to account for yield migration across these regions due to variations in the QCD scales.

Shape Uncertainties Shape uncertainties that account for differences between the nominal and alternative generators are derived using the CARL reweighting method. Alternative samples generated with Powheg+Pythia 8 are used to account for shape uncertainties due to differences in the matrix element and parton shower calculations, while Sherpa 2.2.1 alternative samples are used to account for uncertainties in the fragmentation function. Additionally, uncertainties are derived to account for shape differences due to variations in the QCD scales (μ_R, μ_F) and the effects of the electroweak correction schemes.

QCD Multi-jet

QCD multi-jet events originate primarily from "fake" leptons: hadronic jets misidentified as electrons or photon conversions and non-prompt electrons and muons from heavy-flavor hadron decays. Such leptons must be distinguished from leptons targeted by the $VH(H \to b\bar{b}/c\bar{c})$ analysis, which originate from decays of the W boson. In the 1-lepton channel analysis, the multi-jet background represents a small, but non-negligible contribution, particularly in the low p_{T}^{V} regions. To reduce the multi-jet contamination, several isolation criteria are applied in the electron and muon sub-channels. Additionally, a $m_{\mathrm{T}}^{W} > 20$ GeV cut is used in the 75 GeV $< p_{\mathrm{T}}^{V} <$ 150 GeV region, while a $E_{\mathrm{T}}^{\mathrm{miss}} > 30$ GeV cut is used in all p_{T}^{V} regions to further minimize the multi-jet background. For the remaining multi-jet contribution, as it is difficult to accurately model using MC simulations[14], a data-driven approach is used instead.

The QCD multi-jet background is considered only in the resolved regimes of the analysis, as the contribution in the boosted regime was found to be negligible. The background estimation is performed using a dedicated control region enriched in QCD events, from which a multi-jet template for the shape and normalization of the background is obtained as the difference between the data and the non multi-jet backgrounds obtained from simulation. The distribution of the transverse mass of the W boson candidate, m_{T}^{W}, is used to validate the template extraction procedure, as this variable was found to provide the best discrimination between the multi-jet and the other backgrounds. The multi-jet estimation is performed separately in the electron and muon sub-channels, as well as in different p_{T}^{V} and jet multiplicity regions. Systematic uncertainties that affect the normalization and the shape of the distribution for the multi-jet background are taken into account in the analysis. Shape related uncertainties are obtained by varying the selection for the multi-jet control region and by applying normalization factors to the MC simulated backgrounds before subtraction. These sources are also considered for deriving uncertainties on the normalization. In addition, normalization uncertainties are also derived by using an alternative variable ($\Delta\phi(\ell, E_{\mathrm{T}}^{\mathrm{miss}})$) to perform the template fit, including $E_{\mathrm{T}}^{\mathrm{miss}} < 30$ GeV events in the template fit, and including $m_{\mathrm{T}}^{W} < 20$ GeV events in the template fit.

5.7 Statistical Analysis

A statistical fitting procedure is used to extract the values of parameters of interest relevant to the $VH(H \to b\bar{b}/c\bar{c})$ process. For the analysis presented in this chapter, the parameters of interest consist of the signal strengths for the $WH(H \to b\bar{b})$ and $WH(H \to c\bar{c})$ processes[15]. The signal strength is defined as the ratio between the observed product of the

[14] This is due to the practical limitations of simulating enough events to achieve reasonable statistics in the analysis phase space, as only a small fraction of "fake" leptons are expected to pass the lepton isolation requirements. Additionally, the simulation of "fake" lepton is also known to not be particularly accurate.

[15] In the analysis cross-check measurement, the signal strengths for the diboson processes are extracted instead.

Higgs production cross section and branching ratio and the value predicted by the SM:

$$\mu_{WH(H\to q\bar{q})} = \frac{\sigma^{\text{obs}}_{WH} \times B^{\text{obs}}_{H\to q\bar{q}}}{\sigma^{\text{SM}}_{WH} \times B^{\text{SM}}_{H\to q\bar{q}}}, \text{ where } q \text{ is a } b\text{- or } c\text{-quark.} \tag{5.4}$$

An alternative parametrization is also considered, in which the signal strengths are expressed in terms of modifiers for the Higgs Yukawa couplings to b- and c-quarks. In both parametrizations (i.e. signal strengths μ and coupling modifiers κ or their ratio), a binned likelihood fit is performed to the observed distribution of the VH BDT output score and the parameters of interest and their confidence intervals are simultaneously estimated using a profile likelihood ratio test.

5.7.1 Likelihood Function Definition

The set of parameters that best describe the observed data are determined by maximizing a likelihood function $\mathcal{L}$, which encodes information about the observed data, the theoretical predictions, and the systematic uncertainties. At the LHC, the likelihood function is generally expressed as the product of three distinct components [235–237] and is generally referred to as the profile likelihood[16]:

$$\mathcal{L} = \mathcal{L}_{\text{Pois}} \times \mathcal{L}_{\text{Syst}} \times \mathcal{L}_{\text{Bkg Stat}} \tag{5.5}$$

Working under the assumption of a counting experiment, the first component of the likelihood consists of Poissonian probability terms built using the observed and expected event yields in all the (statistically independent) bins:

$$\mathcal{L}_{\text{Pois}}(\mu) = \prod_{i\in\text{bins}} \text{Pois}(N_i|\mu s_i + b_i) = \prod_{i\in\text{bins}} \frac{(\mu s_i + b_i)^{N_i}}{N_i!} e^{-(\mu s_i + b_i)}. \tag{5.6}$$

Here, N_i represents the number of observed events in bin i, while s_i and b_i are the expected counts for signal and background events in bin i as predicted by simulation. The likelihood is a function of the parameter of interest μ, which represents the signal strength for the target process[17].

The second component of the likelihood accounts for systematic uncertainties, such as those from the physics objects reconstruction and calibration procedures or theoretical uncertainties on the MC predictions. Systematic uncertainties are included in the fit as nuisance parameters (NPs) $\vec{\theta}$, which provide additional degrees of freedom to modify the expected yields, $s_i(\vec{\theta})$ and $b_i(\vec{\theta})$. The central values and uncertainties for the NPs are determined beforehand, as described in Sections 5.5 and 5.6. The NPs are implemented into the likelihood

[16]Note that this is different from the standard meaning of the term *profiling* used within the statistics community, which refers to a specific technique for marginalizing a probability distribution function.

[17]Multiple parameters of interest are usually denoted by writing the signal strength parameter in vector form $\vec{\mu}$.

using Gaussian distributions, where the NPs have been rescaled to have mean zero and unit variance:

$$\mathcal{L}_{\text{Syst}}(\vec{\theta}) = \prod_{\theta \in \vec{\theta}} \frac{1}{\sqrt{2\pi}} e^{-\theta^2/2}. \tag{5.7}$$

Some NPs are implemented without any prior knowledge of their values and are referred to as freely floating parameters. They correspond to the normalizations for the major backgrounds and are constrained exclusively from the observed data. The floating NPs are assigned an initial (pre-fit) central value of 1.

A joint measurement of an NP θ can be obtained by maximizing the likelihood $\mathcal{L}_{\text{Pois}} \times \mathcal{L}_{\text{Syst}}$ with respect to θ. If the measurement is particularly sensitive to that NP, then the data $\mathcal{L}_{\text{Pois}}$ can provide additional constraining power. Hence, the statistical fit can modify the values of the NPs. The post-fit change in the central value of an NP is referred to as the parameter pull and a decrease in the variance is known as the constraint, which reflects the certainty with which the parameter value is known.

The last likelihood component accounts for uncertainties in the expected signal and background counts due to the finite size of the MC simulation samples. The statistical uncertainties are introduced in the fit as γ parameters, which can modify the expected number of background events in each bin: $\gamma_i b_i(\vec{\theta})$. The γ parameters are implemented into the likelihood using Gaussian distributions:

$$\mathcal{L}_{\text{Bkg Stat}}(\vec{\gamma}) = \prod_{i \in \text{bins}} \text{Gauss}(\beta_i | \gamma_i \beta_i, \sqrt{\gamma_i \beta_i}), \text{ where } \beta_i = 1/\sigma_{\text{rel}}^2. \tag{5.8}$$

Here, σ_{rel} represents the relative statistical uncertainty on the expected total background count and is used to compute the parameter β_i, which provides an approximation for the total number of background events.

Putting together Eqns. 5.6, 5.7, and 5.8, the final expression for the likelihood can be written as:

$$\mathcal{L}(\vec{\mu}, \vec{\theta}, \vec{\gamma}) = \prod_{i \in \text{bins}} \text{Pois}(N_i | \vec{\mu} s_i(\vec{\theta}) + \gamma_i b_i(\vec{\theta})) \times \prod_{\theta \in \vec{\theta}} \frac{1}{\sqrt{2\pi}} e^{-\theta^2/2} \times \prod_{i \in \text{bins}} \text{Gauss}(\beta_i | \gamma_i \beta_i, \sqrt{\gamma_i \beta_i}). \tag{5.9}$$

The best-fit parameters of interest are determined by maximizing[18] the likelihood of Eqn. 5.9 with respect to all the parameters $\vec{\mu}, \vec{\theta}, \vec{\gamma}$. The procedure is performed numerically using the `MINUIT` package [238], which implements a gradient-descent based method.

The likelihood function is used to test different hypotheses for the value of $\vec{\mu}$ by constructing a profile likelihood ratio [235]:

$$\lambda(\vec{\mu}) = \frac{\mathcal{L}(\vec{\mu}, \hat{\hat{\vec{\theta}}}, \hat{\hat{\vec{\gamma}}})}{\mathcal{L}(\hat{\vec{\mu}}, \hat{\vec{\theta}}, \hat{\vec{\gamma}})}, \tag{5.10}$$

[18] Maximizing the likelihood function $\mathcal{L}$ is equivalent to minimizing $-\ln \mathcal{L}$. The latter procedure is what is technically performed to determine the best-fit parameter values.

where $\hat{\vec{\mu}}, \hat{\vec{\theta}}, \hat{\vec{\gamma}}$ represent the parameter values that maximize the likelihood in general (unconditional), while $\hat{\hat{\vec{\theta}}}, \hat{\hat{\vec{\gamma}}}$ represent the values that maximize the likelihood for a fixed value of the parameters of interest $\vec{\mu}$ (conditional). The test statistic $q_{\vec{\mu}}$ is then constructed from the profile likelihood ratio as:

$$q_{\vec{\mu}} = \begin{cases} -2\ln\lambda(\vec{\mu}) & \hat{\vec{\mu}} \geq \vec{\mu} \\ 2\ln\lambda(\vec{\mu}) & \hat{\vec{\mu}} < \vec{\mu} \end{cases} \tag{5.11}$$

In particular, an important hypothesis to test is the background-only (i.e. no signal) hypothesis, corresponding to $\vec{\mu} = 0$. The compatibility between the observed data and the background-only hypothesis is quantified through the p-value:

$$p_0 = \int_{q_{0,\mathrm{obs}}}^{\infty} f(q_0|0) dq_0, \tag{5.12}$$

where $q_{0,\mathrm{obs}}$ is the value of q_0 observed in data and $f(q_0|0)$ represents the probability density function[19] of the test statistic under the assumption that $\vec{\mu} = 0$. The p-value p_0 can be understood as the probability of observing data incompatible with the hypothesis $\vec{\mu} = 0$, assuming that the background-only hypothesis is true.

The p-value is often expressed in terms of the equivalent number of Gaussian standard deviations (also known as the significance) Z:

$$Z = \Phi^{-1}(1 - p_0), \tag{5.13}$$

where Φ^{-1} represents the inverse cumulative distribution function of a standard Gaussian. Two important significance values for the particle physics community are those of $Z = 3$, the threshold needed to claim evidence for a particular process, and $Z = 5$, regarded as the standard for rejecting the background-only hypothesis and claiming the discovery of a process[20].

The significance is an easy to understand metric for processes where a significant excess above the background-only prediction is expected, as is the case for the $VH(H \to b\bar{b})$ and diboson processes. For the $VH(H \to c\bar{c})$ process, where the significance is expected to be small, the upper limit at the 95% confidence level (CL) on the signal strength is used as the figure of merit. The 95% CL upper limit is computed following a modified frequentist $\mathrm{CL_S}$ method [235, 236], which uses the following test statistic:

$$q = -2\ln\frac{\mathcal{L}_{S+B}}{\mathcal{L}_B} = -2\ln\frac{\mathcal{L}(\mu = 1, \hat{\hat{\vec{\theta}}}(1), \hat{\hat{\vec{\gamma}}}(1))}{\mathcal{L}(\mu = 0, \hat{\hat{\vec{\theta}}}(0), \hat{\hat{\vec{\gamma}}}(0))}, \tag{5.14}$$

where $\mathcal{L}_{S+B}$ represents the likelihood for the nominal signal+background model (i.e. signal strength $\mu = 1$) and $\mathcal{L}_B$ is the likelihood for the background-only hypothesis $\mu = 0$. The

[19]In the large sample limit (asymptotic approximation), the test statistic $q_{\vec{\mu}}$ follows a χ^2 distribution [235].
[20]A significance of $Z = 3$ corresponds to a p-value of $p_0 = 0.003$, while $Z = 5$ corresponds to $p_0 = 3 \times 10^{-7}$.

95% CL upper limit is obtained by requiring that the $\mathrm{CL_S}$ ratio[21] (derived from the test statistic q) be 5% with respect to the observed data. This implies that, by construction, there is (at least) a 95% probability that the true value of the signal strength μ is smaller than the upper limit.

Before performing the fit on the observed data, the performance and expected sensitivity of the analysis can be evaluated by performing the fit on an Asimov dataset. The Asimov dataset [235] is constructed by adding the simulated signal and background predictions for specific values of the parameters of interests and the NPs and does not include statistical fluctuations. Two different kinds of Asimov datasets are used to study the performance of the fit model. The pre-fit Asimov dataset represents the predictions of the theory and is constructed by setting the NPs to their initial central values (i.e. before the fit to the data). It is used to study the constraints and correlations between the nuisance parameters. The post-fit Asimov dataset is constructed by setting the NPs to their best-fit values from a fit to the observed data and is used to determine the expected results (such as the significance and upper limit).

5.7.2 Fit Model

The likelihood fit model for the $VH(H \to b\bar{b}/c\bar{c})$ 1-lepton channel analysis presented in this chapter is constructed by combining the observed data, the MC templates for the signal and background processes, and the systematic uncertainties. The fit model is implemented using the `WorkSpaceMaker` statistical framework, which uses the `HistFactory` [239] tool together with the `RooFit` [240] and `RooStats` [241] software packages.

The fit model is constructed with two parameters of interest, the signal strengths for the $WH(H \to b\bar{b})$ and $WH(H \to c\bar{c})$ processes[22]. The fit inputs consist of one-dimensional histograms in the 20 signal and 42 control regions considered in the 1-lepton channel, which were previously described in Section 5.3.4. Depending on the analysis region, the histograms are constructed using the following variables:

- The VH BDT output score, used in the signal regions of the analysis.
- The invariant mass of the Higgs candidate (i.e. the mass of small-R di-jet system m_{jj} in the resolved regimes and the mass of the large-R jet m_J in the boosted regime), used in the high ΔR and top control regions.
- The `mvaCRLow` BDT output score, used in the low ΔR control region of the resolved $VH(H \to b\bar{b})$ regime.

[21] $\mathrm{CL_S} = \frac{\mathrm{CL_{S+B}}}{\mathrm{CL_B}} = \frac{p_{\mathrm{S+B}}}{1-p_{\mathrm{B}}}$, where $p_{\mathrm{S+B}}$ and p_{B} are the p-values for the signal+background and background-only hypotheses, respectively.

[22] In the diboson cross-check measurement, the parameters of interest are the two signal strengths for the $WZ(Z \to b\bar{b})$ and $WZ(Z \to c\bar{c})$ processes.

- The transverse momentum of the vector boson, used in the V + light and high ΔR control regions.

Depending on the variable used, the range and binning of the histograms are chosen to maximize signal sensitivity and limit the amount of MC statistical uncertainty in each bin. Events that fall outside of the defined ranges are included in the first and/or last bin of the histograms.

The systematic uncertainties are implemented as nuisance parameters and consist of:

- Experimental uncertainties related to detector performance, as described in Section 5.5.
- Floating normalization parameters for the $W+$jets and top quark backgrounds.
- Modelling uncertainties for the signal and background processes (normalization uncertainties, acceptance ratio uncertainties, and shape uncertainties), as described in Section 5.6.
- Uncertainties due to the limited statistics of the simulated samples.

The fit model includes a dedicated treatment for some systematic uncertainties, to avoid spurious effects in the fit. Special care is also taken to not bias the analysis by prematurely looking at the data in regions expected to contain the signal. These procedures are performed following ATLAS standard procedures [242] and are briefly described in the following paragraphs.

Symmetrization Some uncertainties are only available as a one-sided variation, as in the case of the large-R jet resolution uncertainty or the shape uncertainties derived with the CARL reweighting technique. In such cases, the distribution for the available variation is symmetrized around the nominal distribution to obtain the other variation (for example, a $+1\sigma$ variation is symmetrized to obtain the -1σ variation).

Smoothing Large statistical fluctuations can produce irregular variations in the shapes of the distributions, which in turn can lead to unwanted effects such as over constraints in the fit. To minimize this effect, an iterative algorithm is used to smooth out the distributions by merging bins until the statistical uncertainty is less than 5%, under the assumption that variations between neighboring bins should be monotonic and correlated. Comparisons are performed between the original (unsmoothed) and the smoothed distributions to ensure that the procedure does not introduce systematic biases in the shapes of the distributions.

Pruning Some uncertainties considered in the analysis have a negligible effect on the distributions used in the fit. In order to improve the convergence and running time of the fit, a pruning procedure is used to remove the negligible NPs from the likelihood. Normalization uncertainties are removed if their effect is less than 0.5%. Shape uncertainties are removed if none of the variations are larger than 0.5%. Background processes that have a very small contribution to the total background (up to $\sim 2\%$, depending on the region) are also subject to additional pruning steps. Diagnostic plots are generated and checked to ensure that the pruning is, in fact, only applied to small uncertainties and that the expected performance of the fit is not artificially improved by this procedure.

Blinding A blinding procedure is used to prevent bias in the analysis. The data in signal-rich bins is purposefully not looked at during the development of the fit model. Instead, the signal strengths are fixed to $\mu = 1$ and studies are performed to understand the effect of systematic uncertainties by fitting the background contributions to the data[23] i.e. using the pre-fit and post-fit Asimov datasets. Figure 5.18 provides an example of pre-fit and post-fit plots of the BDT output score distribution in one of the categories of the $VH(H \to c\bar{c})$ regime. The blinding of the data is removed only in the final step of the analysis, when the measurement of the observed signal strengths is performed.

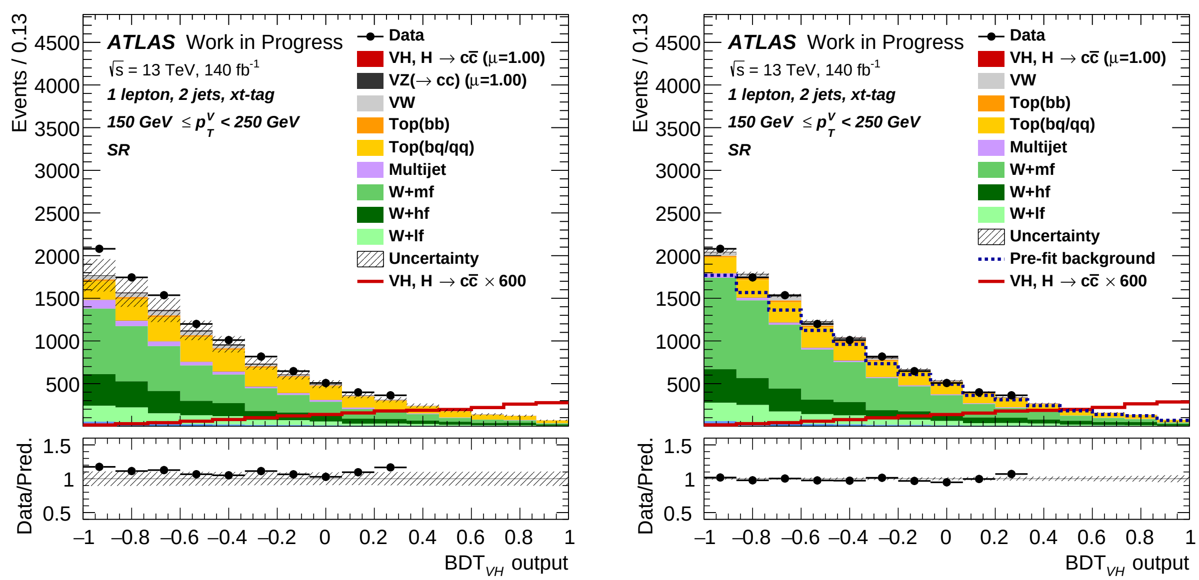

Figure 5.18: Pre-fit (left) and post-fit (right) blinded distributions of the BDT discriminant in one of the categories of the $VH(H \to c\bar{c})$ regime. The bins are blinded starting from the right (i.e. high BDT output score) and cumulatively contain 60% of the signal.

[23] The fits are performed using the data in the entire distribution range, including the blinded bins. However, the data counts in the blinded bins are not shown on the pre-fit or post-fit plots.

5.7.3 The κ Framework

The $VH(H \to b\bar{b}/c\bar{c})$ analysis has enough sensitivity to also directly constrain the coupling of the Higgs boson to the bottom and charm quarks, improving on constraints obtained by the previous ATLAS $VH(H \to c\bar{c})$ analysis [194] and complementing those from measurements of the Higgs boson p_{T} spectrum [243, 244]. This is achieved by interpreting the signal strength results within the κ framework [79, 225], which introduces a scenario in which the Yukawa couplings are modified by the Higgs coupling modifiers κ_i via:

$$y_i \to \kappa_i \times y_i, \tag{5.15}$$

where κ_i is a real-valued number. The modifications to the coupling strengths affect the leading order contributions to the Higgs production and decay processes. While deviations of the κ coupling modifiers from unity could potentially point to BSM, the κ framework is limited by the fact that it cannot provide information about the origin of the new physics. A more general approach would consist of interpreting the measurements within an effective field theory (EFT), in which the SM Lagrangian is extended with specific higher-dimensional operators that encode the low energy limit of the new physics [245–247]. The EFT interpretation will be performed by the general $VH(H \to b\bar{b}/c\bar{c})$ analysis, to be presented in a future ATLAS publication, and will not be considered further within the context of this thesis.

For the $WH(H \to b\bar{b}/c\bar{c})$ process, the coupling modifiers affect the Higgs production in association with the W boson and the Higgs decay to the heavy-flavor quarks. The effect on the measurement of the cross section times branching ratio can be expressed as follows:

$$\sigma_{WH} \times B_{H\to q\bar{q}} = (\sigma_{WH}^{\mathrm{SM}} \times \kappa_W^2) \times \left(B_{H\to q\bar{q}}^{\mathrm{SM}} \times \frac{\kappa_q^2}{\kappa_H^2} \right), \text{ where } q \text{ is a } b\text{- or } c\text{-quark.} \tag{5.16}$$

Note that in Eqn. 5.16 the branching ratio also includes the modification to the total Higgs width decay, parametrized by the κ_H modifier. This modifier contains the contributions from the modifiers for all the SM branching ratios[24]:

$$\kappa_H^2 \sim 0.215\kappa_W^2 + 0.581\kappa_b^2 + 0.029\kappa_c^2 + \ldots \tag{5.17}$$

Eqn. 5.16 can be solved to obtain a parametrization for the signal strengths of the $WH(H \to b\bar{b})$ and $WH(H \to c\bar{c})$ processes in terms of the κ modifiers:

$$\mu_{WH(H\to q\bar{q})} = \frac{\sigma_{WH} \times B_{H\to q\bar{q}}}{\sigma_{WH}^{\mathrm{SM}} \times B_{H\to q\bar{q}}^{\mathrm{SM}}} = \frac{\kappa_W^2 \kappa_q^2}{\kappa_H^2}, \text{ where } q \text{ is a } b\text{- or } c\text{-quark.} \tag{5.18}$$

For the interpretation performed within this analysis, several simplifying assumptions are made. First, only modifications to the Higgs decay into b- or c-quarks are considered, i.e.

[24] The BSM contributions to the Higgs width can manifest as values of κ_i different than 1 or as Higgs decays to invisible or undetected BSM particles. The latter contributions can also be included in the expression for the κ_H modifier.

the couplings of the Higgs boson to the other particles are assumed as predicted by the SM ($\kappa_i = 1$ for $i \neq b, c$). Secondly, no additional BSM contributions to the total Higgs width are considered. Under these assumptions, the parametrizations for the $WH(H \to b\bar{b})$ and $WH(H \to c\bar{c})$ signal strengths reduce to:

$$\mu_{WH(H\to b\bar{b})} = \frac{\kappa_b^2}{1 - B^{\text{SM}}_{H\to b\bar{b}} - B^{\text{SM}}_{H\to c\bar{c}} + B^{\text{SM}}_{H\to b\bar{b}} \times \kappa_b^2 + B^{\text{SM}}_{H\to c\bar{c}} \times \kappa_c^2}, \tag{5.19}$$

and

$$\mu_{WH(H\to c\bar{c})} = \frac{\kappa_c^2}{1 - B^{\text{SM}}_{H\to b\bar{b}} - B^{\text{SM}}_{H\to c\bar{c}} + B^{\text{SM}}_{H\to b\bar{b}} \times \kappa_b^2 + B^{\text{SM}}_{H\to c\bar{c}} \times \kappa_c^2}. \tag{5.20}$$

Using Eqns. 5.19 and 5.20, a fit can be performed to extract the best-fit values for the κ_b and κ_c parameters, using the same setup as for the fit to the signal strengths.

In addition, it is possible to perform the interpretation in terms of the ratio of the two coupling modifiers, which is related to the signal strengths via:

$$\frac{\mu_{WH(H\to c\bar{c})}}{\mu_{WH(H\to b\bar{b})}} = \frac{\kappa_c^2}{\kappa_b^2}. \tag{5.21}$$

By taking the ratio, the expression for the Higgs width modifier in the denominators in Eqns. 5.19 and 5.20 cancels out. Thus, such a measurement can probe the interaction between the Higgs boson and the b- and c-quarks independently of any assumptions on the BSM physics. With this setup, a fit can be performed to constrain the value of the κ_c/κ_b ratio in a model-independent way. An additional advantage of performing this fit is that many systematic uncertainties common between $VH(H \to b\bar{b})$ and $VH(H \to c\bar{c})$ should cancel out when taking the ratio, leading to a smaller uncertainty on κ_c/κ_b.

5.8 Results

5.8.1 Diboson Validation Measurement

A cross-check of the analysis strategy is performed by extracting the signal strengths for the diboson processes $WZ(Z \to b\bar{b})$ and $WZ(Z \to c\bar{c})$. The setup for the likelihood fit is similar to the one used to measure the $WH(H \to b\bar{b})$ and $WH(H \to c\bar{c})$ signal strengths, as described in Section 5.7. However, for the diboson measurement, the fit discriminant in the signal regions consists of the output score of the VZ BDT, which was trained with the $VZ(Z \to b\bar{b})$ and $VZ(Z \to c\bar{c})$ processes as the signal.

The best-fit signal strengths for the $WZ(Z \to b\bar{b})$ and $WZ(Z \to c\bar{c})$ processes are found to be:

$$\mu_{WZ(Z\to b\bar{b})} = 0.92 \pm 0.21 = 0.92 \pm 0.08 \text{ (stat.)} \pm 0.19 \text{ (syst.)} \tag{5.22}$$

$$\mu_{WZ(Z\to c\bar{c})} = 1.06 \pm 0.40 = 1.06 \pm 0.21 \text{ (stat.)} \pm 0.34 \text{ (syst.)}. \tag{5.23}$$

Each of the measured signal strengths are compatible with the SM expectation of unity within the statistical uncertainties. The probability of compatibility with the SM, that is of both signal strengths being equal to 1, is 89%. The correlation between the $WZ(Z \to b\bar{b})$ and $WZ(Z \to c\bar{c})$ signal strengths is estimated to be 31%. The correlation coefficients between the WZ signal strengths and the floating normalizations for the $W+$jets and top quark backgrounds are shown in Figures 5.19 and 5.20. The $WZ(Z \to b\bar{b})$ signal strength is found to be generally anti-correlated with the $W+$jets floating normalizations and does not show much correlation with the Top floating normalizations. The $WZ(Z \to c\bar{c})$ signal strength is found to be anti-correlated with the $W + lf$ normalizations and correlated with the $W + mf$ and Top normalizations. High correlation coefficients are found between the normalizations in different jet multiplicities and p_{T}^{V} regions between the different components of the $W+$jets and top backgrounds, respectively. As expected, the correlation matrices are found to be similar between the unconditional fit to data and an unconditional Asimov fit.

Compared to the background-only hypothesis, the excess observed in the data for the $WZ(Z \to b\bar{b})$ signal corresponds to a significance of 6.8σ, compared to an expectation of 7.4σ. For the $WZ(Z \to c\bar{c})$ signal, the observed data excess corresponds to a significance of 3.2σ, compared to an expectation of 3.0σ. In particular, the $WZ(Z \to c\bar{c})$ result represents first evidence for diboson production with $Z \to c\bar{c}$ decays measured with the ATLAS detector. It also represents an improvement over the findings of the previous ATLAS $VH(H \to c\bar{c})$ analysis [194], which measured the $VZ(Z \to c\bar{c})$ process with an observed (expected) significance of 2.6σ (2.2σ), obtained from a combined fit using data in all three lepton channels.

The values of the floating normalization parameters for the $W+$jets and top quark backgrounds are shown in Table 5.19. The normalizations for the $W + hf$ component are found to be higher than the predictions of the nominal simulated samples. In the resolved regime, the normalizations are higher in the 3-jet regions, where they are pulled $\sim 4\sigma$ away from the pre-fit value of 1, compared to the 2-jet regions, which are pulled by $\lesssim 1\sigma$. A trend with p_{T}^{V} is also seen, with the deviations being largest for the normalizations in the boosted regime.

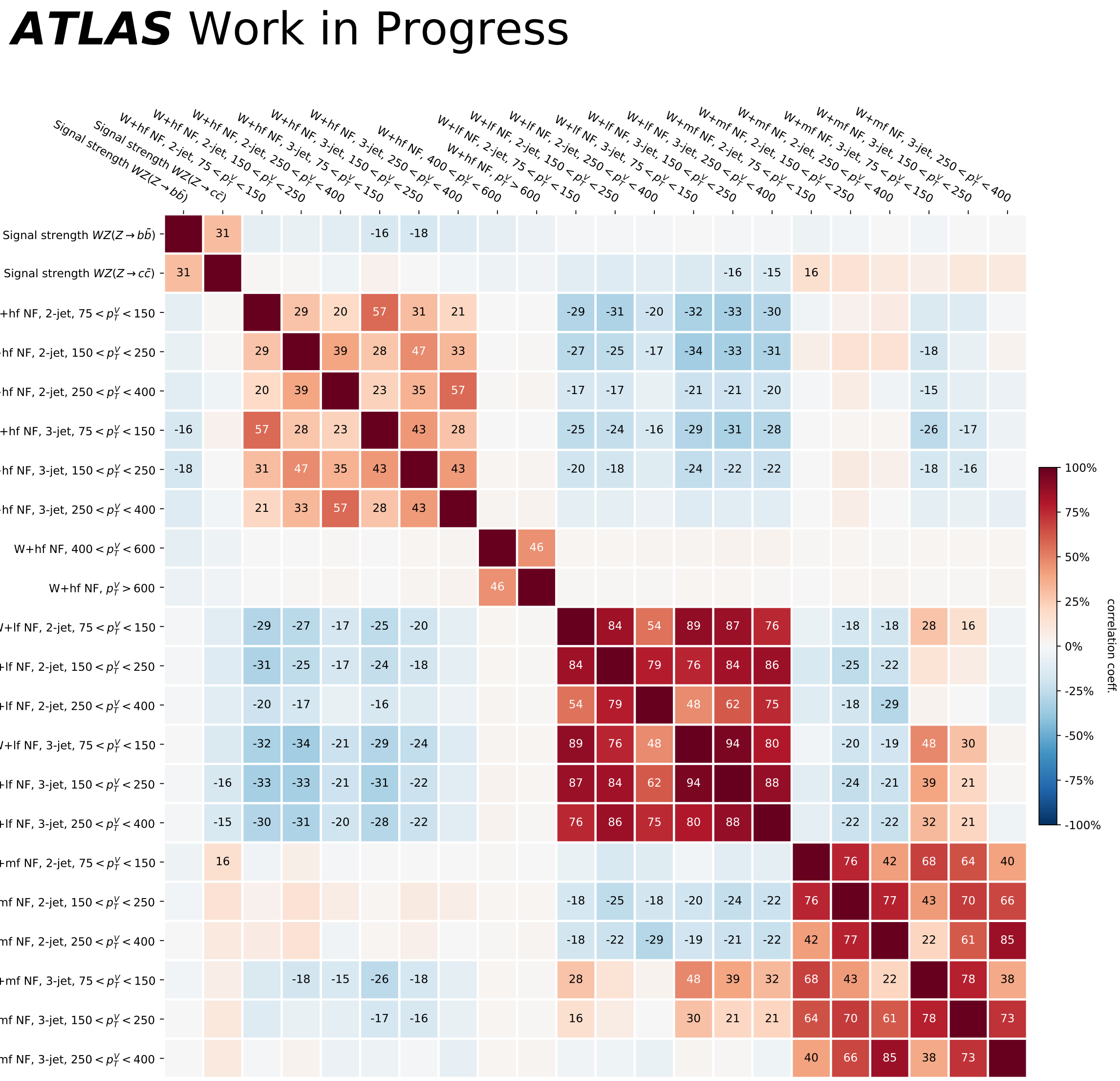

Figure 5.19: Matrix of correlation coefficients between the $WZ(Z \to b\bar{b})$ and $WZ(Z \to c\bar{c})$ signal strengths and the floating normalizations for the $W+$jets background.

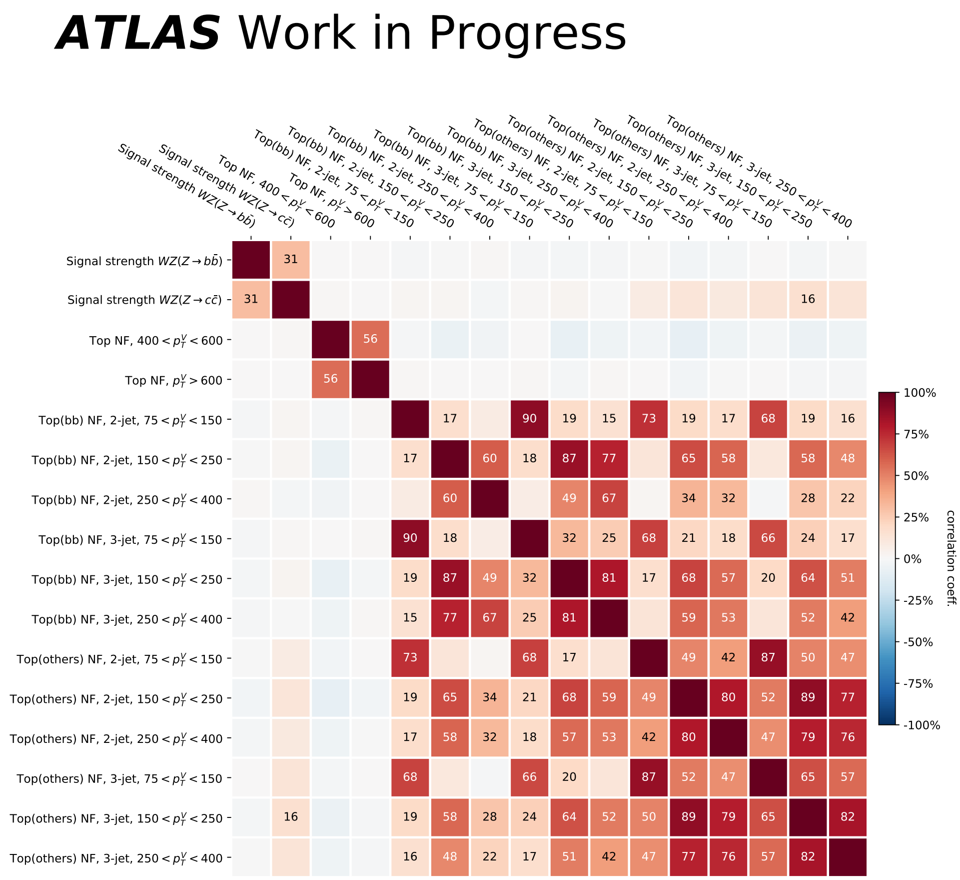

Figure 5.20: Matrix of correlation coefficients between the $WZ(Z \to b\bar{b})$ and $WZ(Z \to c\bar{c})$ signal strengths and the floating normalizations for the top quark background.

A decreasing (increasing) trend in the central value of the normalization with increasing p_T^V can also be seen in the 2-jet (3-jet) regions. In the boosted regime, the normalizations are pulled up by $\sim 4\sigma$ from the pre-fit value. The $W + mf$ normalizations are also higher than the simulation predictions in all regions, being pulled up by $\sim 5\sigma$. The normalizations for $W + lf$ are found to consistent with the pre-fit value within approximately 1σ. A slight increasing trend in the central values of the normalizations with p_T^V is seen for the $W + mf$ and $W + lf$ components. The trends in the floating normalizations with p_T^V can be traced back to the mismodelling of the nominal $W+$jets simulated p_T spectrum [210].

For the top quark backgrounds, the normalizations tend to be lower by up to $\sim 4\sigma$ than the predictions of the nominal $t\bar{t}$ and single-top Wt-channel simulated samples. The normalization are generally consistent, within one standard deviation, between the Top(bb) and Top(others) components and the Top component in the $400 < p_T^V < 600$ GeV region in the boosted regime. The largest deviation in the central value of the NPs is found in the $p_{\mathrm{T}}^{V} > 600$ GeV region of the boosted regime.

Post-fit distributions of the VZ BDT output score are shown in Figure 5.21 for the resolved $VH(H \to b\bar{b})$ and $VH(H \to c\bar{c})$ regimes and in Figure 5.22 for the boosted $VH(H \to b\bar{b})$ regime. In these plots, the stacked filled histograms represent the background predictions, scaled according to the NP values extracted from the likelihood fit. Similarly, the WZ signals are scaled according to the measured signal strengths and are shown as filled, dark grey histograms stacked on top of the background contributions. The unstacked, dark grey line shows the WZ signal prediction, scaled by an arbitrary factor to emphasize the expected signal shape. The total pre-fit background is shown with the dashed blue histogram. The ratio between the data and the post-fit combined signal and background prediction is shown in the lower panel of the plots. Generally, good agreement is found between the measured data and the post-fit prediction in all regions.

Nuisance Parameters Ranking

Almost 1000 nuisance parameters (including the γ parameters) are implemented in the likelihood fit model. However, not all of the parameters have the same impact on the signal strength uncertainty. To determine the largest contributors to the uncertainty, a ranking of the individual NPs is generated as follows. For each NP θ, a fit is performed where the value of the NP is changed by its uncertainties in the upward and downward directions, i.e. $\hat{\theta} \pm \sigma_{\hat{\theta}}$, one time using the pre-fit uncertainties and the other using the post-fit uncertainties. At the two points $\hat{\theta} \pm \sigma_{\hat{\theta}}$, the corresponding change in the value of the fitted signal strength, $\Delta\hat{\mu}$, is determined and used to rank the NPs in decreasing order of their impact.

Figure 5.23 shows the ranking of the nuisance parameters for the $WZ(Z \to b\bar{b})$ and $WZ(Z \to c\bar{c})$ signal strengths. For the $WZ(Z \to b\bar{b})$ signal strength, the NP with the largest impact is related to the uncertainty on the inclusive WZ normalization in the resolved regime. The $WZ(Z \to c\bar{c})$ signal strength is also highly ranked due to its correlation with the $WZ(Z \to b\bar{b})$ signal strength. Other highly ranked NPs consist of extrapolation uncertainties between the signal and low ΔR control region for the $W + hf$ component, the WZ normalization in the boosted regime, floating normalizations for the $W+hf$ component, and shape uncertainties for the $W+$jets, WZ, and single-top Wt-channel processes.

For the $WZ(Z \to c\bar{c})$ signal strength, the highest-ranked nuisance parameter is also the uncertainty on the inclusive WZ normalization in the resolved regime. As expected, the $WZ(Z \to b\bar{b})$ signal strength is also highly ranked due to its correlation with the $WZ(Z \to c\bar{c})$ signal strength. Other highly ranked uncertainties include uncertainties on the flavor tagging of c-jets, a simulation statistics nuisance parameter for a particular bin of the VZ BDT output distribution, floating normalizations for the $W + mf$ and $W + lf$ components of the $W+$jets background and for the top quark background, extrapolation uncertainties between the SR and the high ΔR CR for the $W + hf$ component, and shape uncertainties for the WZ process.

Background	p_{T}^{V} region	Jet multiplicity	Value
$W + hf$	$75 < p_{\mathrm{T}}^{V} < 150$ GeV	2-jet	1.06 ± 0.07
		3-jet	1.28 ± 0.07
	$150 < p_{\mathrm{T}}^{V} < 250$ GeV	2-jet	1.02 ± 0.06
		3-jet	1.29 ± 0.07
	$250 < p_{\mathrm{T}}^{V} < 400$ GeV	2-jet	1.00 ± 0.09
		3-jet	1.50 ± 0.10
	$400 < p_{\mathrm{T}}^{V} < 600$ GeV		1.75 ± 0.19
	$p_{\mathrm{T}}^{V} > 600$ GeV		2.17 ± 0.26
$W + mf$	$75 < p_{\mathrm{T}}^{V} < 150$ GeV	2-jet	1.14 ± 0.04
		3-jet	1.12 ± 0.05
	$150 < p_{\mathrm{T}}^{V} < 250$ GeV	2-jet	1.28 ± 0.05
		3-jet	1.28 ± 0.05
	$250 < p_{\mathrm{T}}^{V} < 400$ GeV	2-jet	1.30 ± 0.08
		3-jet	1.28 ± 0.08
$W + lf$	$75 < p_{\mathrm{T}}^{V} < 150$ GeV	2-jet	0.99 ± 0.05
		3-jet	1.01 ± 0.07
	$150 < p_{\mathrm{T}}^{V} < 250$ GeV	2-jet	1.06 ± 0.04
		3-jet	1.04 ± 0.06
	$250 < p_{\mathrm{T}}^{V} < 400$ GeV	2-jet	1.08 ± 0.04
		3-jet	1.11 ± 0.05
Top(bb)	$75 < p_{\mathrm{T}}^{V} < 150$ GeV	2-jet	0.85 ± 0.04
		3-jet	0.89 ± 0.03
	$150 < p_{\mathrm{T}}^{V} < 250$ GeV	2-jet	0.94 ± 0.06
		3-jet	0.92 ± 0.03
	$250 < p_{\mathrm{T}}^{V} < 400$ GeV	2-jet	0.87 ± 0.09
		3-jet	0.86 ± 0.04
Top(others)	$75 < p_{\mathrm{T}}^{V} < 150$ GeV	2-jet	0.85 ± 0.06
		3-jet	0.88 ± 0.04
	$150 < p_{\mathrm{T}}^{V} < 250$ GeV	2-jet	0.87 ± 0.06
		3-jet	0.87 ± 0.04
	$250 < p_{\mathrm{T}}^{V} < 400$ GeV	2-jet	0.89 ± 0.07
		3-jet	0.81 ± 0.04
Top	$400 < p_{\mathrm{T}}^{V} < 600$ GeV		0.87 ± 0.05
	$p_{\mathrm{T}}^{V} > 600$ GeV		0.77 ± 0.08

Table 5.19: Floating normalizations for the $W+$jets and top quark backgrounds as extracted from the diboson likelihood fit. The values are quoted with their total uncertainties (combined statistical and systematic). The $W + hf$ and $t\bar{t}$ normalizations in the boosted regime are correlated across jet multiplicity regions.

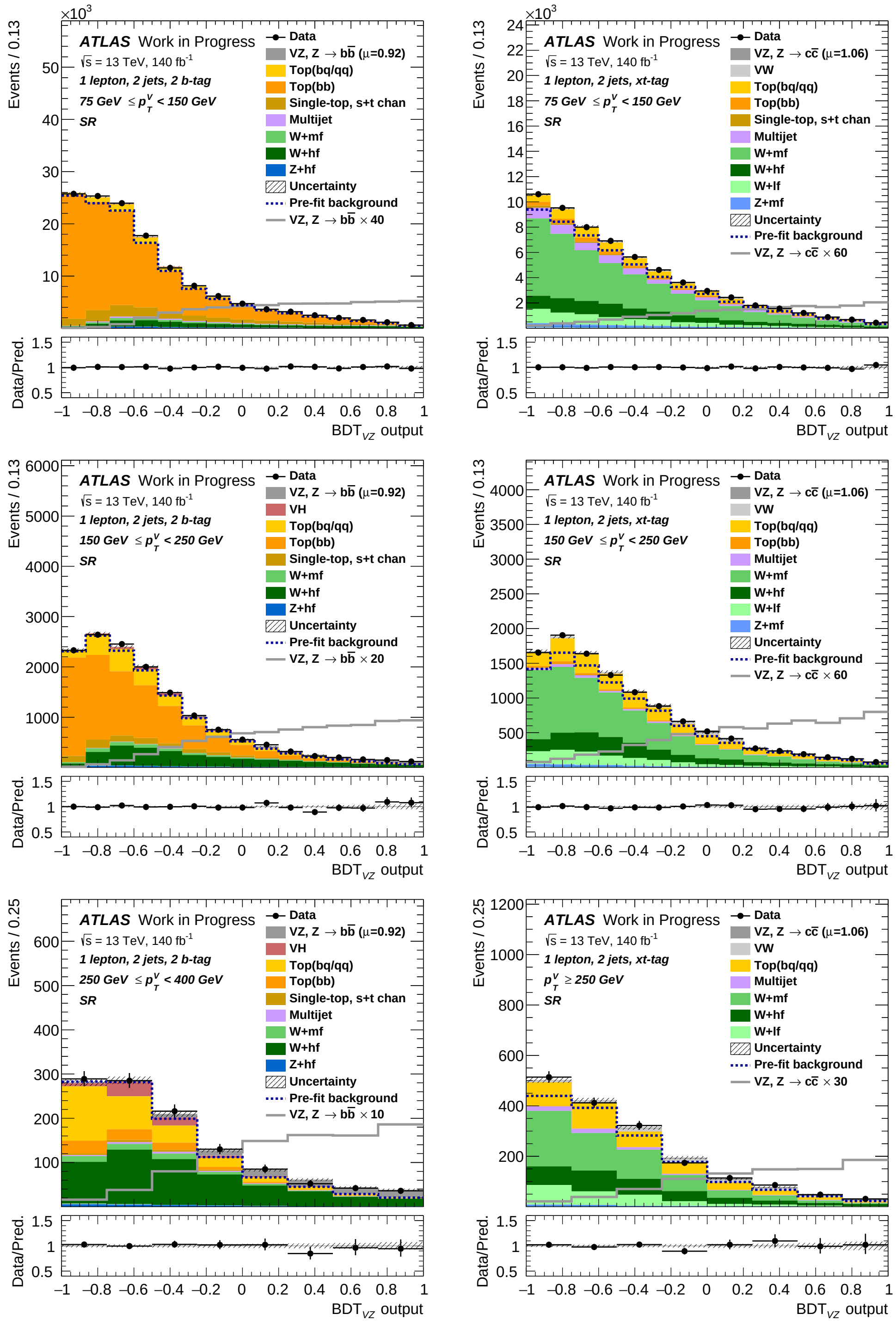

Figure 5.21: Post-fit distributions for the VZ BDT output score in the signal region for the BB tag, 2-jet category of the $VH(H \to b\bar{b})$ regime (left) and the XT tag, 2-jet category of the $VH(H \to c\bar{c})$ regime (right). The distributions are shown separately for the $75 < p_{\mathrm{T}}^{V} < 150$ GeV (top), $150 < p_{\mathrm{T}}^{V} < 250$ GeV (middle) and $p_{\mathrm{T}}^{V} > 250$ GeV (bottom) regions.

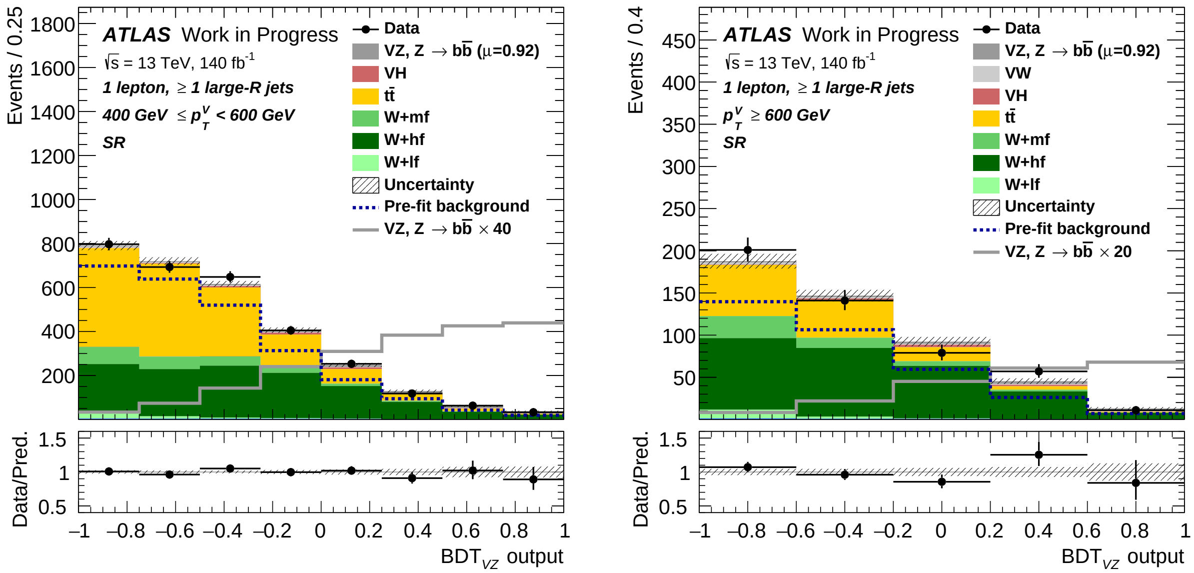

Figure 5.22: Post-fit distributions for the VZ BDT output score in the signal region for the $400 < p_{\mathrm{T}}^{V} < 600$ GeV (left) and $p_{\mathrm{T}}^{V} > 600$ GeV (right) categories of the boosted $VH(H \to b\bar{b})$ regime.

Uncertainty Breakdown

It is also informative to study the impact of broader physics-related categories on the total uncertainty $\sigma_{\hat{\mu}}$ for the fitted signal strength $\hat{\mu}$. Each of the different categories group several NPs and are constructed based on the common origin of the corresponding uncertainty, e.g. all NPs relevant to the modelling of the $W+$jets background are grouped into one category. To determine the impact of a group of NPs, a fit is performed where the NPs that belong to that particular group are fixed to their post-fit values obtained from the nominal fit. This results in a new best-fit parameter value and uncertainty, $\hat{\mu}'$ and $\sigma_{\hat{\mu}'}$. The impact of the group is then computed as the difference in quadrature between the two uncertainties:

$$\text{impact} = \sqrt{\sigma_{\hat{\mu}}^2 - \sigma_{\hat{\mu}'}^2}. \tag{5.24}$$

The statistical uncertainty impact is determined from a fit where all the NPs except the floating normalizations are fixed. The systematic uncertainty is computed as the difference in quadrature between the total and statistical uncertainties. Due to correlations between different NPs, the sum in quadrature of individual systematic contributions may be different from the total.

The uncertainty breakdown for the $WZ(Z \to b\bar{b})$ and $WZ(Z \to c\bar{c})$ signal strengths is shown in Table 5.20. For the $WZ(Z \to b\bar{b})$ signal strength, the systematic uncertainties

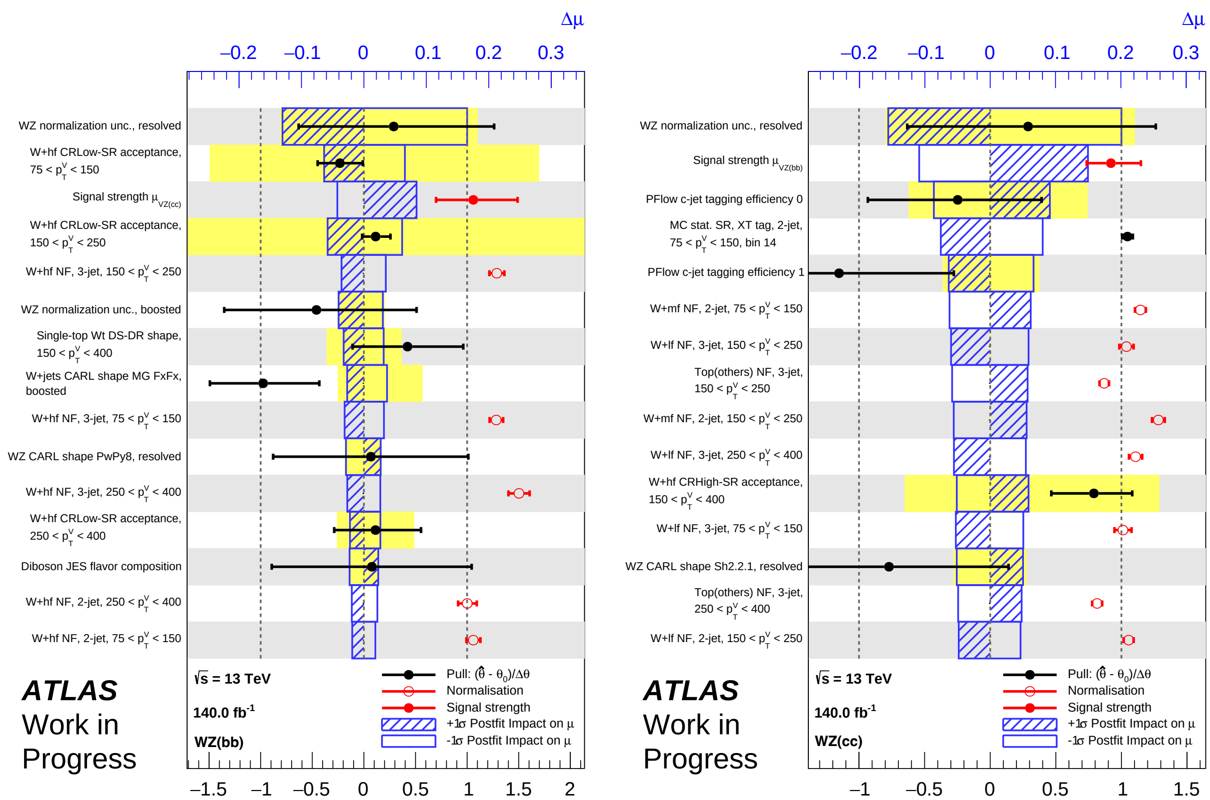

Figure 5.23: Impact of individual systematic uncertainties on the measured signal strengths for the $WZ(Z \to b\bar{b})$ (left) and $WZ(Z \to c\bar{c})$ processes (right). The 15 largest contributions are presented in decreasing order. The impact on the signal strength obtained by varying the NP upwards (downwards) by the post-fit uncertainty is shown as blue hashed (empty) boxes and is read from the top x-axis. The post-fit values and uncertainties for the NPs are shown as filled circles with corresponding error bars and are read from the bottom x-axis.

are almost 2.5 times larger than the statistical uncertainties. The largest contribution to the systematic uncertainties comes from the modelling of the diboson, $W+$jets, and top quark processes, with the diboson modelling having the largest impact. The most sizeable contribution to the experimental uncertainties originates from uncertainties related to the reconstruction and calibration of the small-R jets used in the resolved regimes of the analysis. The $WZ(Z \to c\bar{c})$ signal strength also has a significant impact on the uncertainty, as previously seen in the ranking plots of Figure 5.23.

Similar trends in the breakdown of the uncertainties can be seen for the $WZ(Z \to c\bar{c})$ signal strength. Here, the systematic uncertainties are larger than the statistical ones by $\sim 60\%$. As before, the largest contribution to the systematic uncertainties originates from the modelling of the diboson, $W+$jets, and top quark processes. The estimation of the QCD multi-jet background also has a relatively significant impact on the uncertainty. They are followed by the experimental uncertainties, where the uncertainties related to the reconstruction and calibration of the small-R jets and the uncertainties on the flavor tagging of c-jets and light-flavor jets have the largest effects. The uncertainties due to the size of the simulation samples and the $WZ(Z \to b\bar{b})$ signal strength parameter also have sizeable impacts, that are of similar size to the impact of the experimental uncertainties.

5.8.2 $WH(H \to b\bar{b}/c\bar{c})$ Signal Strength Measurement

As described in Section 5.7, a global likelihood fit is performed to simultaneously measure the signal strengths for the $WH(H \to b\bar{b})$ and $WH(H \to c\bar{c})$ processes. The best-fit signal strength values are found to be:

$$\mu_{WH(H\to b\bar{b})} = 0.88 \pm 0.20 = 0.88 \pm 0.14 \text{ (stat.)} \pm 0.14 \text{ (syst.)} \quad (5.25)$$

$$\mu_{WH(H\to c\bar{c})} = -0.01 \pm 9.60 = 0.02 \pm 6.45 \text{ (stat.)} \pm 7.11 \text{ (syst.)}. \quad (5.26)$$

Each of the measured signal strengths are compatible with the SM expectation of unity within the statistical uncertainties. The probability of compatibility with the SM, that is of both signal strengths being equal to 1, is 81%. The expected and observed best-fit values and their 68% and 95% CL contours, as determined from scans of the profile likelihood as a function of $\mu_{WH(H\to b\bar{b})}$ and $\mu_{WH(H\to c\bar{c})}$, are shown in Figure 5.24.

The correlation between the $WH(H \to b\bar{b})$ and $WH(H \to c\bar{c})$ signal strengths is estimated to be 4%. The correlation coefficients between the WH signal strengths and the floating normalizations for the $W+$jets and top quark backgrounds are shown in Figures 5.25 and 5.26, respectively. The $WH(H \to b\bar{b})$ and $WH(H \to c\bar{c})$ signal strengths are generally found to be negatively correlated with the $W+$jets floating normalizations and positively correlated with the floating normalizations for the top quark backgrounds. High correlations are observed between the floating normalizations for the different background components in different jet multiplicity and p_{T}^{V} regions. The correlations are similar between the unconditional fit to data and the unconditional Asimov fit, providing an additional validation check of the analysis strategy.

Source of uncertainty		$\mu_{WZ(Z\to b\bar{b})}$	$\mu_{WZ(Z\to c\bar{c})}$
Total		0.21	0.40
Statistical		0.08	0.21
Data sample size		0.06	0.18
Floating normalizations		0.06	0.12
Systematic		0.19	0.34
$WZ(Z \to b\bar{b})$ signal strength		–	0.12
$WZ(Z \to c\bar{c})$ signal strength		0.07	–
VH modelling		< 0.01	< 0.01
Background modelling		0.18	0.28
$W+$jets		0.09	0.11
Top ($t\bar{t}$ and single-top Wt-channel)		0.04	0.07
Single-top (s- and t-channel)		0.02	0.02
$Z+$jets		< 0.01	0.02
Diboson		0.15	0.19
Multi-jet		0.01	0.06
Experimental uncertainties		0.05	0.15
Leptons		< 0.01	< 0.01
$E_{\mathrm{T}}^{\mathrm{miss}}$		0.01	0.02
Small-R jets		0.04	0.10
Large-R jets		0.01	0.01
Flavor tagging: PFlow jets	b-jets	0.01	0.02
	c-jets	0.01	0.11
	light-flavor jets	< 0.01	0.06
	τ-jets	< 0.01	< 0.01
	extrapolation	< 0.01	< 0.01
Flavor tagging: VR track-jets	b-jets	< 0.01	< 0.01
	c-jets	< 0.01	< 0.01
	light-flavor jets	< 0.01	< 0.01
	τ-jets	< 0.01	< 0.01
	extrapolation	< 0.01	< 0.01
Pile-up		0.01	< 0.01
Luminosity		0.01	0.01
Simulation sample size		0.03	0.15

Table 5.20: Breakdown of the contributions to the uncertainty on the $WZ(Z \to b\bar{b})$ and $WZ(Z \to c\bar{c})$ signal strengths. The average impact (computed as the mean of the absolute values of the upward and downward variations) on the signal strengths is shown. Due to correlations between different NPs, the sum in quadrature of individual systematic contributions may be different from the total.

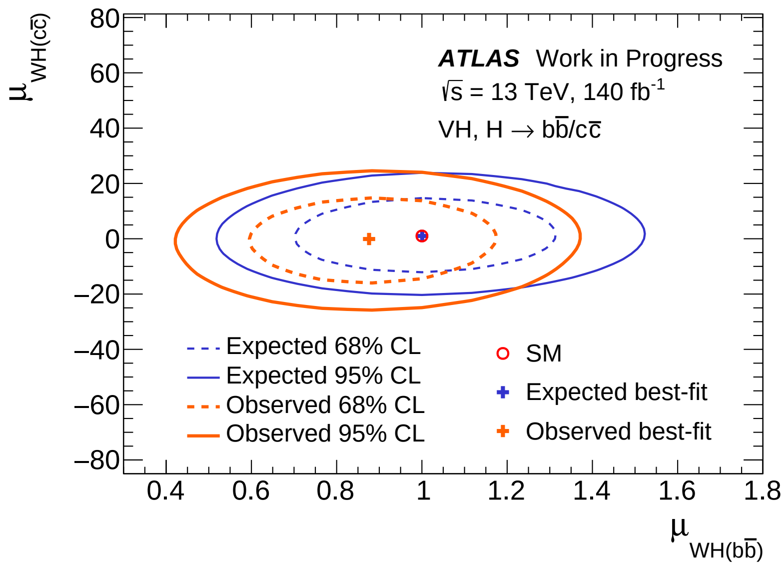

Figure 5.24: Expected and observed best-fit values and 68% and 95% CL contours for the $WH(H \to b\bar{b})$ and $WH(H \to c\bar{c})$ signal strength parameters.

Compared to the background-only hypothesis, the excess observed in the data for the $WH(H \to b\bar{b})$ signal corresponds to a significance of 4.8σ, compared to an expectation of 5.3σ. This can be compared to the results of the previous ATLAS analysis that combined the resolved and boosted $VH(H \to b\bar{b})$ regimes [180]. Using the same full Run 2 dataset, the latter measured the signal strength to be $\mu_{WH(H\to b\bar{b})} = 1.03 \pm 0.19\,(\text{stat.}) \pm 0.20\,(\text{syst.})$, which corresponds to an observed (expected) significance of 4.1σ (3.9σ). The result presented here represents an improvement of ~ 1.5 in the uncertainty and provides strong evidence for the $WH(H \to b\bar{b})$ process. Using a standard z-test[25] for the difference in the μ values, the probability of compatibility between the two measurements for $\mu_{WH(H\to b\bar{b})}$ is found to be 66%. The $WH(H \to b\bar{b})$ result also has a better uncertainty compared to the CMS resolved and boosted $VH(H \to b\bar{b})$ measurement [181], which reported $\mu_{WH(H\to b\bar{b})} = 0.97 \pm 0.23\,(\text{stat.}) \pm 0.22\,(\text{syst.})$ (the probability of compatibility between the two measurements is 81%).

For the $WH(H \to c\bar{c})$ signal, no significant excess over the background-only hypothesis is observed. Instead, a 95% CL upper limit on $\mu_{WH(H\to c\bar{c})}$ is determined. A limit of 19.1 times the SM prediction is observed, compared to an expected limit of 18.4 times the SM prediction. This result represents a significant improvement over the previous ATLAS $VH(H \to c\bar{c})$ measurement [194], also using the full Run 2 dataset, where an upper limit of 50 times the SM prediction was observed (60× SM expected) for the $WH(H \to c\bar{c})$ process. The result

[25] See e.g. Section 14.3.2 of Ref. [248].

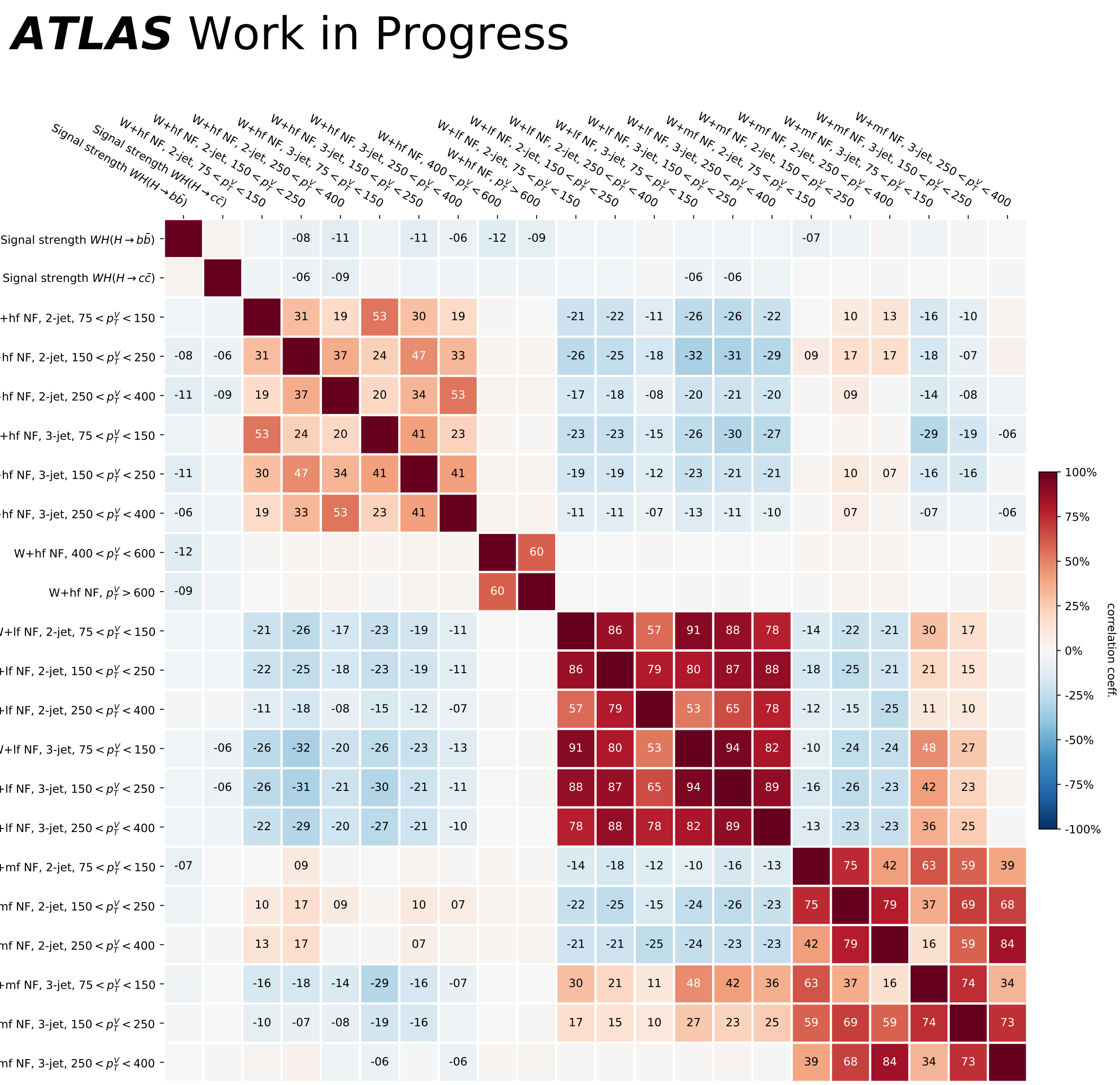

Figure 5.25: Matrix of correlation coefficients between the $WH(H \to b\bar{b})$ and $WH(H \to c\bar{c})$ signal strengths and the floating normalizations for the $W+$jets background.

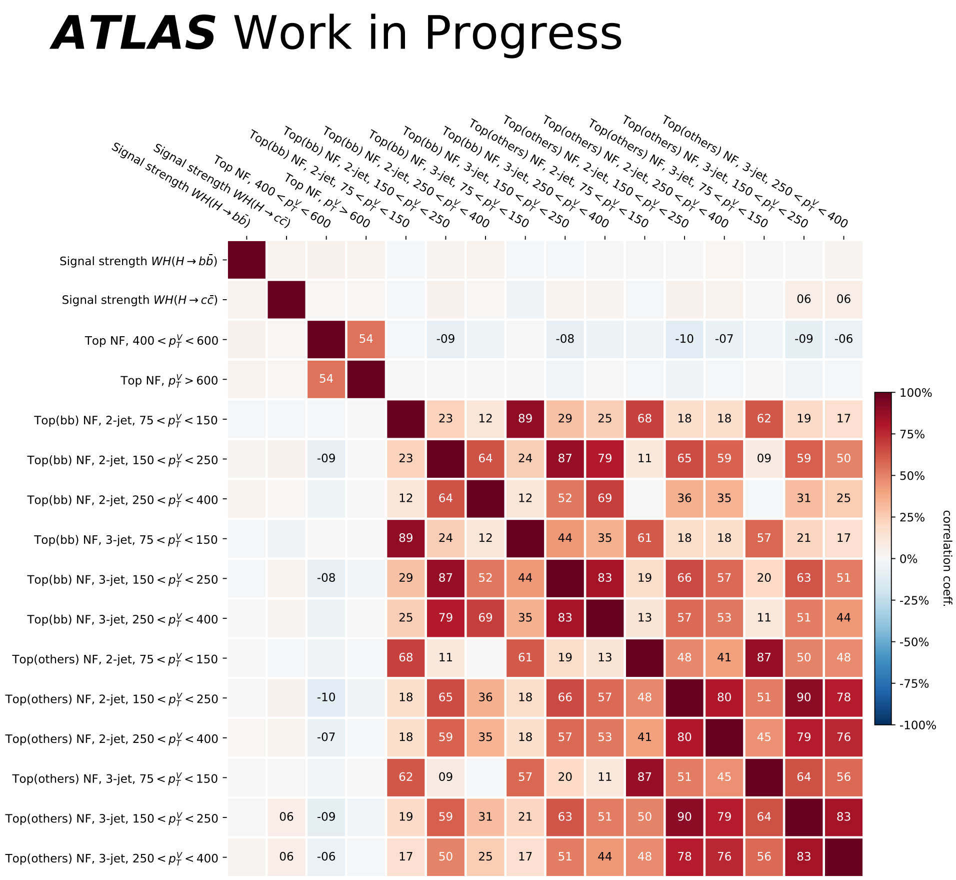

Figure 5.26: Matrix of correlation coefficients between the $WH(H \to b\bar{b})$ and $WH(H \to c\bar{c})$ signal strengths and the floating normalizations for the top quark background.

is similar to the CMS $VH(H \to c\bar{c})$ measurement [195], which observed an upper limit of 19.1 times the SM prediction (11.5× SM expected) for the $WH(H \to c\bar{c})$ process.

The values of the floating normalization parameters for the $W+$jets and top quark backgrounds are shown in Table 5.21. The normalizations for the $W + hf$ component are found to be higher than the predictions of the nominal simulated samples. In the resolved regime, the normalizations are higher in the 3-jet regions, where they are pulled $\sim 5\sigma$ away from the pre-fit value of 1, compared to the 2-jet regions, which are pulled by $\sim 1\sigma$. A trend in the central value of the normalization with increasing p_{T}^{V} can also be seen. In the boosted regime, the normalizations are pulled up by $\sim 4\sigma$ from the pre-fit value. The $W + mf$ normalizations are also higher than the simulation predictions in all regions, being pulled up by $\sim 4\sigma$. The normalizations for $W + lf$ are found to be consistent with the pre-fit value within approximately 1σ. A slight trend in the central values of the normalizations with

p_{T}^{V} can also be seen for the $W + mf$ and $W + lf$ components. The pulls in the floating normalizations are due to known modelling issues for the $W+$jets process [210, 249].

For the top quark backgrounds, the normalizations tend to be lower by $\sim 3\sigma$ than the predictions of the nominal $t\bar{t}$ and single-top Wt-channel simulated samples. Between comparable jet multiplicity and p_{T}^{V} regions, the normalizations are generally consistent within one standard deviation for the Top(bb) and Top(others) components. A downwards trend in the NP central values with p_{T}^{V} can be observed, with the largest deviation being found in the boosted regime.

Post-fit distributions of the BDT output score are shown in Figure 5.27 for the resolved $VH(H \to b\bar{b})$ and $VH(H \to c\bar{c})$ regimes and in Figure 5.28 for the boosted $VH(H \to b\bar{b})$ regime. As before, the stacked filled histograms represent the background predictions, scaled according to the NP values extracted from the likelihood fit. The $WH(H \to b\bar{b}/c\bar{c})$ signals are scaled according to the measured signal strengths, respectively, and shown as filled red histograms on top of the background contribution. The unstacked red line shows the WH signal prediction, scaled by an arbitrary factor to emphasize the expected signal shape. The total pre-fit background is shown with the dashed blue histogram. The ratio between the data and the post-fit combined signal and background prediction is shown in the lower panels of the plots.

Nuisance Parameters Ranking

Figure 5.29 shows the ranking of the 15 nuisance parameters with the largest contributions to the uncertainties on the $WH(H \to b\bar{b})$ and $WH(H \to c\bar{c})$ signal strengths. For the $WH(H \to b\bar{b})$ signal strength, the three NPs with the largest impacts are all related to the extrapolation uncertainty between the signal and low ΔR control region for the $W + hf$ component. Other highly ranked NPs consist of shape uncertainties for the WZ, top, and single-top Wt-channel processes, floating normalizations for the $W + hf$ component in resolved and boosted p_{T}^{V} regions, and experimental uncertainties related to JES and pile-up modelling.

For the $WH(H \to c\bar{c})$ signal strength, the highest-ranked nuisance parameters are related to shape uncertainties for the top quark background. Other highly ranked uncertainties include simulation statistics nuisance parameters for particular bins of the BDT output distribution, experimental uncertainties related to JES/JER and pile-up modelling, uncertainties on the flavor tagging of c-jets and light-flavor jets, $E_{\mathrm{T}}^{\mathrm{miss}}$ related uncertainties, and extrapolation and shape uncertainties for the $W + hf$ component.

Uncertainty Breakdown

The uncertainty breakdown for the $WH(H \to b\bar{b})$ and $WH(H \to c\bar{c})$ signal strengths is shown in Table 5.22. For the $WH(H \to b\bar{b})$ signal strength, the statistical and systematic components contribute equally to the total uncertainty. The statistical uncertainty is dominated by the limited data sample size, which has a ~ 2.5 times larger impact than

Background	p_T^V region	Jet multiplicity	Value
$W+hf$	$75 < p_T^V < 150$ GeV	2-jet	1.09 ± 0.07
		3-jet	1.35 ± 0.07
	$150 < p_T^V < 250$ GeV	2-jet	1.06 ± 0.06
		3-jet	1.35 ± 0.08
	$250 < p_T^V < 400$ GeV	2-jet	1.01 ± 0.09
		3-jet	1.50 ± 0.11
	$400 < p_T^V < 600$ GeV		1.70 ± 0.29
	$p_T^V > 600$ GeV		2.21 ± 0.30
$W+mf$	$75 < p_T^V < 150$ GeV	2-jet	1.15 ± 0.04
		3-jet	1.09 ± 0.05
	$150 < p_T^V < 250$ GeV	2-jet	1.29 ± 0.05
		3-jet	1.27 ± 0.05
	$250 < p_T^V < 400$ GeV	2-jet	1.32 ± 0.08
		3-jet	1.28 ± 0.08
$W+lf$	$75 < p_T^V < 150$ GeV	2-jet	0.98 ± 0.05
		3-jet	0.99 ± 0.07
	$150 < p_T^V < 250$ GeV	2-jet	1.05 ± 0.04
		3-jet	1.02 ± 0.06
	$250 < p_T^V < 400$ GeV	2-jet	1.07 ± 0.04
		3-jet	1.10 ± 0.06
Top(bb)	$75 < p_T^V < 150$ GeV	2-jet	0.93 ± 0.04
		3-jet	0.93 ± 0.03
	$150 < p_T^V < 250$ GeV	2-jet	0.91 ± 0.06
		3-jet	0.90 ± 0.03
	$250 < p_T^V < 400$ GeV	2-jet	0.84 ± 0.09
		3-jet	0.84 ± 0.04
Top(others)	$75 < p_T^V < 150$ GeV	2-jet	0.92 ± 0.06
		3-jet	0.93 ± 0.04
	$150 < p_T^V < 250$ GeV	2-jet	0.85 ± 0.06
		3-jet	0.86 ± 0.04
	$250 < p_T^V < 400$ GeV	2-jet	0.86 ± 0.07
		3-jet	0.80 ± 0.04
Top	$400 < p_T^V < 600$ GeV		0.89 ± 0.05
	$p_T^V > 600$ GeV		0.78 ± 0.08

Table 5.21: Floating normalizations for the $W+$jets and top quark backgrounds as extracted from the global likelihood fit. The values are quoted with their total uncertainties (combined statistical and systematic). The $W+hf$ and Top normalizations in the boosted regime are correlated across jet multiplicity regions.

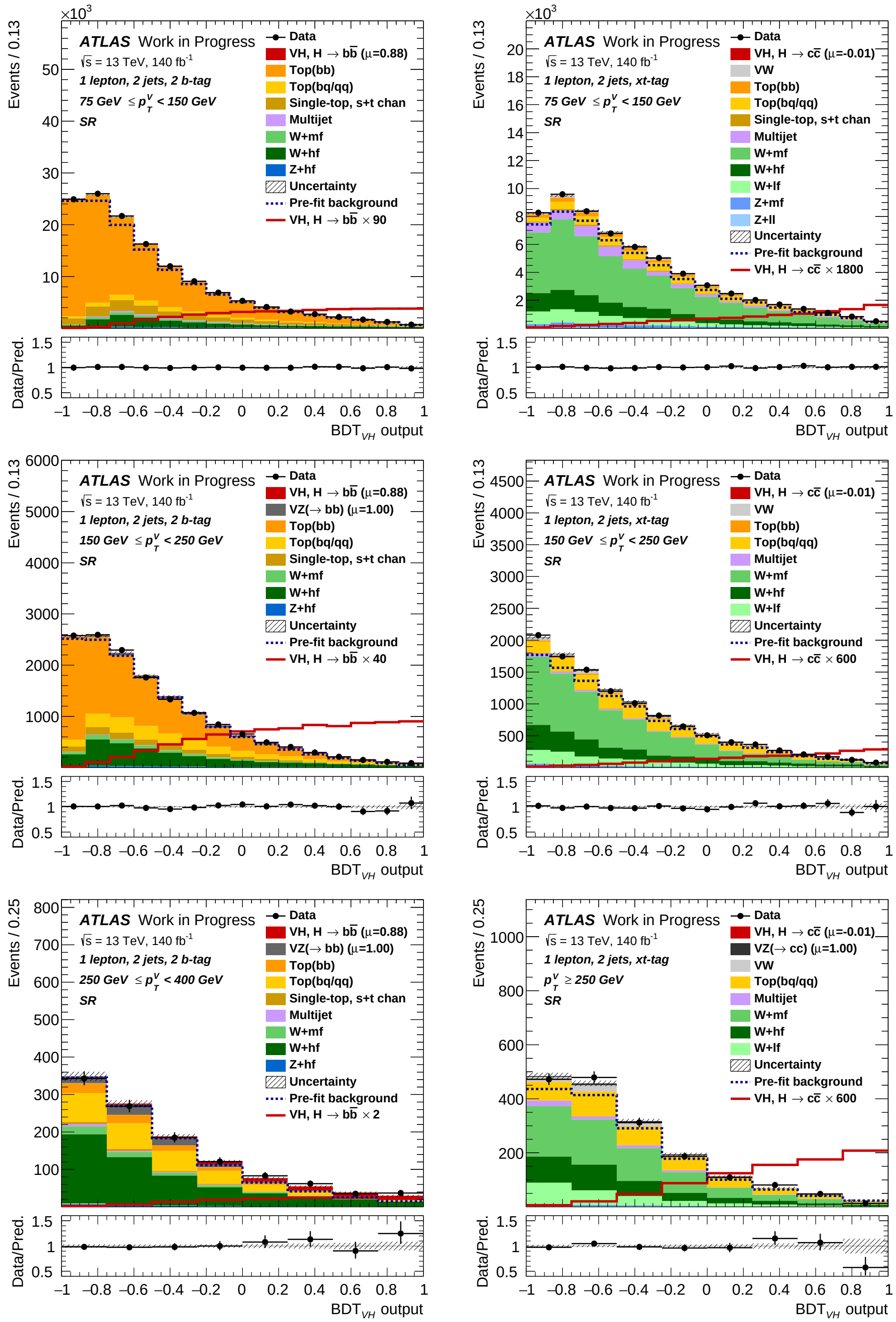

Figure 5.27: Post-fit distributions for the BDT output score in the signal region for the BB tag, 2-jet category of the $VH(H \to b\bar{b})$ regime (left) and the XT tag, 2-jet category of the $VH(H \to c\bar{c})$ regime (right). The distributions are shown separately for the $75 < p_T^V < 150$ GeV (top), $150 < p_T^V < 250$ GeV (middle) and $p_T^V > 250$ GeV (bottom) regions.

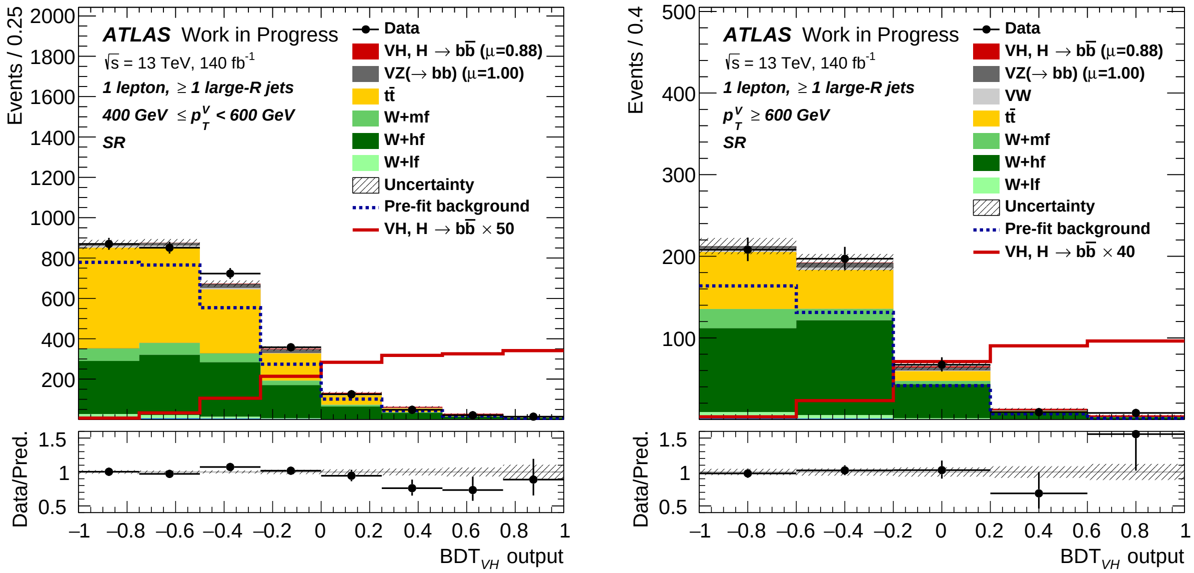

Figure 5.28: Post-fit distributions for the BDT output score in the signal region for the $400 < p_{\mathrm{T}}^{V} < 600$ GeV (left) and $p_{\mathrm{T}}^{V} > 600$ GeV (right) categories of the boosted $VH(H \to b\bar{b})$ regime.

the floating normalizations of the main backgrounds. The largest contribution to the systematic uncertainties comes from the modelling uncertainties for the background processes, particularly $W+$jets, top ($t\bar{t}$ and single-top Wt-channel), and diboson. The most sizeable contribution to the experimental uncertainties originates from uncertainties related to the reconstruction and calibration of the small-R jets used in the resolved regimes of the analysis. The uncertainties due to the size of the simulation samples also have a sizeable impact, slightly smaller than the impact of the experimental uncertainties.

In the case of the $WH(H \to c\bar{c})$ signal strength, the systematic uncertainties are slightly larger than the statistical ones, by $\sim 10\%$. As seen before for $\mu_{WH(H\to b\bar{b})}$, the statistical uncertainty is dominated by the limited data sample size, which has a ~ 2 times larger impact than the floating normalizations. The largest contribution to the systematic uncertainties originates from the modelling of the top quark and $W+$jets processes. The estimation of the QCD multi-jet background also has a sizeable contribution. They are followed by the experimental uncertainties, where the uncertainties related to the reconstruction and calibration of the small-R jets, the $E_{\mathrm{T}}^{\mathrm{miss}}$ uncertainties, and the uncertainties on the flavor tagging of c-jets and light-flavor jets have the largest effects. The uncertainties due to the limited size of the simulation samples also have a significant contribution.

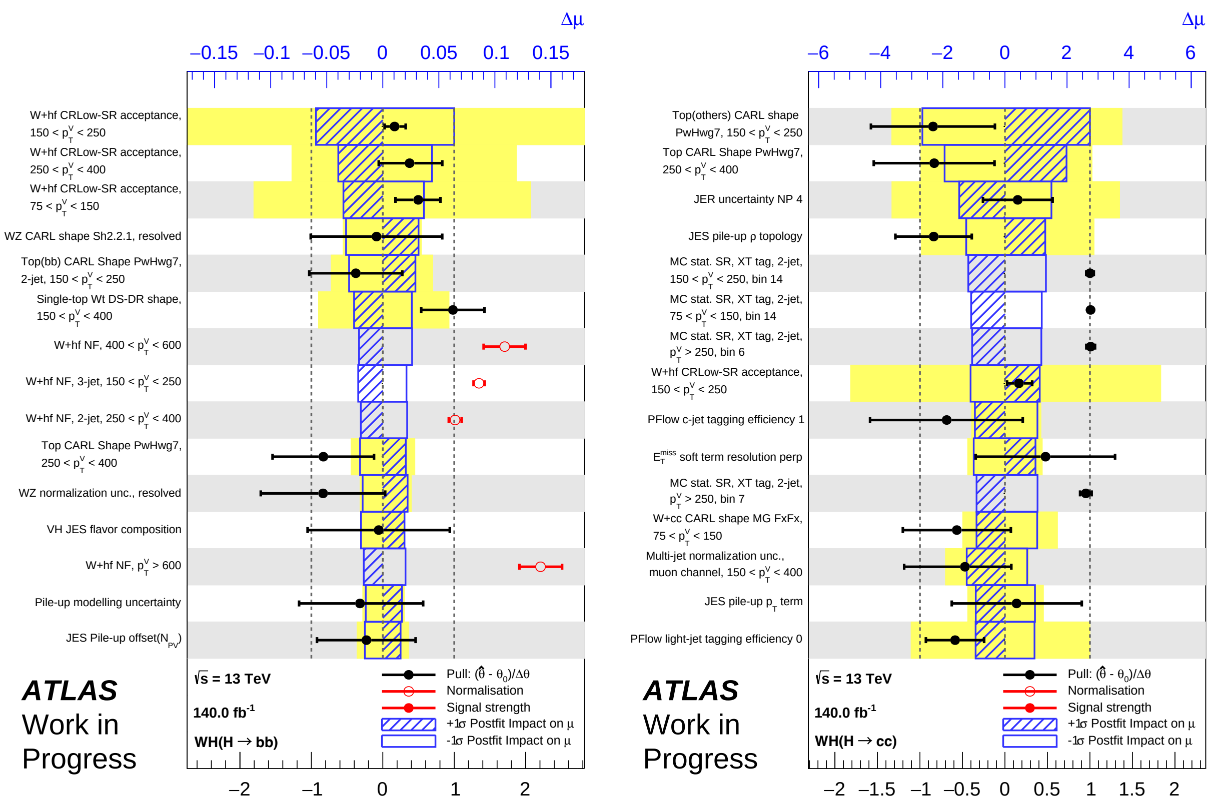

Figure 5.29: Impact of individual systematic uncertainties on the measured signal strengths for the $WH(H \to b\bar{b})$ (left) and $WH(H \to c\bar{c})$ processes (right). The 15 largest contributions are presented in decreasing order. The impact on the signal strength obtained by varying the NP upwards (downwards) by the post-fit uncertainty is shown as blue hashed (empty) boxes and is read from the top x-axis. The post-fit values and uncertainties for the NPs are shown as filled circles with corresponding error bars and are read from the bottom x-axis.

Source of uncertainty		$\mu_{WH(H\to b\bar{b})}$	$\mu_{WH(H\to c\bar{c})}$
Total		0.20	9.60
Statistical		0.14	6.45
Data sample size		0.13	5.94
Floating normalizations		0.05	2.55
Systematic		0.14	7.11
$WH(H \to b\bar{b})$ signal strength		–	0.35
$WH(H \to c\bar{c})$ signal strength		< 0.01	–
VH modelling		0.02	0.80
Background modelling		0.12	6.01
$W+$jets		0.08	3.21
Top ($t\bar{t}$ and single-top Wt-channel)		0.05	3.79
Single-top (s- and t-channel)		0.02	0.72
$Z+$jets		< 0.01	0.53
Diboson		0.04	0.85
Multi-jet		< 0.01	1.45
Experimental uncertainties		0.06	3.80
Leptons		< 0.01	0.18
$E_{\mathrm{T}}^{\mathrm{miss}}$		< 0.01	1.22
Small-R jets		0.05	3.21
Large-R jets		0.01	0.46
Flavor tagging: PFlow jets	b-jets	0.01	0.52
	c-jets	0.02	1.32
	light-flavor jets	< 0.01	1.09
	τ-jets	< 0.01	0.03
	extrapolation	< 0.01	< 0.01
Flavor tagging: VR track-jets	b-jets	0.01	0.11
	c-jets	< 0.01	0.12
	light-flavor jets	< 0.01	0.03
	τ-jets	< 0.01	< 0.01
	extrapolation	< 0.01	0.15
Pile-up		0.02	0.42
Luminosity		< 0.01	0.08
Simulation sample size		0.04	3.40

Table 5.22: Breakdown of the contributions to the uncertainty on the $WH(H \to b\bar{b})$ and $WH(H \to c\bar{c})$ signal strengths. The average impact (computed as the mean of the absolute values of the upward and downward variations) on the signal strengths is shown. Due to correlations between different NPs, the sum in quadrature of individual systematic contributions may be different from the total.

5.8.3 Constraints on the κ_b and κ_c Coupling Modifiers

As described in Section 5.7.3, the signal strength results can be interpreted within the κ framework to set direct constraints on the Higgs Yukawa coupling modifiers κ_b and κ_c. A simultaneous fit to the κ_b and κ_c parameters is performed, using the same fit setup as for the previous results, but replacing the $WH(H \to b\bar{b})$ and $WH(H \to c\bar{c})$ signal strengths with the expressions of Eqns. 5.19 and 5.20, respectively.

Figures 5.30 and 5.31 show the resulting scans of the profile likelihood as a function of κ_b and κ_c[26]. As seen in the plot on the left side of Figure 5.31, the results are compatible with the SM prediction as the point $(\kappa_b, \kappa_c) = (1, 1)$ is found within the 68% confidence region defined by the data. The results are comparable to the κ_b and κ_c constraints reported in the previous ATLAS $VH(H \to c\bar{c})$ analysis [194] (right side plots in Figures 5.30 and 5.31), which performed a statistical combination with the $VH(H \to b\bar{b})$ analysis [178] using data in all three lepton channels.

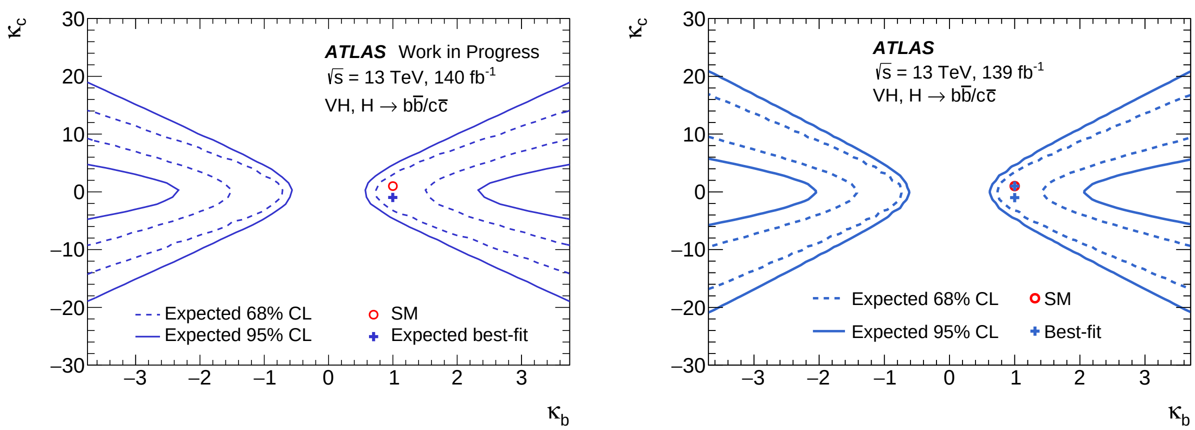

Figure 5.30: Expected constraints, at the 68% and 95% confidence levels, for the κ_b and κ_c coupling modifiers. The results obtained in this thesis (left) are comparable to those obtained from a similar fit performed by the previous ATLAS $VH(H \to c\bar{c})$ analysis [194] (right).

Although using only data in the 1-lepton channel, the present analysis benefits from the implementation of a coherent treatment in terms of flavor tagging strategy, the use of a BDT based discriminant in all analysis regimes, and the modelling of systematic uncertainties between $VH(H \to b\bar{b})$ and $VH(H \to c\bar{c})$, which allows for similar constraints to be set on the κ_b and κ_c parameters. The full $VH(H \to b\bar{b}/c\bar{c})$ analysis will benefit from additional constraining power provided by the data in the 0-lepton and 2-lepton channels and further

[26]The particular shape of the contours is a result of substituting Eqns. 5.19 and 5.20 into the profile likelihood, which is shaped like a parabola around the best-fit points $(\hat{\mu}_{WH(H\to b\bar{b})}, \hat{\mu}_{WH(H\to c\bar{c})})$.

refinements in the fit model, which will allow for tighter limits to be set. These limits would complement the current best constraints on the coupling modifiers, obtained from combining ATLAS measurements of the Higgs boson p_{T} spectrum in the $H \to \gamma\gamma$ and $H \to ZZ^* \to 4\ell$ channels with the measurements of Higgs bosons produced in association with a W or Z boson and decaying to b- or c-quark pairs [250].

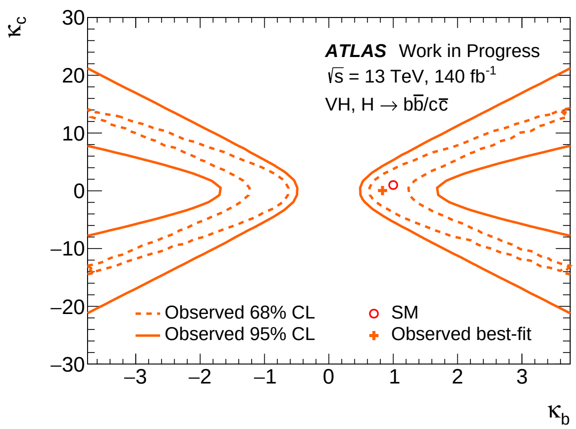

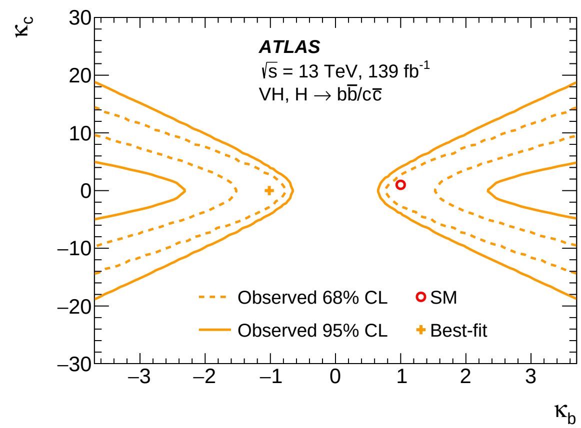

Figure 5.31: Observed constraints, at the 68% and 95% confidence levels, for the κ_b and κ_c coupling modifiers. The results obtained in this thesis (left) are comparable to those obtained from a similar fit performed by the previous ATLAS $VH(H \to c\bar{c})$ analysis [194] (right).

A fit is also performed to constrain the ratio of the coupling modifiers, κ_c/κ_b. In this case, the two parameters of interest consist of the ratios κ_c/κ_b and κ_b/κ_H, which removes any assumptions on the Higgs width (that is, no explicit dependence on the other coupling modifiers is assumed for κ_H) via the following parametrization:

$$\mu_{WH(H\to b\bar{b})} = \left(\frac{\kappa_b}{\kappa_H}\right)^2 \tag{5.27}$$

$$\mu_{WH(H\to c\bar{c})} = \left(\frac{\kappa_c}{\kappa_b}\right)^2 \left(\frac{\kappa_b}{\kappa_H}\right)^2. \tag{5.28}$$

The profile likelihood scans as a function of the parameters κ_c/κ_b and κ_b/κ_H are shown in Figure 5.32. The results are found to be compatible with the prediction of the SM.

Figure 5.33 shows the profile likelihood scan as a function of κ_c/κ_b, where κ_b/κ_H is a free parameter. The observed limit at the 95% CL is found to be $|\kappa_c/\kappa_b| < 4.9$, compared to an expected limit of $|\kappa_c/\kappa_b| < 4.5$. This result can be compared to the findings of the $VH(H \to b\bar{b})$ and $VH(H \to c\bar{c})$ statistical combination performed by the previous ATLAS $VH(H \to c\bar{c})$ analysis [194], which reported an observed (expected) limit of $|\kappa_c/\kappa_b| <$

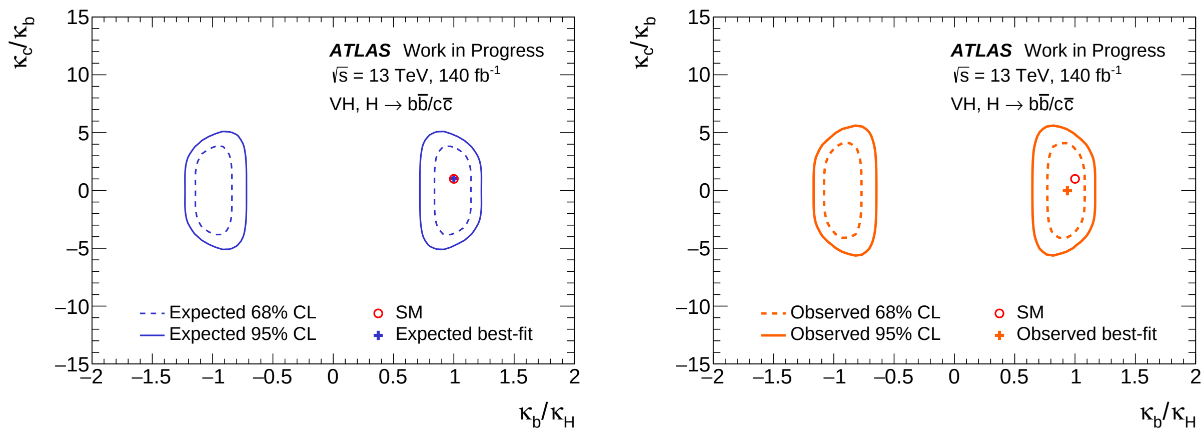

Figure 5.32: Expected (left) and observed (right) constraints for the κ_c/κ_b and κ_b/κ_H parameters, at the 68% and 95% confidence levels.

4.5 ($|\kappa_c/\kappa_b| < 5.1$) at the 95% CL[27]. Once again, the present analysis can set comparable constraints on $|\kappa_c/\kappa_b|$ while using only the data in the 1-lepton channel.

5.9 Conclusions

This chapter presented a measurement of $H \to b\bar{b}/c\bar{c}$ decays in the VH production mode, using pp collision data collected by the ATLAS detector during Run 2 of the LHC, corresponding to an integrated luminosity of 140 fb^{-1} at center-of-mass energy of $\sqrt{s} = 13$ TeV. The analysis was performed considering events categorized in the 1-lepton channel, which targets the leptonic decay modes of the W boson: $WH \to \ell\nu q\bar{q}$. Jets originating from the decay of b- or c-quarks were selected using flavor tagging algorithms based on machine learning techniques. Analysis regions were defined using different categories based on the jet flavor tagging, the jet multiplicity, and the transverse momentum of the vector boson. The main backgrounds for this analysis, originating from $W+$jets and top quark processes, were constrained from data using dedicated control regions. Multi-variate analysis techniques (in the form of boosted decision trees) were used to enhance the sensitivity of the measurement. The distribution of the BDT output score in the signal regions was used as the fit variable in a binned likelihood fit which extracted the signal strengths for the $WH(H \to b\bar{b})$ and $WH(H \to c\bar{c})$ processes.

The analysis strategy was validated by performing a measurement of the diboson processes $WZ(Z \to b\bar{b})$ and $WZ(Z \to c\bar{c})$. The diboson signal strengths were found to agree

[27] These results were obtained from a likelihood scan as a function of κ_c/κ_b and κ_b, which contains a residual parametrization of the Higgs width in terms of these two parameters.

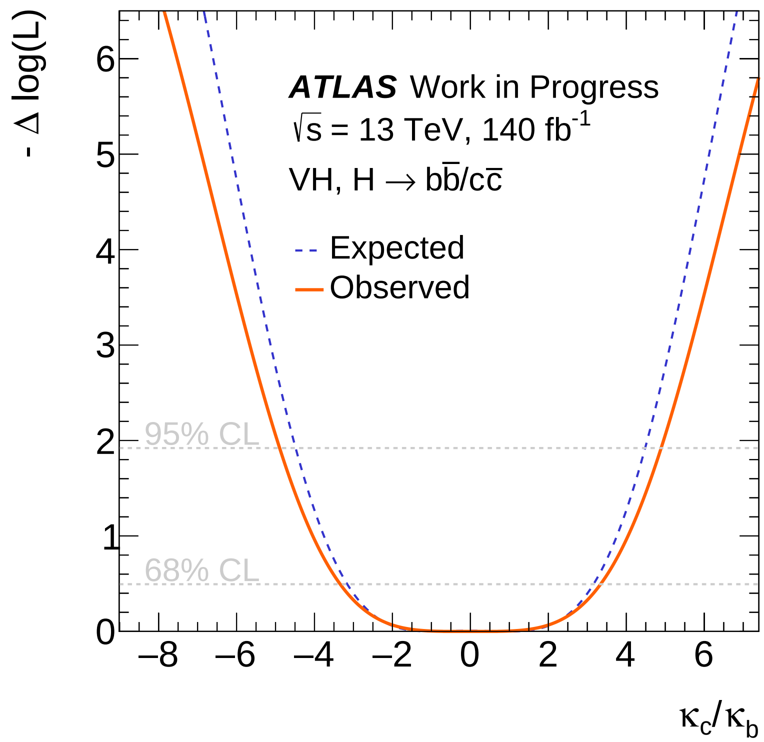

Figure 5.33: Expected and observed profile likelihood scans as a function of κ_c/κ_b, where κ_b/κ_H is a free parameter.

with the Standard Model predictions, with observed (expected) significances of 6.8 (7.4) and 3.2 (3.0) standard deviations for the $WZ(Z \to b\bar{b})$ and $WZ(Z \to c\bar{c})$ processes, respectively.

The $WH(H \to b\bar{b}/c\bar{c})$ processes were also found to be in agreement with the SM. The $WH(H \to b\bar{b})$ process was observed with a significance of 4.8σ, compared to an expectation of 5.3σ. For the $WH(H \to c\bar{c})$ process, an observed (expected) upper limit of 19.1 (18.4) times the SM predicted cross section times the branching ratio was set. These results represent significant improvements on the previous iterations of the ATLAS combination of resolved and boosted $VH(H \to b\bar{b})$ [180] and $VH(H \to c\bar{c})$ [194] analyses, particularly for $WH(H \to c\bar{c})$ where the upper limit is reduced by a factor of 2.5. The improvements are due to the implementation of a coherent treatment in terms of the flavor tagging strategy, the use of a BDT based discriminant in all analysis regimes, and the modelling of systematic uncertainties between $VH(H \to b\bar{b})$ and $VH(H \to c\bar{c})$.

The signal strength results were interpreted within the κ framework to set constraints on the couplings between the Higgs boson and the bottom and charm quarks. The constraints obtained for the κ_b and κ_c coupling modifiers were found to agree with the SM predictions.

The constraints are comparable to those obtained from a statistical combination of $VH(H \rightarrow b\bar{b})$ and $VH(H \rightarrow c\bar{c})$ measurements performed by the previous ATLAS $VH(H \rightarrow c\bar{c})$ analysis [194]. The current results were also used to set a constraint on the ratio of the coupling modifiers, κ_c/κ_b, without any assumptions on the Higgs decay width. The observed ratio was constrained to be $|\kappa_c/\kappa_b| < 4.9$ ($\kappa_c/\kappa_b| < 4.5$ expected) at the 95% CL.

Chapter 6

Performance of the ATLAS Seed Finding Algorithm for Run 3

The set of reconstructed tracks corresponding to the trajectories of charged particles produced in a collision at the Large Hadron Collider [251] and recorded by the ATLAS detector [75, 252] is an essential input for many downstream data reconstruction tasks such as jet reconstruction [148] and flavor tagging [159, 167], as well as for many physics analyses, including the one presented in Chapter 5. As described in Section 4.1.1, track reconstruction from ATLAS Inner Detector data [132] is based on a combinatorial variant of the Kalman filter algorithm [253] augmented by track candidate ambiguity resolution and a global χ^2 track fit. This algorithm achieves high track reconstruction efficiency and a low fake track creation rate, even in the challenging environment of LHC collisions. However, the Kalman filter algorithm is not self-initializing and needs an initial estimate of the parameters of a helical track that will then be refined by progressively incorporating information from sensitive detector elements. As the Inner Detector sensor elements by themselves only yield information about the crossing positions of the particles, a dedicated initial track candidate finding algorithm is needed to bridge the gap from space-points to track parameters – such algorithms are typically referred to as seed finding algorithms.

Seed finding algorithms need to achieve very high seed finding efficiency performance because any inefficiency at this stage cannot be recovered by the track finding stage. In addition, a low fake seed rate is also desirable in order to minimize the amount of reconstructed track candidates that are discarded during later stages. The combinatorics of track formation from space-points are especially challenging at the LHC, where, during Run 3, the expected number of inelastic proton-proton interactions per event, μ, has a distribution with a mean around 45 and a tail reaching upwards of 70.

This chapter presents a study of the performance of the seed finding algorithm used in the Run 3 ATLAS software. The material presented in this chapter was originally published as Ref. [1]. Some text modifications have been made in order to integrate this chapter with the rest of the thesis.

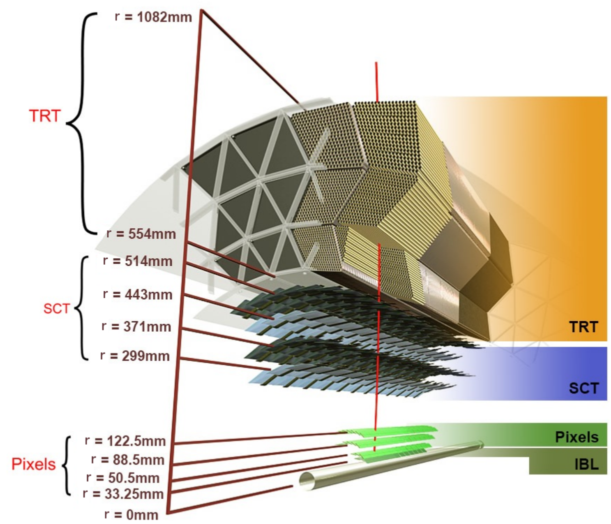

Figure 6.1: Cross-section illustration of the ATLAS Inner Detector showing each of the major elements with their active dimensions [254].

6.1 The ATLAS Detector

The ATLAS detector is a general-purpose, forward-backward symmetric, cylindrical particle detector with near complete coverage of the solid angle around the LHC interaction point[1]. From the inside-out, it comprises an inner tracking detector, electromagnetic and hadronic calorimeters, and a muon spectrometer installed within a toroidal magnet system.

The ATLAS sub-detector relevant for the study presented in this chapter is the Inner Detector, and a brief summary of its configuration for Run 3 [252] is provided in the following. The ID covers the pseudorapidity range $|\eta| < 2.5$ and is housed inside a thin superconducting solenoid which provides a 2 T axial magnetic field. The ID is composed of three sub-systems, as can be seen in Figure 6.1: a silicon Pixel Detector, a silicon Strip Detector (SCT), and the Transition Radiation Tracker (TRT). The Pixel Detector provides high-precision two-dimensional measurements per track. It comprises four barrel layers in the central region and three end-cap disk layers in the forward and backward regions. The nominal pixel size in the three outer barrel layers and in the end-cap disks is 50 μm $\times$ 400 μm, and the innermost barrel layer (IBL) [114] has finer grained sensors with a pixel size of 50 μm $\times$ 250 μm. The SCT detector has four barrel layers and nine end-cap disks in the forward and backward regions. Each module is made up of a pair of silicon strip sensors at a stereo angle

[1] ATLAS uses a right-handed coordinate system with its origin at the nominal interaction point (IP) in the center of the detector and the z-axis along the beam pipe. The x-axis points from the IP to the center of the LHC ring, and the y-axis points upward. Cylindrical coordinates (r, ϕ) are used in the transverse plane, with ϕ being the azimuthal angle around the z-axis. The pseudorapidity is defined in terms of the polar angle θ as $\eta = -\ln\tan(\theta/2)$.

of 40 mrad, each with a nominal strip pitch of 80 μm and with each strip providing a one-dimensional measurement. This subsystem provides precise one-dimensional measurement pairs for each charged particle intersection with a module. The TRT is a gaseous straw-tube detector providing typically 30 lower precision measurements per track at large radius.

6.2 Seed Finding Algorithm Description

The ATLAS seed finding algorithm [255] builds tracks using triplets of three-dimensional space-points, with each space-point being reconstructed from the measurements recorded by the detector elements. This requires a precise knowledge of the location and orientation of the ID active sensors, which is determined through the process of alignment [256]. As the measurements from the ID are not inherently three-dimensional, they are first converted to the appropriate representation in the lab-frame. The Pixel Detector yields two-dimensional measurements and the third dimension is defined by the sensor position, which means that the conversion is a simple coordinate transformation from the local frame of reference of the module to the lab-frame. The procedure is more complex for the SCT, because a particle crossing a module yields two one-dimensional measurements per module. The pair of measurements is combined into a single two-dimensional measurement using the stereo angle between the silicon strips on opposite module sides. A coordinate transformation from the local frame of reference of the module to the lab-frame is then performed, supplemented with a projective correction to obtain a three-dimensional space-point situated between the two strip clusters.

Seed tracks (seeds) are formed by identifying sets of three pixel or three SCT space-points. Seeds formed by a combination of pixel and SCT measurements are no longer considered as they were found to yield a high number of fake tracks at Run 3 pile-up levels. A set of geometrical cuts is used to build the seed tracks from triplets of space-points while minimizing the combinatorics. As the Pixel Detector is closest to the interaction point, the space-points from this subsystem are closer together, which means that the geometrical cuts are less efficient. To minimize the execution time, the seed finding and subsequent track finding pass proceed in three stages. First, seeds are formed from the SCT space-points which have a lower fake rate. Next, the Kalman filter-based track finding algorithm is run starting from the SCT seeds. The SCT seeds are then used to compute a region-of-interest (ROI) in z corresponding to the luminous region of the bunch crossing. Finally, seed and track finding are performed in the Pixel Detector, discarding seeds whose z parameter falls outside the ROI.

Seed finding proceeds by first segmenting the 3D space of the Pixel or SCT detector into bins of $\phi - z$, which are optimized according to the maximum azimuthal deflection given the position of the sensitive layer on the detector and the lowest allowed seed p_{T} value (450 MeV, which corresponds to 90% of the track finding p_{T} cut of 500 MeV). When moving radially outwards from the interaction point, the central space-points for the seeds are identified in each bin. For each central space-point, lists of space-points from detector layers above and below the central space-point, referred to as top and bottom candidates, respectively, are identified in the same or neighboring $\phi - z$ bins. The selection of neighboring $\phi - z$ bins is based on geometrical assumptions relative to the interaction point, while the collection of central, top, and bottom space-point candidates within the considered bins relies on geometrical requirements derived from the detector layout. For instance, the radial position of the central space-point and the radial positions of the top and bottom space-point candidates, along with the maximum and minimum distance (in r and z) between them and the central space-point, are taken into account.

Individual top and bottom space-point candidates are then filtered based on the angle in $z - r$ space between the candidate and the central space-point, in order to quickly remove seed tracks likely to have $|\eta| > 2.7$. A cut is also imposed on the z value of each segment extrapolated to the beam line, $z(r = 0)$, in order to quickly remove seeds which are outside the acceptance in z. For SCT seeds, the cut values are set to $|z(r = 0)| < 250$ mm, while for pixel seeds they are set based on the ROI computed from the SCT-seeded track finding pass.

At this point, the algorithm works out which space-point doublets, bottom-central and central-top space-point combinations, can successfully build up seeds. This is done by checking the compatibility between the $r - z$ slopes of the bottom-central and central-top space-point doublets, assuming the largest possible multiple scattering effect given the minimum allowed p_{T} value. Exploiting the inverse conformal transformation, the p_{T} of the seed candidates is measured to further reject space-point combinations; it is required to be larger than 450 MeV and is used to refine the multiple scattering term for the $r - z$ slopes compatibility of the seed space-point doublets. The remaining seed candidates are described using the perigee parametrization [130] $\tau = (d_0, z_0, \phi, \theta, q/p)$, where the parameters define the seed track at the point of closest approach in the transverse plane with respect to the beam spot. The transverse impact parameter d_0 represents the distance of closest approach in the transverse plane, while the longitudinal impact parameter z_0 gives the z-coordinate of the track at the point of closest approach. ϕ and θ are the azimuthal and polar angle of the seed track, respectively. The ratio q/p is the charge q multiplied by the inverse of the momentum p and is determined from the measurement of the track curvature. The remaining space-point triplet combinations are required to fulfill $d_0 < 5$ mm.

Each seed is then assigned a quality score which emphasizes seeds with small d_0 and small curvature in the longitudinal plane. During the scoring phase, each seed is checked for compatibility with an extra space-point, by exchanging the topmost space-point for one in a different layer and verifying that the resulting seed has a curvature in the transverse plane that is compatible with the original seed. If such a space-point is found, the seed is deemed "confirmed" and receives a scoring bonus. Otherwise, the d_0 cut is tightened by an amount proportional to the curvature of the seed in the longitudinal plane. The resulting quality score determines which seeds are ultimately kept, separately for pixel and SCT seeds. For the pixel case, all confirmed seeds are kept, otherwise at most one seed per central space-point is kept. For the SCT case, at most five seeds per central space-point are kept.

To reduce the number of duplicate tracks, seeds for which all space-points are used by already found tracks are discarded at the start of the subsequent track finding stage. As this study considers the seeding algorithm before the track finding stage, these duplicate seeds are included in the results presented in Section 6.4.

6.3 Simulated Datasets and Performance Metrics

All metrics are evaluated on a sample of $t\bar{t}$ events modelled using the Powheg Box v2 [62–64, 211] generator at NLO with the NNPDF3.0nlo [198] PDF set and the h_{damp} parameter[2] set to 1.5 m_{top} [257]. The events were interfaced to Pythia 8.230 [58] to model the parton shower, hadronization, and underlying event, with parameters set according to the A14 tune [258] and using the NNPDF2.3lo set of PDFs [54]. The decays of bottom and charm hadrons were performed by EvtGen 1.6.0 [259]. The effect of multiple interactions in the same and neighboring bunch crossings (pile-up) was modelled by overlaying the simulated hard scattering event with inelastic proton-proton events generated with Pythia 8.186 [260] using the NNPDF2.3lo set of parton distribution functions [54] and the A3 set of tuned parameters [261]. The nominal number of overlaid pp collisions was sampled uniformly in the $\mu \in (0, 80)$ range for each signal event, with the actual number sampled from a Poisson distribution. The generated events are then processed through a simulation of the ATLAS detector and reconstructed using an extensive software suite [262], the same that is used for real collision data.

To determine the performance of the seed finding algorithm, seeds are linked to their most likely truth particle by tracing the origin of the seed measurements (clusters), using the following procedure. For each seed, a seed-truth particle matching probability is computed by dividing the number of measurements that the seed has in common with the truth particle by the total number of measurements per seed. Each seed has three measurements for pixel seeds and six for SCT seeds, because each SCT space-point is made up of two measurements. The truth matching probability is computed for all the truth particles that have measurements in common with the seed. The truth particle with the highest matching probability is chosen as the best truth match for the seed. If no matching truth particle is found, the seed is assigned a truth matching probability of zero. This procedure is repeated for all seeds in the event.

To determine the seed finding efficiency, the seed-to-particle mapping is inverted using the seed-truth matching probabilities. If all the potential seed matches for a truth particle have a matching probability of less than 50%, the particle is considered to have no seed match, otherwise it is matched to one or more seeds.

The performance metrics considered in this study are: seed finding efficiency, seed duplication rate, seed fake rate, and seed parameter resolutions. The seed finding efficiency, seed duplication rate, and seed parameter resolutions are computed using the truth parti-

[2] The h_{damp} parameter is a resummation damping factor and one of the parameters that controls the matching of Powheg matrix elements to the parton shower and thus effectively regulates the high-p_{T} radiation against which the $t\bar{t}$ system recoils.

cles that pass the selection cuts shown in Table 6.1. The transverse momentum, p_{T}, and pseudorapidity selection criteria correspond to the reconstructed p_{T} and the ID acceptance, respectively. Stable particles are labeled as such during event generation and identify those particles that are included in the final state produced by the Monte Carlo generator. Particles produced from interactions with the detector material are excluded. Particles produced near the interaction point are selected with a requirement on the production vertex radius.

Property	Selection
Stable & charged	True
p_{T}	> 500 MeV
$\lvert\eta\rvert$	< 2.5
Production vertex radius	< 30 mm

Table 6.1: Acceptance cuts applied to the truth particles.

The seed finding efficiency is defined as the fraction of truth particles that are matched to at least one seed. This quantity is computed inclusively for all the seeds, as well as separately for pixel and SCT seeds. The pixel (SCT) seeding efficiency is defined as the fraction of truth particles that are matched to at least one pixel (SCT) seed.

The seed duplication rate is defined as the fraction of truth particles matched to at least two seeds. This metric is computed inclusively for all seeds as well as separately for pixel and SCT seeds, in which case the definition is modified to include the requirement that more than 50% of the seed matches per particle originate from pixel or SCT seeds, respectively.

A seed is considered to be fake if its seed-truth particle matching probability is less than 50%, in which case the seed is likely arising from random combinatorics or includes space-points arising from noise. The fraction of fake seeds (fake rate) is computed inclusively for all seeds, as well as separately for pixel and SCT seeds.

Seed parameter resolutions are determined for the transverse impact parameter d_0, the longitudinal impact parameter z_0, and the ratio q/p_{T}, computed as $q/p_{\mathrm{T}} = q/p \cdot 1/\sin\theta$. For each parameter, the resolution is defined as the root-mean-square (RMS) of the truncated residual between the true parameter value and the parameter value estimated from the seed. The resolution metrics are computed separately for pixel and SCT seeds by restricting the calculation to truth particles where the best matching seed is a pixel or SCT seed, respectively.

6.4 Results

The seed finding efficiency and seed duplicate rate are shown in Figure 6.2. As shown in the top plots, the efficiency for SCT seeds is observed to be lower in the end-caps and at low p_{T}. The overall efficiency stays high over the whole phase space, but shows a slight trend with

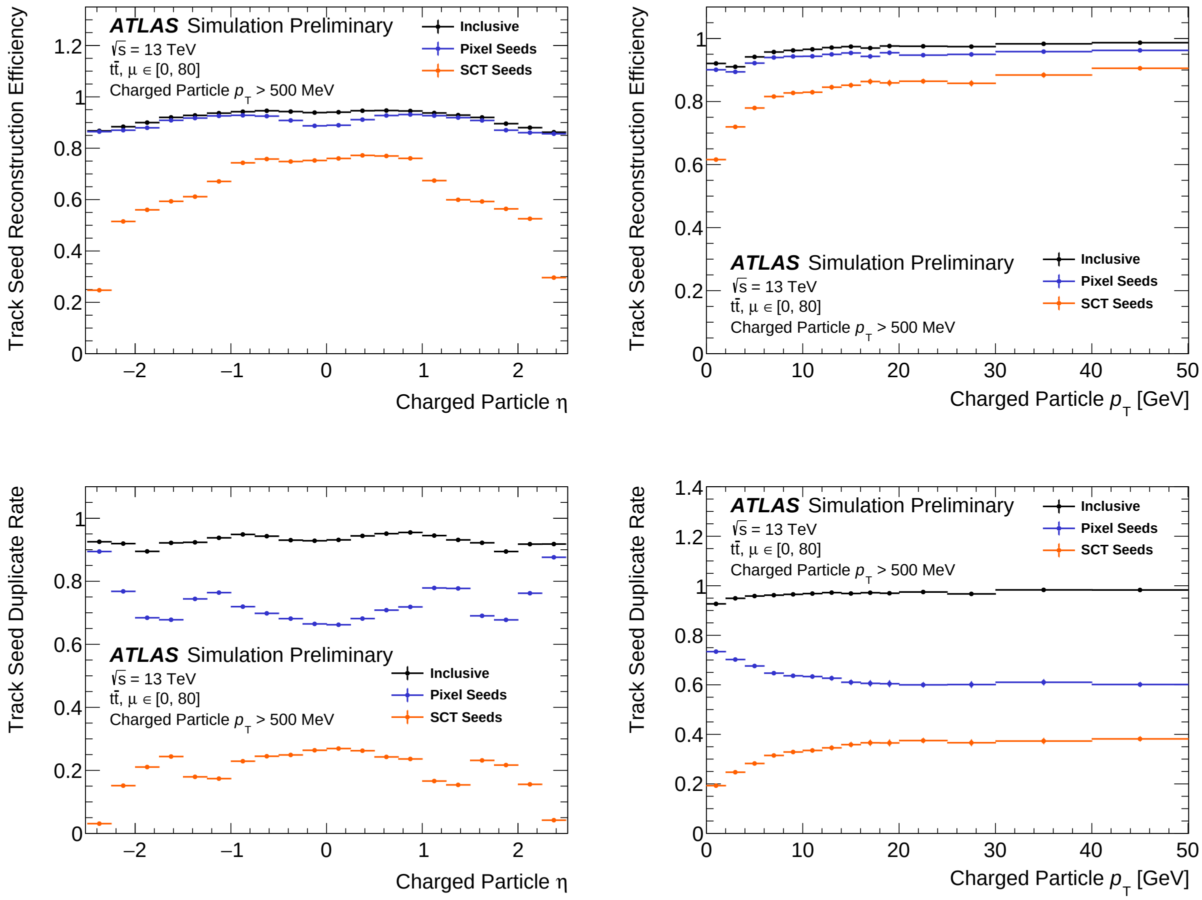

Figure 6.2: Seed track finding efficiency (top) and duplicate rate (bottom) as a function of the true charged particle η (left) and p_{T} (right). These metrics are defined as the fraction of particles to which at least one or two seeds are matched, respectively. The particles considered must be stable, charged, and satisfy $p_T > 500$ MeV, $|\eta| < 2.5$, and $R_{\text{prod}} < 30$ mm. The efficiency metric includes particles not reconstructed due to material interactions.

lower efficiency in the end-caps ($\sim 85\%$) compared to the barrel ($\sim 95\%$). This definition of efficiency includes particles lost to hadronic interactions with the ID material [263], and less importantly due to sensor inefficiency, gaps in the geometry and dead detector channels and modules.

The duplicate rates shown in the bottom plots of Figure 6.2 and fake rates shown in Figure 6.3 are found to be lower for SCT seeds than for pixel seeds. This behavior is expected, since the higher density of space-points in the Pixel detector, due to its closeness to the interaction point, leads to more combinatorial seed candidates.[3]

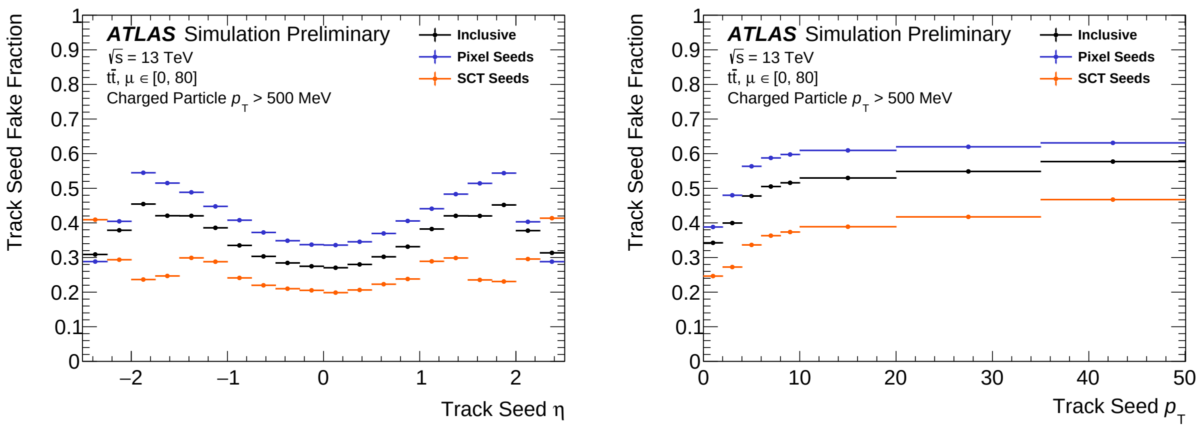

Figure 6.3: Seed track fake rate as a function of seed η (left) and p_{T} (right).

Figure 6.4 shows the dependence of the efficiency, duplicate rate, and fake rate on the number of proton-proton interactions, μ, in an event. As expected, the fake rate increases with μ due to increased ambiguity in space-point combinations in higher-occupancy events. The seeding efficiency drops slightly with μ due to pattern recognition and seed selection mistakes arising from the harder combinatorics. The duplicate rate also drops slightly with μ for the same reason.

The seed parameter resolutions are shown in Figure 6.5. As a function of the truth particle transverse momentum, the transverse (d_0) and longitudinal (z_0) impact parameter resolutions (top right and middle right plots) are better for pixel seeds, owing to the closeness of the Pixel Detector to the beam line and the finer segmentation of pixel sensors. As can be seen in the equivalent η-dependent distributions (top left and middle left plots of Figure 6.5), this behavior depends on the particle's angle of production with respect to the beam line. This is primarily due to the variation in the amount of detector material as a function of η, which results in better resolution at central η where the material in minimized. The pixel seed z_0 resolution has a slight degradation at low $|\eta|$, due to the smaller track length when projected into the longitudinal plane and a projective effect owing to the perigee being defined with respect to d_0, causing uncertainties in d_0 to transfer to z_0.

The relative seed p_{T} resolution is shown in the bottom plots of Figure 6.5. The η-dependence similarly depends on the amount of detector material, but the SCT seed p_{T} resolution is better than the pixel seed p_{T} resolution due to the longer lever arms of the SCT seeds.

[3] While there is a relationship between duplicate rate and time spent in the subsequent track reconstruction stage, some amount of duplication is desirable for robustness against potential seeding inefficiencies.

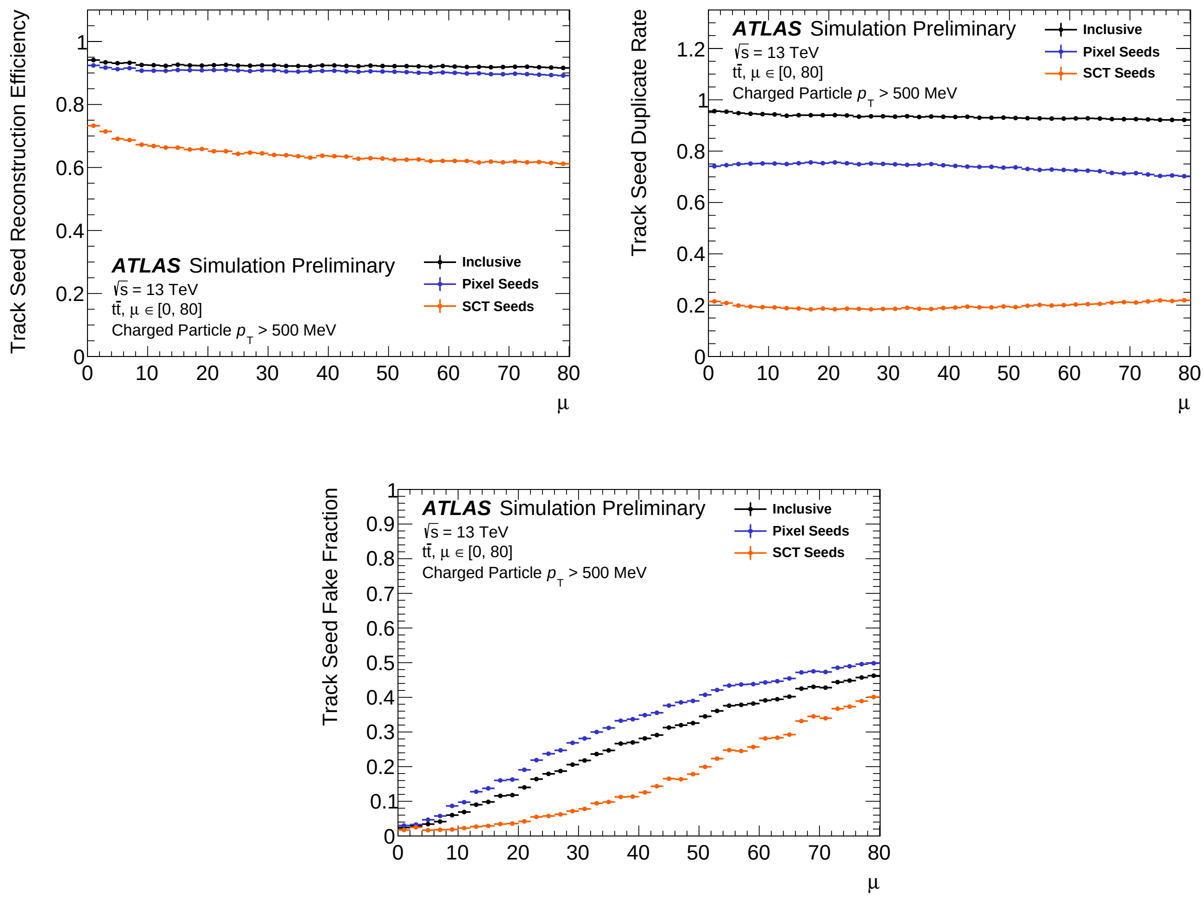

Figure 6.4: Seed track finding efficiency (top left), duplicate rate (top right), and fake rate (bottom) as a function of the number of proton-proton interaction per event (μ). The particles considered must be stable, charged, and satisfy $p_T > 500$ MeV, $|\eta| < 2.5$, and $R_{\text{prod}} < 30$ mm. The efficiency metric includes particles not reconstructed due to material interactions.

6.5 Conclusions

This chapter presented the implementation and performance of the seed finding algorithm used to initialize the Kalman filter-based track finding algorithm. As the efficiency of the seed finding stage represents an upper limit on the subsequent track finding algorithm used for Run 3 reconstruction, the seeding efficiency must be very high, and it was shown to be $85\% - 95\%$ (compatible with the expected efficiency loss due to hadronic interactions) in $t\bar{t}$ events for a fiducial selection of stable and charged particles with $p_{\text{T}} > 500$ MeV, $|\eta| < 2.5$, and production radius < 30 mm. This comes with comparatively high duplicate and fake track seed creation rates, the latter depending directly on the number of interaction per bunch crossing, μ. The seeding algorithm has been extensively optimized for Run 3, but since the high-luminosity upgrade of the LHC (HL-LHC), slated to begin operation around 2029, is expected to have μ up to 200 – well in excess of the average value of $\langle\mu\rangle = 45$ seen in Run 3 – the seed finding algorithm is being revisited to cope with the much harder combinatorics. Its configuration is also being updated to exploit the characteristics of the ATLAS Inner Tracker (ITk) [115, 264], which will replace the current Inner Detector in time for the inauguration of the HL-LHC.

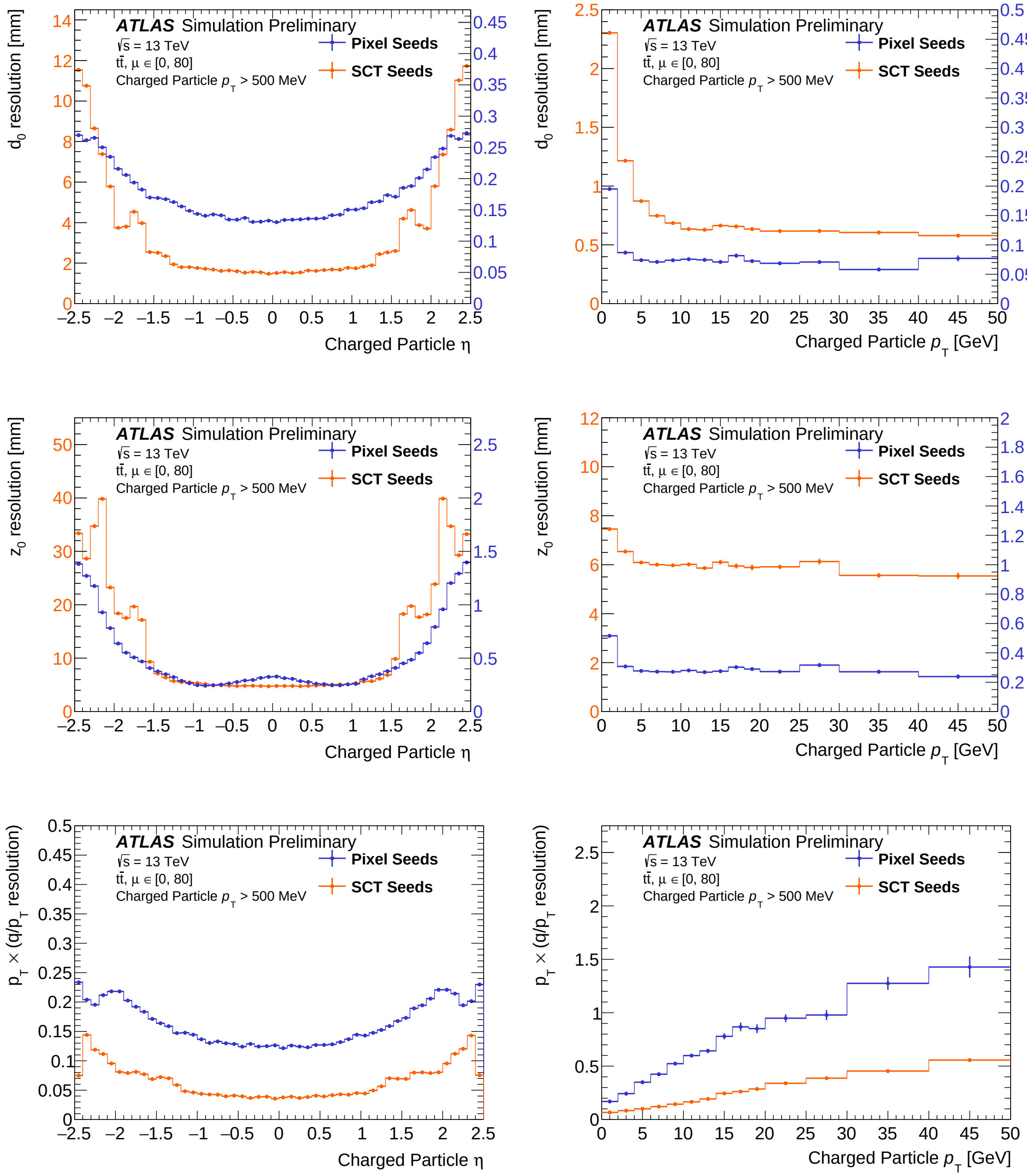

Figure 6.5: Seed track parameter resolutions: d_0 (top), z_0 (middle), and relative p_{T} (bottom) as a function of the true charged particle η (left) and p_{T} (right). The resolution is defined as the root-mean-square (RMS) of the residual in a given η or p_{T} bin. The particles considered must be stable, charged, and satisfy $p_T > 500$ MeV, $|\eta| < 2.5$, and $R_{\mathrm{prod}} < 30$ mm.

Chapter 7

Fast Track Reconstruction for the High-Luminosity LHC

As mentioned in Chapter 3, in preparation for the expected increase in instantaneous luminosity and pile-up at the High-Luminosity LHC, the ATLAS experiment has developed a Phase-II detector upgrade program. Key parts of the upgrade program are the replacement of the Inner Detector with the Inner Tracker, a new all-silicon detector designed for optimal track reconstruction in high pile-up conditions, and the upgrade of the ATLAS Trigger and Data Acquisition System, which will consist of a hardware-based Level-0 Trigger, a Data Acquisition System, and the Event Filter System. Details about the ITk detector layout and the upgraded TDAQ system can be found in Section 3.4.

Since the reconstruction of complex event scales combinatorially with increasing levels of pile-up, the track reconstruction software for the ITk was also modified to minimize the total processing time per event, in order to stay within the limited computing budget even in conditions of as many as 200 pile-up interactions per event. Figure 7.1 demonstrates how the careful tuning of the offline track reconstruction for ITk leads to event processing times that are expected to be smaller than the corresponding processing times for Run 2 software for pile-up levels of $\langle\mu\rangle = 60$. On the TDAQ side, the EF will run different event reconstruction algorithms, such as track reconstruction, topological clustering, and muon reconstruction. One of the options being considered for track reconstruction consists of running algorithms on commercially available CPUs[1].

Currently, software-based track reconstruction at ATLAS is performed in two regimes: the online regime, which is used at trigger level for quick event selection, and the offline regime, which is used for full event reconstruction of data that passed the trigger and is saved on permanent storage for later use. The proposal for track reconstruction at the EF level would then be based on using a version of the offline ATLAS ITk track reconstruction chain that is adapted for running at trigger level. Since the latency requirements for the trigger reconstruction ($\ll 1$ s) are much stricter than for offline reconstruction (~ 10 s), the

[1] Other options being considered are commercially available accelerators such as GPUs and FPGAs [2].

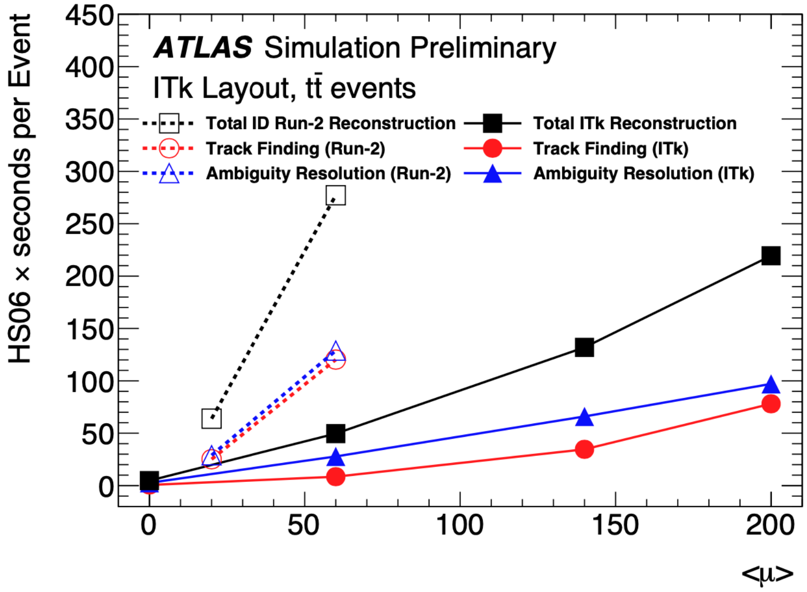

Figure 7.1: Total CPU time required to reconstruct $t\bar{t}$ events with the ITk as a function of average pile-up [128]. Also shown are the CPU times required for Silicon Track Finding and Ambiguity Resolution. The performance of the Run 2 track reconstruction is shown for events with average pile-up of 20 and 60.

offline ITk track reconstruction chain must be modified to achieve low event reconstruction times while still maintaining a high level of tracking performance. This approach is based on using the fast ITk track reconstruction chain, a prototype version of track reconstruction that was developed to have significantly reduced CPU requirements compared to the offline ITk reconstruction chain [265]. The fast ITk prototype was also previously found to be suitable as a software-based solution for track reconstruction at the EF [266, 267].

This chapter presents a study of the CPU timing and tracking performance of the fast ITk track reconstruction chain. While the fast ITk track reconstruction prototype was initially developed with the goal of reducing the CPU requirements for offline event reconstruction at the HL-LHC, this chapter focuses on more recent developments, such as porting the algorithm to a software release appropriate for Run 4 and other code improvements, considered within the context of an updated Technical Design Report (TDR) concerning the EF implementation for the Phase-II upgrade of the ATLAS Trigger and Data Acquisition System [2]. The particular ITk layout used for the study presented in this chapter is identified by tag 22-02-00, for which a schematic view is shown in Figure 3.9. The results presented in this chapter were used to demonstrate the feasibility of the updated fast ITk track reconstruction as a software-based solution for tracking at the EF level within the previously mentioned TDR, which also explored options for running track reconstruction on GPU and FPGA accelerators.

7.1 The Offline ITk Track Reconstruction Strategy

As the fast ITk track reconstruction is derived from the offline track reconstruction strategy, this section provides a summary of the main steps of the offline ITk reconstruction chain [127, 128]. Within this chapter, the offline reconstruction chain is also referred to as the default reconstruction chain, since track reconstruction is performed with the offline algorithms by default and a specialized configuration is needed to run the fast ITk reconstruction chain.

The first step in the default ITk track reconstruction chain consists of decoding the raw data from the detector. The readout chip for the ITk Strip detector will provide hits that are already clustered (that is, energy deposits in neighboring sensors that originate from the same particle are grouped together into clusters). The hits will then need to be converted into C++ objects by the Strip Cluster Finding algorithm. For the Pixel detector, the readout chip will provide the hit information in a compressed format. The Pixel Cluster Finding algorithm will then perform a 2D connected component analysis to find the hit clusters and will apply an analogue calibration algorithm[2] [127] to determine the location of the clusters.

The next step in the reconstruction chain consists of running the Space Point Finding algorithm. For the Pixel detector, the Space Point Finding algorithm essentially provides a copy of the pixel cluster information in the form of a different C++ object type. For the Strip detector, hits from both sides of a barrel stave or end-cap petal are combined, using the small stereo angle information, into a 3D measurement. This step is more complicated for the ITk due to the large distance between the strip modules on both sides of a stave or petal.

The Pixel and Strip space-points are then used to reconstruct track candidates, a task which is performed by the Silicon Track Finding algorithm. The algorithm begins by constructing initial track estimates (seeds) from combinations of either three Pixel or Strip space-points. After some initial quality cuts are applied, the seed space-point triplets are checked for compatibility with an extra space point in a 4th layer, to further reject combinations arising from random combinatorics or noise. A search road is then defined for each seed, which contains detector modules that have clusters compatible with the estimated trajectory of the seed. A combinatorial Kalman filter is used to find all the track candidates that are compatible with the initial seed and that pass some loose candidate selection cuts.

The collection of track candidates found by the Silicon Track Finding algorithm is then used by the Ambiguity Resolution algorithm to select the final tracks. A χ^2 track fit is performed to remove bad quality tracks and outlier clusters (clusters that give too large contributions to the fit χ^2). The track parameter resolution estimation is also performed at this point using the full detector material model. The Ambiguity Resolution algorithm uses a Neural Network based cluster splitting [136] to improve the track reconstruction efficiency in the core of high p_{T} jets and applies the final track selection cuts.

[2] The analogue calibration uses the analogue information capabilities of the read-out chip to interpolate the charge measurement of the first and last pixel hits, which leads to an improvement in the precision of the cluster positions.

Requirement	Pseudorapidity range		
	$\lvert\eta\rvert < 2.0$	$2.0 < \lvert\eta\rvert < 2.6$	$2.6 < \lvert\eta\rvert < 4.0$
Pixel+Strip hits	≥ 9	≥ 8	≥ 7
Pixel hits	≥ 1	≥ 1	≥ 1
Holes	< 2	< 2	< 2
p_{T} [MeV]	> 900	> 400	> 400
$\lvert d_0\rvert$ [mm]	≤ 2	≤ 2	≤ 10
$\lvert z_0\rvert$ [cm]	≤ 20	≤ 20	≤ 20

Table 7.1: Tracking cuts used in the default ITk track reconstruction, as a function of pseudorapidity range [128]. Holes are recorded when the track candidate crosses active sensors where no hit is found. The transverse d_0 and longitudinal z_0 impact parameters are defined with respect to the mean position of the beamspot.

The track selection cuts used in the default ITk reconstruction chain are summarized in Table 7.1. Different cuts are applied in different pseudorapidity bins to account for variations in hit coverage and expected resolutions. The default ITk reconstruction cuts have been tuned to be much tighter than the Run 2 tracking cuts [268] in order to reduce the effects of the increased number of hits coming from the higher levels of pile-up. As a result, the fake rate for the ITk is expected to be two to three orders of magnitudes lower than the corresponding fake rate for the Run 2 detector.

7.2 The Fast ITk Track Reconstruction Strategy

The starting point for the fast reconstruction prototype was the default ITk track reconstruction implementation available in software release[3] 20.20 and the performance of this initial version of the fast ITk track reconstruction is presented in Ref. [265]. The results of the study presented in this chapter are obtained with a newer version of the fast ITk track reconstruction algorithm as implemented in software release 21.9, which collects algorithmic developments and improvements relevant for Run 4. This section provides a summary of the main algorithmic changes and improvements implemented in the latest fast ITk reconstruction version available at the time of this study.

The default ITk reconstruction time is dominated by the Ambiguity Resolution step (see Table 2 in Ref. [265]), with about 60% of the input track candidates passing this step. In order to improve the CPU times, the Ambiguity Resolution algorithm is omitted from the fast ITk reconstruction chain. It is instead replaced by a tighter track selection in the Silicon Track Finding (including limiting the number of shared hits between output

[3] The ATLAS software release system is described at the beginning of Chapter 4.

tracks), which has a similar effect of reducing the number of duplicate and fake tracks. Track parameter estimation is obtained from the fast Kalman filter track fit, which is applied by the combinatorial filter in the Silicon Track Finding algorithm. While the fast Kalman filter uses the offline cluster calibrations (i.e. the analogue calibration mentioned in Section 7.1), it still applies some approximations to the material model calculations in order to reduce computation times. Hence, the fast Kalman filter track fit is expected to produce slightly degraded resolutions compared to the full offline track fit.

Due to the change in detector layout and the significant increase in pile-up, the seed finding step of the Silicon Track Finding also has an increased computational footprint when running the default ITk track reconstruction chain. For example, the fraction of CPU time spent in seed finding increases from $\sim 20\%$ in Run 2 to up to 50% for the ITk in a sample with average pile-up of 200. Thus, in the fast ITk reconstruction chain, the seed finding step is modified to reduce the execution time and a careful tuning of the selection cuts is performed to improve the purity of the output seed collection. The improvements in seed finding subsequently reduce the CPU time spent in the road building and combinatorial track finding steps, which then significantly reduces the overall CPU time needed for reconstruction. As the five layer Pixel Detector covers the full ITk pseudorapidity range $-4 < \eta < 4$, the fast ITk track reconstruction version of Seed Finding uses only Pixel hit combinations, omitting the Strip seed iteration.

Additionally, the cut on the final number of hits and non-shared hits is moved from the Ambiguity Resolution to the Silicon Track Finding to remove duplicate and fake track candidates from the output track collection. Other changes implemented for the fast ITk reconstruction include raising the p_{T} cut in the central region from 900 MeV to 1 GeV and setting the longitudinal impact parameter cut to $|z_0| < 150$ mm to match the length of the beam interaction region for HL-LHC. Table 7.2 provides the full list of changes implemented in the fast ITk version of Silicon Track Finding compared to those used in the default ITk version. As mentioned in Section 4.1.1, an optional procedure can be performed during the track finding step to allow for the correct reconstruction of tracks that show kinks (changes in the track direction) due to electrons emitting Bremsstrahlung photons. This is referred to as Bremsstrahlung recovery and is used to improve the efficiency of electron reconstruction. For the results presented in this study, the optional Bremsstrahlung recovery procedure is temporarily disabled in the Silicon Track Finding step.

The Pixel Space Point Formation and Strip and Pixel Clustering have been previously optimized to improve the CPU times of the fast ITk track reconstruction [266]. In software release 21.9, these improvements were ported to the default ITk reconstruction as well, leading to minimal differences in the timing performance between the default and fast ITk reconstruction. The only difference consists of a reduction in the number of neighboring pixels used during clustering, from 8 for the default pixel clustering to 4 for the fast clustering. Additionally, space points are only used during reconstruction to find track seeds. As the fast ITk reconstruction leaves out the Strip seed iteration, the CPU time is further reduced by also omitting running Space Point Finding on the Strip clusters.

Unlike the Inner Detector, the ITk Pixel Detector will use the RD53 readout chip [269]

Requirement	Pseudorapidity range		
	$\lvert\eta\rvert < 2.0$	$2.0 < \lvert\eta\rvert < 2.6$	$2.6 < \lvert\eta\rvert < 4.0$
Pixel+Strip hits	≥ 9 (7)	≥ 8 (7)	≥ 7 (7)
Unique hits	≥ 7 (1)	≥ 6 (1)	≥ 5 (1)
Shared hits	≤ 2 (no cut)	≤ 2 (no cut)	≤ 2 (no cut)
p_{T} [MeV]	> 1000 (900)	> 400 (400)	> 400 (400)
$\lvert z_0\rvert$ [cm]	≤ 15 (20)	≤ 15 (20)	≤ 15 (20)

Table 7.2: Tracking cuts used in the Silicon Track Finding for the fast (default) ITk track reconstruction, as a function of pseudorapidity range [2, 265]. The longitudinal impact parameter z_0 is defined with respect to the mean position of the beamspot.

that features improved data compression. For a sample of $t\bar{t}$ events with $\langle\mu\rangle = 200$, the average event size is expected to be 1.6 MB for the Pixel Detector (compared to 0.5 MB for the Strip Detector). The unpacking of the ITk Pixel and Strip raw data (byte stream decoding) is expected to take a similar amount of time per kB as unpacking the current raw data. Hence, the CPU time spent on Pixel and SCT raw data decoding is measured for the Inner Detector using a sample of high pile-up events from 2017. Then, the results are scaled by the ITk event size for Pixel and Strip raw data for $\langle\mu\rangle = 140$ and 200. For simulation, the decoding of the byte stream raw data has to be replaced by the decoding of the file containing the simulated hits.

7.3 Performance of the Fast ITk Track Reconstruction

The CPU and tracking performance of the fast ITk track reconstruction algorithm have been previously presented in Refs. [265] and [267]. The results presented in this section have been generated using a newer software release (21.9), an updated detector geometry, and additional tuning of the track reconstruction algorithm. The simulated MC samples used for this study were generated using $50 \times 50\ \mu\mathrm{m}^2$ pixel sensors[4].

7.3.1 CPU Performance

The CPU performance of the fast ITk track reconstruction is studied on $t\bar{t}$ samples with average pile-up values of 140 and 200. The timing numbers are reported in units of HEP-SPEC06 (HS06), which represents the default benchmark for high-energy physics (HEP)

[4] To further improve the b-tagging performance, the final ITk design will use 3D pixel sensors with a pitch of $25 \times 100\ \mu\mathrm{m}^2$ for pixel layer-0 in the barrel staves. Details can be found in Ref. [270].

applications [271] at the time of this study. The performance of a particular CPU model is rated in HS06 per core (e.g. 11 HS06 per core); often, this number can be looked up on the HEPiX website [272], which contains a database of HS06 scores for a range of CPU models. In case a particular CPU cannot be found in the HEPiX database, the performance can be measured directly using a dedicated benchmarking suite, which consists of running a subset of tests (from a commercially available benchmark suite) with configurations appropriate for HEP computing workloads[5]. Once the HS06 score for a CPU model is determined, the CPU time needed to run an algorithm can then be computed in HS06 $\times$ second by multiplying the run time in seconds by the HS06 score for the CPU model.

$\langle\mu\rangle$	Tracking	Release	Byte Stream Decoding	Cluster Finding	Space Points Finding	Si Track Finding	Ambiguity Resolution	Total ITk
140	default	21.9	2.2	6.1	3.4	33.9	40.3	85.9
	fast			6.1	1.2	14.6	–	24.1
200	default	21.9	3.2	8.1	4.9	73.8	63.9	153.9
	fast			7.9	1.6	25.7	–	38.4

Table 7.3: CPU times required to reconstruct $t\bar{t}$ events with average pile-up of 140 and 200 using the default and fast ITk track reconstruction chains. The times are reported in HS06 $\times$ seconds and shown for the different stages in the track reconstruction chain.

The HS06-scaled CPU times are shown in Table 7.3 for both the default and fast ITk track reconstruction. The numbers corresponding to the Byte Stream Decoding step are estimated as described in Section 7.2. For the other steps of the reconstruction chain, the CPU times are measured using the Cori supercomputer provided by the National Energy Research Scientific Computing Center (NERSC), a U.S. Department of Energy Office of Science User Facility located at Lawrence Berkeley National Laboratory. Each Cori computing node is running an Intel Xeon E5-2698 v3, 2.3 GHz CPU with a total of 32 cores, that has an estimated performance score of 19.4 HS06 for single core running (measured directly with the benchmarking suite as outlined in the previous paragraph). For consistency, the same computing node is used to measure the performance for both the default and fast ITK track reconstruction.

The CPU timing results show that the fast version of Silicon Track Finding is slightly more than five times faster than the combined Silicon Track Finding and Ambiguity Resolution steps for the default ITk reconstruction for both $\langle\mu\rangle = 140$ and 200. The fast Silicon Track Finding is about 1.8 times faster for the $\langle\mu\rangle = 140$ sample compared to the $\langle\mu\rangle = 200$ sample.

[5] The latest version of the HS06 suite was released in September 2011, hence running the benchmarks on more recent CPU architectures involves a non-negligible amount of code adjustments, which are necessary in order to properly compile the source code and run the benchmarking executable programs. The source code adjustments can vary depending on the combination of CPU and operating system under test, and, for this study, were determined on a trial-and-error basis.

About 40% of the CPU time required for the fast ITk track reconstruction is spent on Byte Stream Decoding, Cluster Finding, and Space Points Finding. Adding the CPU needs for all steps in the reconstruction chain, the total time for the fast ITk reconstruction is 3.6 (4.0) times smaller than that for the default ITk reconstruction for the $\langle\mu\rangle$= 140 (200) sample[6].

The fast ITk reconstruction in software release 21.9 has also been updated to account for an increase in the amount of passive material, particularly due to the services in the Inner Support Tube, and to use more precise cluster calibrations. As a result, the tracking performance of the fast ITk reconstruction is now expected to be closer to the default ITk tracking performance, as will be shown in the next section.

7.3.2 Tracking Performance

The tracking performance is studied on simulated samples consisting of single muon samples with $p_{\mathrm{T}} = 2$ GeV and 100 GeV and $t\bar{t}$ samples with $\langle\mu\rangle = 140$ and 200. The former are used to illustrate the technical performance of the track reconstruction algorithms, while the latter are used to estimate the tracking performance in hadronic jet events with levels of pile-up similar to those expected at the HL-LHC. For the performance plots corresponding to the $t\bar{t}$ samples, a p_{T} cut of 2 GeV is applied to the truth particles in order to avoid turn-off effects stemming from the track reconstruction efficiency (defined below) variation at the reconstruction p_{T} cut of ~ 1 GeV.

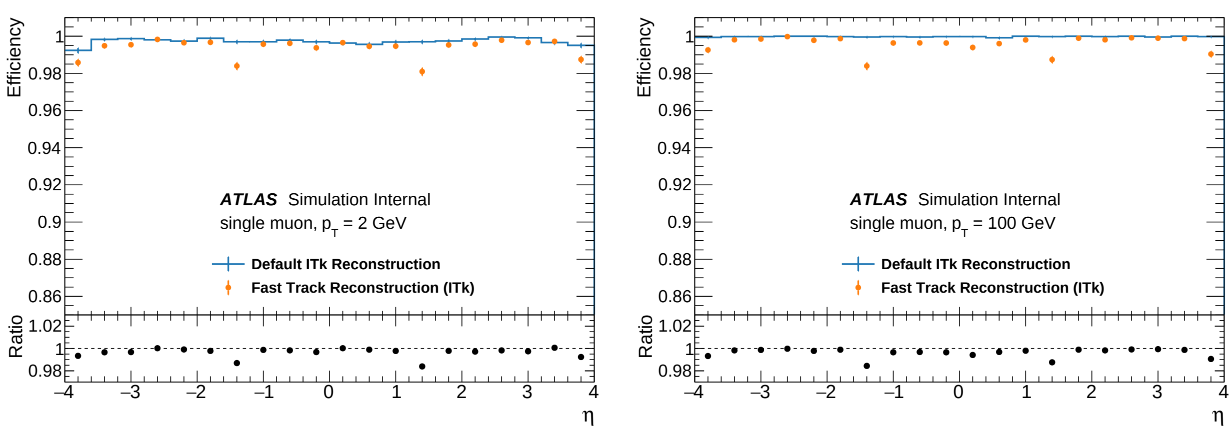

Figure 7.2: Track reconstruction efficiency as a function of pseudorapidity for single muon samples with p_{T} of 2 GeV (left) and 100 GeV (right) for the default and fast ITk track reconstruction. The ratio corresponds to dividing the efficiency for the fast reconstruction by the efficiency for the default reconstruction.

[6]The CPU performance results presented in Ref. [2] include additional CPU optimizations to the fast ITk track reconstruction chain, which reduce the timing requirements by an additional 5% – 10% compared to what is shown in this study.

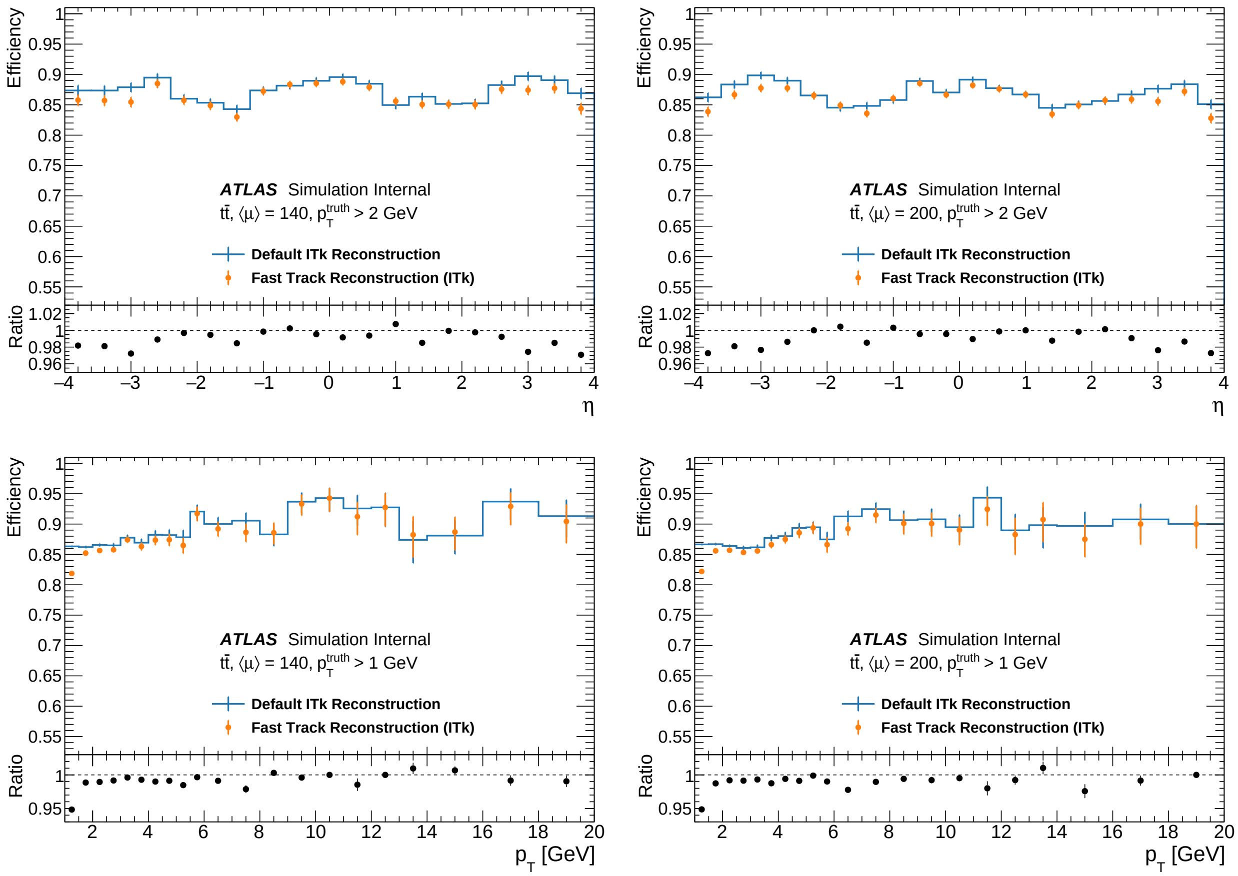

Figure 7.3: Track reconstruction efficiency as a function of η (top) and p_{T} (bottom) for $t\bar{t}$ samples with average pile-up of 140 (left) and 200 (right) for the default and fast ITk track reconstruction. To avoid turn-on effects, a 2 GeV p_{T} cut is used for the generated particles. The ratio corresponds to dividing the efficiency for the fast reconstruction by the efficiency for the default reconstruction.

The track reconstruction efficiency is defined as the fraction of particles for which at least one good-quality track can be reconstructed given the measurements recorded in the detector. This metric is shown in Figure 7.2 as function of η for single muon samples and for both the default and fast ITk track reconstruction chains. For both 2 GeV and 100 GeV muons, the efficiency of the fast ITk reconstruction is generally found to be very similar to the efficiency of the default ITk reconstruction. However, the fast ITk reconstruction does have slightly lower efficiency at $|\eta| \sim 4$ and in the barrel/end-cap transition region of the Strip Detector (see Figure 3.9). These losses in efficiency are a result of the preliminary status of the parameter tuning for the fast track reconstruction algorithm.

Figure 7.3 shows the track reconstruction efficiency for the $t\bar{t}$ samples with $\langle\mu\rangle = 140$

and 200. The efficiency is shown as a function of η and p_{T} for the default and fast ITk track reconstruction chains. Compared to the default reconstruction, the fast ITk reconstruction shows slightly lower efficiency at large η. The efficiency is found to be independent of pile-up, with the dominant source of inefficiency coming from hadronic interactions in the detector material. The fast ITk reconstruction efficiency as a function of p_{T} shows a stronger turn-on effect at 1 GeV, which results from increasing the p_{T} cut from 900 (400) MeV to 1 (0.4) GeV in the central (forward) part of the detector.

The average number of reconstructed tracks per event is shown in Figure 7.4 as a function of η. This metric provides an inclusive measure of the rate of additional tracks found by the fast ITk reconstruction compared to the default reconstruction. As the default reconstruction has been shown to have a fake rate of $\sim 10^{-4}$ for $\langle\mu\rangle = 200$ [270], the number of tracks found by the default reconstruction effectively sets the baseline for the number of good-quality tracks that can be found. Any additional tracks found by the fast ITk reconstruction (over the default reconstruction baseline number) would then correspond to fake or duplicate tracks. For the majority of the η range, the fast ITk reconstruction shows similar number of reconstructed tracks as the default reconstruction with no noticeable dependence on pile-up. The fast ITk reconstruction finds a slightly larger number of tracks in the very forward ($|\eta| \gtrsim 3$) region of the detector.

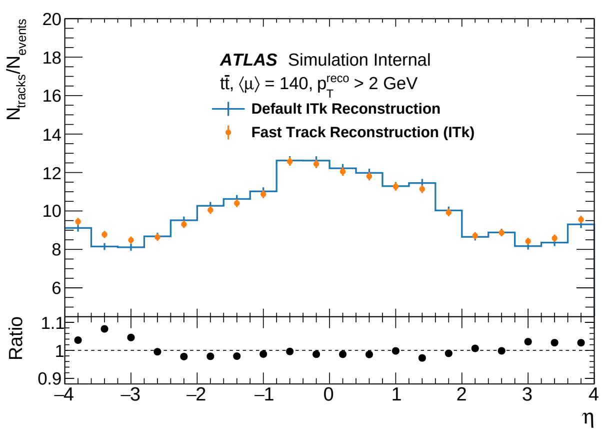

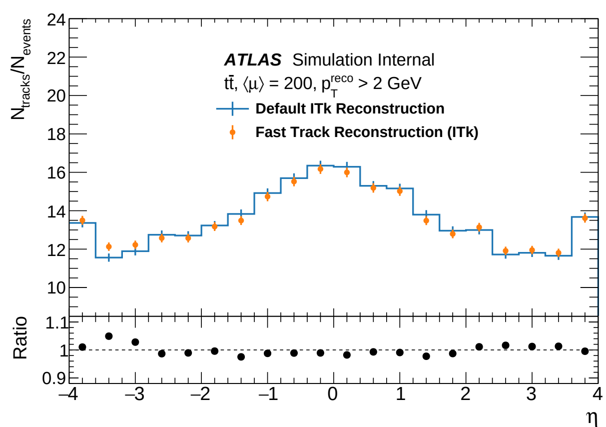

Figure 7.4: Inclusive track rate as a function of pseudorapidity for $t\bar{t}$ samples with average pile-up of 140 (left) and 200 (right) for the default and fast ITk track reconstruction. To avoid turn-on effects, a 2 GeV p_{T} cut is used for the reconstructed tracks. The ratio corresponds to dividing the number of tracks for the fast reconstruction by the number of tracks for the default reconstruction.

Figure 7.5 shows the average number of pixel and strip hits associated to reconstructed tracks, providing a measure of the hit association efficiency of the reconstruction. The fast ITk track reconstruction shows a similar level of hit association to tracks compared to the default ITK reconstruction across the full pseudorapidity range.

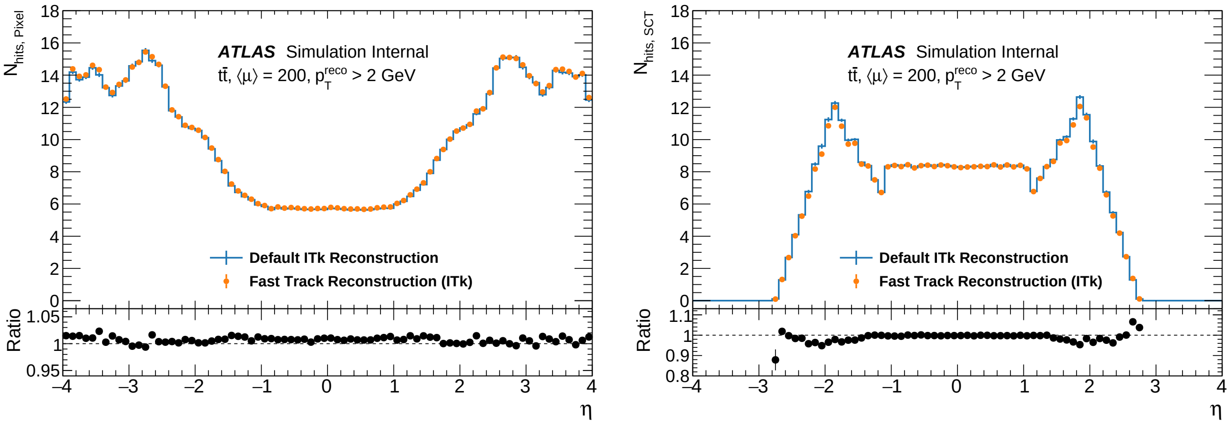

Figure 7.5: Number of pixel (left) and strip (right) hits on tracks as a function of pseudorapidity for a $t\bar{t}$ sample with average pile-up of 200 for the default and fast ITk track reconstruction. To avoid turn-on effects, a 2 GeV p_{T} cut is used for the reconstructed tracks. The ratio corresponds to dividing the number of hits on tracks for the fast reconstruction by the number of hits on tracks for the default reconstruction.

The transverse (d_0) and longitudinal (z_0) impact parameter resolutions and the relative resolution of the inverse transverse momentum for the single muon samples with $p_{\mathrm{T}} = 2$ and 100 GeV are shown as a function of η in Figure 7.6. The resolutions for the fast ITk reconstruction are not vastly different from those of the default ITk reconstruction. In the low p_{T} regime, degradations in the track parameter resolutions can be observed in the very forward region, with $\sim 10\%$ worse resolution for d_0 and up to 40% worse resolution for the inverse transverse momentum. For the high p_{T} samples, the fast ITk track parameter resolutions also show deviations from the default reconstruction values. The observed differences can be attributed to approximations used in the material model of the fast Kalman filter track fit compared to the default version.

Figure 7.7 shows the d_0 and z_0 resolutions and the relative resolution for the inverse transverse momentum for the $t\bar{t}$ sample with $\langle\mu\rangle = 200$ as a function of η. The resolutions for the fast ITk reconstruction in the forward region are up to 40% worse than those of the default reconstruction, similar to what was shown for 2 GeV muons in Figure 7.6. Considering the use case (that is, running at trigger level, which emphasizes low latency at the expense of some loss in precision) and the fact that the fast ITk reconstruction chain demonstrates very close to offline level tracking performance with reduced CPU requirements, the $\sim 20-50\%$ loss in performance for the track parameter resolutions represents an acceptable trade-off.

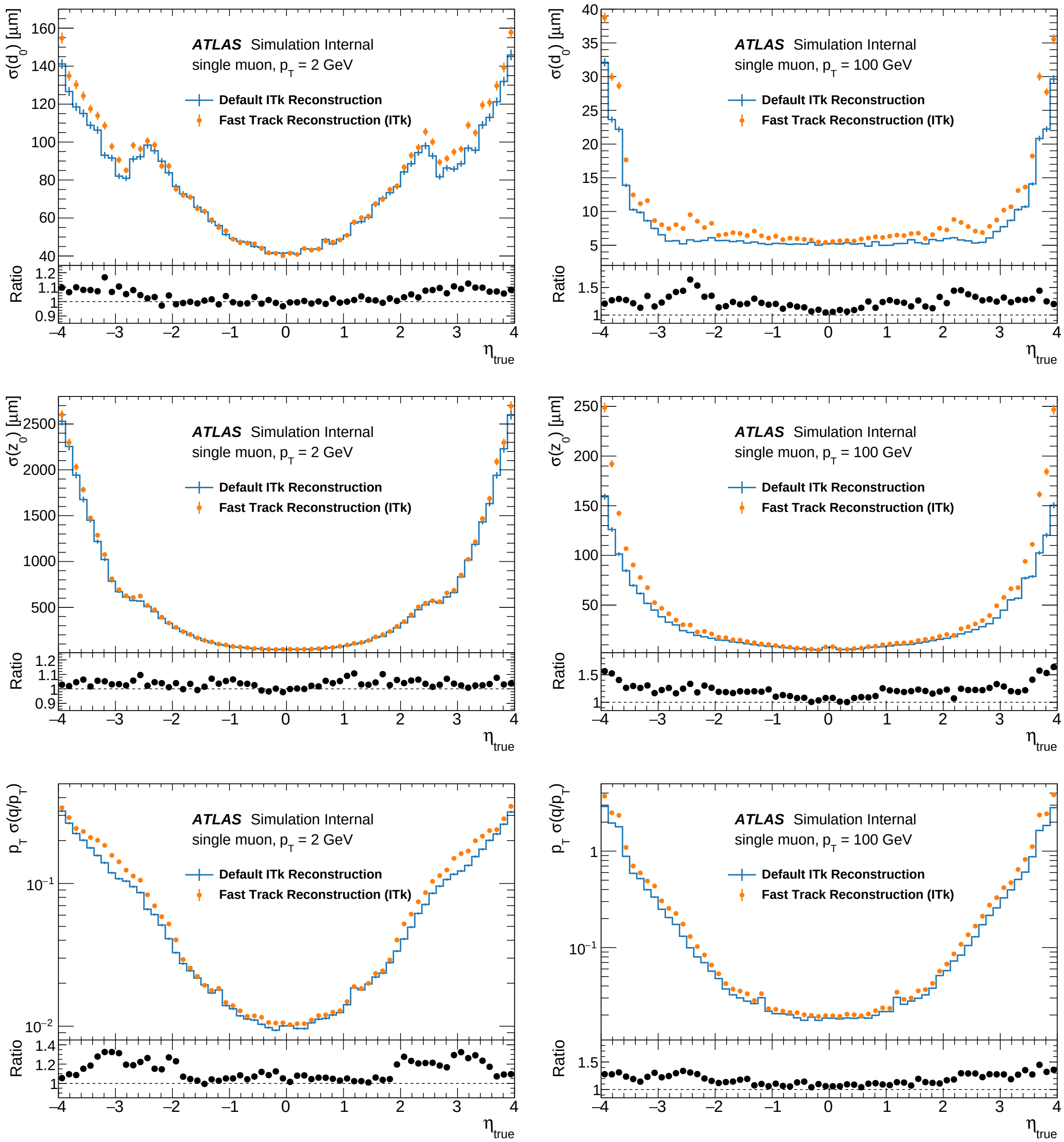

Figure 7.6: Track parameter resolutions as a function of pseudorapidity for single muon samples with p_{T} of 2 GeV (left) and 100 GeV (right) for the default and fast ITk track reconstruction. The resolutions are shown for the transverse d_0 (top) and longitudinal z_0 (middle) impact parameters and relative inverse transverse momentum (bottom). The ratio corresponds to dividing the resolution for the fast reconstruction by the resolution for the default reconstruction.

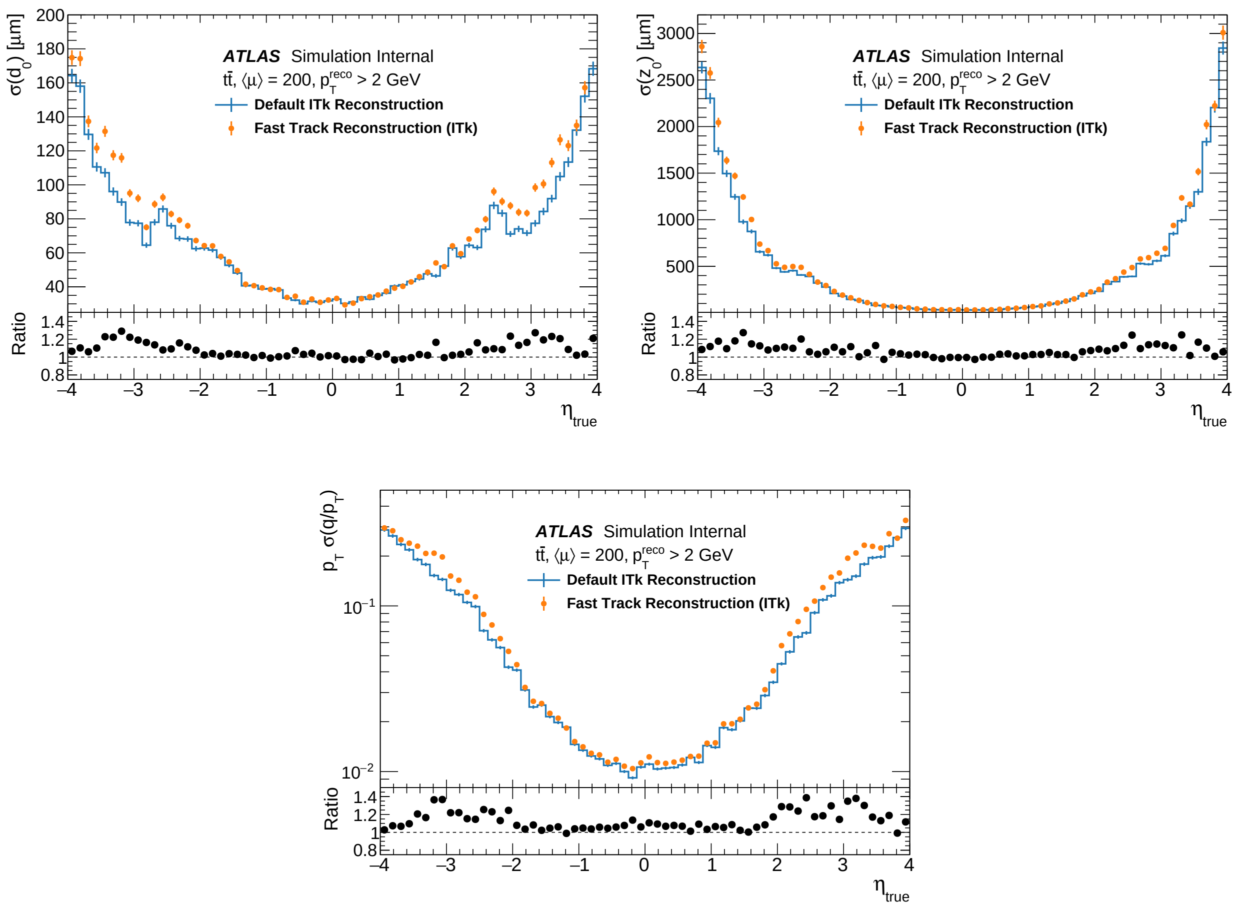

Figure 7.7: Track parameter resolutions as a function of pseudorapidity for a $t\bar{t}$ sample with average pile-up 200 for the default and fast ITk track reconstruction. The resolutions are shown for the transverse d_0 (top left) and longitudinal z_0 (top right) impact parameters and relative inverse transverse momentum (bottom). To avoid turn-on effects, a 2 GeV p_{T} cut is used for the reconstructed tracks. The ratio corresponds to dividing the resolution for the fast reconstruction by the resolution for the default reconstruction.

7.4 Conclusions

This chapter presented an updated study of the CPU timing and tracking performance of the fast ITk track reconstruction chain, using a more recent upgrade software release and an updated ITk detector geometry, superseding the previously existing results of Refs. [265–267]. It was shown that the fully functional software prototype for fast reconstruction can demonstrate a level of track reconstruction performance that is very near to offline quality. It is important to note that this is achieved with significantly reduced CPU resource requirements (a factor of ~ 4 reduction in the total reconstruction time) compared to running the offline reconstruction, making it a viable candidate for track reconstruction at trigger level. The results presented in this chapter were used to highlight the fast ITk track reconstruction as a software-based demonstrator for tracking at the Event Filter level and are included in an addendum to the Technical Design Report for the Phase-II upgrade of the ATLAS Trigger and Data Acquisition System [2].

Chapter 8

Conclusions

The study of the Higgs boson and its properties represents an important part of the physics program of the ATLAS experiment at the LHC. The Higgs production and decay channels observed so far have all been found to agree with the predictions of the Standard Model, including the decay of the Higgs boson into bottom quark pairs produced in association with a W or Z boson. However, there are still many properties left to measure, such as the coupling of the Higgs boson to first and second generation fermions, which is yet to be firmly established. For studying the coupling to lower generation quarks, the decay of the Higgs boson into charm quark pairs represents the most promising avenue to explore, given that it represents the most common decay mode that has yet to be observed.

This thesis presented a measurement of Higgs boson decays to b-quarks and c-quarks in the WH production mode, using 140 fb^{-1} of pp collision data collected at a center-of-mass energy of $\sqrt{s} = 13$ TeV with the ATLAS detector during Run 2 of the LHC. This measurement improved on the previous ATLAS $VH(H \to b\bar{b})$ and $VH(H \to c\bar{c})$ analyses by implementing a coherent treatment in terms of the flavor tagging strategy, the use of a BDT based discriminant in all analysis regimes, and the modelling of systematic uncertainties between the $VH(H \to b\bar{b})$ and $VH(H \to c\bar{c})$ regimes. In addition to measuring the $WH(H \to b\bar{b})$ and $WH(H \to c\bar{c})$ processes, a measurement of the diboson processes $WZ(Z \to b\bar{b})$ and $WZ(Z \to c\bar{c})$ was performed to validate the analysis strategy. The diboson measurements were found to be compatible with the Standard Model predictions, with observed (expected) significances of 6.8σ (7.4σ) and 3.2σ (3.0σ) for the $WZ(Z \to b\bar{b})$ and $WZ(Z \to c\bar{c})$ processes, respectively, corresponding to observation of the $WZ(Z \to b\bar{b})$ process and evidence for the $WZ(Z \to c\bar{c})$ process. The measurements of the $WH(H \to b\bar{b}/c\bar{c})$ processes were also found to agree with the SM expectations. The measurement for the $WH(H \to b\bar{b})$ process was very close to observation, with an observed significance of 4.8σ (5.3σ expected). For the $WH(H \to c\bar{c})$ process, an observed (expected) upper limit of 19.1 (18.4) times the SM predicted cross section times the branching ratio was set, which represents a significant improvement over previous constraints. By reinterpreting the results within the κ framework, direct constraints on the Higgs-bottom and Higgs-charm couplings were set. In particular, the 95% confidence level upper limit on the ratio of the coupling modifiers, $|\kappa_c/\kappa_b|$, was found to be $|\kappa_c/\kappa_b| < 4.9$ ($|\kappa_c/\kappa_b| < 4.5$ expected), without making any assumptions on the total Higgs decay width.

As described in this thesis, the reconstructed tracks corresponding to charged particle trajectories represent a key input to many data reconstruction tasks, such as jet reconstruction or flavor tagging, which in turn are crucial in the identification of decays of the Higgs boson to bottom and charm quarks. The ATLAS track reconstruction algorithm is based on a combinatorial Kalman filter, which requires an initial estimate of the track parameters, that is further refined into a complete track by incorporating information from sensitive detector elements. This thesis presented the implementation and performance of the seed finding algorithm used to initialize the Kalman filter based track finding algorithm used by ATLAS during Run 3 of the LHC. As the efficiency of the seed finding represents an upper limit on the subsequent efficiency of track finding, the seeding efficiency must be very high, and it was found to be $85\% - 95\%$ for a fiducial selection of charged particles produced in $t\bar{t}$ events, compatible with the expected efficiency loss due to hadronic interactions. The duplicate and fake track seed creation rates were found to be comparatively high, with the latter depending directly on the number of interactions per bunch crossing. The seed finding algorithm has been extensively optimized for Run 3, where the average number of pile-up interactions is $\langle\mu\rangle = 45$. However, as the high-luminosity upgrade of the LHC is expected to have μ up to 200, the seed finding algorithm must be revisited to cope with the harder combinatorics.

The $\sim 3000 - 4000$ fb^{-1} of data that is expected to be collected during the operation of the HL-LHC will significantly benefit the measurement of Higgs decays to charm quark pairs. In preparation for the expected increase in luminosity and pile-up, the ATLAS Inner Detector will be replaced by the Inner Tracker, an all-silicon detector designed for optimal track reconstruction in the high pile-up conditions expected at the HL-LHC. Since the reconstruction of complex events scales combinatorially with increasing levels of pile-up, the track reconstruction software for the ITk must be able to minimize the total processing time per event, in order to stay within the limited computing budget even in conditions of as many as 200 pile-up interactions per event. This is particularly important when running track reconstruction in online mode, at trigger level, where the latency requirements are particularly stringent. This thesis presented a study of the CPU timing and tracking performance of the fast ITk track reconstruction chain, a prototype version of track reconstruction that has significantly reduced CPU requirements compared to the offline ITk reconstruction chain. It was shown that the fully functional software prototype for fast ITk reconstruction can demonstrate a level of track reconstruction performance that is very near to offline quality. This was achieved with significantly reduced CPU resource requirements (a factor of ~ 4 reduction in the total reconstruction time) compared to running the offline reconstruction chain, making it a viable candidate for track reconstruction at trigger level.

Bibliography

[1] ATLAS Collaboration. *ATLAS Run 3 charged particle track seed finding performance.* Tech. rep. Geneva: CERN, 2023. URL: https://cds.cern.ch/record/2882156.

[2] ATLAS Collaboration. *Technical Design Report for the Phase-II Upgrade of the ATLAS Trigger and Data Acquisition System - Event Filter Tracking Amendment.* Tech. rep. Geneva: CERN, 2022. DOI: 10.17181/CERN.ZK85.5TDL. URL: https://cds.cern.ch/record/2802799.

[3] Irina Ene et al. "The MASSIVE Survey - X. Misalignment between kinematic and photometric axes and intrinsic shapes of massive early-type galaxies". In: *The Monthly Notices of the Royal Astronomical Society* 479.2 (Sept. 2018), pp. 2810–2826. DOI: 10.1093/mnras/sty1649. arXiv: 1802.00014 [astro-ph.GA].

[4] Irina Ene et al. "The MASSIVE Survey XIII. Spatially Resolved Stellar Kinematics in the Central 1 kpc of 20 Massive Elliptical Galaxies with the GMOS-North Integral Field Spectrograph". In: *The Astrophysical Journal* 878.1, 57 (June 2019), p. 57. DOI: 10.3847/1538-4357/ab1f04. arXiv: 1904.08929 [astro-ph.GA].

[5] Irina Ene et al. "The MASSIVE Survey XIV — Stellar Velocity Profiles and Kinematic Misalignments from 200 pc to 20 kpc in Massive Early-type Galaxies". In: *The Astrophysical Journal* 891.1, 65 (Mar. 2020), p. 65. DOI: 10.3847/1538-4357/ab7016. arXiv: 2001.11046 [astro-ph.GA].

[6] P. A. M. Dirac. "The Quantum Theory of the Emission and Absorption of Radiation". In: *Special Relativity and Quantum Theory: A Collection of Papers on the Poincaré Group.* Ed. by M. E. Noz and Y. S. Kim. Dordrecht: Springer Netherlands, 1988, pp. 157–179. ISBN: 978-94-009-3051-3. DOI: 10.1007/978-94-009-3051-3_9. URL: https://doi.org/10.1007/978-94-009-3051-3_9.

[7] P. A. M. Dirac. "The quantum theory of the electron". In: *Proc. R. Soc. Lond. A* 117 (1928), pp. 610–624. DOI: 10.1098/rspa.1928.0023. URL: http://doi.org/10.1098/rspa.1928.0023.

[8] S. Tomonaga. "On a relativistically invariant formulation of the quantum theory of wave fields". In: *Prog. Theor. Phys.* 1 (1946), pp. 27–42. DOI: 10.1143/PTP.1.27.

[9] R. P. Feynman. "Space - time approach to quantum electrodynamics". In: *Phys. Rev.* 76 (1949). Ed. by L. M. Brown, pp. 769–789. DOI: 10.1103/PhysRev.76.769.

[10] R. P. Feynman. "The Theory of positrons". In: *Phys. Rev.* 76 (1949). Ed. by L. M. Brown, pp. 749–759. DOI: 10.1103/PhysRev.76.749.

[11] R. P. Feynman. "Mathematical formulation of the quantum theory of electromagnetic interaction". In: *Phys. Rev.* 80 (1950). Ed. by L. M. Brown, pp. 440–457. DOI: 10.1103/PhysRev.80.440.

[12] Julian S. Schwinger. "On Quantum electrodynamics and the magnetic moment of the electron". In: *Phys. Rev.* 73 (1948), pp. 416–417. DOI: 10.1103/PhysRev.73.416.

[13] Julian S. Schwinger. "Quantum electrodynamics. I A covariant formulation". In: *Phys. Rev.* 74 (1948). Ed. by K. A. Milton, p. 1439. DOI: 10.1103/PhysRev.74.1439.

[14] Murray Gell-Mann. *The Eightfold Way: A Theory of strong interaction symmetry.* CTSL-20; TID-12608. Mar. 1961. DOI: 10.2172/4008239.

[15] Yuval Ne'eman. "Derivation of strong interactions from a gauge invariance". In: *Nucl. Phys.* 26 (1961). Ed. by R. Ruffini and Y. Verbin, pp. 222–229. DOI: 10.1016/0029-5582(61)90134-1.

[16] Murray Gell-Mann. "A Schematic Model of Baryons and Mesons". In: *Phys. Lett.* 8 (1964), pp. 214–215. DOI: 10.1016/S0031-9163(64)92001-3.

[17] G. Zweig. *An SU_3 model for strong interaction symmetry and its breaking. Version 1.* Tech. rep. Geneva: CERN, 1964. DOI: 10.17181/CERN-TH-401. URL: https://cds.cern.ch/record/352337.

[18] G. Zweig. *An SU_3 model for strong interaction symmetry and its breaking. Version 2.* Tech. rep. 1964. DOI: 10.17181/CERN-TH-412. URL: https://cds.cern.ch/record/570209.

[19] O. W. Greenberg. "Spin and Unitary Spin Independence in a Paraquark Model of Baryons and Mesons". In: *Phys. Rev. Lett.* 13 (1964), pp. 598–602. DOI: 10.1103/PhysRevLett.13.598.

[20] M. Y. Han and Yoichiro Nambu. "Three Triplet Model with Double SU(3) Symmetry". In: *Phys. Rev.* 139 (1965). Ed. by T. Eguchi, B1006–B1010. DOI: 10.1103/PhysRev.139.B1006.

[21] H. Fritzsch, Murray Gell-Mann, and H. Leutwyler. "Advantages of the Color Octet Gluon Picture". In: *Phys. Lett. B* 47 (1973), pp. 365–368. DOI: 10.1016/0370-2693(73)90625-4.

[22] David J. Gross and Frank Wilczek. "Ultraviolet Behavior of Nonabelian Gauge Theories". In: *Phys. Rev. Lett.* 30 (1973). Ed. by J. C. Taylor, pp. 1343–1346. DOI: 10.1103/PhysRevLett.30.1343.

[23] H. David Politzer. "Reliable Perturbative Results for Strong Interactions?" In: *Phys. Rev. Lett.* 30 (1973). Ed. by J. C. Taylor, pp. 1346–1349. DOI: 10.1103/PhysRevLett.30.1346.

[24] S. S. Gershtein and Ya. B. Zel'dovich. "Meson corrections in the theory of beta decay". In: *Soviet Phys. JETP* 2 (May 1956), p. 576. URL: https://www.osti.gov/biblio/4361821.

[25] R. P. Feynman and Murray Gell-Mann. "Theory of Fermi interaction". In: *Phys. Rev.* 109 (1958). Ed. by L. M. Brown, pp. 193–198. DOI: 10.1103/PhysRev.109.193.

[26] S. L. Glashow. "Partial Symmetries of Weak Interactions". In: *Nucl. Phys.* 22 (1961), pp. 579–588. DOI: 10.1016/0029-5582(61)90469-2.

[27] Steven Weinberg. "A Model of Leptons". In: *Phys. Rev. Lett.* 19 (1967), pp. 1264–1266. DOI: 10.1103/PhysRevLett.19.1264.

[28] Abdus Salam. "Weak and Electromagnetic Interactions". In: *Conf. Proc. C* 680519 (1968), pp. 367–377. DOI: 10.1142/9789812795915_0034.

[29] J. Goldstone. "Field Theories with Superconductor Solutions". In: *Nuovo Cim.* 19 (1961), pp. 154–164. DOI: 10.1007/BF02812722.

[30] Peter W. Higgs. "Broken Symmetries and the Masses of Gauge Bosons". In: *Phys. Rev. Lett.* 13 (1964). Ed. by J. C. Taylor, pp. 508–509. DOI: 10.1103/PhysRevLett.13.508.

[31] F. Englert and R. Brout. "Broken Symmetry and the Mass of Gauge Vector Mesons". In: *Phys. Rev. Lett.* 13 (1964). Ed. by J. C. Taylor, pp. 321–323. DOI: 10.1103/PhysRevLett.13.321.

[32] G. S. Guralnik, C. R. Hagen, and T. W. B. Kibble. "Global Conservation Laws and Massless Particles". In: *Phys. Rev. Lett.* 13 (1964). Ed. by J. C. Taylor, pp. 585–587. DOI: 10.1103/PhysRevLett.13.585.

[33] R. L. Workman et al. "Review of Particle Physics". In: *PTEP* 2022 (2022), p. 083C01. DOI: 10.1093/ptep/ptac097.

[34] E. Noether. "Invariante Variationsprobleme". ger. In: *Nachrichten von der Gesellschaft der Wissenschaften zu Göttingen, Mathematisch-Physikalische Klasse* 1918 (1918), pp. 235–257. URL: http://eudml.org/doc/59024.

[35] Enrico Fermi. "Sulla quantizzazione del gas perfetto monoatomico". In: *Rendiconti Lincei* 3 (1926). Translated as Alberto Zannoni, On the Quantization of the Monoatomic Ideal Gas (1999). arXiv: cond-mat/9912229 [cond-mat.stat-mech].

[36] Paul A. M. Dirac. "On the Theory of quantum mechanics". In: *Proc. Roy. Soc. Lond. A* 112 (1926), pp. 661–677. DOI: 10.1098/rspa.1926.0133.

[37] S. N. Bose. "Planck's law and light quantum hypothesis". In: *Z. Phys.* 26 (1924), pp. 178–181. DOI: 10.1007/BF01327326.

[38] Albert Einstein. "Quantum theory of the monatomic ideal gas". In: *Sitzungsberichte der Preussischen Akademie der Wissenschaften, Physikalisch-mathematische Klasse* (1924), pp. 261–267. DOI: https://doi.org/10.1002/3527608958.ch27.

[39] LHCb collaboration. "Observation of structure in the J/ψ-pair mass spectrum". In: *Science Bulletin* 65.23 (Dec. 2020), pp. 1983–1993. DOI: 10.1016/j.scib.2020.08.032. arXiv: 2006.16957 [hep-ex].

[40] Roel Aaij et al. "Observation of New Resonances Decaying to $J/\psi K^{+}+$ and $J/\psi\phi$". In: *Phys. Rev. Lett.* 127.8 (2021), p. 082001. DOI: 10.1103/PhysRevLett.127.082001. arXiv: 2103.01803 [hep-ex].

[41] Roel Aaij et al. "Observation of the resonant character of the $Z(4430)^{-}$ state". In: *Phys. Rev. Lett.* 112.22 (2014), p. 222002. DOI: 10.1103/PhysRevLett.112.222002. arXiv: 1404.1903 [hep-ex].

[42] Roel Aaij et al. "Observation of $J/\psi\phi$ structures consistent with exotic states from amplitude analysis of $B^{+} \to J/\psi\phi K^{+}$ decays". In: *Phys. Rev. Lett.* 118.2 (2017), p. 022003. DOI: 10.1103/PhysRevLett.118.022003. arXiv: 1606.07895 [hep-ex].

[43] Georges Aad et al. "Observation of an Excess of Dicharmonium Events in the Four-Muon Final State with the ATLAS Detector". In: *Phys. Rev. Lett.* 131.15 (2023), p. 151902. DOI: 10.1103/PhysRevLett.131.151902. arXiv: 2304.08962 [hep-ex].

[44] Roel Aaij et al. "Observation of $J/\psi p$ Resonances Consistent with Pentaquark States in $\Lambda_b^0 \to J/\psi K^{-} p$ Decays". In: *Phys. Rev. Lett.* 115 (2015), p. 072001. DOI: 10.1103/PhysRevLett.115.072001. arXiv: 1507.03414 [hep-ex].

[45] R. Aaij et al. "Observation of a $J/\psi\Lambda$ Resonance Consistent with a Strange Pentaquark Candidate in $B \to J/\psi\Lambda\bar{p}$ Decays". In: *Phys. Rev. Lett.* 131.3 (2023), p. 031901. DOI: 10.1103/PhysRevLett.131.031901. arXiv: 2210.10346 [hep-ex].

[46] Michelangelo L Mangano. "Introduction to QCD". In: *1998 European School of High-Energy Physics*. 2000, pp. 53–97. DOI: 10.5170/CERN-1999-004.53. URL: https://cds.cern.ch/record/454171.

[47] John C. Collins, Davison E. Soper, and George F. Sterman. "Factorization of Hard Processes in QCD". In: *Adv. Ser. Direct. High Energy Phys.* 5 (1989), pp. 1–91. DOI: 10.1142/9789814503266_0001. arXiv: hep-ph/0409313.

[48] Peter W. Higgs. "Broken symmetries, massless particles and gauge fields". In: *Phys. Lett.* 12 (1964), pp. 132–133. DOI: 10.1016/0031-9163(64)91136-9.

[49] Yoichiro Nambu. "Quasi-Particles and Gauge Invariance in the Theory of Superconductivity". In: *Phys. Rev.* 117 (3 Feb. 1960), pp. 648–663. DOI: 10.1103/PhysRev.117.648. URL: https://link.aps.org/doi/10.1103/PhysRev.117.648.

[50] Makoto Kobayashi and Toshihide Maskawa. "CP Violation in the Renormalizable Theory of Weak Interaction". In: *Prog. Theor. Phys.* 49 (1973), pp. 652–657. DOI: 10.1143/PTP.49.652.

[51] R. P. Feynman. "The behavior of hadron collisions at extreme energies". In: *Conf. Proc. C* 690905 (1969), pp. 237–258. URL: https://api.semanticscholar.org/CorpusID:121244309.

[52] J. Pumplin et al. "New Generation of Parton Distributions with Uncertainties from Global QCD Analysis". In: *JHEP* 07 (2002), p. 012. DOI: 10.1088/1126-6708/2002/07/012. arXiv: hep-ph/0201195.

[53] A. Sherstnev and R. S. Thorne. "Parton Distributions for LO Generators". In: *Eur. Phys. J. C* 55 (2008), p. 553. DOI: 10.1140/epjc/s10052-008-0610-x. arXiv: 0711.2473 [hep-ph].

[54] Richard D. Ball et al. "Parton distributions with LHC data". In: *Nucl. Phys. B* 867 (2013), p. 244. DOI: 10.1016/j.nuclphysb.2012.10.003. arXiv: 1207.1303 [hep-ph].

[55] Jon Butterworth et al. "PDF4LHC recommendations for LHC Run II". In: *J. Phys. G* 43 (2016), p. 023001. DOI: 10.1088/0954-3899/43/2/023001. arXiv: 1510.03865 [hep-ph].

[56] Florin Pop. "High Performance Numerical Computing for High Energy Physics: A New Challenge for Big Data Science". In: *Adv. High Energy Phys.* 2014 (2014), p. 507690. DOI: 10.1155/2014/507690.

[57] Stefan Höche. "Introduction to parton-shower event generators". In: *Theoretical Advanced Study Institute in Elementary Particle Physics: Journeys Through the Precision Frontier: Amplitudes for Colliders*. 2015, pp. 235–295. DOI: 10.1142/9789814678766_0005. arXiv: 1411.4085 [hep-ph].

[58] Torbjörn Sjöstrand et al. "An introduction to PYTHIA 8.2". In: *Comput. Phys. Commun.* 191 (2015), p. 159. DOI: 10.1016/j.cpc.2015.01.024. arXiv: 1410.3012 [hep-ph].

[59] T. Gleisberg et al. "Event generation with SHERPA 1.1". In: *JHEP* 02 (2009), p. 007. DOI: 10.1088/1126-6708/2009/02/007. arXiv: 0811.4622 [hep-ph].

[60] Stefan Höche et al. "QCD matrix elements and truncated showers". In: *JHEP* 05 (2009), p. 053. DOI: 10.1088/1126-6708/2009/05/053. arXiv: 0903.1219 [hep-ph].

[61] Fabio Cascioli, Philipp Maierhöfer, and Stefano Pozzorini. "Scattering Amplitudes with Open Loops". In: *Phys. Rev. Lett.* 108 (2012), p. 111601. DOI: 10.1103/PhysRevLett.108.111601. arXiv: 1111.5206 [hep-ph].

[62] Paolo Nason. "A new method for combining NLO QCD with shower Monte Carlo algorithms". In: *JHEP* 11 (2004), p. 040. DOI: 10.1088/1126-6708/2004/11/040. arXiv: hep-ph/0409146.

[63] Stefano Frixione, Paolo Nason, and Carlo Oleari. "Matching NLO QCD computations with parton shower simulations: the POWHEG method". In: *JHEP* 11 (2007), p. 070. DOI: 10.1088/1126-6708/2007/11/070. arXiv: 0709.2092 [hep-ph].

[64] Simone Alioli et al. "A general framework for implementing NLO calculations in shower Monte Carlo programs: the POWHEG BOX". In: *JHEP* 06 (2010), p. 043. DOI: 10.1007/JHEP06(2010)043. arXiv: 1002.2581 [hep-ph].

[65] Johannes Bellm et al. "Herwig 7.0/Herwig++ 3.0 release note". In: *Eur. Phys. J. C* 76.4 (2016), p. 196. DOI: 10.1140/epjc/s10052-016-4018-8. arXiv: 1512.01178 [hep-ph].

[66] J. Alwall et al. "The automated computation of tree-level and next-to-leading order differential cross sections, and their matching to parton shower simulations". In: *JHEP* 07 (2014), p. 079. DOI: 10.1007/JHEP07(2014)079. arXiv: 1405.0301 [hep-ph].

[67] Marek Schönherr. "Parton shower matching and merging". In: *PoS* CORFU2017 (2018), p. 110. DOI: 10.22323/1.318.0110. arXiv: 1804.10643 [hep-ph].

[68] Stefan Höche et al. "A critical appraisal of NLO+PS matching methods". In: *JHEP* 09 (2012), p. 049. DOI: 10.1007/JHEP09(2012)049. arXiv: 1111.1220 [hep-ph].

[69] S. Catani et al. "QCD Matrix Elements + Parton Showers". In: *JHEP* 11 (2001), p. 063. DOI: 10.1088/1126-6708/2001/11/063. arXiv: hep-ph/0109231.

[70] Stefan Höche et al. "QCD matrix elements + parton showers. The NLO case". In: *JHEP* 04 (2013), p. 027. DOI: 10.1007/JHEP04(2013)027. arXiv: 1207.5030 [hep-ph].

[71] Rikkert Frederix and Stefano Frixione. "Merging meets matching in MC@NLO". In: *JHEP* 12 (2012), p. 061. DOI: 10.1007/JHEP12(2012)061. arXiv: 1209.6215 [hep-ph].

[72] ATLAS Collaboration. "The ATLAS Simulation Infrastructure". In: *Eur. Phys. J. C* 70 (2010), p. 823. DOI: 10.1140/epjc/s10052-010-1429-9. arXiv: 1005.4568 [physics.ins-det].

[73] GEANT4 Collaboration, S. Agostinelli, et al. "Geant4 – a simulation toolkit". In: *Nucl. Instrum. Meth. A* 506 (2003), p. 250. DOI: 10.1016/S0168-9002(03)01368-8.

[74] ATLAS Collaboration. *ATLAS Computing: Technical Design Report*. ATLAS-TDR-17; CERN-LHCC-2005-022. 2005. URL: https://cds.cern.ch/record/837738.

[75] ATLAS Collaboration. "The ATLAS Experiment at the CERN Large Hadron Collider". In: *JINST* 3 (2008), S08003. DOI: 10.1088/1748-0221/3/08/S08003.

[76] Y. Unno. "ATLAS silicon microstrip detector system (SCT)". In: *Nucl. Instrum. Meth. A* 511 (2003). Ed. by S. L. Olsen and D. Bortoletto, pp. 58–63. DOI: 10.1016/S0168-9002(03)01751-0.

[77] GEANT4 Collaboration. *Geant4 Logo*. URL: https://geant4.web.cern.ch/collaboration/logo (visited on 04/01/2024).

[78] Maximilien Brice and Julien Marius Ordan. *LHC tunnel pt1 various angle*. General Photo. 2018. URL: https://cds.cern.ch/record/2302977.

[79] D. de Florian et al. *Handbook of LHC Higgs Cross Sections: 4. Deciphering the Nature of the Higgs Sector*. FERMILAB-FN-1025-T, CERN-2017-002-M. 2016. DOI: 10.23731/CYRM-2017-002. arXiv: 1610.07922 [hep-ph].

[80] H. M. Georgi et al. "Higgs Bosons from Two Gluon Annihilation in Proton Proton Collisions". In: *Phys. Rev. Lett.* 40 (1978), p. 692. DOI: 10.1103/PhysRevLett.40.692.

[81] ATLAS Collaboration. "Observation of a new particle in the search for the Standard Model Higgs boson with the ATLAS detector at the LHC". In: *Phys. Lett. B* 716 (2012), p. 1. DOI: 10.1016/j.physletb.2012.08.020. arXiv: 1207.7214 [hep-ex].

[82] CMS Collaboration. "Observation of a new boson at a mass of 125 GeV with the CMS experiment at the LHC". In: *Phys. Lett. B* 716 (2012), p. 30. DOI: 10.1016/j.physletb.2012.08.021. arXiv: 1207.7235 [hep-ex].

[83] Georges Aad et al. "Combined measurement of the Higgs boson mass from the $H \to \gamma\gamma$ and $H \to ZZ^* \to 4\ell$ decay channels with the ATLAS detector using $\sqrt{s} = 7$, 8 and 13 TeV *pp* collision data". In: *Phys. Rev. Lett.* 131 (2023), p. 251802. DOI: 10.1103/PhysRevLett.131.251802. arXiv: 2308.04775 [hep-ex].

[84] ATLAS Collaboration. "A detailed map of Higgs boson interactions by the ATLAS experiment ten years after the discovery". In: *Nature* 607 (2022), pp. 52–59. DOI: 10.1038/s41586-022-04893-w. arXiv: 2207.00092 [hep-ex].

[85] Oliver S. Bruning et al., eds. *LHC Design Report Vol.1: The LHC Main Ring*. CERN Yellow Reports: Monographs. Geneva: CERN, June 2004. DOI: 10.5170/CERN-2004-003-V-1. URL: https://cds.cern.ch/record/782076.

[86] O. Bruning et al., eds. *LHC Design Report Vol.2: The LHC infrastructure and general services*. CERN Yellow Reports: Monographs. Geneva: CERN, Nov. 2004. DOI: 10.5170/CERN-2004-003-V-2. URL: https://cds.cern.ch/record/815187.

[87] M. Benedikt et al., eds. *LHC Design Report Vol.3: The LHC injector chain*. CERN Yellow Reports: Monographs. Geneva: CERN, Dec. 2004. DOI: 10.5170/CERN-2004-003-V-3. URL: https://cds.cern.ch/record/823808.

[88] Ewa Lopienska. *The CERN accelerator complex, layout in 2022. Complexe des accélérateurs du CERN en janvier 2022*. General Photo. 2022. URL: https://cds.cern.ch/record/2800984.

[89] ATLAS Collaboration. *ATLAS: Technical Proposal for a General-Purpose pp Experiment at the Large Hadron Collider at CERN*. CERN-LHCC-94-043; LHCC-P-2. 1994. URL: https://cds.cern.ch/record/290968.

[90] CMS Collaboration. "The CMS experiment at the CERN LHC". In: *JINST* 3 (2008), S08004. DOI: 10.1088/1748-0221/3/08/S08004.

[91] CMS Collaboration. *CMS, the Compact Muon Solenoid: Technical proposal*. CERN-LHCC-94-38, CERN-LHCC-P-1. Dec. 1994. URL: https://cds.cern.ch/record/290969.

[92] A. Augusto Alves Jr. et al. "The LHCb Detector at the LHC". In: *JINST* 3 (2008), S08005. DOI: 10.1088/1748-0221/3/08/S08005.

[93] K. Aamodt et al. "The ALICE experiment at the CERN LHC". In: *JINST* 3 (2008), S08002. DOI: 10.1088/1748-0221/3/08/S08002.

[94] V. Berardi et al. *TOTEM: Technical design report. Total cross section, elastic scattering and diffraction dissociation at the Large Hadron Collider at CERN*. CERN-LHCC-2004-002, TOTEM-TDR-001. Jan. 2004. URL: https://cds.cern.ch/record/704349.

[95] O. Adriani et al. *Technical design report of the LHCf experiment: Measurement of photons and neutral pions in the very forward region of LHC*. CERN-LHCC-2006-004. Feb. 2006. URL: https://cds.cern.ch/record/926196.

[96] James Pinfold. "The MoEDAL Experiment at the LHC - Searching for Physics Beyond the Standard Model". In: *EPJ Web Conf.* 182 (2018). Ed. by Y. Aharonov, L. Bravina, and S. Kabana, p. 02096. DOI: 10.1051/epjconf/201818202096.

[97] James Pinfold. "The MoEDAL-MAPP Experiment at the LHC – The Continuation of the LHC's 1st Dedicated Search Experiment". In: *PoS* ICHEP2022 (Nov. 2022), p. 168. DOI: 10.22323/1.414.0168.

[98] Akitaka Ariga et al. *Technical Proposal for FASER: ForwArd Search ExpeRiment at the LHC*. CERN-LHCC-2018-036, LHCC-P-013, UCI-TR-2018-22, KYUSHU-RCAPP-2018-07. Dec. 2018. arXiv: 1812.09139 [physics.ins-det].

[99] C. Ahdida et al. *SND@LHC*. CERN-LHCC-2020-002, LHCC-I-035. Feb. 2020. arXiv: 2002.08722 [physics.ins-det].

[100] ATLAS Collaboration. *Luminosity Public Results Run 2*. URL: https://twiki.cern.ch/twiki/bin/view/AtlasPublic/LuminosityPublicResultsRun2 (visited on 01/22/2024).

[101] ATLAS Collaboration. "Luminosity determination in pp collisions at $\sqrt{s} = 13$ TeV using the ATLAS detector at the LHC". In: *Eur. Phys. J. C* 83.10 (2023), p. 982. DOI: 10.1140/epjc/s10052-023-11747-w. arXiv: 2212.09379 [hep-ex]. URL: https://cds.cern.ch/record/2844887.

[102] Stephane Fartoukh et al. *LHC Configuration and Operational Scenario for Run 3*. Tech. rep. Geneva: CERN, 2021. URL: https://cds.cern.ch/record/2790409.

[103] Joao Pequenao and Paul Schaffner. "How ATLAS detects particles: diagram of particle paths in the detector". 2013. URL: https://cds.cern.ch/record/1505342.

[104] ATLAS Collaboration. *ATLAS Inner Detector: Technical Design Report, Volume 1*. ATLAS-TDR-4; CERN-LHCC-97-016. 1997. URL: https://cds.cern.ch/record/331063.

[105] ATLAS Collaboration. *ATLAS Inner Detector: Technical Design Report, Volume 2*. ATLAS-TDR-5, CERN-LHCC-97-017. 1997. URL: https://cds.cern.ch/record/331064.

[106] ATLAS Collaboration. “The ATLAS Inner Detector commissioning and calibration”. In: *Eur. Phys. J. C* 70 (2010), p. 787. DOI: 10.1140/epjc/s10052-010-1366-7. arXiv: 1004.5293 [hep-ex].

[107] ATLAS Collaboration. *ATLAS Liquid Argon Calorimeter: Technical Design Report*. ATLAS-TDR-2; CERN-LHCC-96-041. 1996. URL: https://cds.cern.ch/record/331061.

[108] ATLAS Collaboration. “Readiness of the ATLAS liquid argon calorimeter for LHC collisions”. In: *Eur. Phys. J. C* 70 (2010), p. 723. DOI: 10.1140/epjc/s10052-010-1354-y. arXiv: 0912.2642 [hep-ex].

[109] ATLAS Collaboration. *ATLAS Tile Calorimeter: Technical Design Report*. ATLAS-TDR-3; CERN-LHCC-96-042. 1996. URL: https://cds.cern.ch/record/331062.

[110] ATLAS Collaboration. “Readiness of the ATLAS Tile Calorimeter for LHC collisions”. In: *Eur. Phys. J. C* 70 (2010), p. 1193. DOI: 10.1140/epjc/s10052-010-1508-y. arXiv: 1007.5423 [hep-ex].

[111] ATLAS Collaboration. *ATLAS Muon Spectrometer: Technical Design Report*. ATLAS-TDR-10; CERN-LHCC-97-022. CERN, 1997. URL: https://cds.cern.ch/record/331068.

[112] ATLAS Collaboration. “Commissioning of the ATLAS Muon Spectrometer with cosmic rays”. In: *Eur. Phys. J. C* 70 (2010), p. 875. DOI: 10.1140/epjc/s10052-010-1415-2. arXiv: 1006.4384 [hep-ex].

[113] B. Abbott et al. “Production and integration of the ATLAS Insertable B-Layer”. In: *JINST* 13 (2018), T05008. DOI: 10.1088/1748-0221/13/05/T05008. arXiv: 1803.00844 [physics.ins-det].

[114] ATLAS Collaboration. *ATLAS Insertable B-Layer: Technical Design Report*. ATLAS-TDR-19; CERN-LHCC-2010-013. 2010. URL: https://cds.cern.ch/record/1291633. Addendum: ATLAS-TDR-19-ADD-1; CERN-LHCC-2012-009. 2012. URL: https://cds.cern.ch/record/1451888.

[115] ATLAS Collaboration. *ATLAS Inner Tracker Pixel Detector: Technical Design Report*. ATLAS-TDR-030; CERN-LHCC-2017-021. 2017. URL: https://cds.cern.ch/record/2285585.

[116] G. Mullier. “The upgraded Pixel Detector of the ATLAS experiment for Run-2 at the Large Hadron Collider”. In: *JINST* 11.02 (2016), p. C02061. DOI: 10.1088/1748-0221/11/02/C02061.

[117] A. Ahmad et al. “The silicon microstrip sensors of the ATLAS semiconductor tracker”. In: *Nuclear Instruments and Methods in Physics Research Section A: Accelerators, Spectrometers, Detectors and Associated Equipment* 578.1 (2007), pp. 98–118. ISSN: 0168-9002. DOI: https://doi.org/10.1016/j.nima.2007.04.157. URL: https://www.sciencedirect.com/science/article/pii/S0168900207007644.

[118] T. Akesson et al. "Status of design and construction of the Transition Radiation Tracker (TRT) for the ATLAS experiment at the LHC". In: *Nucl. Instrum. Meth. A* 522 (2004). Ed. by C. Favuzzi et al., pp. 131–145. DOI: 10.1016/j.nima.2004.01.033.

[119] G Aad et al. "ATLAS pixel detector electronics and sensors". In: *Journal of Instrumentation* 3.07 (July 2008), P07007. DOI: 10.1088/1748-0221/3/07/P07007. URL: https://dx.doi.org/10.1088/1748-0221/3/07/P07007.

[120] ATLAS Collaboration. *ATLAS Insertable B-Layer Technical Design Report*. ATLAS-TDR-19; CERN-LHCC-2010-013. 2010. URL: https://cds.cern.ch/record/1291633. Addendum: ATLAS-TDR-19-ADD-1; CERN-LHCC-2012-009. 2012. URL: https://cds.cern.ch/record/1451888.

[121] ATLAS Collaboration. "Performance of the ATLAS Transition Radiation Tracker in Run 1 of the LHC: tracker properties". In: *JINST* 12 (2017), P05002. DOI: 10.1088/1748-0221/12/05/P05002. arXiv: 1702.06473 [hep-ex].

[122] ATLAS Collaboration. *ATLAS New Small Wheel: Technical Design Report*. ATLAS-TDR-020; CERN-LHCC-2013-006. 2013. URL: https://cds.cern.ch/record/1552862.

[123] ATLAS Collaboration. "Performance of the ATLAS trigger system in 2015". In: *Eur. Phys. J. C* 77 (2017), p. 317. DOI: 10.1140/epjc/s10052-017-4852-3. arXiv: 1611.09661 [hep-ex].

[124] ATLAS Collaboration. *Approved Plots DAQ*. URL: https://twiki.cern.ch/twiki/bin/view/AtlasPublic/ApprovedPlotsDAQ (visited on 01/22/2024).

[125] *The Grid: A system of tiers*. 2012. URL: https://cds.cern.ch/record/1997396.

[126] O. Aberle et al. *High-Luminosity Large Hadron Collider (HL-LHC): Technical design report*. CERN Yellow Reports: Monographs. Geneva: CERN, 2020. DOI: 10.23731/CYRM-2020-0010. URL: https://cds.cern.ch/record/2749422.

[127] ATLAS Collaboration. *Technical Design Report for the ATLAS ITk Pixel Detector*. Tech. rep. Geneva: CERN, 2018. URL: https://cds.cern.ch/record/2310230.

[128] ATLAS Collaboration. *Expected Tracking Performance of the ATLAS Inner Tracker at the HL-LHC*. ATL-PHYS-PUB-2019-014. 2019. URL: https://cds.cern.ch/record/2669540.

[129] ATLAS Collaboration. *ATLAS TDAQ Phase-II Upgrade: Technical Design Report*. ATLAS-TDR-029; CERN-LHCC-2017-020. 2017. URL: https://cds.cern.ch/record/2285584.

[130] P F Åkesson et al. *ATLAS Tracking Event Data Model*. Tech. rep. Geneva: CERN, 2006. URL: https://cds.cern.ch/record/973401.

[131] ATLAS Collaboration. "Performance of the ATLAS track reconstruction algorithms in dense environments in LHC Run 2". In: *Eur. Phys. J. C* 77 (2017), p. 673. DOI: 10.1140/epjc/s10052-017-5225-7. arXiv: 1704.07983 [hep-ex].

[132] T Cornelissen et al. "The new ATLAS track reconstruction (NEWT)". In: *Journal of Physics: Conference Series* 119.3 (July 2008), p. 032014. DOI: 10.1088/1742-6596/119/3/032014. URL: https://dx.doi.org/10.1088/1742-6596/119/3/032014.

[133] Heather M Gray. "The Charged Particle Multiplicity at Center of Mass Energies from 900 GeV to 7 TeV measured with the ATLAS Experiment at the Large Hadron Collider". Presented on 09 Nov 2010. Pasadena, USA, California Institute of Technology, 2010. URL: https://cds.cern.ch/record/1309943.

[134] Andreas Salzburger. "Optimisation of the ATLAS Track Reconstruction Software for Run-2". In: *Journal of Physics: Conference Series* 664 (Dec. 2015), p. 072042. DOI: 10.1088/1742-6596/664/7/072042.

[135] R. Frühwirth. "Application of Kalman filtering to track and vertex fitting". In: *Nuclear Instruments and Methods in Physics Research Section A: Accelerators, Spectrometers, Detectors and Associated Equipment* 262.2 (1987), pp. 444–450. ISSN: 0168-9002. DOI: https://doi.org/10.1016/0168-9002(87)90887-4. URL: https://www.sciencedirect.com/science/article/pii/0168900287908874.

[136] ATLAS Collaboration. "A neural network clustering algorithm for the ATLAS silicon pixel detector". In: *JINST* 9 (2014), P09009. DOI: 10.1088/1748-0221/9/09/P09009. arXiv: 1406.7690 [hep-ex].

[137] T G Cornelissen et al. "The global χ^2 track fitter in ATLAS". In: *Journal of Physics: Conference Series* 119.3 (July 2008), p. 032013. DOI: 10.1088/1742-6596/119/3/032013. URL: https://dx.doi.org/10.1088/1742-6596/119/3/032013.

[138] ATLAS Collaboration. "Reconstruction of primary vertices at the ATLAS experiment in Run 1 proton–proton collisions at the LHC". In: *Eur. Phys. J. C* 77 (2017), p. 332. DOI: 10.1140/epjc/s10052-017-4887-5. arXiv: 1611.10235 [hep-ex].

[139] ATLAS Collaboration. *Performance of primary vertex reconstruction in proton–proton collisions at $\sqrt{s} = 7$ TeV in the ATLAS experiment*. ATLAS-CONF-2010-069. 2010. URL: https://cds.cern.ch/record/1281344.

[140] Walter Lampl et al. *Calorimeter Clustering Algorithms: Description and Performance*. ATL-LARG-PUB-2008-002. 2008. URL: https://cds.cern.ch/record/1099735.

[141] ATLAS Collaboration. "Topological cell clustering in the ATLAS calorimeters and its performance in LHC Run 1". In: *Eur. Phys. J. C* 77 (2017), p. 490. DOI: 10.1140/epjc/s10052-017-5004-5. arXiv: 1603.02934 [hep-ex].

[142] ATLAS Collaboration. “Electron and photon performance measurements with the ATLAS detector using the 2015–2017 LHC proton–proton collision data”. In: *JINST* 14 (2019), P12006. DOI: 10.1088/1748-0221/14/12/P12006. arXiv: 1908.00005 [hep-ex].

[143] ATLAS Collaboration. “Electron reconstruction and identification in the ATLAS experiment using the 2015 and 2016 LHC proton–proton collision data at $\sqrt{s} = 13\,\text{TeV}$”. In: *Eur. Phys. J. C* 79 (2019), p. 639. DOI: 10.1140/epjc/s10052-019-7140-6. arXiv: 1902.04655 [hep-ex].

[144] ATLAS Collaboration. “Muon reconstruction and identification efficiency in ATLAS using the full Run 2 pp collision data set at $\sqrt{s} = 13\,\text{TeV}$”. In: *Eur. Phys. J. C* 81 (2021), p. 578. DOI: 10.1140/epjc/s10052-021-09233-2. arXiv: 2012.00578 [hep-ex].

[145] G. P. Salam. “Towards jetography”. In: *The European Physical Journal C* 67.3-4 (May 2010), pp. 637–686. ISSN: 1434-6052. DOI: 10.1140/epjc/s10052-010-1314-6.

[146] Matteo Cacciari, Gavin P. Salam, and Gregory Soyez. “The anti-k_t jet clustering algorithm”. In: *JHEP* 04 (2008), p. 063. DOI: 10.1088/1126-6708/2008/04/063. arXiv: 0802.1189 [hep-ph].

[147] Matteo Cacciari, Gavin P. Salam, and Gregory Soyez. “FastJet user manual”. In: *Eur. Phys. J. C* 72 (2012), p. 1896. DOI: 10.1140/epjc/s10052-012-1896-2. arXiv: 1111.6097 [hep-ph].

[148] ATLAS Collaboration. “Jet reconstruction and performance using particle flow with the ATLAS Detector”. In: *Eur. Phys. J. C* 77 (2017), p. 466. DOI: 10.1140/epjc/s10052-017-5031-2. arXiv: 1703.10485 [hep-ex].

[149] ATLAS Collaboration. “Identification of boosted, hadronically decaying W bosons and comparisons with ATLAS data taken at $\sqrt{s} = 8\,\text{TeV}$”. In: *Eur. Phys. J. C* 76 (2016), p. 154. DOI: 10.1140/epjc/s10052-016-3978-z. arXiv: 1510.05821 [hep-ex].

[150] David Krohn, Jesse Thaler, and Lian-Tao Wang. “Jets with Variable R”. In: *JHEP* 06 (2009), p. 059. DOI: 10.1088/1126-6708/2009/06/059. arXiv: 0903.0392 [hep-ph].

[151] ATLAS Collaboration. *Variable Radius, Exclusive-k_T, and Center-of-Mass Subjet Reconstruction for Higgs($\rightarrow b\bar{b}$) Tagging in ATLAS*. ATL-PHYS-PUB-2017-010. 2017. URL: https://cds.cern.ch/record/2268678.

[152] ATLAS Collaboration. “Jet energy scale and resolution measured in proton–proton collisions at $\sqrt{s} = 13\,\text{TeV}$ with the ATLAS detector”. In: *Eur. Phys. J. C* 81 (2020), p. 689. DOI: 10.1140/epjc/s10052-021-09402-3. arXiv: 2007.02645 [hep-ex].

[153] ATLAS Collaboration. “Performance of jet substructure techniques for large-R jets in proton–proton collisions at $\sqrt{s} = 7\,\text{TeV}$ using the ATLAS detector”. In: *JHEP* 09 (2013), p. 076. DOI: 10.1007/JHEP09(2013)076. arXiv: 1306.4945 [hep-ex].

[154] ATLAS Collaboration. "In situ calibration of large-radius jet energy and mass in 13 TeV proton–proton collisions with the ATLAS detector". In: *Eur. Phys. J. C* 79 (2019), p. 135. DOI: 10.1140/epjc/s10052-019-6632-8. arXiv: 1807.09477 [hep-ex].

[155] ATLAS Collaboration. *Tagging and suppression of pileup jets with the ATLAS detector*. ATLAS-CONF-2014-018. 2014. URL: https://cds.cern.ch/record/1700870.

[156] ATLAS Collaboration. *Pileup jet recommendations*. URL: https://twiki.cern.ch/twiki/bin/viewauth/AtlasProtected/PileupJetRecommendations#Jet_Pile_up_Tagging_Recommen_AN1 (visited on 03/29/2024).

[157] ATLAS Collaboration. *Forward jet vertex tagging using the particle flow algorithm*. ATL-PHYS-PUB-2019-026. 2019. URL: https://cds.cern.ch/record/2683100.

[158] Izaak Neutelings. *B tagging jets*. URL: https://tikz.net/jet_btag/ (visited on 03/29/2024).

[159] ATLAS Collaboration. *Graph Neural Network Jet Flavour Tagging with the ATLAS Detector*. ATL-PHYS-PUB-2022-027. 2022. URL: https://cds.cern.ch/record/2811135.

[160] ATLAS Collaboration. *Transformer Neural Networks for Identifying Boosted Higgs Bosons decaying into $b\bar{b}$ and $c\bar{c}$ in ATLAS*. Tech. rep. Geneva: CERN, 2023. URL: https://cds.cern.ch/record/2866601.

[161] ATLAS Collaboration. *Expected performance of the ATLAS b-tagging algorithms in Run-2*. ATL-PHYS-PUB-2015-022. 2015. URL: https://cds.cern.ch/record/2037697.

[162] ATLAS Collaboration. *Optimisation and performance studies of the ATLAS b-tagging algorithms for the 2017-18 LHC run*. ATL-PHYS-PUB-2017-013. 2017. URL: https://cds.cern.ch/record/2273281.

[163] ATLAS Collaboration. *Secondary vertex finding for jet flavour identification with the ATLAS detector*. ATL-PHYS-PUB-2017-011. 2017. URL: https://cds.cern.ch/record/2270366.

[164] ATLAS Collaboration. *Topological b-hadron decay reconstruction and identification of b-jets with the JetFitter package in the ATLAS experiment at the LHC*. ATL-PHYS-PUB-2018-025. 2018. URL: https://cds.cern.ch/record/2645405.

[165] ATLAS Collaboration. "ATLAS b-jet identification performance and efficiency measurement with $t\bar{t}$ events in pp collisions at $\sqrt{s} = 13$ TeV". In: *Eur. Phys. J. C* 79 (2019), p. 970. DOI: 10.1140/epjc/s10052-019-7450-8. arXiv: 1907.05120 [hep-ex].

[166] ATLAS Collaboration. "Measurements of b-jet tagging efficiency with the ATLAS detector using $t\bar{t}$ events at $\sqrt{s} = 13$ TeV". In: *JHEP* 08 (2018), p. 089. DOI: 10.1007/JHEP08(2018)089. arXiv: 1805.01845 [hep-ex].

[167] ATLAS Collaboration. "ATLAS flavour-tagging algorithms for the LHC Run 2 pp collision dataset". In: *Eur. Phys. J. C* 83 (2023), p. 681. DOI: 10.1140/epjc/s10052-023-11699-1. arXiv: 2211.16345 [physics.data-an]. URL: https://cds.cern.ch/record/2842028.

[168] ATLAS Collaboration. "Measurement of the c-jet mistagging efficiency in $t\bar{t}$ events using pp collision data at $\sqrt{s} = 13\,\text{TeV}$ collected with the ATLAS detector". In: *Eur. Phys. J. C* 82 (2021), p. 95. DOI: 10.1140/epjc/s10052-021-09843-w. arXiv: 2109.10627 [hep-ex].

[169] ATLAS Collaboration. *Reconstruction, Energy Calibration, and Identification of Hadronically Decaying Tau Leptons in the ATLAS Experiment for Run-2 of the LHC*. ATL-PHYS-PUB-2015-045. 2015. URL: https://cds.cern.ch/record/2064383.

[170] ATLAS Collaboration. "Reconstruction of hadronic decay products of tau leptons with the ATLAS experiment". In: *Eur. Phys. J. C* 76 (2016), p. 295. DOI: 10.1140/epjc/s10052-016-4110-0. arXiv: 1512.05955 [hep-ex].

[171] ATLAS Collaboration. *Identification of hadronic tau lepton decays using neural networks in the ATLAS experiment*. ATL-PHYS-PUB-2019-033. 2019. URL: https://cds.cern.ch/record/2688062.

[172] ATLAS Collaboration. "Performance of missing transverse momentum reconstruction with the ATLAS detector using proton–proton collisions at $\sqrt{s} = 13\,\text{TeV}$". In: *Eur. Phys. J. C* 78 (2018), p. 903. DOI: 10.1140/epjc/s10052-018-6288-9. arXiv: 1802.08168 [hep-ex].

[173] ATLAS and CMS Collaborations. "Measurements of the Higgs boson production and decay rates and constraints on its couplings from a combined ATLAS and CMS analysis of the LHC pp collision data at $\sqrt{s} = 7$ and $8\,\text{TeV}$". In: *JHEP* 08 (2016), p. 045. DOI: 10.1007/JHEP08(2016)045. arXiv: 1606.02266 [hep-ex].

[174] ATLAS Collaboration. "Observation of Higgs boson production in association with a top quark pair at the LHC with the ATLAS detector". In: *Phys. Lett. B* 784 (2018), p. 173. DOI: 10.1016/j.physletb.2018.07.035. arXiv: 1806.00425 [hep-ex].

[175] CMS Collaboration. "Observation of $t\bar{t}H$ Production". In: *Phys. Rev. Lett.* 120 (2018), p. 231801. DOI: 10.1103/PhysRevLett.120.231801. arXiv: 1804.02610 [hep-ex].

[176] ATLAS Collaboration. "Observation of $H \to b\bar{b}$ decays and VH production with the ATLAS detector". In: *Phys. Lett. B* 786 (2018), p. 59. DOI: 10.1016/j.physletb.2018.09.013. arXiv: 1808.08238 [hep-ex].

[177] CMS Collaboration. "Observation of Higgs Boson Decay to Bottom Quarks". In: *Phys. Rev. Lett.* 121 (2018), p. 121801. DOI: 10.1103/PhysRevLett.121.121801. arXiv: 1808.08242 [hep-ex].

[178] ATLAS Collaboration. "Measurements of WH and ZH production in the $H \to b\bar{b}$ decay channel in pp collisions at 13 TeV with the ATLAS detector". In: *Eur. Phys. J. C* 81 (2021), p. 178. DOI: 10.1140/epjc/s10052-020-08677-2. arXiv: 2007.02873 [hep-ex].

[179] ATLAS Collaboration. "Measurement of the associated production of a Higgs boson decaying into b-quarks with a vector boson at high transverse momentum in pp collisions at $\sqrt{s} = 13$ TeV with the ATLAS detector". In: *Phys. Lett. B* 816 (2021), p. 136204. DOI: 10.1016/j.physletb.2021.136204. arXiv: 2008.02508 [hep-ex].

[180] ATLAS Collaboration. *Combination of measurements of Higgs boson production in association with a W or Z boson in the $b\bar{b}$ decay channel with the ATLAS experiment at $\sqrt{s} = 13$ TeV*. ATLAS-CONF-2021-051. 2021. URL: https://cds.cern.ch/record/2782535.

[181] CMS Collaboration. *Simplified template cross section measurements of Higgs boson produced in association with vector bosons in the $H \to b\bar{b}$ decay channel in proton-proton collisions at $\sqrt{s} = 13$ TeV*. Tech. rep. Geneva: CERN, 2022. URL: https://cds.cern.ch/record/2827421.

[182] CMS Collaboration. "Evidence for Higgs boson decay to a pair of muons". In: *JHEP* 01 (2021), p. 148. DOI: 10.1007/JHEP01(2021)148. arXiv: 2009.04363 [hep-ex].

[183] ATLAS Collaboration. "A search for the dimuon decay of the Standard Model Higgs boson with the ATLAS detector". In: *Phys. Lett. B* 812 (2021), p. 135980. DOI: 10.1016/j.physletb.2020.135980. arXiv: 2007.07830 [hep-ex].

[184] ATLAS Collaboration. "Search for the Decay of the Higgs Boson to Charm Quarks with the ATLAS Experiment". In: *Phys. Rev. Lett.* 120 (2018), p. 211802. DOI: 10.1103/PhysRevLett.120.211802. arXiv: 1802.04329 [hep-ex].

[185] CMS Collaboration. "A search for the standard model Higgs boson decaying to charm quarks". In: *JHEP* 03 (2020), p. 131. DOI: 10.1007/JHEP03(2020)131. arXiv: 1912.01662 [hep-ex].

[186] ATLAS Collaboration. "Search for the Higgs boson decays $H \to ee$ and $H \to e\mu$ in pp collisions at $\sqrt{s} = 13$ TeV with the ATLAS detector". In: *Phys. Lett. B* 801 (2020), p. 135148. DOI: 10.1016/j.physletb.2019.135148. arXiv: 1909.10235 [hep-ex].

[187] CMS Collaboration. "Search for a standard model-like Higgs boson in the $\mu^+\mu^-$ and e^+e^- decay channels at the LHC". In: *Phys. Lett. B* 744 (2015), p. 184. DOI: 10.1016/j.physletb.2015.03.048. arXiv: 1410.6679 [hep-ex].

[188] ATLAS Collaboration. "Search for exclusive Higgs and Z boson decays to $\phi\gamma$ and $\rho\gamma$ with the ATLAS detector". In: *JHEP* 07 (2018), p. 127. DOI: 10.1007/JHEP07(2018)127. arXiv: 1712.02758 [hep-ex].

[189] CMS Collaboration. "Search for decays of the 125 GeV Higgs boson into a Z boson and a ρ or ϕ meson". In: *JHEP* 11 (2020), p. 039. DOI: 10.1007/JHEP11(2020)039. arXiv: 2007.05122 [hep-ex].

[190] ATLAS Collaboration. "Searches for exclusive Higgs and Z boson decays into $J/\psi\gamma$, $\psi(2\mathrm{S})\gamma$, and $\Upsilon(n\mathrm{S})\gamma$ at $\sqrt{s} = 13\,\mathrm{TeV}$ with the ATLAS detector". In: *Phys. Lett. B* 786 (2018), p. 134. DOI: 10.1016/j.physletb.2018.09.024. arXiv: 1807.00802 [hep-ex].

[191] G. C. Branco et al. "Theory and phenomenology of two-Higgs-doublet models". In: *Phys. Rept.* 516 (2012), pp. 1–102. DOI: 10.1016/j.physrep.2012.02.002. arXiv: 1106.0034 [hep-ph].

[192] Daniel Egana-Ugrinovic, Samuel Homiller, and Patrick Roddy Meade. "Higgs bosons with large couplings to light quarks". In: *Phys. Rev. D* 100.11 (2019), p. 115041. DOI: 10.1103/PhysRevD.100.115041. arXiv: 1908.11376 [hep-ph].

[193] A. Djouadi, J. Kalinowski, and M. Spira. "HDECAY: A program for Higgs boson decays in the Standard Model and its supersymmetric extension". In: *Comput. Phys. Commun.* 108 (1998), p. 56. DOI: 10.1016/S0010-4655(97)00123-9. arXiv: hep-ph/9704448.

[194] ATLAS Collaboration. "Direct constraint on the Higgs-charm coupling from a search for Higgs boson decays into charm quarks with the ATLAS detector". In: *Eur. Phys. J. C* 82 (2022), p. 717. DOI: 10.1140/epjc/s10052-022-10588-3. arXiv: 2201.11428 [hep-ex].

[195] CMS Collaboration. "Search for Higgs boson decay to a charm quark-antiquark pair in proton–proton collisions at $\sqrt{s} = 13\,\mathrm{TeV}$". In: *Phys. Rev. Lett.* 131 (2023), p. 061801. DOI: 10.1103/PhysRevLett.131.061801. arXiv: 2205.05550 [hep-ex]. URL: https://cds.cern.ch/record/2809290.

[196] Andrew Chisholm et al. *Measurements of Higgs boson decays to bottom and charm quarks produced in association with a W or Z boson using the ATLAS experiment: "VH(bb/cc) Legacy Analysis"*. Tech. rep. Geneva: CERN, 2020. URL: https://cds.cern.ch/record/2743096.

[197] Gavin Cullen et al. "Automated one-loop calculations with GoSam". In: *Eur. Phys. J. C* 72 (2012), p. 1889. DOI: 10.1140/epjc/s10052-012-1889-1. arXiv: 1111.2034 [hep-ph].

[198] Richard D. Ball et al. "Parton distributions for the LHC run II". In: *JHEP* 04 (2015), p. 040. DOI: 10.1007/JHEP04(2015)040. arXiv: 1410.8849 [hep-ph].

[199] Oliver Brein, Abdelhak Djouadi, and Robert Harlander. "NNLO QCD corrections to the Higgs-strahlung processes at hadron colliders". In: *Phys. Lett. B* 579 (2004), pp. 149–156. DOI: 10.1016/j.physletb.2003.10.112. arXiv: hep-ph/0307206.

[200] Richard D. Ball et al. "Parton Distribution Benchmarking with LHC Data". In: *JHEP* 04 (2013), p. 125. DOI: 10.1007/JHEP04(2013)125. arXiv: 1211.5142 [hep-ph].

[201] Ansgar Denner et al. "Electroweak corrections to Higgs-strahlung off W/Z bosons at the Tevatron and the LHC with HAWK". In: *JHEP* 03 (2012), p. 075. DOI: 10.1007/JHEP03(2012)075. arXiv: 1112.5142 [hep-ph].

[202] Ansgar Denner et al. "HAWK 2.0: A Monte Carlo program for Higgs production in vector-boson fusion and Higgs strahlung at hadron colliders". In: *Comput. Phys. Commun.* 195 (2015), pp. 161–171. DOI: 10.1016/j.cpc.2015.04.021. arXiv: 1412.5390 [hep-ph].

[203] Gionata Luisoni et al. "$HW^{\pm}/HZ$ + 0 and 1 jet at NLO with the POWHEG BOX interfaced to GoSam and their merging within MiNLO". In: *JHEP* 10 (2013), p. 083. DOI: 10.1007/JHEP10(2013)083. arXiv: 1306.2542 [hep-ph].

[204] Enrico Bothmann et al. "Event generation with Sherpa 2.2". In: *SciPost Phys.* 7.3 (2019), p. 034. DOI: 10.21468/SciPostPhys.7.3.034. arXiv: 1905.09127 [hep-ph].

[205] Tanju Gleisberg and Stefan Höche. "Comix, a new matrix element generator". In: *JHEP* 12 (2008), p. 039. DOI: 10.1088/1126-6708/2008/12/039. arXiv: 0808.3674 [hep-ph].

[206] Federico Buccioni et al. "OpenLoops 2". In: *Eur. Phys. J. C* 79.10 (2019), p. 866. DOI: 10.1140/epjc/s10052-019-7306-2. arXiv: 1907.13071 [hep-ph].

[207] Ansgar Denner, Stefan Dittmaier, and Lars Hofer. "Collier: A fortran-based complex one-loop library in extended regularizations". In: *Comput. Phys. Commun.* 212 (2017), pp. 220–238. DOI: 10.1016/j.cpc.2016.10.013. arXiv: 1604.06792 [hep-ph].

[208] Steffen Schumann and Frank Krauss. "A parton shower algorithm based on Catani–Seymour dipole factorisation". In: *JHEP* 03 (2008), p. 038. DOI: 10.1088/1126-6708/2008/03/038. arXiv: 0709.1027 [hep-ph].

[209] Jan-Christopher Winter, Frank Krauss, and Gerhard Soff. "A modified cluster-hadronization model". In: *Eur. Phys. J. C* 36 (2004), pp. 381–395. DOI: 10.1140/epjc/s2004-01960-8. arXiv: hep-ph/0311085.

[210] ATLAS Collaboration. "Modelling and computational improvements to the simulation of single vector-boson plus jet processes for the ATLAS experiment". In: *JHEP* 08 (2021), p. 089. DOI: 10.1007/JHEP08(2022)089. arXiv: 2112.09588 [hep-ex].

[211] Stefano Frixione, Giovanni Ridolfi, and Paolo Nason. "A positive-weight next-to-leading-order Monte Carlo for heavy flavour hadroproduction". In: *JHEP* 09 (2007), p. 126. DOI: 10.1088/1126-6708/2007/09/126. arXiv: 0707.3088 [hep-ph].

[212] M. Beneke et al. "Hadronic top-quark pair production with NNLL threshold resummation". In: *Nucl. Phys. B* 855 (2012), pp. 695–741. DOI: 10.1016/j.nuclphysb.2011.10.021. arXiv: 1109.1536 [hep-ph].

[213] Matteo Cacciari et al. "Top-pair production at hadron colliders with next-to-next-to-leading logarithmic soft-gluon resummation". In: *Phys. Lett. B* 710 (2012), pp. 612–622. DOI: 10.1016/j.physletb.2012.03.013. arXiv: 1111.5869 [hep-ph].

[214] Peter Bärnreuther, Michal Czakon, and Alexander Mitov. “Percent-Level-Precision Physics at the Tevatron: Next-to-Next-to-Leading Order QCD Corrections to $q\bar{q} \to t\bar{t}+X$”. In: *Phys. Rev. Lett.* 109 (2012), p. 132001. DOI: 10.1103/PhysRevLett.109.132001. arXiv: 1204.5201 [hep-ph].

[215] Michal Czakon and Alexander Mitov. “NNLO corrections to top-pair production at hadron colliders: the all-fermionic scattering channels”. In: *JHEP* 12 (2012), p. 054. DOI: 10.1007/JHEP12(2012)054. arXiv: 1207.0236 [hep-ph].

[216] Michal Czakon and Alexander Mitov. “NNLO corrections to top pair production at hadron colliders: the quark-gluon reaction”. In: *JHEP* 01 (2013), p. 080. DOI: 10.1007/JHEP01(2013)080. arXiv: 1210.6832 [hep-ph].

[217] Michal Czakon, Paul Fiedler, and Alexander Mitov. “Total Top-Quark Pair-Production Cross Section at Hadron Colliders Through $O(\alpha_S^4)$”. In: *Phys. Rev. Lett.* 110 (2013), p. 252004. DOI: 10.1103/PhysRevLett.110.252004. arXiv: 1303.6254 [hep-ph].

[218] Michal Czakon and Alexander Mitov. “Top++: A program for the calculation of the top-pair cross-section at hadron colliders”. In: *Comput. Phys. Commun.* 185 (2014), p. 2930. DOI: 10.1016/j.cpc.2014.06.021. arXiv: 1112.5675 [hep-ph].

[219] Simone Alioli et al. “NLO single-top production matched with shower in POWHEG: s- and t-channel contributions”. In: *JHEP* 09 (2009), p. 111. DOI: 10.1088/1126-6708/2009/09/111. arXiv: 0907.4076 [hep-ph]. Erratum: in: *JHEP* 02 (2010), p. 011. DOI: 10.1007/JHEP02(2010)011.

[220] M. Aliev et al. “HATHOR – HAdronic Top and Heavy quarks crOss section calculatoR”. In: *Comput. Phys. Commun.* 182 (2011), pp. 1034–1046. DOI: 10.1016/j.cpc.2010.12.040. arXiv: 1007.1327 [hep-ph].

[221] P. Kant et al. “HatHor for single top-quark production: Updated predictions and uncertainty estimates for single top-quark production in hadronic collisions”. In: *Comput. Phys. Commun.* 191 (2015), pp. 74–89. DOI: 10.1016/j.cpc.2015.02.001. arXiv: 1406.4403 [hep-ph].

[222] Emanuele Re. “Single-top Wt-channel production matched with parton showers using the POWHEG method”. In: *Eur. Phys. J. C* 71 (2011), p. 1547. DOI: 10.1140/epjc/s10052-011-1547-z. arXiv: 1009.2450 [hep-ph].

[223] Nikolaos Kidonakis. “Two-loop soft anomalous dimensions for single top quark associated production with a W^- or H^-”. In: *Phys. Rev. D* 82 (2010), p. 054018. DOI: 10.1103/PhysRevD.82.054018. arXiv: 1005.4451 [hep-ph].

[224] Nikolaos Kidonakis. “Top Quark Production”. In: *Proceedings, Helmholtz International Summer School on Physics of Heavy Quarks and Hadrons (HQ 2013).* (JINR, Dubna, Russia, July 15–28, 2013), pp. 139–168. DOI: 10.3204/DESY-PROC-2013-03/Kidonakis. arXiv: 1311.0283 [hep-ph].

[225] S Heinemeyer et al. *Handbook of LHC Higgs Cross Sections: 3. Higgs Properties: Report of the LHC Higgs Cross Section Working Group*. Ed. by S Heinemeyer. CERN Yellow Reports: Monographs. 2013. DOI: 10.5170/CERN-2013-004. URL: https://cds.cern.ch/record/1559921.

[226] M. Bähr et al. "Herwig++ physics and manual". In: *Eur. Phys. J. C* 58 (2008), p. 639. DOI: 10.1140/epjc/s10052-008-0798-9. arXiv: 0803.0883 [hep-ph].

[227] Stefano Frixione et al. "Single-top hadroproduction in association with a W boson". In: *JHEP* 07 (2008), p. 029. DOI: 10.1088/1126-6708/2008/07/029. arXiv: 0805.3067 [hep-ph].

[228] ATLAS Collaboration. *Flavor Tagging Efficiency Parametrisations with Graph Neural Networks*. ATL-PHYS-PUB-2022-041. 2022. URL: https://cds.cern.ch/record/2825433.

[229] G. Avoni et al. "The new LUCID-2 detector for luminosity measurement and monitoring in ATLAS". In: *JINST* 13.07 (2018), P07017. DOI: 10.1088/1748-0221/13/07/P07017.

[230] William Buttinger. *Using Event Weights to account for differences in Instantaneous Luminosity and Trigger Prescale in Monte Carlo and Data*. Tech. rep. Geneva: CERN, 2015. URL: https://cds.cern.ch/record/2014726.

[231] Luca Ambroz et al. *Object selections for SM Higgs boson produced in association with a vector boson in which $H \to b\bar{b}$ and V decays leptonically with Run-2 data*. Tech. rep. Geneva: CERN, 2019. URL: https://cds.cern.ch/record/2690090.

[232] Kyle Cranmer, Juan Pavez, and Gilles Louppe. "Approximating Likelihood Ratios with Calibrated Discriminative Classifiers". In: *arXiv e-prints* (June 2015). arXiv: 1506.02169 [stat.AP].

[233] Enrico Bothmann, Marek Schönherr, and Steffen Schumann. "Reweighting QCD matrix-element and parton-shower calculations". In: *Eur. Phys. J. C* 76.11 (2016), p. 590. DOI: 10.1140/epjc/s10052-016-4430-0. arXiv: 1606.08753 [hep-ph].

[234] Andy Buckley et al. "LHAPDF6: parton density access in the LHC precision era". In: *Eur. Phys. J. C* 75 (2015), p. 132. DOI: 10.1140/epjc/s10052-015-3318-8. arXiv: 1412.7420 [hep-ph].

[235] Glen Cowan et al. "Asymptotic formulae for likelihood-based tests of new physics". In: *Eur. Phys. J. C* 71 (2011), p. 1554. DOI: 10.1140/epjc/s10052-011-1554-0. arXiv: 1007.1727 [physics.data-an]. Erratum: in: *Eur. Phys. J. C* 73 (2013), p. 2501. DOI: 10.1140/epjc/s10052-013-2501-z.

[236] Alexander L. Read. "Presentation of search results: the CL_S technique". In: *J. Phys. G* 28 (2002), p. 2693. DOI: 10.1088/0954-3899/28/10/313.

[237] Eilam Gross and A. Klier. "Higgs statistics for pedestrians". In: *10th International Conference on Supersymmetry and Unification of Fundamental Interactions (SUSY02)*. Nov. 2002, pp. 4–25. arXiv: hep-ex/0211058.

[238] F. James and M. Roos. "Minuit: A System for Function Minimization and Analysis of the Parameter Errors and Correlations". In: *Comput. Phys. Commun.* 10 (1975), pp. 343–367. DOI: 10.1016/0010-4655(75)90039-9.

[239] Kyle Cranmer et al. *HistFactory: A tool for creating statistical models for use with RooFit and RooStats*. Tech. rep. New York: New York U., 2012. DOI: 10.17181/CERN-OPEN-2012-016. URL: https://cds.cern.ch/record/1456844.

[240] Wouter Verkerke and David Kirkby. "The RooFit toolkit for data modeling". In: *Proceedings, 13th International Conference on Computing in High-Energy and Nuclear Physics (CHEP 2003)*. (La Jolla, California, Mar. 24–28, 2003), pp. 186–189. arXiv: physics/0306116 [physics.data-an].

[241] Lorenzo Moneta et al. "The RooStats Project". In: *PoS* ACAT2010 (2010). Ed. by T. Speer et al., p. 057. DOI: 10.22323/1.093.0057. arXiv: 1009.1003 [physics.data-an].

[242] Simone Amoroso et al. *Recommendations on the treatment of theoretical systematic uncertainties in statistical analysis of ATLAS data*. Tech. rep. Geneva: CERN, 2020. URL: https://cds.cern.ch/record/2715689.

[243] ATLAS Collaboration. "Measurements of the Higgs boson inclusive and differential fiducial cross sections in the 4ℓ decay channel at $\sqrt{s} = 13\,\text{TeV}$". In: *Eur. Phys. J. C* 80 (2020), p. 942. DOI: 10.1140/epjc/s10052-020-8223-0. arXiv: 2004.03969 [hep-ex].

[244] ATLAS Collaboration. "Measurements of the Higgs boson inclusive and differential fiducial cross-sections in the diphoton decay channel with pp collisions at $\sqrt{s} = 13\,\text{TeV}$ with the ATLAS detector". In: *JHEP* 08 (2022), p. 027. DOI: 10.1007/JHEP08(2022)027. arXiv: 2202.00487 [hep-ex].

[245] B. Grzadkowski et al. "Dimension-Six Terms in the Standard Model Lagrangian". In: *JHEP* 10 (2010), p. 085. DOI: 10.1007/JHEP10(2010)085. arXiv: 1008.4884 [hep-ph].

[246] Roberto Contino et al. "Effective Lagrangian for a light Higgs-like scalar". In: *JHEP* 07 (2013), p. 035. DOI: 10.1007/JHEP07(2013)035. arXiv: 1303.3876 [hep-ph].

[247] Ilaria Brivio, Yun Jiang, and Michael Trott. "The SMEFTsim package, theory and tools". In: *JHEP* 12 (2017), p. 070. DOI: 10.1007/JHEP12(2017)070. arXiv: 1709.06492 [hep-ph].

[248] A. G. Frodesen, O. Skjeggestad, and H. Tofte. *Probability and Statistics in Particle Physics*. Bergen, Norway: Universitetsforlaget, 1979. ISBN: 978-82-00-01906-0.

[249] ATLAS Collaboration. *Precise measurements of W and Z transverse momentum spectra with the ATLAS detector at $\sqrt{s} = 5.02$ TeV and 13 TeV*. Tech. rep. Geneva: CERN, 2023. URL: https://cds.cern.ch/record/2861057.

[250] ATLAS Collaboration. "Measurement of the total and differential Higgs boson production cross-sections at $\sqrt{s} = 13$ TeV with the ATLAS detector by combining the $H \to ZZ^* \to 4\ell$ and $H \to \gamma\gamma$ decay channels". In: *JHEP* 2305 (2023), p. 028. DOI: 10.1007/JHEP05(2023)028. arXiv: 2207.08615 [hep-ex]. URL: https://cds.cern.ch/record/2816107.

[251] Lyndon Evans and Philip Bryant. "LHC Machine". In: *JINST* 3 (2008), S08001. DOI: 10.1088/1748-0221/3/08/S08001.

[252] ATLAS Collaboration. *The ATLAS Experiment at the CERN Large Hadron Collider: A Description of the Detector Configuration for Run 3*. Geneva, May 2023. arXiv: 2305.16623 [physics.ins-det]. URL: https://cds.cern.ch/record/2859916.

[253] R. Frühwirth. "Application of Kalman Filtering to Track and Vertex Fitting". In: *Nucl. Instrum. Meth. A* 262.2-3 (Dec. 1987), pp. 444–450. DOI: 10.1016/0168-9002(87)90887-4.

[254] ATLAS Collaboration. *Track Reconstruction Performance of the ATLAS Inner Detector at $\sqrt{s} = 13$ TeV*. ATL-PHYS-PUB-2015-018. 2015. URL: https://cds.cern.ch/record/2037683.

[255] ATLAS Collaboration. *SiSpacePointsSeedMaker_ATLxk.cxx*. 2021. URL: https://gitlab.cern.ch/atlas/athena/-/blob/release/22.0.41.3/InnerDetector/InDetRecTools/SiSpacePointsSeedTool_xk/src/SiSpacePointsSeedMaker_ATLxk.cxx (visited on 09/15/2021).

[256] ATLAS Collaboration. *Inner Detector alignment development and performance in preparation for Run 3*. ATL-PHYS-PUB-2022-028. 2022. URL: https://cds.cern.ch/record/2811212.

[257] ATLAS Collaboration. *Studies on top-quark Monte Carlo modelling for Top2016*. ATL-PHYS-PUB-2016-020. 2016. URL: https://cds.cern.ch/record/2216168.

[258] ATLAS Collaboration. *ATLAS Pythia 8 tunes to 7 TeV data*. ATL-PHYS-PUB-2014-021. 2014. URL: https://cds.cern.ch/record/1966419.

[259] D. J. Lange. "The EvtGen particle decay simulation package". In: *Nucl. Instrum. Meth. A* 462 (2001), p. 152. DOI: 10.1016/S0168-9002(01)00089-4.

[260] T. Sjöstrand, S. Mrenna, and P. Skands. "A brief introduction to PYTHIA 8.1". In: *Comput. Phys. Commun.* 178 (2008), pp. 852–867. DOI: 10.1016/j.cpc.2008.01.036. arXiv: 0710.3820 [hep-ph].

[261] ATLAS Collaboration. *The Pythia 8 A3 tune description of ATLAS minimum bias and inelastic measurements incorporating the Donnachie–Landshoff diffractive model*. ATL-PHYS-PUB-2016-017. 2016. URL: https://cds.cern.ch/record/2206965.

[262] ATLAS Collaboration. *The ATLAS Collaboration Software and Firmware*. ATL-SOFT-PUB-2021-001. 2021. URL: https://cds.cern.ch/record/2767187.

[263] ATLAS Collaboration. "Study of the material of the ATLAS inner detector for Run 2 of the LHC". In: *JINST* 12 (2017), P12009. DOI: 10.1088/1748-0221/12/12/P12009. arXiv: 1707.02826 [hep-ex].

[264] ATLAS Collaboration. *ATLAS Inner Tracker Strip Detector: Technical Design Report*. ATLAS-TDR-025; CERN-LHCC-2017-005. 2017. URL: https://cds.cern.ch/record/2257755.

[265] ATLAS Collaboration. *Fast Track Reconstruction for HL-LHC*. ATL-PHYS-PUB-2019-041. 2019. URL: https://cds.cern.ch/record/2693670.

[266] John Baines et al. *Report of the ATLAS Alternative Event Filter Tracking Working Group*. Tech. rep. Geneva: CERN, 2019. URL: https://cds.cern.ch/record/2693094.

[267] *ATLAS HL-LHC Computing Conceptual Design Report*. Tech. rep. Geneva: CERN, 2020. URL: https://cds.cern.ch/record/2729668.

[268] ATLAS Collaboration. *Early Inner Detector Tracking Performance in the 2015 Data at $\sqrt{s} = 13$ TeV*. ATL-PHYS-PUB-2015-051. 2015. URL: https://cds.cern.ch/record/2110140.

[269] Maurice Garcia-Sciveres. *RD53B Design Requirements*. Tech. rep. Geneva: CERN, 2019. URL: https://cds.cern.ch/record/2663161.

[270] ATLAS Collaboration. *Expected tracking and related performance with the updated ATLAS Inner Tracker layout at the High-Luminosity LHC*. ATL-PHYS-PUB-2021-024. 2021. URL: https://cds.cern.ch/record/2776651.

[271] Michele Michelotto et al. "A comparison of HEP code with SPEC1 benchmarks on multi-core worker nodes". In: *Journal of Physics: Conference Series* 219.5 (Apr. 2010), p. 052009. DOI: 10.1088/1742-6596/219/5/052009. URL: https://dx.doi.org/10.1088/1742-6596/219/5/052009.

[272] HEPiX Benchmarking Working Group. *HEP-SPEC06 (HS06)*. URL: https://w3.hepix.org/benchmarking/HS06.html (visited on 09/29/2023).